UC Berkeley
UC Berkeley Electronic Theses and Dissertations

Title

I. Seismic Moment Tensor Analysis of Micro-Earthquakes in an Evolving Fluid-Dominated System, II. Ambient Noise Cross-Correlation for Evaluating Velocity Structure and Instrument Orientations in a Geothermal Environment

Permalink

https://escholarship.org/uc/item/09p8w3bj

Author

Nayak, Avinash

Publication Date

2017

Peer reviewed|Thesis/dissertation

eScholarship.org Powered by the California Digital Library
University of California

I. Seismic Moment Tensor Analysis of Micro-Earthquakes in an Evolving Fluid-Dominated System

II. Ambient Noise Cross-Correlation for Evaluating Velocity Structure and Instrument Orientations in a Geothermal Environment

by

Avinash Nayak

A dissertation submitted in partial satisfaction of the
requirements for the degree of

Doctor of Philosophy

in

Earth and Planetary Science

in the

Graduate Division

of the

University of California, Berkeley

Committee in charge:

Professor Douglas S. Dreger, Chair
Professor Michael Manga
Professor Bruce Buffett
Professor Steven D. Glaser

Fall 2017

I. Seismic Moment Tensor Analysis of Micro-Earthquakes in an Evolving Fluid-Dominated System

II. Ambient Noise Cross-Correlation for Evaluating Velocity Structure and Instrument Orientations in a Geothermal Environment

© 2017 Avinash Nayak
All rights reserved

Abstract

I. Seismic Moment Tensor Analysis of Micro-Earthquakes in an Evolving Fluid-Dominated System

II. Ambient Noise Cross-Correlation for Evaluating Velocity Structure and Instrument Orientations in a Geothermal Environment

by

Avinash Nayak

Doctor of Philosophy in Earth and Planetary Science

University of California, Berkeley

Professor Douglas S. Dreger, Chair

This dissertation presents a detailed analysis of recorded seismic waves in terms of their source and their propagation through the Earth in multiple scenarios. First, I investigate the source mechanisms of some highly unusual seismic events associated with the formation of a large sinkhole at Napoleonville salt dome, Assumption Parish, Louisiana in August 2012. I implemented a grid-search approach for automatic detection, location and moment tensor inversion of these events. First, the effectiveness of this technique is demonstrated using low frequency (0.1-0.2 Hz) displacement waveforms and two simple 1D velocity models for the salt dome and the surrounding sedimentary strata for computation of Green's functions in the preliminary analysis. In the revised, and more detailed analysis, I use Green's functions computed using a finite-difference wave propagation method and a 3D velocity model that incorporates the currently known approximate geometry of the salt dome and the overlying anhydrite-gypsum cap rock, and features a large velocity contrast between the high velocity salt dome and low velocity sediments overlying and surrounding it. I developed a method for source-type-specific inversion of moment tensors utilizing long-period complete waveforms and first-motion polarities, which is useful for assessing confidence and uncertainties in the source-type characterization of seismic events. I also established an empirical method to rigorously assess uncertainties in the centroid location, M_W and the source type of the events at the Napoleonville salt dome through changing network geometry, using the results of synthetic tests with real seismic noise. During 24-31 July 2012, the events with the best waveform fits are primarily located at the western edge of the salt dome at most probable depths of ~0.3-0.85 km, close to the horizontal positions of the cavern and the future sinkhole.

The data are fit nearly equally well by opening crack moment tensors in the high velocity salt medium or by isotropic volume-increase moment tensors in the low velocity sediment layers. The addition of more stations further constrains the events to slightly shallower depths and to the lower velocity media just outside the salt dome with preferred isotropic volume-increase moment tensor solutions. I find that Green's functions computed with the 3D velocity model generally result in better fit to the data than Green's functions computed with the 1D velocity models, especially for the smaller amplitude tangential and vertical components, and result in better resolution of event locations and event source type. The dominant seismicity during 24-31 July 2012 is characterized by the steady occurrence of seismic events with similar locations and moment tensor solutions at a near-characteristic inter-event time. The steady activity is sometimes interrupted by tremor-like sequences of multiple events in rapid succession, followed by quiet periods of little of no seismic activity, in turn followed by the resumption of seismicity with a reduced seismic moment-release rate. The dominant volume-increase moment tensor solutions and the steady features of the seismicity indicate a crack-valve-type source mechanism possibly driven by pressurized natural gas.

Accurate and properly calibrated velocity models are essential for the recovery of correct seismic source mechanisms. I retrieved empirical Green's functions in the frequency range ~ 0.2–0.9 Hz for interstation distances ranging from ~1 to ~30 km (~0.22 to ~6.5 times the wavelength) at The Geysers geothermal field, northern California, from cross-correlation of ambient seismic noise recorded by a wide variety of sensors. I directly compared noise-derived Green's functions with normalized displacement waveforms of complete single-force synthetic Green's functions computed with various 1D and 3D velocity models using the frequency-wavenumber integration method, and a 3D finite-difference wave propagation method, respectively. These comparisons provide an effective means of evaluating the suitability of different velocity models to different regions of The Geysers, and assessing the quality of the sensors and the noise cross-correlations. In the T-Tangential, R-Radial, Z-Vertical reference frame, the TT, RR, RZ, ZR and ZZ components (first component: force direction, second component: response direction) of noise-derived Green's functions show clear surface-waves and even body-wave phases for many station pairs. They are also broadly consistent in phase and relative inter-component amplitudes with the synthetic Green's functions for the known local seismic velocity structure that was derived primarily from body wave travel-time tomography, even at interstation distances less than one wavelength. I also found anomalous large amplitudes in TR, TZ, RT and ZT components of noise-derived Green's functions at small interstation distances ($\lesssim$4 km) that can be attributed to ~10°-30° sensor misalignments at many stations inferred from analysis of longer period teleseismic waveforms. After correcting for sensor misalignments, significant residual amplitudes in these components for some longer interstation distance ($\gtrsim$ 8 km) paths are better reproduced by the 3D velocity model than by the 1D models incorporating known values and fast axis directions of crack-induced shear-wave anisotropy in the geothermal field. I also analyzed the decay of Fourier spectral amplitudes of the TT component of the noise-derived Green's functions at 0.72 Hz with distance in terms of geometrical spreading and attenuation. While there is considerable scatter in the amplitudes of noise-derived Green's functions, the average decay is consistent with the decay expected from the amplitudes of synthetic Green's functions and with the decay of tangential component local-earthquake ground-motion amplitudes with distance at the same frequency.

Dedicated to my mother

Table of Contents

List of Figures

List of Tables

Acknowledgements

First and foremost, I would like to thank my advisor Prof. Douglas S. Dreger for his teaching, guidance, encouragement and patience that were critical in completion of my PhD. My current knowledge and skills in observational seismology are due to him. He also accepted me and guided me as an undergraduate intern, which opened doors to other opportunities for me. He is a great PhD advisor and was very supportive throughout my time here and also in pursuit of future career opportunities. I also want to thank my qualifying exam committee and dissertation committee members Professors Michael Manga, Bruce Buffett and Steven D. Glaser for their help and support in my qualifying exam, my research and my dissertation work. Outside seismology, I attended many inspiring classes taught by Prof. Michael Manga, who also provided me the opportunity to attend an incredible field trip. I also had very helpful interactions with Professors Richard Allen, Roland Bürgmann, Chi-Yuen Wang and Horst Rademacher, and I learned many things from them.

I also want to thank many collaborators and mentors for their help, support and guidance in my work here: Taka'aki Taira, Roland Gritto and Shaul Hurwitz (U.S. Geological Survey). I also want to thank Prof. Robert Herrmann (Saint Louis Univ.) for his help on his very useful software on numerous occasions. Julie Shemeta (MEQ Geo Inc.) provided a lot of resources in the analysis of the seismicity at the Napoleonville salt dome. More acknowledgements specific to each chapter in this thesis are listed at the end of the chapters.

I would not have been able to come this far without guidance, technical help and support from numerous colleagues, mentors and other students, especially members of the Dreger group. I will cherish my friendship and numerous meals and coffee breaks with Seung-Hoon Yoo who taught me a lot of things in seismology and coding, and remained a pillar of support and help throughout my PhD. Mong-Han Huang is a great source of inspiration; he was very helpful and supportive, especially during some very stressful periods. I am very fortunate to have a very kind friend in Noah Randolph-Flagg who helped me on numerous occasions throughout these years. Aurélie Guilhem mentored me during my internship, encouraged me to go for grad school and was very supportive during my initial years. I greatly benefited from discussions and suggestions from Andrea Chiang who was my immediate mentor and teacher here. Sierra Boyd accompanied me during numerous weekends and late-night shifts in the Seismolab. I am very thankful to Sierra Boyd, Shan Dou, Katie Wooddell, Voon Hui Lai and Nate Lindsey for their help, friendship and support throughout my PhD.

In BSL, Peggy Hellweg provided valuable insights into earthquakes and seismometers on numerous occasions. I had great fun times with Cheng Cheng, Felipe Orellana and Robert Martin-Short. I thank my senior officemates Zhao Zheng and Scott French for their support during my initial years. I also thank other members and visitors at Berkeley Seismology Lab and Department of Earth and Planetary Science for their friendship and technical help on many occasions: Chris Johnson, William Hawley, Qingkai Kong, Carolina Muñoz Saez, Seth Saltiel, Brent Delbridge, Kaiqing Yuan, Kathryn Materna, Kristen Fauria, Stephen Breen, Matthew Diamond, Alexander Minakov (Univ. of Oslo), Rob Porritt, Lian Xue, Landon

Damiao, Laura Maclean and Zhaoling Wang. I also thank BSL researchers Robert Nadeau, Robert Uhrhammer and Zachary Alexy for helpful interactions. Charley Paffenbarger and Stephen Thompson helped me with computer resources throughout the course of my study. EPS/BSL staff Jennifer Taggart, Margie Winn and Judith Coyote dealt with technical, administrative and financial details of my stay here.

Berkeley Seismology Lab has been my workplace and home for the last 5 years. I am very grateful and fortunate to have spent time here and to have interacted with brilliant and highly motivated researchers here.

I was primarily funded by NSF Grant 1447006, BSL Tocher Fellowship, NSF Grant EAR-1053211 and USGS contract GS-35F-0023P. The clusters *Comet* at the San Diego Supercomputing Center and *Baribu* at the BSL were crucial for the heavy computation of synthetic seismograms for the 3D velocity models. None of the research in this thesis would have been possible without the seismic data, and I thank people involved in deployment and maintenance of seismometers, archival of data and operations of the seismic networks. Google and Stack Overflow helped me in solving coding problems. I benefitted from the IRIS workshop at Indiana Univ. and the CIG workshops at UC Davis and Lawrence Livermore National Lab.

I want to thank my housemates Aamod Shanker, Song Zhang and Chin Shen Ong for their support during my stay here. Last but not the least, I want to thank Caldining, UC Berkeley for providing me cheap, convenient and great dinners during last three years. My IIT Kharagpur friends Amol Sawant, Pankaj Mishra and Anand Singh hosted me at KGP on my annual trips. Never-ending supply of entertainment from Aniket “Grayfox” Nayak kept my spirits high. Yui and Sera Senshi kept my mental health in check during the final year of grad school.

My mother, sister and brother-in-law were unconditionally supportive, helpful and patient while I was busy working during the last five years. My sister checked on me on numerous occasions to make sure that I didn’t miss my morning appointments.

I apologize: (1) for any shortcomings in the work in this dissertation, (2) for the work I was unable to complete during my stay here, (3) to anyone I have disappointed or hurt unintentionally and (4) to anyone I forgot to include in the acknowledgements.

Avinash Nayak
October 2017
BSL/UC Berkeley

Chapter 1

Introduction

This dissertation presents detailed analysis of recorded seismic waves in terms of their source and their propagation through the Earth at local distances. This chapter provides a brief introduction to the content in the remaining chapters. **Abstract** and **Introduction** sections at the beginning of each of the following chapters provide further details about their content.

The seismic moment tensor (MT) is routinely used to describe the source mechanism of seismic events in terms of moments of body-force equivalents (Jost & Herrmann 1989; Julian *et al.*1998; Aki & Richards 2002; Minson & Dreger 2008). It also determines the strength of the seismic waves radiated from seismic sources along with their radiation patterns. **Chapter 2** analyzes source mechanisms of some highly unusual seismic events associated with the formation of a sinkhole at Napoleonville salt dome (NSD), Assumption Parish, Louisiana (published as **Nayak & Dreger 2014**). The sinkhole had developed in response to the sidewall collapse of an abandoned brine cavern at the edge of the salt dome. This complex seismic sequence was also accompanied by intense natural gas influx into the shallow aquifer, evident from gas bubbling in surface water bodies. It is believed that the natural gas was likely moving through the disturbed rock column between the failed cavern and the sinkhole at the surface (Chicago Bridge & Iron Company [CB&I] 2013a; Louisiana Department of Natural Resources, Office of Conservation [LADNR, OOC] 2013).

There are considerable uncertainties in the travel-time locations of these seismic events; moreover, the large number of events in the sequence makes the standard event-by-event MT analysis approach impractical. Therefore, we adopt a grid-search based technique, GRiD MT (Kawakatsu 1998; Tsuruoka *et al.* 2009), for autonomous detection, location and MT inversion of these seismic events using data recorded by temporary U.S. Geological Survey stations. This study area is characterized by a large seismic velocity contrast between the high velocity salt dome and the low velocity soft sediments surrounding and overlying the dome-shaped salt body. Determination of source characteristics of seismic events requires corrections for wave propagation effects that are controlled by the seismic velocity structure. For the analysis in **chapter 2**, we use low-frequency (~0.1-0.2 Hz) displacement waveforms that justify a point source assumption and the approximation of the subsurface velocity structure with two simple 1D velocity models. Paths to stations above the sedimentary strata are assumed to conform to the lower velocity sediment model and paths to stations over the salt dome are assumed to conform to the higher velocity salt model. Green's functions (GFs) for the 1D models (1DGFs) are computed using the frequency-wavenumber integration method (Wang & Herrmann 1980; Herrmann *et al.* 2013a). We were able to detect ~62 events within a day just before the appearance of the sinkhole on 3 August 2012. We find that the events are occurring at depths ~0.47 km at the western edge of the salt dome. The MT solutions show large isotropic volume-increase components (~61%-82%). For one example event, we find the large volume-increase component in the full MT solution to be stable and

significant over the deviatoric MT solution (zero volume change), with respect to: (1) the choices of 1D velocity models, (2) contamination from noise and the degree-of-misfit and (3) the uncertainties in the centroid location and the MT solution itself. Based on the large volume-increase components in the MT solutions and the intense natural gas activity in the subsurface, we attribute these seismic events to high-pressure flow of natural gas or water–gas mixture through voids or pre-existing zones of weaknesses, such as cracks, fractures or faults at the edge of the salt dome, by volumetric expansion or tensile failure mechanisms similar to those observed in geothermal or volcanic environments (e.g. Julian *et al.* 1998; Chouet & Matoza 2013).

As demonstrated in **chapter 2**, MT analysis helps us to analyze the physical source mechanisms of regular earthquakes and also of exotic seismic events, i.e. those that deviate from pure double-couple tectonic earthquakes. The seismic MT is a 3x3 symmetric matrix. The ratios of its eigenvalues determine its source type. Source-type discrimination and assessing confidence and uncertainties in source-type characterization of seismic events is of great importance, especially for monitoring nuclear explosions (volume-increase MTs; e.g., Ford *et al.* 2009a,b, 2010, 2012; Chiang *et al.* 2014) and underground collapses (volume-decrease MTs; Ford *et al.* 2008), and analysis of induced seismic events (e.g., Šílený *et al.* 2009; Guilhem *et al.* 2014). In **chapter 3** (published as **Nayak & Dreger 2015**), we design an iterative damped least-squares inversion scheme to invert waveforms and/or *P*-wave first motions for best-fitting MT solutions for specific source types. In this framework, the MT elements are expressed as a function of: (1) normalized eigenvalues that determine the source type, (2) orthonormal eigenvectors that determine the orientation of the MT in 3D space and (3) a moment scale factor that scales the normalized eigenvalues to the absolute size or scalar moment of the MT. In the inversion scheme, a source type is assigned and the inversion solves for the best-fitting eigenvectors and moment scale factor with the source type kept fixed. The inversion scheme is first applied to synthetic data and demonstrated to be successful. Thereafter, we invert MT solutions of an example event from the NSD sinkhole sequence, assuming various source types – an explosion, an opening crack in the sediment medium, an opening crack in the salt and a pure double-couple (DC) source. The greatest benefit of this inversion method is the faster and more reliable construction of the network sensitivity solution (NSS, Ford *et al.* 2010) that is used to assess recovery of source-type information under changing network topology and to assess confidence and uncertainties in the MT solution of a seismic event with respect to its source type. We test our NSS-inversion method on three example events: (1) the example event at the NSD sinkhole, (2) a very shallow industrial quarry explosion, and (3) an earthquake at The Geysers geothermal field, northern California. We find that our inversion method is more accurate and successful than the commonly used random-search approach in recovering the region of best-fitting MT solutions or source types and is substantially faster. The approach also enables the determination of the best-fitting MT for specified source types such as pure double couples, tensile cracks, or explosions, as well as compound mechanisms in a single numerical framework.

In **chapter 4**, we further analyze and refine the source mechanisms of the seismic events at the NSD. We perform MT inversions using waveforms in a higher frequency passband (~0.1-0.3 Hz) that improves the signal-to-noise of the data for relatively smaller events. We also use

GFs computed with a 3D velocity model (3DGFs). The 3D model incorporates the currently known approximate geometry of the salt dome and the overlying anhydrite-gypsum cap rock, and features the large velocity contrast between the high velocity salt dome and low velocity sediments overlying and surrounding it. In some source inversion studies of earthquakes at regional distances, GFs of properly calibrated 3D velocity models have been found to be helpful in improving fits to higher frequency waveforms (e.g., Covellone & Savage 2012; Zhu & Zhou 2016). In some other studies, it has been reported that small non-double-couple components commonly found in MT solutions of earthquakes estimated assuming GFs for 1D velocity models (1DGFs) can be caused by unaccounted-for path effects resulting from the real 3D velocity structure (Panning *et al.* 2001; Covellone & Savage 2012). The strong 3D nature of the subsurface velocity structure at the western side of the NSD motivates our study. For each possible location on the source grid, GFs to each station were computed using source-receiver reciprocity (Eisner & Clayton 2001) and the finite-difference seismic wave propagation software SW4 (Sjögreen & Petersson 2012; Petersson & Sjögreen 2015). We also establish an empirical method modified after Almendros & Chouet (2003) to rigorously assess uncertainties in the centroid location, M_W and source type of these events under evolving network geometry, using the results of synthetic tests with hypothetical events and real seismic noise. The methods are applied on the entire duration of data (~6 months) recorded by the temporary US Geological Survey network.

During an energetic phase of the sequence from 24-31 July 2012 when 4 stations were operational, the events with the best waveform fits are primarily located at the western edge of the salt dome at most probable depths of ~0.3-0.85 km, close to the horizontal positions of the cavern (which extends from ~1.0 km to ~1.7 km depth) and the future sinkhole. The presence of a strong material interface in the source region introduces large uncertainties in centroid location and the MT solution (Vavryčuk 2013). The data are fit nearly equally well by opening crack MTs in the high velocity salt medium or by isotropic volume-increase MTs in the low velocity sediment layers. The addition of more stations further constrains the events to slightly shallower depths. We find that data recorded by 6 stations during 1-2 August 2012, right before the appearance of the sinkhole, indicate that some events are likely located in the lower velocity media just outside the salt dome at depths ~0.35-0.65 km, with preferred isotropic volume-increase MT solutions. We find that 3DGFs generally result in better fit to the data than 1DGFs, especially for the smaller amplitude tangential and vertical components, and result in better resolution of event locations and event source type.

We describe the evolution of the seismicity from 15 July to 2 August 2012 in terms of M_W, percentage of isotropic moment in the MT solution, displacement amplitudes at the farthest stations, centroid location and the goodness-of-fit between the observed waveforms and predicted waveforms for the best-fitting MT solution. We obtained centroid MT solutions of more than 1,500 events. The dominant seismicity during 24-31 July 2012 is characterized by steady occurrence of seismic events with similar locations and MT solutions at a near-characteristic inter-event time. The steady activity is sometimes interrupted by tremor-like sequences of multiple events in rapid succession, followed by quiet periods of little of no seismic activity, in turn followed by the resumption of seismicity with a reduced seismic moment-release rate. We compare the features of the seismicity at the NSD with other cases of seismicity associated with underground salt cavity collapses (Trifu & Shumila 2010;

Jousset & Rohmer 2012; Kinscher *et al.* 2015) and volcanic activity (Chouet & Matoza 2013). The dominant volume-increase MT solutions and the steady features of the seismicity indicate a crack-valve-type source mechanism possibly driven by pressurized natural gas.

The analysis of the seismicity at NSD in **chapter 4** reinforces the importance of reliable, well-calibrated 3D velocity models for accurate determination of seismic source mechanisms. In the last ~10 years, ambient noise cross-correlation has emerged as a very important tool for determination of subsurface velocity structure especially in regions with dense continuously recording seismic networks and relatively fewer earthquakes (Shapiro *et al.* 2005; Bensen *et al.* 2007). Cross-correlation of ambient noise recorded by 3-component sensors leads to a complete 9-component noise-derived Green's functions (NGFs). Typically, only surface waves retrieved from the primary components of NGFs (TT, RR, RZ, ZR, ZZ; T: tangential, R: radial, Z: vertical; first letter: force direction, second letter: response direction) at far-field distances (interstation distance $\gtrsim 3\lambda$, where λ is the surface-wave wavelength) are generally used in surface-wave tomography studies (e.g. Lin *et al.* 2008). NGFs at near-field distances ($< \lambda$) and the amplitudes in the off-diagonal components of NGFs (TR, TZ, RT, ZT) have not been fully explored or analyzed. In **chapter 5**, we retrieve NGFs in the frequency range (~ 0.2-0.9 Hz) for interstation distances ranging from ~1 to ~30 km (~0.22 λ to ~6.5 λ) at The Geysers geothermal field, northern California, from cross-correlation of seismic noise being recorded by a variety of sensors (broadband, short-period [1.0 Hz, 4.5 Hz or 8.0 Hz] surface and borehole sensors, and one accelerometer). The Geysers geothermal field is the largest complex of geothermal power plants in the world today. It has witnessed a considerable increase in the number of small-magnitude earthquakes (M_W 1.5–4.0) in response to steam production and water injection for reservoir recharge since the 1960s (Majer & Peterson 2007). Investigations of focal mechanisms and MTs of these earthquakes have shed some light on various aspects of their source mechanisms such as anomalous isotropic components in full MT solutions of many $M_W > 3.5$ earthquakes (Oppenheimer 1986; Ross *et al.* 1999; Guilhem *et al.* 2014; Boyd *et al.* 2015). However, imperfect knowledge of subsurface seismic velocity structure and assumption of 1D velocity models are believed to introduce considerable uncertainties in synthetic ray paths and in synthetic GFs required for source inversion. 3D *P*-wave and *S*-wave travel-time tomography studies have revealed considerable heterogeneities in the subsurface (Julian *et al.* 1996; Ross *et al.* 1999; Gritto *et al.* 2013a) that must be taken into account for recovery of accurate source mechanisms.

We directly compare NGFs at The Geysers with normalized displacement waveforms of complete single-force synthetic Green's Functions (SGFs) computed with various 1D and 3D velocity models using the frequency-wavenumber integration method and a 3D finite-difference wave propagation method, respectively. We evaluate the similarity of NGF and SGF waveforms in terms of waveform fits, phase and relative inter-component amplitudes. NGFs with little or no coherent energy in the ballistic wave arrival time window or NGFs that bear little or no resemblance to SGFs expected for a wide variety of reasonable and expected velocity models are interpreted to be contaminated with errors possibly due to poor sensor coupling, or non-uniformity of ambient noise source distribution. After discarding these erroneous NGFs, we use the remaining NGFs to evaluate the applicability of various 1D velocity models and the 3D velocity model to different sub-regions of The Geysers as NGFs contain information about real Earth 3D wave propagation (e.g., Ma *et al.* 2008). For the data

at The Geysers, the primary components (TT, RR, RZ, ZR and ZZ) of NGFs show clear surface-waves and even body-wave phases for many station pairs. They are also broadly consistent in phase and relative inter-component amplitudes with SGFs for the known local seismic velocity structure that was derived primarily from body wave travel-time tomography, even at interstation distances less than 1λ. For example, SGFs computed with the faster model VSP0 and the slower model REF preferentially provide better waveform fits to the NGFs for interstation paths across southeast and northwest Geysers, respectively. Our study additionally includes: (1) an analysis of long period teleseismic waveforms to verify sensor orientations (e.g. Grigoli *et al.* 2012), (2) application of the Optimal Rotation Algorithm (Roux 2009) on the NGFs to detect any dominant noise source illumination direction, and (3) comparison with SGFs computed using the 1D models incorporating known values and fast axis directions of crack-induced V_S anisotropy in the geothermal field (Crampin 1984; Elkibbi *et al.* 2005). We find significant non-zero amplitudes in TR, TZ, RT and ZT components of NGFs for many stations pairs that can be attributed to a combination of sensor misalignments (> 10°) at many stations and the effects of the 3D velocity structure of the reservoir based on the above-mentioned evaluations.

We also analyze the decay of Fourier spectral amplitudes of the TT component of NGFs at 0.72 Hz with distance in terms of geometrical spreading and attenuation. While there is considerable scatter in the NGF amplitudes, we find the average decay to be consistent with the decay expected from SGF amplitudes and with the decay of tangential component local-earthquake ground-motion amplitudes with distance at the same frequency. The flattening of RR component spectral amplitudes at distances ~9-16 km suggests possible recovery of the near-field term.

Chapter 2

Preliminary Moment Tensor Analysis of Seismic Events associated with the Sinkhole at Napoleonville Salt Dome, Louisiana in the 0.1-0.2 Hz Frequency Band

Published as:
Nayak, A. & Dreger, D.S., 2014. Moment tensor inversion of seismic events associated with the sinkhole at Napoleonville Salt Dome, Louisiana, *Bull. Seism. Soc. Am.*, **104** (4), 1763-1776, doi: 10.1785/0120130260.

2.1 Chapter Abstract

The formation of a large sinkhole at Napoleonville salt dome, Assumption Parish, Louisiana in August 2012 was accompanied by a rich sequence of complex seismic events. We implement a grid-search approach for automatic detection, location and full moment tensor (MT) inversion of these events using 0.1-0.2 Hz displacement waveforms and 1D velocity models for the salt dome and the surrounding sedimentary strata. We were able to detect 62 events, with a 70% variance reduction (VR) detection threshold, during the one-day period (19:00 hours, 01 August – 19:00 hours, 02 August, 2012) just before the discovery of the sinkhole. The source mechanisms of these events show large isotropic volume-increase components (61%-82%) with magnitudes varying from M_W 1.3 to 1.6 and good waveform fits (71%-86% VR). Locations are well constrained to an approximate depth of 470 m at the western edge of the salt dome, close to the sinkhole. For one representative event, the large volume-increase component in the full MT solution is statistically significant over the deviatoric MT solution and stable with respect to: (1) the velocity models and stations used in the inversion, and (2) the uncertainties in the hypocenter and the MT solution itself. The network sensitivity solution computed for this event using both waveforms and *P*-wave first motion polarities provides greater confidence in the dominantly explosive source mechanism, which can be attributed to high-pressure flow of natural gas or gas-water mixture through the disturbed rock zone below the sinkhole or pre-existing zones of weaknesses in the source region.

2.2 Introduction

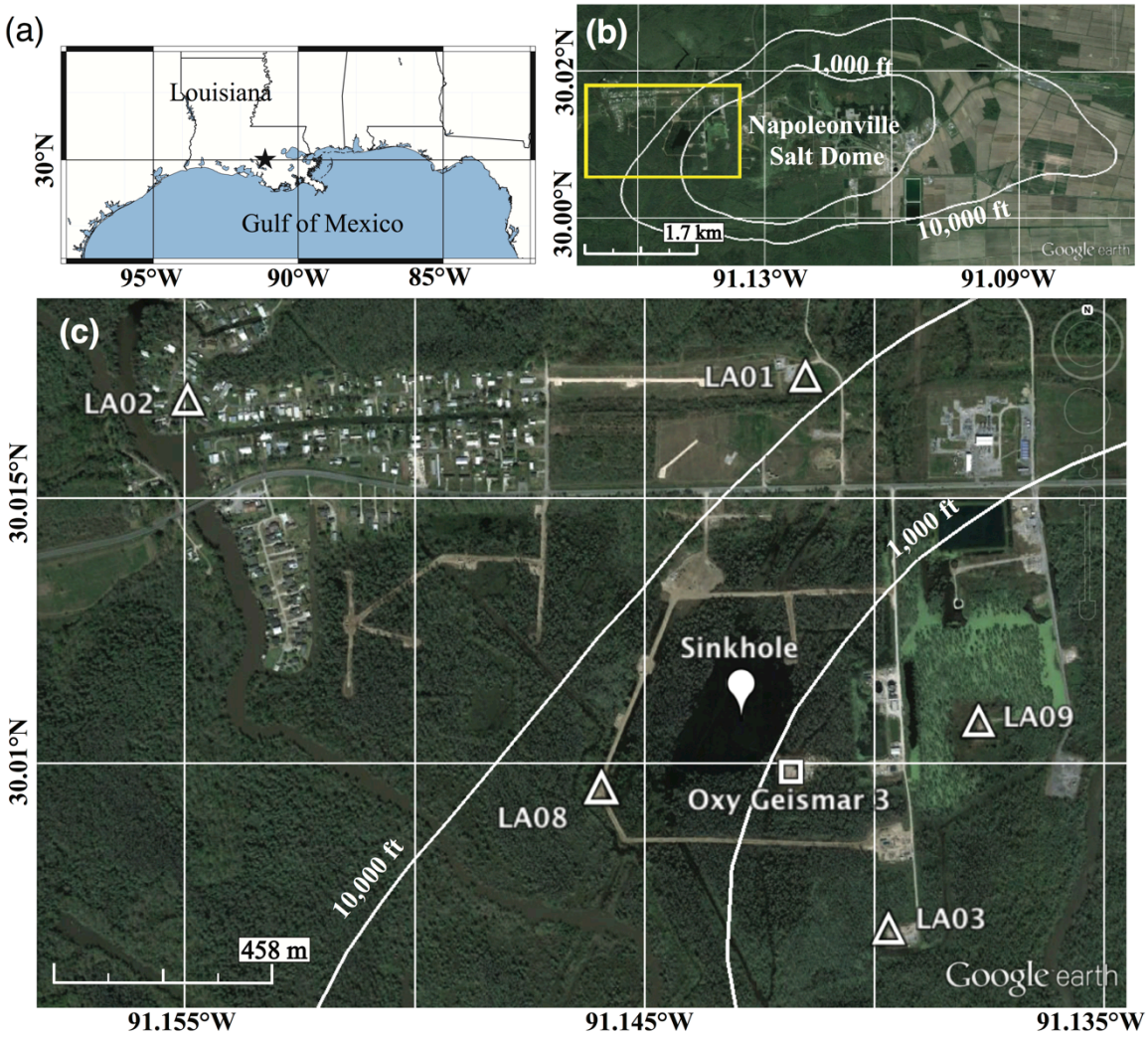

Figure 2.1: (a) Location of the study region (black star) relative to the state of Louisiana (southeastern USA). Google Earth Images (dated 12 March 2013) show- (b) the study region, indicated by the rectangle and expanded in (c), at the western edge of NSD (approximately known 1000 ft and 10,000 ft contours indicated by white lines; William Ellsworth, personal comm., 2012); (c) Locations of the five U.S. Geological Survey broadband stations used for waveform inversion (white triangles), approximate location of Oxy Geismar 3 (OG3) cavern (white square) and an average point location of the sinkhole (white balloon).

The Napoleonville salt dome (NSD) is located at -91.13°E, 30.01°N, near Bayou Corne, Assumption Parish, southeast Louisiana (Fig. 2.1). It is a part of the Gulf Coast salt basin, which exhibits many salt structures formed by upward flow of sedimentary salt (primarily evaporites) due to the low density of salt and overburden pressures caused by younger sedimentary deposits (Beckman & Williamson 1990). It penetrates the Mississippi River

Valley Alluvial Aquifer (MRAA) zone, which is primarily composed of upper Pleistocene-Holocene sediments, to an approximate depth of 200 m (Beckman & Williamson 1990). Salt domes are commonly used for solution mining of salt; and caverns thus formed are also used for storage of hydrocarbons and industrial wastes because of the strong impermeability of salt (Thoms & Gehle 2000). 54 caverns distributed over an area of 1.6 km (N-S) to 4.8 km (E-W) have been operating in NSD at various times since 1950, both for brine mining and storage. Beginning in June 2012, residents of Bayou Corne reported frequent tremors and unusual gas bubbling in local surface-water bodies (Chicago Bridge & Iron Company [CB&I] 2013a). The parish requested the assistance of the United States Geological Survey (USGS) to monitor the continuous seismic activity. A temporary network of seismic stations was set up, which revealed a sequence of numerous seismic events (Ellsworth *et al.* 2012; Horton *et al.* 2013). On 03 August 2012, a large sinkhole was discovered close to the western edge of the salt dome (Fig. 2.1b), leading to a declaration of emergency and evacuation of nearby residents (Louisiana Department of Natural Resources, Office of Conservation [LADNR, OOC] 2013). The sinkhole, filled with a slurry of water, crude oil and debris, was swallowing cypress trees, and its geometry has been actively changing ever since, with recent estimates of surface area exceeding than 20,000 m^2 and maximum depth varying between ~ 30 and 100 m over time (CB&I 2013a). Subsidence, intermittent seismicity and bubbling of natural gas have been observed in the affected region. Preliminary investigations suggest that possible collapse of the lower sidewall of a plugged and abandoned brine cavern, Oxy Geismar 3 (OG3), might be a potential cause of the sinkhole (CB&I 2013a; LADNR, OOC 2013). It has been hypothesized that the collapse fractured to the surface, creating a disturbed rock zone which provides a pathway for formation fluids, natural gas and crude oil from deeper strata that are now accumulating in the sinkhole and the surrounding subsurface (CB&I 2013a).

Historical seismicity in the state of Louisiana includes a widely felt magnitude 4.2 earthquake (peak intensity VI on MMI scale) on 19 October 1930 near Napoleonville, Assumption Parish (Stover & Coffman 1993); the epicenter might have been close to the present location of the sinkhole. However, this region (-91.16°E to –91.13°E, 30°N to 30.025°N) has experienced little or no seismicity in recent years, with no earthquakes reported in the National Earthquake Information Center's Preliminary Determination of Epicenters (PDE) Bulletin between January 1973 and April 2012. Therefore, the synchronous nature of seismicity and development of the sinkhole suggests that the two phenomena are most likely related. In this study, we investigate source mechanisms of seismic events at the sinkhole, represented by a general 2^{nd} order point-source centroid seismic moment tensor (MT). We implement a grid-search approach, GRiD MT (Kawakatsu 1998; Tsuruoka *et al.* 2009) for automatic detection, location and MT inversion of these events using available seismic-wave velocity models for this area. We show results for the time period of one day just prior to formation of the sinkhole. We check the stability and reliability of the MT solutions and interpret them in terms of possible physical processes.

2.3 Data and Moment Tensor Inversion

Three-component waveforms were continuously recorded at 40 samples per second by a temporary USGS network consisting of Trillium Compact broadband seismometers and a Reftek RT130 digitizer (Fig. 2.1c), which enables the study of this seismic sequence in great detail. We examine events starting from 19:00 hours, 01 August 2012 (just after station LA09 became operational). As signals at station LA06 (not shown in Fig. 2.1c, but located east-southeast of the sinkhole, at –91.12858°E, 30.00771°N) are very weak and have higher noise levels, we did not use its data in the waveform inversion. Fig. 2.2a shows the five-hour (19:00 – 24:00 hours, 01 August 2012), three-component raw seismograms at station LA02. A cursory examination shows more than 30 small and large events spanning one order in peak amplitude.

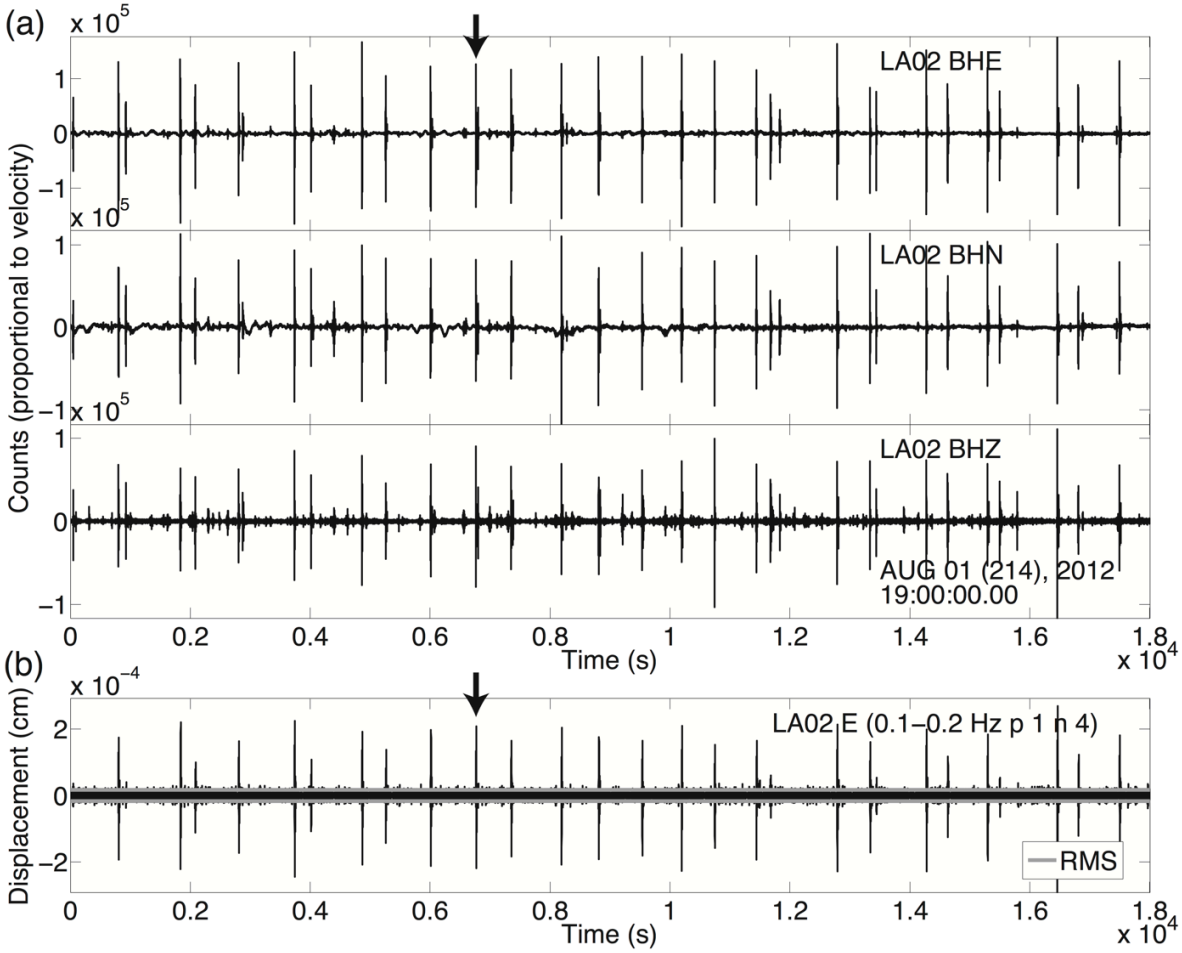

Figure 2.2: (a) Raw five-hour record on 1 August 2012 at station LA02. The arrow at the top points to the event TE1, which is analyzed in detail in the following sections. (b) East-west displacement at LA02 in the frequency range used in this study for the same time period as (a). Gray lines indicate the overall background signal level (± root mean square [RMS]), in which RMS = 1.76×10^{-5} cm.

Three-component velocity waveforms at station LA08 for two of these events are shown in Fig. 2.3. The records primarily show strong surface waves. Our analysis of multiple events indicates that the waveforms are quite similar to each other, indicating closely spaced hypocenters and a repetitive source process. For most events, the duration of the strongest ground motions is limited to 5-15 seconds.

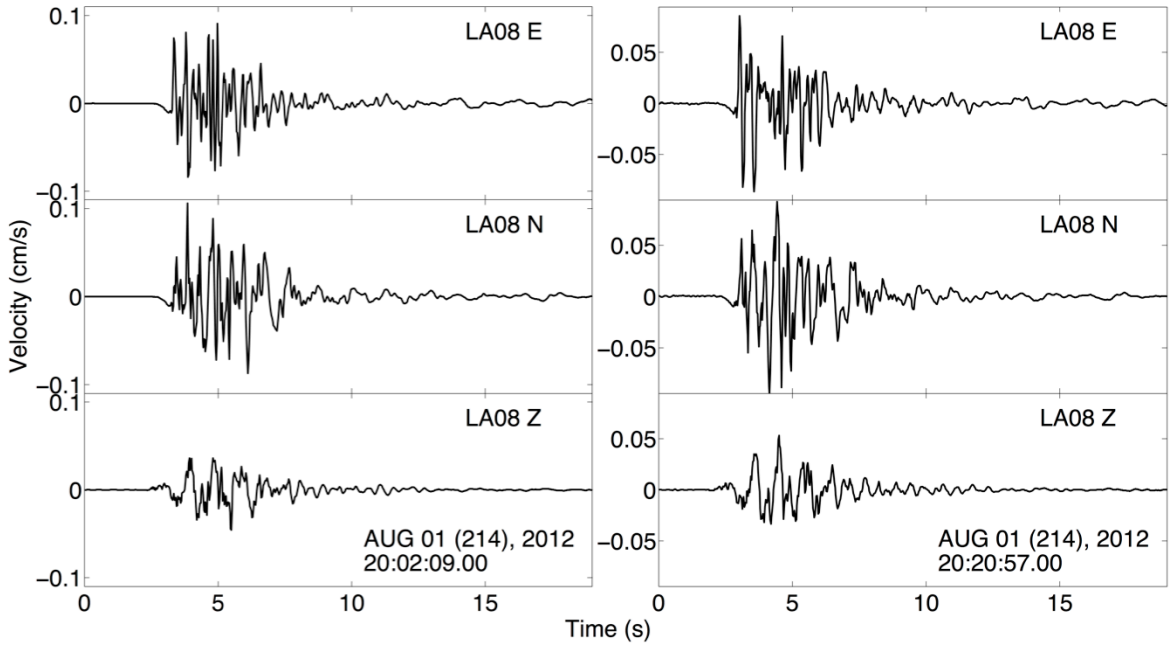

Figure 2.3: Velocity waveforms for two different events at station LA08.

Variations in the seismic properties of the subsurface along the specific paths are evident from different characteristics of the broadband, ~0.1–15 Hz, vertical-component velocity waveforms (Fig. 2.4). Stations LA08, LA01 and LA02 are on sedimentary deposits surrounding the salt dome and show waveforms which are very similar to each other but quite different from waveforms at stations LA09 and LA03, which are on sediments over the salt dome. This suggests that the salt dome structure affects seismic wave propagation over these relatively short source-receiver distances.

The time-independent, 2nd order, 6-component general MT (Jost & Herrmann 1989; Minson & Dreger 2008) is routinely used to describe the source mechanisms of seismic events. The scalar seismic moment (M_0), and therefore the M_W are determined, and the MT describes the mechanism in terms of body force equivalents, that is, double couples and linear vector dipoles, assuming a point source in space and time. It can be decomposed into isotropic (volume change) and deviatoric (zero volume change) components. Typically earthquakes are adequately described by a double-couple (DC) mechanism in which one of the eigenvalues is zero and the other two are equal and opposite in sign, although small non-DC solutions are often found due to noise in the data, unaccounted path effects (Panning *et al.* 2001), or possible complications in the source process involving non-planar rupture (Julian *et al.* 1998). The MT also enables the study of seismic source processes for non-earthquake events, such as

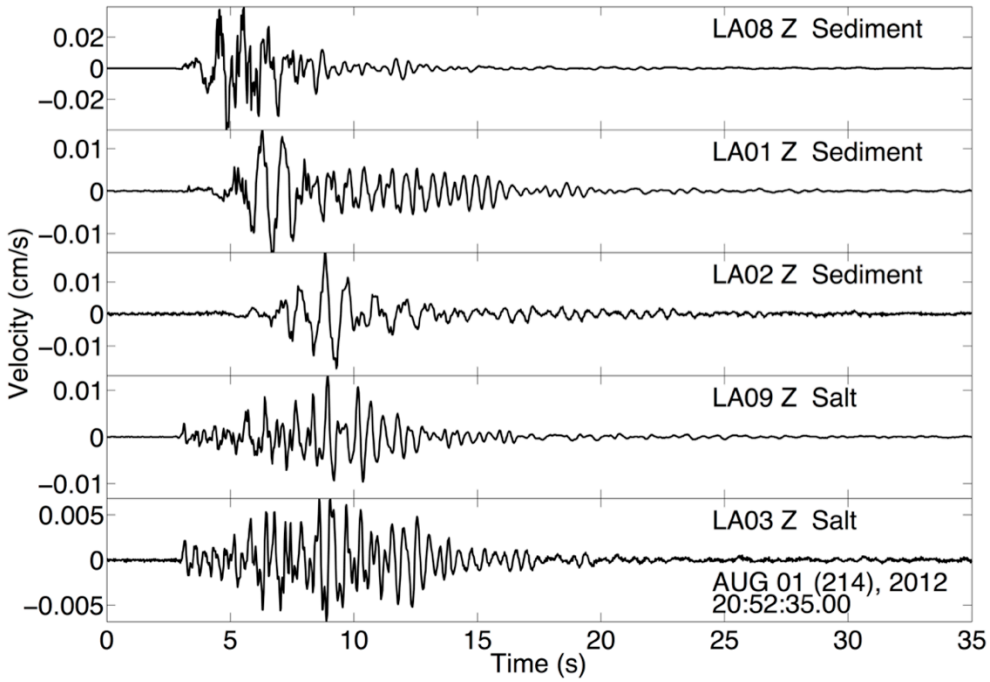

Figure 2.4: Vertical-component velocity records for one event (TE1) at all five stations.

nuclear explosions (Ford *et al.* 2009a, b) and mine collapses (Ford *et al.* 2008) that involve volume changes that result in significant isotropic components (ISO) in their MT solutions. The MT inversion methodology is described in detail in Jost & Herrmann (1989), Julian *et al.* (1998), and Minson & Dreger (2008). The requirements of a standard MT inversion are a hypocenter and a sufficiently accurate velocity model. The inversion then solves for the MT and the source depth. The emergent nature of first arrivals in waveforms of the seismic events at the Louisiana sinkhole (Figs 2.3 and 2.4) makes accurate picking of *P*-wave and *S*-wave arrivals difficult. Moreover, given that the distances are very small, a small uncertainty in arrival times will translate to a large relative error in event location. The available 1D velocity models (Fig. 2.5) of the study region (William Ellsworth, *personal communication*, 2012) show large differences between seismic-wave velocities at the salt dome and surrounding sedimentary structure, which are in turn reflected in the broadband seismic waveforms as already explained in Fig. 2.4. The sediment velocity model shows smoothly increasing velocities with gradients decreasing with increasing depth. The velocity model over the salt dome consists of steep velocity gradients associated with sediments over the salt dome up to a depth of ~250 m. The salt dome is considered to be a fast half-space (V_P = 4.5 km/s and V_S = 2.5 km/s), surrounded and overlain by slower sedimentary layers. The 3D nature of the subsurface is bound to influence estimates of the source location and *MT* solution at shorter periods, however, considering two 1D velocity models as a first approximation is a reasonable approach if long-period data are used. The *P*-wave and *S*-wave first arrival times computed using these velocity models and the ray-tracing algorithm of Um & Thurber (1987) are weakly sensitive to depth, leading to large uncertainties in depth estimates. Moreover, the large number of seismic events, more than 100 on some days, makes a standard event-by-event analysis of location and MT impractical.

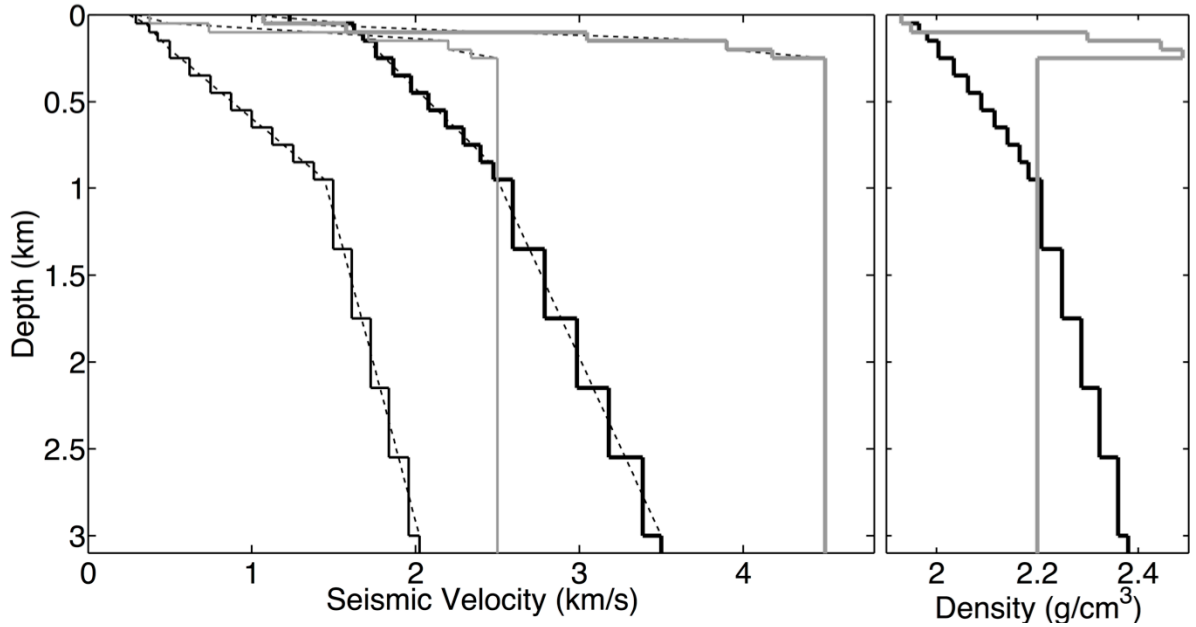

Figure 2.5: Velocity and density models used in this study. Gray and black lines represent salt and sediment models, respectively. For velocities, thick and thin lines represent V_P and V_S, respectively. The thin dashed black lines are original smooth velocity models with gradients, which were discretized into layers and used to compute the Green's functions.

In light of these difficulties, we employ the grid-search approach, GRiD MT, of Kawakatsu (1998), which continuously scans the seismic wavefield and performs MT inversions of relatively low-frequency waveforms, assuming a discrete 3D grid of point sources. For a given time window of data, the source location and MT solution which give the best Variance Reduction (VR), a measure of normalized goodness of fit between observed and synthetic waveforms (Minson & Dreger 2008), is inferred to be the true seismic source. This approach has been used for detection and source characterization of offshore earthquakes in Japan using streaming long-period waveforms (Tsuruoka *et al.* 2009) and has been modified for a tsunami early warning application for megathrust earthquakes (Guilhem & Dreger 2011; Guilhem *et al.* 2013). Based on preliminary analyses, we construct a grid extending from 30.007°N to 30.0136°N, –91.1452°E to –91.138°E and depth 0.02–1.77 km, with grid spacing of 0.0006° and 50 m in horizontal and vertical directions, respectively. This grid spans the present volume extent of the probable source regions: (1) the sinkhole, and (2) the OG3 cavern, which extends in depth from ~1.0 to ~1.7 km (CB&I 2013a). The three-component broadband velocity waveforms are first corrected for instrument response and then integrated to displacement. At sufficiently low frequencies, the seismic waveforms become less sensitive to small-scale heterogeneities in earth structure making simplified and approximate velocity models applicable, and the seismic source can be treated as an effective point source in space and time. We have tried a range of filters with different corner frequencies and pole orders and found that a causal 4-pole Butterworth band-pass filter with corner frequencies at 0.1 Hz and 0.2 Hz greatly simplifies the displacement waveforms while clearly distinguishing signals of larger events from the noise floor (Fig. 2.2b). This filter is subsequently applied to both observed and synthetic waveforms. It is also important to note that there is a narrowband weakly damped harmonic signal at 0.4 Hz in many of the events that precludes using shorter

periods, but which may be indicative of a triggered acoustic-wave phenomena within the brine filled cavity or resonance possibly induced by unsteady fluid flow through a tensile crack (Chouet 1986; Kumagai *et al.* 2005). Detailed analysis and modeling of this harmonic signal is beyond the scope of this paper that focuses on the MT analysis, and will be investigated in future works.

For waveform modeling in subsequent sections, seismic paths to stations LA01, LA02 and LA08 are assumed to conform to the sediment velocity model, and seismic paths to stations LA03 and LA09 are assumed to conform to the salt dome velocity model. For $V_P > 1.5$ km/s, density values for sedimentary layers are computed from V_P values using Gardener's rule, $\rho = 1.74\ V_P^{0.25}$ (Gardener *et al.* 1974). For $V_P < 1.5$ km/s, density is kept constant at 1.93 g/cm^3. Salt density is assumed to be 2.2 g/cm^3. At such small distances (< 2.0 km), which are smaller or comparable to the seismic wavelengths being used, waveforms are expected to be weakly affected by anelastic attenuation. Therefore, regional Q_P and Q_S values are assumed to be 200 and 100, respectively. The effects of different values of Q on synthetic waveforms were analyzed afterwards, and displacement amplitudes at these low frequencies were found to be insensitive to Q_S values down to 25, with $Q_P = 2 \times Q_S$ (Fig. 2.A.1 in section **2.11 Appendix**). The smoothly varying 1D sediment and salt dome velocity models were discretized to layered models and Greens' functions (GF) were computed for all grid point depths and all distances from 0.01 km to 2.15 km with a precision of 0.01 km, using the frequency-wavenumber integration software *FKRPROG* developed by C.K. Saikia based on the methods of Haskell (1964), Dunkin (1965), Watson (1970), Wang & Herrmann (1980), and Saikia (1994). GFs are filtered in the same way as data and decimated to 0.5 s sampling. A 25 s time window is extracted from filtered data and then decimated to 0.5 s. Assuming each grid point as a virtual source, a full six-component (M_{xx}, M_{yy}, M_{zz}, M_{xy}, M_{yz}, M_{zx}) MT inversion is performed using expressions from Minson & Dreger (2008). The VR is calculated for each inversion and is used to assess goodness of fit and to identify the best-fitting solution. The time shift to select the next time window is 0.25, 0.5, or 1.0 s depending on the value of the best VR from the previous time window (< 35%, between 35% and 55% or > 55%, respectively). This ensures that the grid search traverses noise windows faster, which typically return poor values of VR, while maintaining the origin time resolution at 0.25 s. Coarse sampling of waveforms and adaptive time shifting make the algorithm computationally fast.

GRiD MT is applied to data shown in Fig. 2.2b. The results, in the form of the change in VR with time, are shown in Fig. 2.6. After assuming a threshold VR of 70%, which is well above the mean background VR, we find 23 events during this period. We have also detected some other unusual signals, both long period and tremor-like, which are usually restricted to the closer stations (LA03, LA08 and LA09) and might be related to tilts or some near-field deformation in the source region, unsteady fluid flow, or local noise sources (signals not correlated across multiple stations). Because broadband characteristics of these signals are completely different from the signals of the discrete seismic events we are focusing on, they are not included in this study.

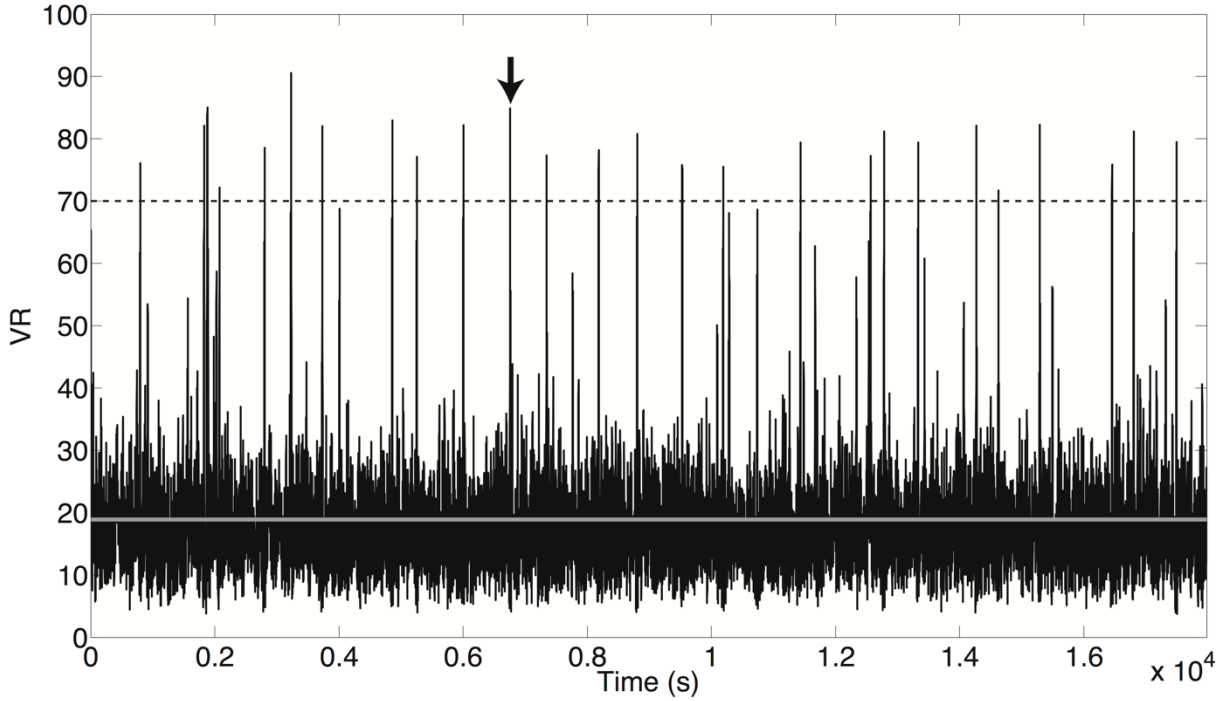

Figure 2.6: Variance Reduction (VR) with time for data shown in Fig. 2.2b. Peaks with VR > 70% (dashed line) are considered to be probable seismic events. The arrow at the top points to event TE1, indicated in Fig. 2.2. The gray line indicates the mean background VR (18.9 %) for this time period.

Details of the MT solution and corresponding waveform fits for the best event in this time period, event TE1 (indicated in Figs 2.2 and 2.6) are shown in Fig. 2.7a. This event was located at grid point –91.1422°E, 30.0112°N, depth 0.47 km, and centroid time 1 August 2012, 20:52:39.00 hours. The solution fits the data very well at VR 84.8% and can explain most of the strong radial and vertical components. We find a large volume-increase component (ISO 72%) in the full MT solution. Following the definition of Bowers & Hudson (1999), the M_0 of the events is calculated as, $M_0 = M_I + M_D$, in which $M_I = |(m_1 + m_2 + m_3)/3|$ is the isotropic moment, $M_D = \max(|m_j - (m_1 + m_2 + m_3)/3|)$ is the deviatoric moment, and m_1, m_2 and m_3 are the eigenvalues of a general moment tensor. Event TE1 has a scalar moment thus defined of 2.4×10^{18} dyne.cm, corresponding to M_W 1.53. The spatial distribution of VR in Figs 2.7b,c shows that our centroid location is fairly well constrained, and located east of the sinkhole, at the edge of the salt dome. Despite the long seismic wavelengths, the use of three-component complete waveforms provides both arrival time and azimuth dependent polarity information for various phases, thereby strongly constraining the locations. We suspect that these events are occurring within the salt, but at this point, we are unable to precisely put the event in the salt or the surrounding sediments due to the coarse grid spacing (~ 60 m), the long seismic wavelengths of data used in the inversion, and the uncertainties in 3D geometry of the salt dome and the seismic velocity structure.

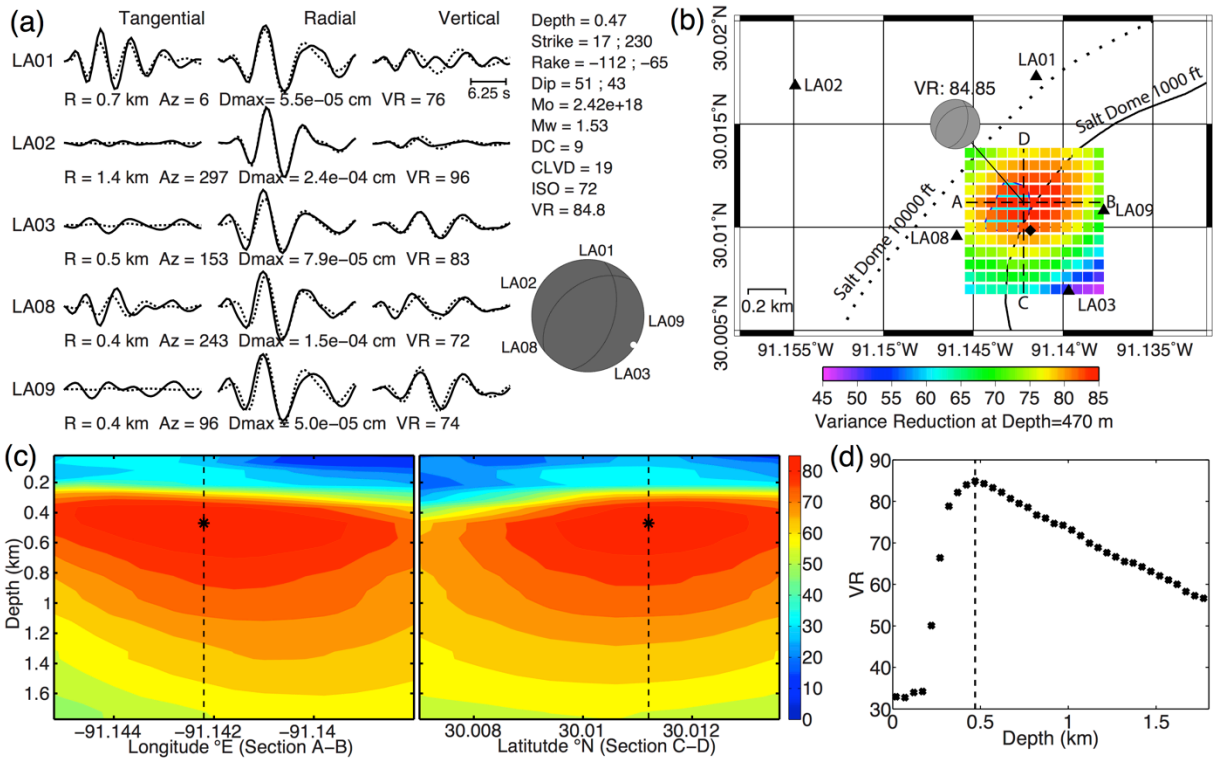

Figure 2.7: (a) Observed (solid lines) and synthetic (dashed lines) 0.1-0.2 Hz displacement waveforms and full MT solution for event TE1; *R* = epicentral distance, Az = azimuth (°), *D*max = maximum displacement amplitude at a station. (b) Grid-search results for full MT solution of event TE1 shown in (a). Squares show VR at grid points at 470 m depth. Solid and dotted lines are 1,000 ft and 10,000 ft depth contours of NSD. The depth sections of VR across profiles A-B and C-D (dashed lines) through the best-fitting centroid location are shown in (c). The shaded polygon (below the grid) shows the approximate surface extent of the sinkhole in July 2013; black triangles are station locations; the black diamond is the OG3 cavern. (c) Depth sections across profiles A-B and C-D show smoothed variations of VR. The black asterisk is the best-fitting centroid hypocenter of event TE1, and the thin dashed line is the line of intersection of the two sections. (d) Values of best VR at various grid-point depths.

Fig. 2.8 shows spatial distribution of MT solutions represented by *P*-wave first motion mechanisms for all 23 events detected during the time period of Fig. 2.2. Reflecting the similarity in waveforms, mechanisms for all events are very similar to each other. The events are approximately concentrated at the western edge of the salt dome, very close to the sinkhole.

We have also analyzed the data of 2 August 2012 up to 19:00 hours. We observe a drop in seismicity after 2 August 2012, corresponding to the day when the sinkhole was first discovered. Fig. 2.A.2 shows the spatial distribution of MT solutions represented by *P*-wave first motion mechanisms for 39 events detected during 00:00 and 19:00 hours, 2 August 2012. Overall, the mechanisms and locations are very similar. We get an overall isotropic volume-increase component 61%-82 % and VR 71%-86%.

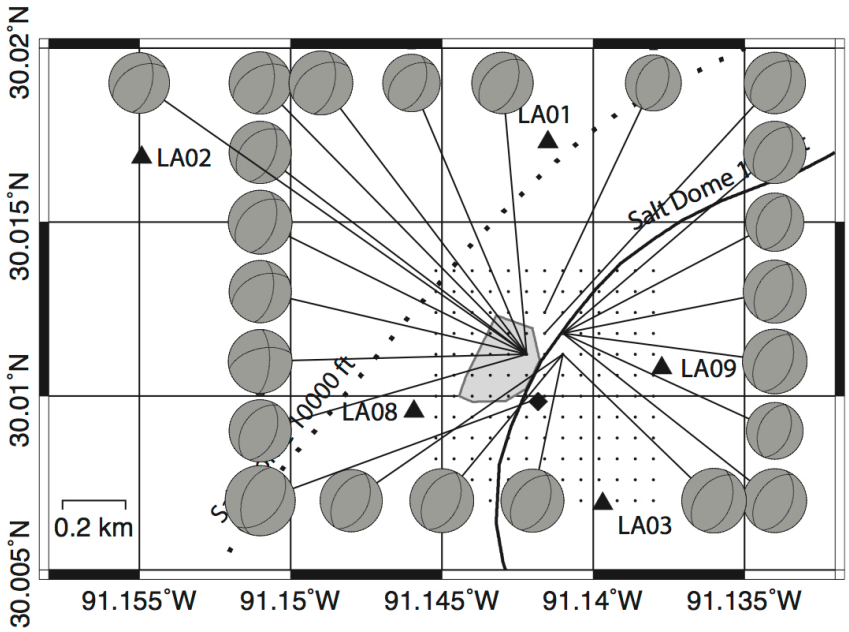

Figure 2.8: Mechanisms and locations of the events detected in the time period shown in Fig. 2.2. Meaning of other symbols is the same as in Fig. 2.7b.

Fig. 2.9 shows magnitude and depth distribution of all events. M_W varies from 1.3 to 1.6, and most events are concentrated at grid-point depth 470 m. We reiterate that these are not the only events observed during this time period, but these are the larger events, which have amplitudes distinguishable from the noise floor in the low-frequency band 0.1-0.2 Hz (Fig. 2.2b), for which the preliminary velocity models produce GFs similar to observed waveforms. Future work will involve trying to model waveforms at higher frequencies using more realistic velocity models.

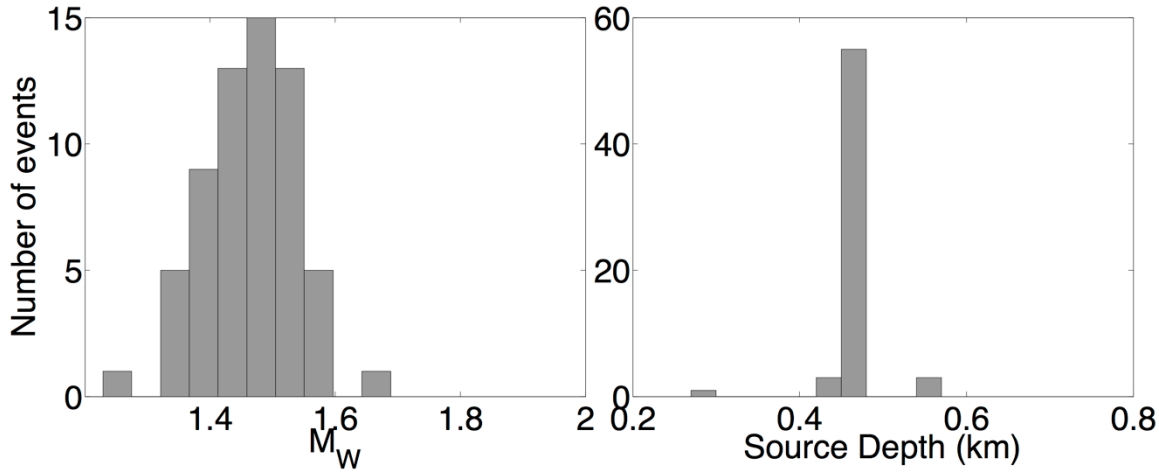

Figure 2.9: M_W and source depth distribution of all 62 events detected with VR > 70%.

2.4 Sensitivity Analysis

Because of poor VR values at greater depths (Fig. 2.7d), we restrict sensitivity analyses to a maximum depth of 0.97 km. Since the waveforms, locations and MT solutions of all events are similar, subsequent sensitivity and GRiD MT uncertainty analyses have been performed for the event TE1 only. To study the significance of the volume-increase component, we apply GRiD MT for a zero volume change deviatoric MT solution in which M_{zz} is constrained to $M_{zz} = -(M_{xx} + M_{yy})$. The results are shown in Fig. 2.10. The VR for the best-fitting deviatoric solution is ~69% which is substantially smaller than that for the full MT solution. The radiation pattern of the deviatoric solution comprised of an unusually large Compensated Linear Vector Dipole (CLVD) component is unable to fit the uniform-phase long-period *S* waves observed in the radial components at all stations. There is no change in source depth; the shift in epicenter with respect to the full MT solution is shown in Fig. 2.11, indicating that the locations obtained are not dependent on the assumptions regarding the possible nature of the seismic source.

We use the *F*-test to check the statistical significance of the improvement in waveform fits caused by the additional degree of freedom in the full MT solution. Following the approach of Templeton & Dreger (2006), for three-component waveforms at 5 stations, each of length 50 samples (25 s long at 0.5 s sampling interval) and filtered between 10 and 20 samples (5–10 s, or 0.1–0.2 Hz), the total number of uncorrelated data points is set to 75. The numbers of independent model parameters are 9 and 10, respectively, for the deviatoric and full MT with latitude, longitude, depth and time, respectively. The *F*-test statistic is calculated to be 1.997, which suggests that the full MT solution fits the displacement waveforms significantly better than the deviatoric MT solution at 99.69% confidence level.

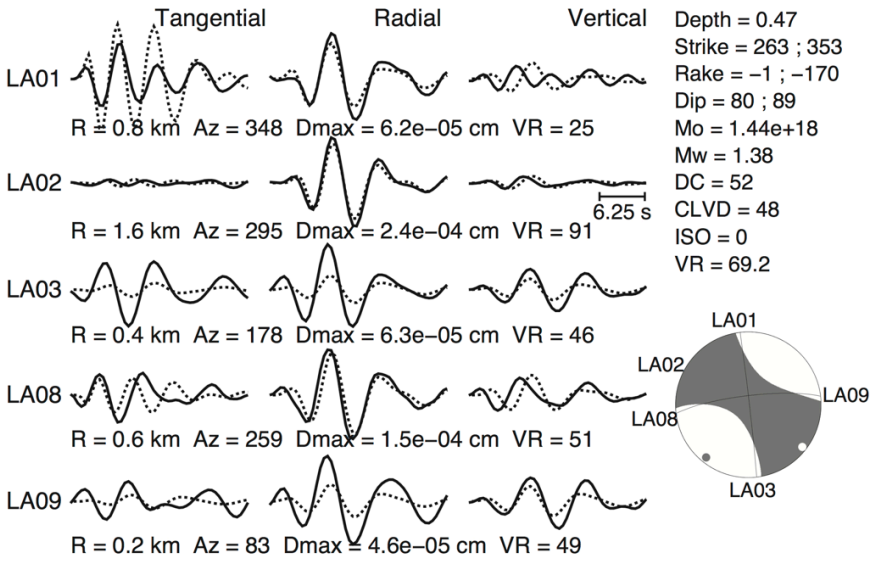

Figure 2.10: Deviatoric MT solution and waveform fits for event TE1. The meaning of symbols is the same as in Fig. 2.7a.

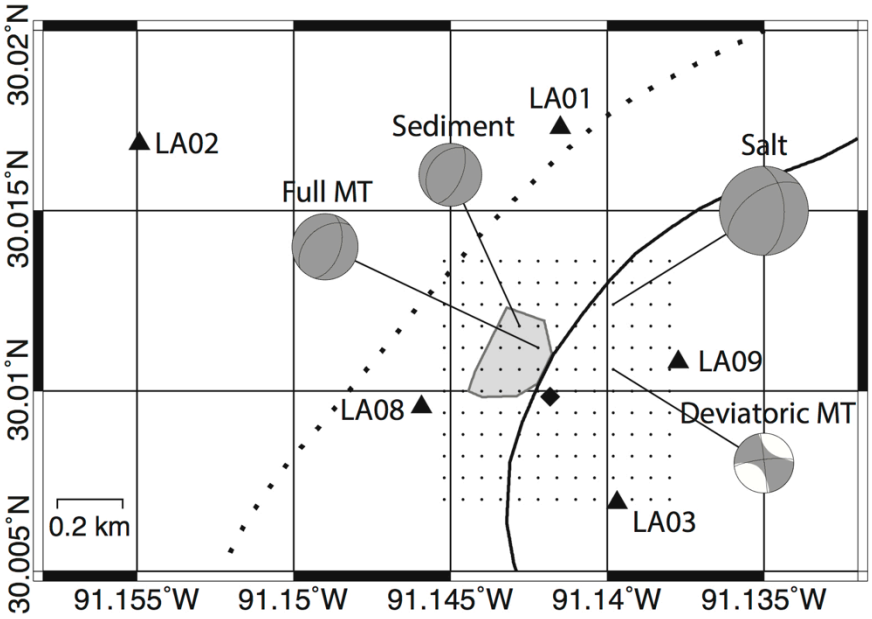

Figure 2.11: Map showing various MT solutions from the sensitivity analyses of event TE1. Full: Original full MT solution (Fig. 2.7a); Deviatoric MT: Deviatoric MT solution (Fig. 2.10); Sediment: Full MT solution using GFs from the sediment velocity model (Fig. 2.12a); Salt: Full MT solution using GFs from the salt dome velocity model (Fig. 2.12b). The meaning of other symbols is the same as in Fig. 2.7b.

To examine the stability of the MT solutions with respect to velocity models, we first apply GRiD MT using GFs only from the sediment velocity model, thereby assuming seismic paths to all stations conform to the sediment velocity model. Details of the MT solution and waveform fits are shown in Fig. 2.12a. There is only a negligible decrease in VR from 84.8% to 84.6%, and the solution and the dominant volume-increase component are approximately the same as before. Second, we use only the salt dome velocity model GFs, thereby assuming seismic paths to all stations conform to the salt dome velocity model. The corresponding results are shown in Fig. 2.12b. There is a significant decrease in the overall quality of waveform fits from 84.8% to 74.8%. However, the MT solution is able to fit long period *S* waves waves on the radial components of all stations, and the MT solutions remains stable in that the dominant component is a volume increase (ISO ~50%). The estimated M_W also increases due to the increase in shear-wave velocity at the source depth for the salt dome model. In both end-member velocity model MT inversions, there is only a minor change in source depth, but we see systematic shifts in source locations consistent with the velocity model changes (Fig. 2.11).

Using the hypocenter obtained from the 5-station GRiD MT results (Figs 2.7b,c), we estimate full MT solutions for event TE1 for various 4-station combinations (Fig. 2.13). The dominant isotropic volume-increase component persists in all cases, which suggests that it is not an artifact caused by data of one particular station.

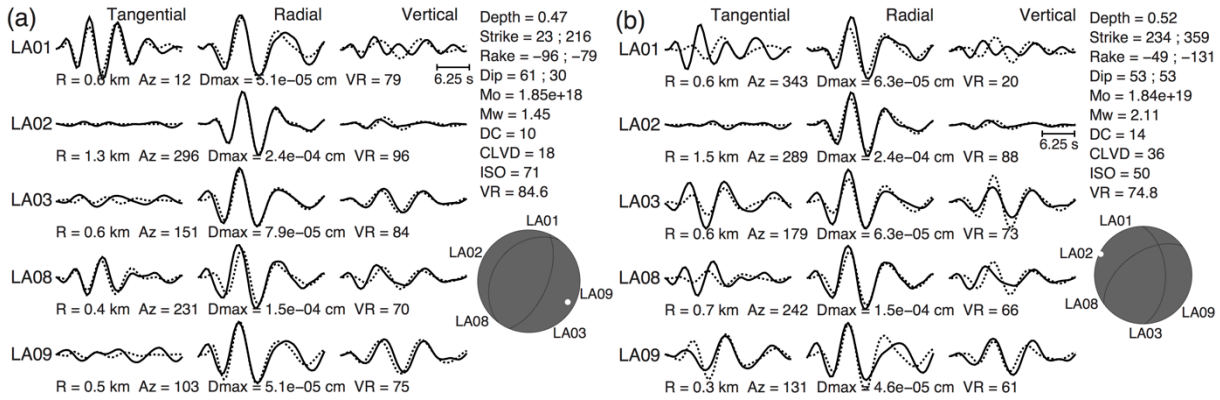

Figure 2.12: Results for event TE1, assuming seismic paths to all stations conform to (a) the sediment velocity model, and (b) the salt dome velocity model. The meaning of symbols is the same as in Fig. 2.7a.

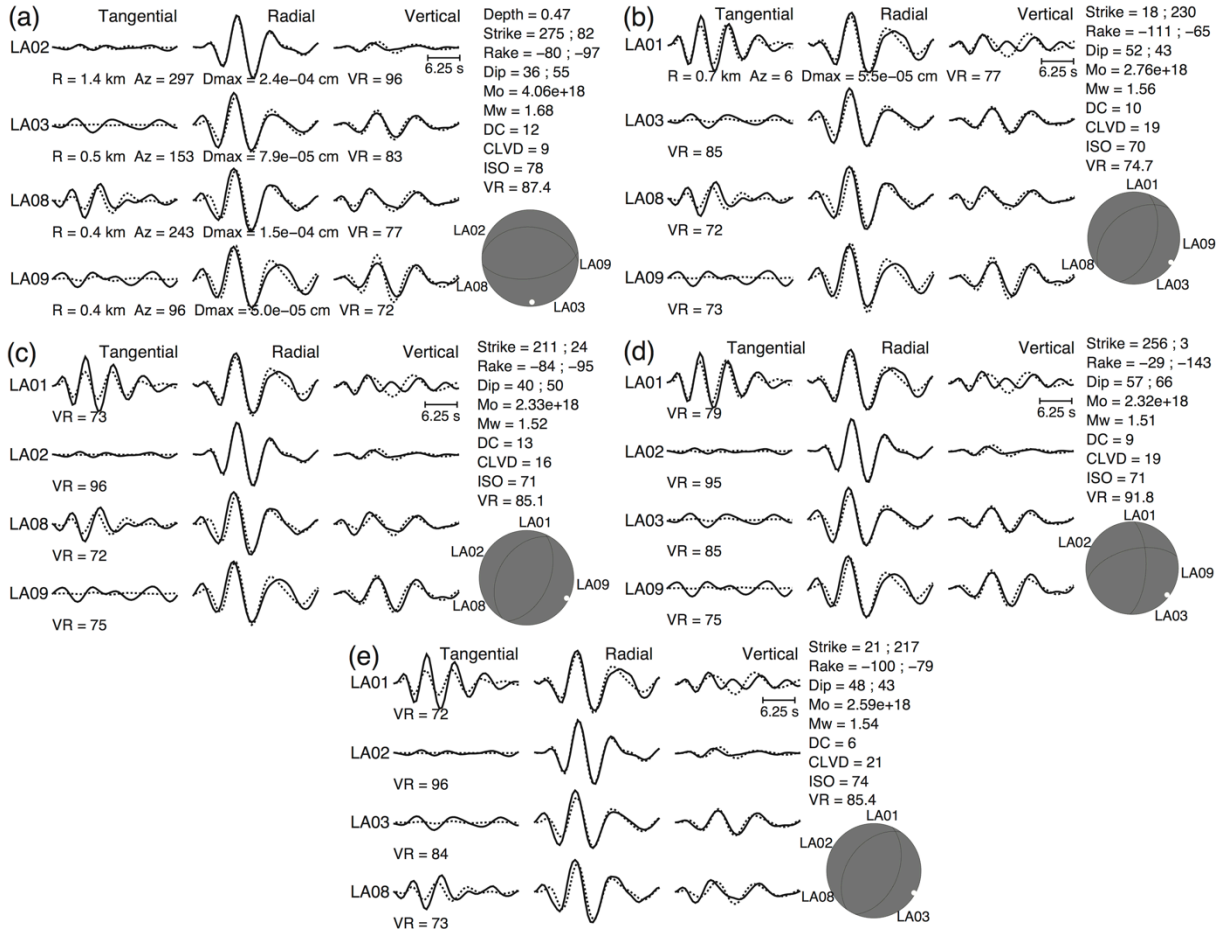

Figure 2.13: Full MT 4-station solutions and waveform fits (solid = observed, dashed = synthetic) for event TE1 computed excluding stations (a) LA01, (b) LA02, (c) LA03, (d) LA08 and (e) LA09. The meaning of other symbols is the same as in Fig. 2.7a. Event depth and station-specific *R*, Az and *D*max are same in all subplots.

2.5 GRiD MT Uncertainties

We adopt the following approach to assess the uncertainties in the GRiD MT location and MT solution of event TE1. Fig. 2.14a shows a comparison of grid-point epicenters of all events in this study with available travel-time locations (Stephen Horton, *personal communication*, 2014), which were estimated using *P*-wave and *S*-wave arrival times, a 1D velocity model similar to the sediment model used in this study, and the HYPOELLIPSE code (Lahr 1999). Although the distributions of the epicenters show general agreement, most travel-time depth estimates are shallower (0–0.35 km) than GRiD MT depth estimates (~470 m), which returns poor waveform fits at shallow depths (Figs 2.7c,d). We apply GRiD MT to TE1 data using a slightly larger grid and select all grid points (485) with VR ≥ 90% of the maximum VR (corresponding to a VR of 76.4%). The VR ≥ 76.4% region covers the horizontal extent of all event locations determined from low-frequency waveform inversion in this study, including those estimated assuming end-member sediment and salt dome velocity models separately, the deviatoric MT solution, and independently determined high-frequency travel-time locations (Fig. 2.14a). Therefore, it can be considered to be a reasonable threshold of goodness of fit for selecting a population of well-fitting solutions. The distribution of spatial coordinates and the DC, CLVD and ISO components in MT solutions for all grid points with VR ≥ 76.4 % is shown in Fig. 2.14b. The distributions can be conveniently approximated as normal to the first order, and their mean and standard deviations are indicative of the mean values and uncertainties in the quantities, respectively. Based on this analysis, uncertainties in TE1's epicenter are ±165 m and ±125 m in east-west and north-south directions, respectively, and the best-fitting depths range from 420 m to 620 m. The distribution of ISO, DC and CLVD components identifies event TE1 as dominantly isotropic (ISO > 50 %) and involving a volume increase (positive sum of eigenvalues for all MT solutions) over a wide range of spatial coordinates (mean ISO = 73%). The uncertainties in ISO, DC and CLVD contributions to the full MT solution as a result of uncertainty in GRiD MT location are of the order of ~ 5%–8%.

2.6 MT Solutions

The MT solutions show a dominant volume-increase component, which is quite the opposite to what one would expect in a collapse environment if the energy release were purely due to gravity-driven collapse alone (Ford *et al.* 2008). We calculate the two MT source-type parameters ε and k for all events and plot them on the Hudson source-type plot (Hudson *et al.* 1989) shown in Fig. 2.15. The horizontal axis plots the ratio of the deviatoric eigenvalues ε, and the vertical axis plots the relative isotropic component k. MT solutions for the Louisiana sinkhole seismic sequence plot somewhere close to tensile cracks and explosions, quite far away from natural DC earthquakes and expected implosions or closing cracks. Decomposition of full MT solutions of these events returns ~6%-32% DC and ~0%-27% CLVD components in addition to the spherical tensile source. Although the DC components are very small, the corresponding fault-plane solutions are remarkably similar for all events, indicating that the small deviatoric components in the full MT solutions are not random and are possibly due to

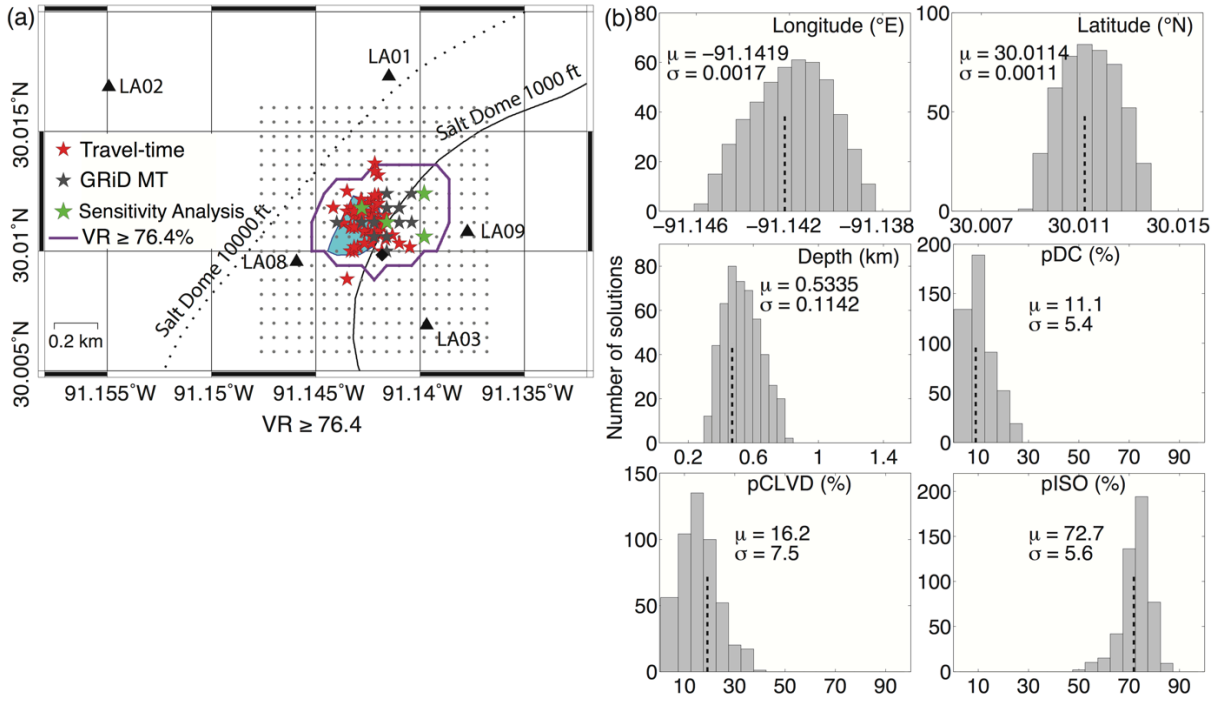

Figure 2.14: (a) A comparison of travel-time locations (Stephen Horton, *personal communication*, 2014), GRiD MT locations, locations of event TE1 from GRiD MT sensitivity analyses (Fig. 2.11) and horizontal extent of grid points with VR ≥ 76.4 % for event TE1. The Meaning of other symbols is same as in Fig. 2.7b. (b) The distribution of spatial coordinates and DC, CLVD and ISO components in MT solutions for all grid points with VR ≥ 76.4% for event TE1. μ = mean; σ = standard deviation. The dashed lines represent values corresponding to the best-fitting full *MT* solution.

systematic source or path effects. The two mean fault planes (along with standard deviations) consistent with the DC components of the MT solutions are (strike 229°±19°, rake -65°±22°, dip 47°±7°) and (strike 18°±7°, rake -112°±19°, dip 53°±9°). Using the hypocenter from the GRiD MT results for the full MT solution (Figs 2.7b,c), we also perform a grid search of source parameters for a shear-tensile (crack + DC) MT solution for event TE1 (Minson *et al.* 2007). A shear-tensile source mechanism combines tensile opening with shear slip along a single fault plane (Minson *et al.* 2007; Šílený *et al.* 2009). Assuming a Poisson's ratio (v) of 0.39 for a source in sediments, we obtain shear-tensile seismic scalar moments, $M_{0,\mathrm{CRACK}} = 1.71\text{x}10^{18}$ dyne.cm and $M_{0,\mathrm{DC}} = 3.7\text{x}10^{17}$ dyne.cm on fault planes (strike 225°, rake –58°, dip 67°) or (strike 23°, rake –120°, dip 76°), which fit the waveforms well, at almost the same VR (~84.8%) as the full MT solution. A source in salt (v = 0.28) yields a solution that fits the waveforms poorly at VR ~78.4%. This is also reflected in the Hudson plot in Fig. 2.15a, in which the sinkhole events plot much closer to a theoretical tensile crack in sediments (v = 0.39) than to one in salt (v = 0.28). Keeping the hypocenter fixed, a pure crack in sediments (v = 0.39) also yields good waveform fits at VR = 83.1%, whereas a pure isotropic explosion and a pure DC source fit the waveforms poorly at VR 38.5% and 60.2%, respectively. MT solutions and waveform fits for four of these source mechanisms are shown in Fig. 2.16: (a) shear-tensile crack and (b) pure crack in sediments (v = 0.39), (c) pure isotropic explosion, and (d) pure DC.

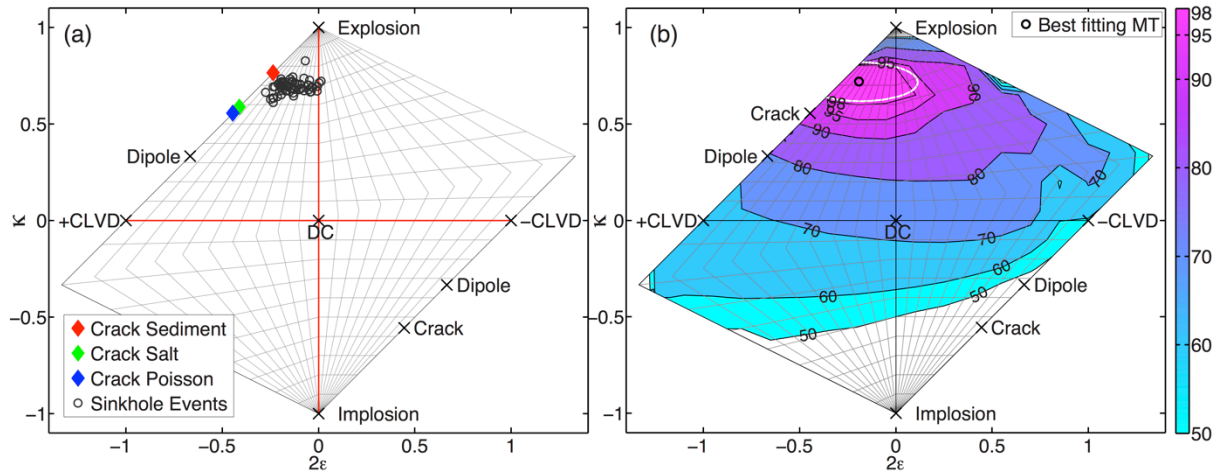

Figure 2.15: (a) Hudson source-type plot showing major theoretical seismic source mechanisms (black crosses), tensile cracks in various media, and 62 events of the Louisiana sinkhole seismic sequence. (b) Network sensitivity solution for event TE1 using waveforms only. The white polygon is the 99% confidence ellipse of the distribution of MT solutions computed by bootstrapping residuals.

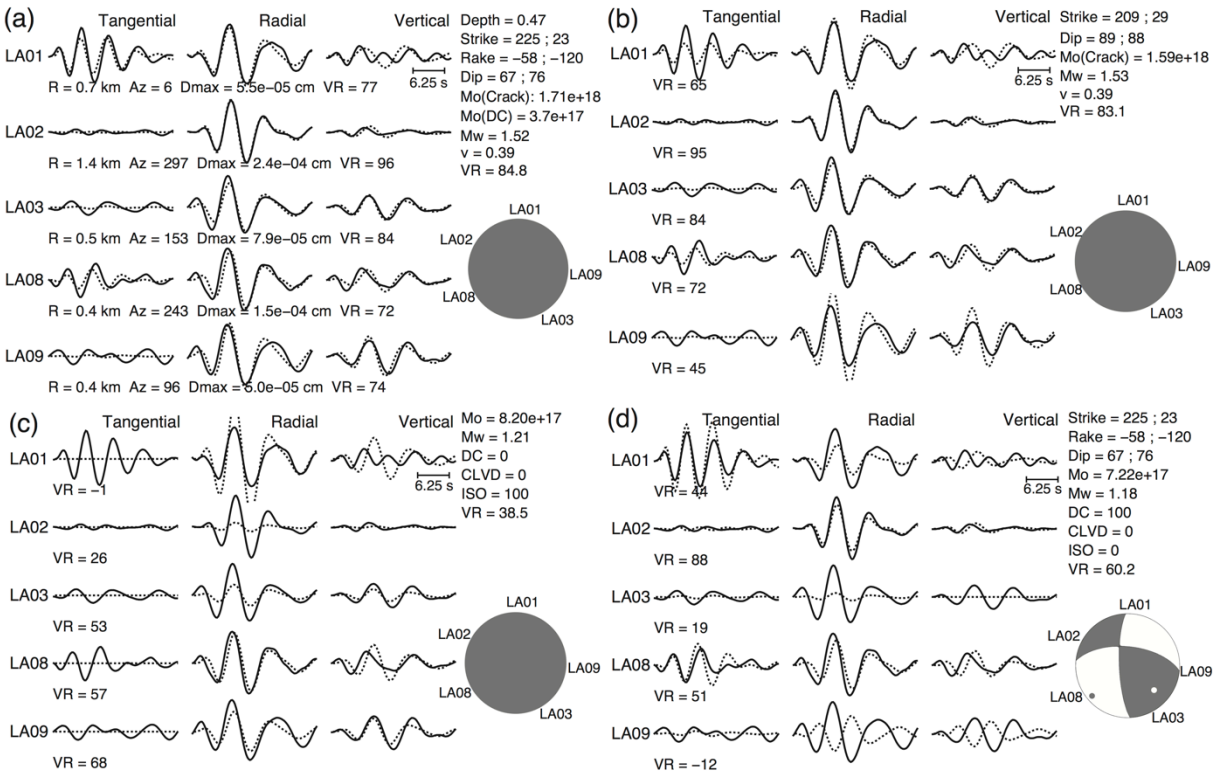

Figure 2.16: MT solutions and waveform fits (solid = observed, dashed = synthetic) for event TE1, assuming the source mechanism to be: (a) shear-tensile (crack + DC) and (b) pure crack in sediments (v = 0.39), (c) pure isotropic explosion, and (d) pure DC. Event depth and station-specific R, Az and Dmax are same in all subplots. The meaning of other symbols is the same as in Fig. 2.7a.

To assess confidence in the source mechanisms thus obtained, we compute the network sensitivity solution (NSS) (Ford *et al.* 2010) for event TE1. The NSS compares fits between observed and synthetic waveforms for a large population ($3x10^7$) of source types, uniformly distributed MTs that generate a distribution of goodness of fit in source-type space that allows identification of the uniqueness of the source type and of the existence of possible tradeoffs, as is common in nuclear explosions (Ford *et al.* 2010). For each coordinate on the Hudson source-type plot (ε, k), the best VR value from all MT solutions corresponding to that coordinate is selected and normalized with respect to the maximum VR from the entire space (Fig. 2.15b). MT solutions that produce best fits (> 95%) are clustered tightly in a region between theoretical explosions and tensile cracks, quite far away from theoretical deviatoric mechanisms, which produce fits only up to 70%-75% of the best possible VR.

To estimate uncertainties in MT solution of event TE1, we compute 10,000 full MT solutions by bootstrapping residuals from waveform fits for the best-fitting full MT solution at the same location and depth (Ford *et al.* 2009a,b). The bootstrapped residuals are first filtered using the same filter applied to waveforms and are then rescaled so that their peak amplitude is equal to the peak amplitude of the original residuals. The 99% confidence ellipse of distribution of these solutions in Hudson space is shown in Fig. 2.15b. The distributions of MT elements and DC, CLVD and ISO components for these solutions are shown in Fig. 2.17. The standard deviations of normal-like distributions of the MT elements represent the uncertainties in the MT solution. The uncertainties in the larger MT elements, M_{xx}, M_{yy} and M_{zz}, are of the order of ~ $2x10^{17}$ – $4x10^{17}$ dyne.cm which is ~9%–30% of their absolute values (~$1.3x10^{18}$ – $2.1x10^{18}$ dyne.cm). Although the uncertainties in the smaller MT elements, M_{xy}, M_{yz} and M_{zx}, are large (about 30%, 50% and 1000% of the absolute values, respectively), their absolute values and maximum range considering 2 standard deviations are smaller than the absolute values of M_{xx}, M_{yy} and M_{zz} by an order of magnitude, thereby strongly constraining the mean ISO component to ~70% with a small uncertainty (± 4%). The uncertainty in M_{xy}, M_{yz} and M_{zx} makes discerning between a vertical tensile crack versus shear-tensile failure uncertain. The shape of the 99% confidence ellipse estimated by bootstrapping waveform residuals closely follows the shape of the 98% contour of best-fitting source types in the NSS, indicating an overall consistency in these estimates.

For shallow events, Ford *et al.* (2009b; 2010; 2012) observed that CLVD sources with the vertical axis in compression provided similar quality of fits to explosion waveforms due to their mimicking of the explosion source radiation pattern near the equator of the focal sphere, which is the region usually sampled by shallow-source intermediate-period waveforms. In this case, we do not see the same sort of tradeoff in the NSS because the near-vertical tensile crack with a primarily horizontal major vector dipole produces strong azimuthal variation in amplitudes, which is not produced by explosions or vertical CLVD sources (compare waveform fits for crack and pure explosion MT solutions in Fig. 2.16). To better constrain the source radiation patterns of shallow explosion events, Ford *et al.* (2012) introduced the inclusion of teleseismic *P*-wave first motion polarities in NSS for more uniform sampling of the entire focal sphere. Since these events were not adequately recorded at other regional stations, we analyze first motion polarities at stations of the same temporary USGS network. Fig. 2.18 shows *P*-wave first motions in vertical components. Although the dominant polarity of initial displacements is positive (compression) at all stations, LA06 and LA08 show a very

weak dilatational (negative) phase at the first arrival. Following the methodology of Ford *et al.* (2012), we also compute the NSS of event TE1 using both waveforms and first motions, which further rules out deviatoric and MT solutions involving volume-decrease components.

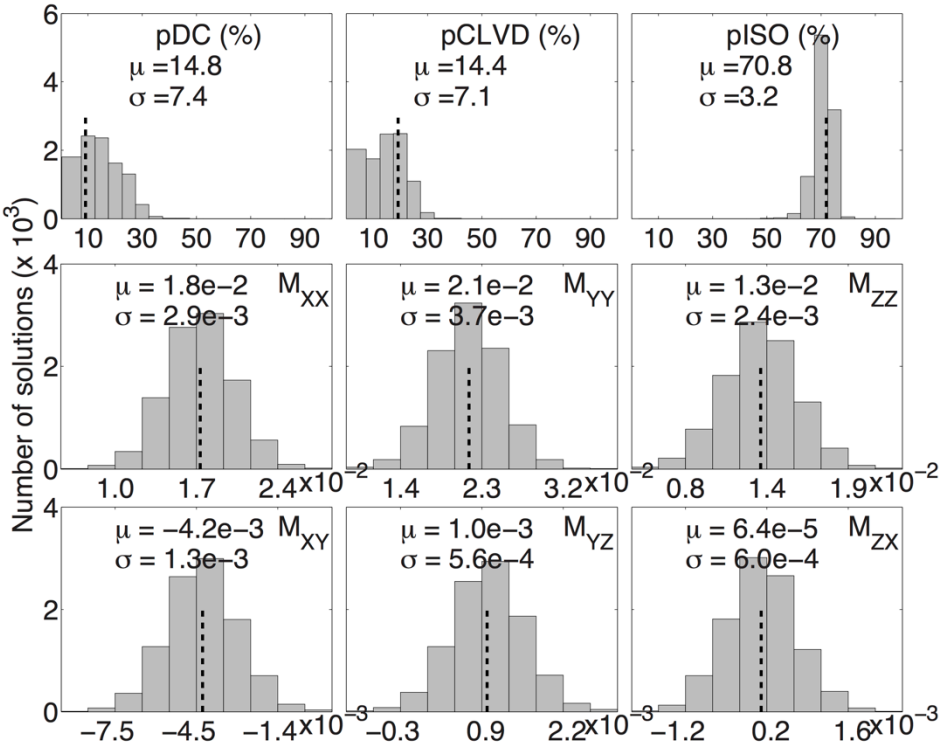

Figure 2.17: Distribution of DC, CLVD and ISO components and MT elements (units are $1x10^{20}$ dyne.cm) from the bootstrap uncertainty analysis of event TE1. The dashed lines represent values corresponding to the best-fitting full MT solution.

2.7 Discussions

There are studies of earlier incidents similar to the seismicity, cavern-collapse and sinkhole formation at NSD, Louisiana. Trifu & Shumila (2010) computed *MT* solutions of micro-seismicity during controlled collapse of a large solution-mined brine-filled cavern in salt deposits of Ocnele Mari, Romania, by inversion of low-frequency displacement amplitudes and polarities of *P*, *SV* and *SH* waves (Trifu *et al.* 2000; Trifu & Shumila 2002). They reported strike-slip and normal-faulting mechanisms for most of the events around the cavern ceiling and up to 30% volume-increase failure components, which they attributed to caving of the roof by a gravity-driven collapse. Development of a much smaller sinkhole near the U.S. Strategic Petroleum Reserve Facility at Weeks Island salt dome, Louisiana, during 1990-1991 was attributed to a combination of hydrological, geological and mining-induced factors (Neal & Magorian, 1997; Neal *et al.* 1998). It is believed that cracks developed in the mine periphery due to tensional stresses induced by mine geometry and excavation operations.

Seeping of undersaturated groundwater led to increasing dissolution of salt, creating a void at the top of the salt dome, which led to the collapse environment (Neal *et al.* 1998).

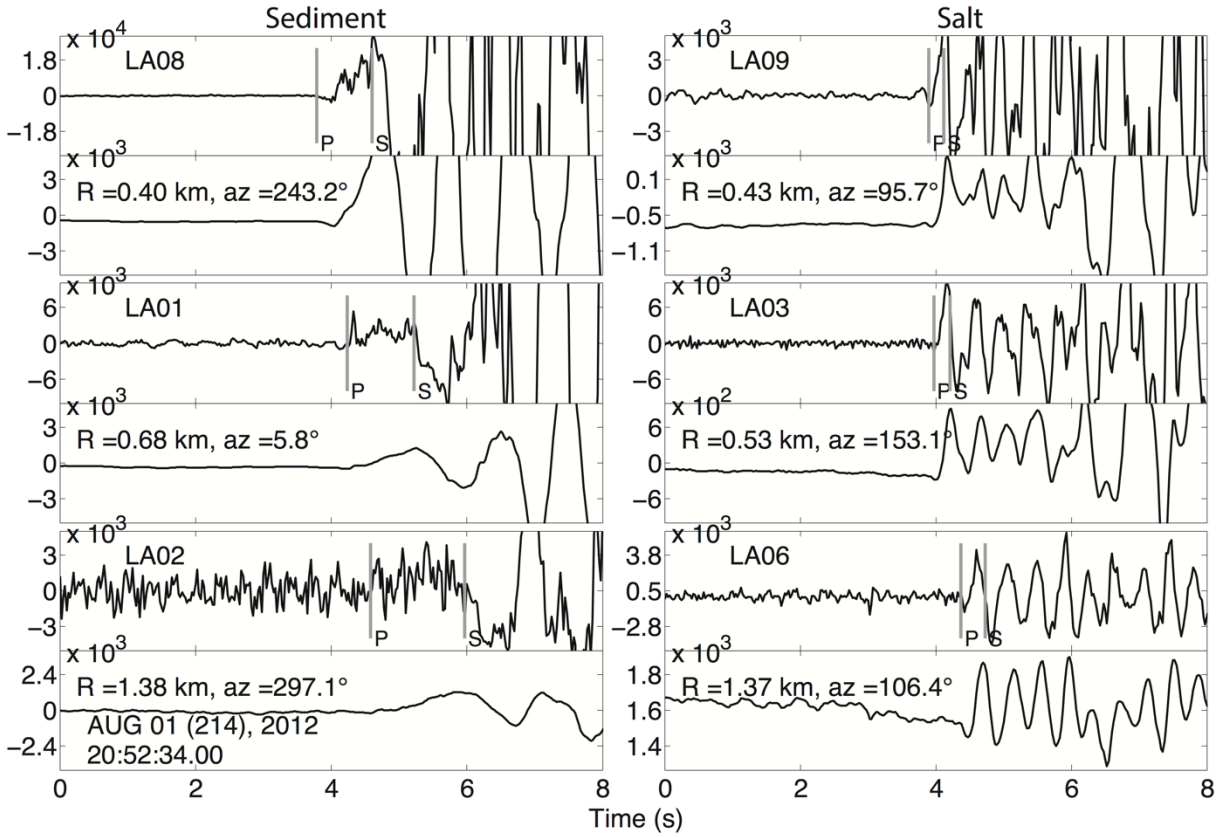

Figure 2.18: Vertical component first motions. For each station, upper panel shows raw velocity records and lower panel shows raw displacement (integrated velocity), without any instrument response correction or filtering. *P*-wave and *S*-wave picks are indicated; *P*-wave first arrivals were picked manually; *S*-wave arrival times are from theoretical *S*-*P* times calculated using the smooth 1D velocity models (Fig. 2.5) and the ray-tracing algorithm of Um & Thurber (1987), assuming hypocenter from GRiD MT results (Figs 2.7b,c). The y-axis units are counts. Left and right panels show stations on the sediments and over the salt dome, respectively, and they are arranged in the order of increasing epicentral distance from top to bottom.

In this study, we have implemented a procedure for independent continuous detection, location and *MT* inversion of seismic events at the sinkhole at NSD, Louisiana. The computational efficiency and simplicity of the approach makes it suitable for real-time applications or analyzing large volumes of microseismic data in reservoir and mine settings, especially if events are numerous or one is not confident in hypocenter estimates based on travel times alone. Furthermore, the use of low-frequency waveforms makes simplified source and velocity models applicable. The seismic events just before the sinkhole formation are located to the edge of the salt dome, close to the sinkhole and above the OG3 cavern, at approximately 470 m depth. They could be in the westernmost edge of the salt dome, or in the

adjacent sediments. The presence of large, statistically significant volume-increase components in MT solutions of events before a major collapse process is surprising but is consistent with the results of Trifu & Shumila (2010). Sensitivity tests of the full MT solution with respect to velocity models, uncertainty analyses and the NSS computed using waveforms for one representative event (TE1), result in greater confidence in stability and reliability of the non-DC source mechanism.

Other than chemical or nuclear explosions (Ford *et al.* 2009a,b), coseismic volume-increase components are primarily found in MT solutions of seismic events in active volcanic and geothermal environments, usually attributed to involvement of magmatic or hydrothermal fluids (Miller *et al.* 1998). For example, some earthquakes in Long Valley volcanic region may have been triggered by high-pressure fluid injection or magmatic heating of fluid-saturated faults, leading to net reduction of normal stress (Julian & Sipkin 1985; Dreger *et al.* 2000; Templeton & Dreger 2006). Earthquakes in the Miyakejima volcanic earthquake swarm were modeled by a tensile opening and shear failure (crack + DC) on a single fault plane and attributed to intrusion of a dike (Minson *et al.* 2007). Source mechanisms of volcanic seismic events in numerous regions around the world show large volume-increase components, usually explained by mechanisms like– injection of magma into cracks or conduits, the opening and resonance of a fluid-filled crack due to increased fluid pressures caused by magmatic heating, and ascent-expansion-burst cycles of gas slugs in conduits (Kumagai *et al.* 2002; Nakano *et al.* 2003; Kumagai *et al.* 2005; Chouet *et al.* 2008, 2010; Chouet & Dawson 2011). Although there is no known heat source similar to those in geothermal or volcanic regions in or around NSD, the region around the sinkhole has experienced intense natural gas influx from the disturbed rock zone below the sinkhole, as is clearly visible on the surface as bubbling of gas in local water bodies (CB&I 2013a). Natural gas, primarily methane, is believed to be accumulating and spreading laterally in the MRAA over an area of 5 km^2 around the sinkhole (CB&I 2013a). Subsurface pressure is being monitored at various sites; and, as a remediation measure, multiple vent wells have been established to flare the accumulated gas from subsurface. Some probable and possible gas source horizons have also been identified (CB&I 2013a; LADNR, OOC 2013). We believe that the events in this study are caused by the high-pressure flow of natural gas or water-gas mixture through voids in the disturbed rock zone or pre-existing zones of weaknesses, such as fractures or faults at the edge of the salt dome, by volumetric expansion or tensile failure mechanisms similar to those observed in geothermal or volcanic environments. The solutions obtained for the studied events range from an isotropic volume-increase source to a near-vertical tensile crack coupled with a north-northeast-striking normal-style DC. Preliminary interpretation of active seismic data also suggests faults at the edge of the salt dome (Texas Brine, Corp. 2013). It is possible that a sidewall collapse of the brine cavern might have produced a disturbed or deformed rock zone up to the surface and caused a breakout in a nearby reservoir or gas pocket, which is presently releasing the natural gas. Because all 62 events analyzed in this study share very similar location and source mechanism, it is possible that material damage and weakening brought on by repeated failure of the same source region by high-pressure fluids might have led to the final collapse which formed the sinkhole on 2 or 3 August 2012. However, this is conjecture, as presently we don't have any evidence in support of this hypothesis. It is also possible that basal filling of the brine-filled cavern from sinkhole debris could lead to elevated fluid pressure in the cavern that is leading to the tensile nature of the events that are

apparently located above and to the west of the cavern. Future work will involve the examination of entire volume of data made available by USGS using the procedure established in this study.

2.8 Data and Software

The data used in the study was recorded by a USGS temporary network (network code GS) and downloaded through the website of Incorporated Research Institutions in Seismology (IRIS) Data Management Center (http://www.iris.edu/dms/nodes/dmc/, last accessed August 2013). *Seismic Analysis Code* (Goldstein *et al.* 2003) was used for basic analysis of seismograms. Some figures were prepared using *Google Earth* and *Generic Mapping Tools* (Wessel & Smith 1998).

2.9 Acknowledgements

We thank William Ellsworth (USGS) for preliminary velocity models, data, mapping resources and helpful discussions. We are grateful to BSSA Associate Editor Heather DeShon, Stephen Horton (CERI, University of Memphis) and an anonymous reviewer for their comments and suggestions that greatly helped in improving this study. Stephen Horton is also thanked for providing the travel-time catalog of events in this study. We also thank Aurélie Guilhem (ETH Zurich) and Seung-Hoon Yoo (Weston Geophysical Corp.) for helpful discussions.

2.10 Appendix

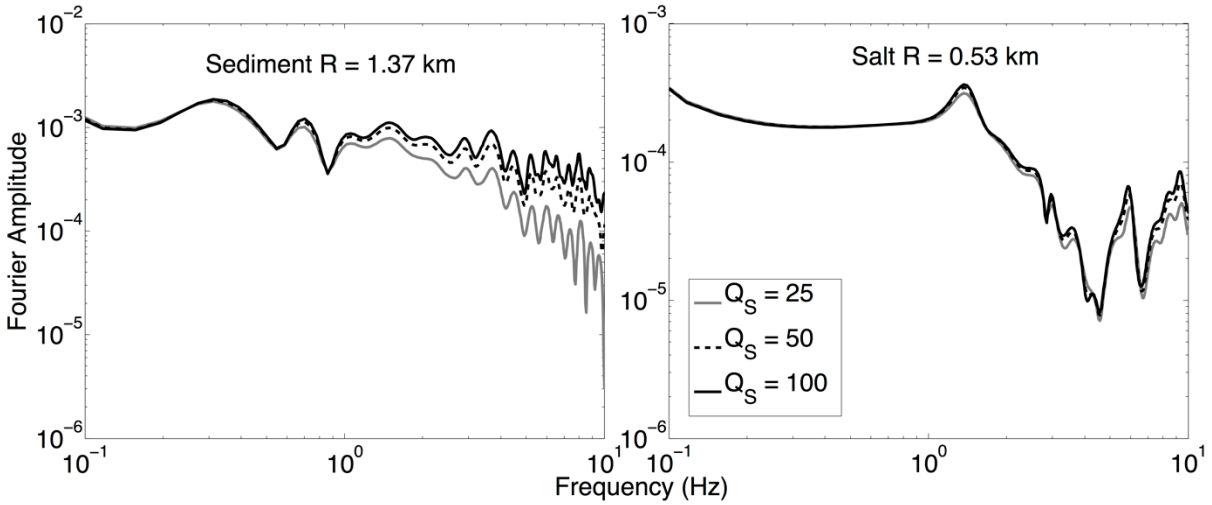

Figure 2.A.1: Fourier amplitude spectra of synthetic radial displacements at stations LA02 (sediment) and LA03 (salt) for event TE1 using GFs computed for different values of Q_P (= 2 × Q_S) and Q_S. *R* is the epicentral distance.

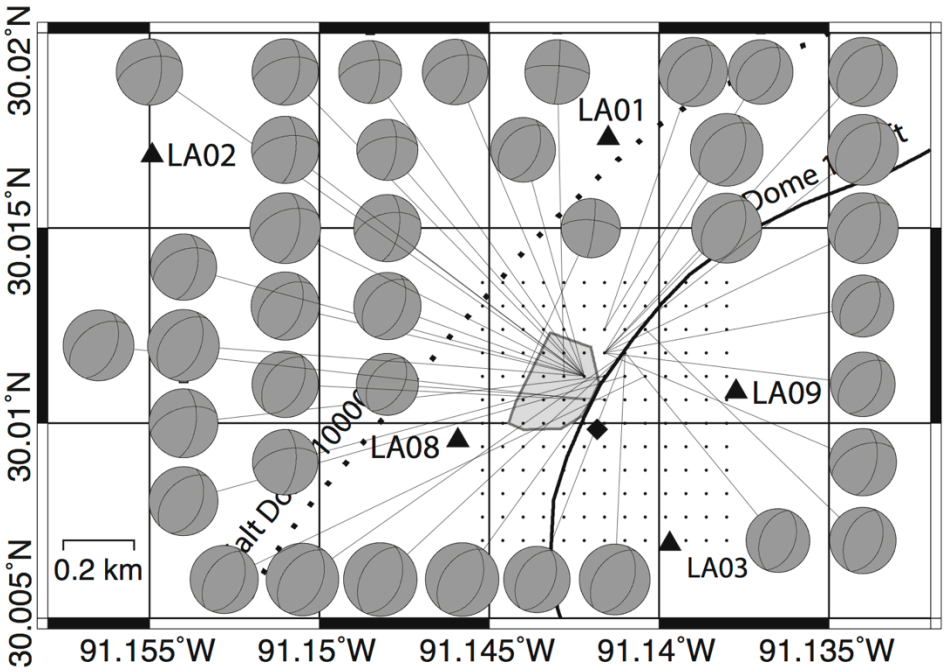

Figure 2.A.2: Mechanisms and locations of 39 events detected from 00:00 to 19:00 hours, 2 August 2012. The meaning of symbols is same as in Fig. 2.7b.

Chapter 3

Source-Type-Specific Inversion of Moment Tensors

Published as:
Nayak, A. & Dreger, D.S., 2015. Source-type-specific inversion of moment tensors, *Bull. Seism. Soc. Am.*, **105**(6), 2987–3000, doi: 10.1785/0120140334.

3.1 Chapter Abstract

The mapping of the fit of seismic moment tensor (MT) solutions in source-type space helps to characterize uncertainty and solution uniqueness. Current practice relies on the forward testing of a distribution of randomly generated MTs in source-type space, which is slow and does not necessarily recover the true maximum fit surface. We design an iterative damped least-squares inversion scheme to invert waveforms and/or *P*-wave first-motions (FM) for best-fitting MT solutions for specific source types. An event associated with the sinkhole at the Napoleonville salt dome, Louisiana, an industrial quarry explosion, and an earthquake at The Geysers geothermal field, northern California are presented as examples. We find that the inversion method is more accurate and successful than the random-search approach in recovering the region of best-fitting MT solutions or source types and is substantially faster. The approach also enables the determination of the best-fitting MT for specified source types such as pure double couples, tensile cracks or explosions, as well as compound mechanisms in a single numerical framework.

3.2 Introduction

The 2nd order general seismic moment tensor (MT) is routinely used to describe source mechanisms of seismic events (Jost & Herrmann 1989; Julian *et al.*1998; Aki & Richards 2002; Minson & Dreger 2008). The general MT is mathematically defined to be a symmetric 3x3 matrix and has six independent components ($M_{xx}, M_{yy}, M_{zz}, M_{xy}, M_{yz}, M_{zx}$), which describe the seismic source mechanism in terms of moments of body force equivalents, that is, double couples and linear vector dipoles. Recently, there has been renewed interest in the geometric representation, decomposition and interpretation of the general MT (Vavryčuk 2011; Tape & Tape 2012a, b, 2013; Vavryčuk 2015), which facilitate interpretation of seismic sources. Source-type discrimination and assessing confidence and uncertainties in source-type characterization of seismic events is of great importance, especially for monitoring of nuclear explosions (e.g., Ford *et al.* 2009a, b, 2010, 2012; Chiang *et al.* 2014) and analysis of induced seismic events (e.g., Šílený *et al.* 2009; Guilhem *et al.* 2014). In this study, we describe the concept of a source-type-specific MT inversion. We provide the expressions for a general MT in terms of its normalized eigenvalues, eigenvectors and the moment scale factor. Then we describe an iterative damped least-squares (LS) inversion scheme to invert for best-fitting eigenvectors and the moment scale factor for an event using its displacement waveforms for a given source type, that is, its normalized eigenvalues that enable the construction of the maximum goodness-of-fit surface in the source-type space. We validate the inversion scheme by applying it on synthetic and observed seismic waveforms and analyze the results. Finally, we also test a method to incorporate *P*–wave first motion (FM) polarities in the inversion.

3.3 Methodology

3.3.1 Basic formulation

Let a given general MT, $\mathbf{M}$, have eigenvalues, $\boldsymbol{\lambda_0} = [\lambda_{0,1}, \lambda_{0,2}, \lambda_{0,3}]$ and corresponding eigenvectors $\mathbf{e_1}, \mathbf{e_2}$ and $\mathbf{e_3}$ ($\mathbf{e_i} = [e_{i1}, e_{i2}, e_{i3}]$). The general MT, being real and symmetric, has eigenvalues and eigenvectors that are real and orthonormal, respectively. $\boldsymbol{\lambda_0}$ determines the seismic scalar moment and the source type, and can be normalized to a unit vector $\boldsymbol{\lambda}$ by its L2-norm, m_0^2 ($= \sqrt{\sum_{i=1}^{3} \lambda_{0,i}^2}$).

$$\lambda_i = \frac{\lambda_{0,i}}{m_0^2} \text{ for } i=1, 2, 3 \tag{3.1}$$

in which m_0^2 is a moment scale factor, defined as a square so that it remains nonnegative and characterizes the absolute size of MT eigenvalues (or of MT elements) independent of their sign. Substituting $\lambda_{0,i} = \lambda_i \times m_0^2$ in equation 22 in Jost & Herrmann (1989), each MT

element M_{ij} can be expressed as a scalar function of the moment scale factor, normalized eigenvalues, and orthonormal eigenvectors, where

$$M_{ij} = m_0^2 \left(\lambda_1 e_{1i} e_{1j} + \lambda_2 e_{2i} e_{2j} + \lambda_3 e_{3i} e_{3j}\right) \text{ for } i = 1, 2, 3 \text{ and } j = 1, 2, 3 \quad (3.2)$$

Here, 1, 2 and 3 represent *x*, *y* and *z* for the MT elements. The aim of this study is to assume specific values of $\boldsymbol{\lambda}$, and then solve for m_0^2 and MT eigenvectors $\mathbf{e_1}, \mathbf{e_2}$ and $\mathbf{e_3}$, using seismic waveforms and/or polarities. We also discuss the utility of MT inversions for which the solutions are constrained to specific values of $\boldsymbol{\lambda}$.

3.3.2 Parameterization of eigenvectors

The orthonormal eigenvectors $\mathbf{e_1}, \mathbf{e_2}$ and $\mathbf{e_3}$ can be expressed in terms of either spherical $(\theta_1, \theta_2, \theta_3)$ or Cartesian $(a_1, a_2, a_3, b_1, b_2)$ parameters. In this study, we develop the Cartesian parameterization because we found it to have better convergence properties. In the **Appendix** section **3.A.2**, we provide the alternative parameterization in spherical coordinates and show that it can be used with the same inversion scheme to obtain nearly the same results, albeit with slower convergence towards the best-fitting solution.

Assuming the five unconstrained real parameters $(a_1, a_2, a_3, b_1, b_2)$ of the 3D Cartesian system, we can define $\mathbf{e_1}$ and $\mathbf{e_2}$

$$\mathbf{e_1} = \frac{[a_1, a_2, a_3]}{r_1} \quad (3.3)$$

$$\mathbf{e_2} = \frac{[a_3 b_1, a_3 b_2, -(a_1 b_1 + a_2 b_2)]}{r_2} \quad (3.4)$$

$$r_1 = \sqrt{\sum_{i=1}^{3} a_i^2}, \; r_2 = \sqrt{(a_3 b_1)^2 + (a_3 b_2)^2 + (a_1 b_1 + a_2 b_2)^2} \quad (3.5)$$

$$\mathbf{e_3} = \mathbf{e_1} \times \mathbf{e_2} \quad (3.6)$$

It is important to note that there is innate numerical non-uniqueness in solutions of orthonormal eigenvectors for a particular MT. There are 4 combinations $(\pm\mathbf{e_1}, \pm\mathbf{e_2})$ of $\mathbf{e_1}, \mathbf{e_2}$ and $\mathbf{e_3}$ that give the same MT (equation 3.2). In addition, the number of independent parameters required for defining three orthonormal eigenvectors is three. For the Cartesian formulation in equations 3.3 to 3.6, our model is overparameterized to allow the model parameters to assume any value, as long as $\mathbf{e_1}$ and $\mathbf{e_2}$ are not zero vectors. As a result, there can be infinite combinations of $(a_1, a_2, a_3, b_1, b_2)$ that lead to the same values of $\mathbf{e_1}, \mathbf{e_2}$ and $\mathbf{e_3}$.

3.3.3 Inverse problem formulation

Elements of $\mathbf{e_1}, \mathbf{e_2}$ and $\mathbf{e_3}$ in equation 3.2 can be substituted by a_1, a_2, a_3, b_1 and b_2 to obtain scalar expressions of MT elements M_{ij} in terms of m_0^2, $\boldsymbol{\lambda}$ and the eigenvector parameters.

$$\mathbf{m}' = \mathbf{f}(\boldsymbol{\lambda}, m_0^2, a_1, a_2, a_3, b_1, b_2) \tag{3.7}$$

in which $\mathbf{m}'$ and $\mathbf{f}$ are column vectors containing MT elements and their scalar expressions, respectively.

Now the MT elements in the expressions relating transverse ($\mathbf{u_T}$), radial ($\mathbf{u_R}$) and vertical ($\mathbf{u_Z}$) displacements to the MT and Green's Functions (GFs) matrix ($\mathbf{G}$) in Minson & Dreger (2008) can be replaced by their functions in terms of $\boldsymbol{\lambda}, m_0^2, a_1, a_2, a_3, b_1$, and b_2.

$$\mathbf{u_{T,R,Z}} = \mathbf{G}\mathbf{m}' \tag{3.8}$$

$$\mathbf{u_{T,R,Z}} = \mathbf{G}\,\mathbf{f}(\boldsymbol{\lambda}, m_0^2, a_1, a_2, a_3, b_1, b_2) \tag{3.9}$$

Equation 3.8 is valid for a point source that assumes the source time function to be an impulse or a Dirac delta function in space and time that is common for all MT elements. For constant and known source type $\boldsymbol{\lambda}$, we can invert for the six unknown parameters $(m_0, a_1, a_2, a_3, b_1, b_2)$. Since we know the exact expressions for $\mathbf{f}$ and its derivatives, we choose to solve the problem using an iterative damped LS inversion scheme as follows

$$\mathbf{du_{T,R,Z}} = \mathbf{G}\left(\frac{\partial \mathbf{f}}{\partial m_0} dm_0 + \sum_{i=1}^{3} \frac{\partial \mathbf{f}}{\partial a_i} da_i + \sum_{i=1}^{2} \frac{\partial \mathbf{f}}{\partial b_i} db_i\right) \tag{3.10}$$

The model parameter vector $\mathbf{dx}$ is defined:

$$\mathbf{dx} = [dm_0, da_1, da_2, da_3, db_1, db_2]^T \tag{3.11}$$

$$\mathbf{P} = \mathbf{G}\left[\frac{\partial \mathbf{f}}{\partial m_0} \;\; \frac{\partial \mathbf{f}}{\partial a_1} \;\; \frac{\partial \mathbf{f}}{\partial a_2} \;\; \frac{\partial \mathbf{f}}{\partial a_3} \;\; \frac{\partial \mathbf{f}}{\partial b_1} \;\; \frac{\partial \mathbf{f}}{\partial b_2}\right] \tag{3.12}$$

$$\mathbf{du_{T,R,Z}} = \mathbf{P}\mathbf{dx} \tag{3.13}$$

$$\mathbf{dx} = (\mathbf{P}^T\mathbf{P} + k\mathbf{I})^{-1}\mathbf{P}^T\mathbf{du_{T,R,Z}} \tag{3.14}$$

where k is a damping parameter. The data goodness-of-fit parameter is the variance reduction (VR; expressed in percentage), a measure of normalized goodness of fit between observed and synthetic data (Pasyanos *et al.* 1996).

The expressions of partial derivatives in equation 3.12 are provided in the **Appendix** section **3.A.1**. Equation 3.9 is exact, and the user can choose to solve it using any appropriate numerical inversion technique. This approach to the problem also implies that it would be possible to estimate the best-fitting source type or eigenvalues, for specific orientation or eigenvectors, such as for a specific crack plane or double-couple (DC) focal mechanism.

3.3.4 Inversion parameters

The iterative damped LS inversion procedure depends on many parameters like the damping parameter, initial model parameters and number of iterations. A few trials ($\lesssim 15$) with different initial model parameters are usually sufficient for convergence to the best-fitting MT solution. We use randomly generated real numbers of the order ~ 1 for initial values of a_1, a_2, a_3, b_1 and b_2. For m_0, we use initial values logarithmically distributed over an order of magnitude around $\sim\sqrt{M_0/1.0\times10^{13}}$, where M_0 is the scalar seismic moment (in N.m) computed from preliminary analyses or general MT inversion using the definition of Bowers & Hudson (1999). It is important to note that the Cartesian eigenvector model is over-parameterized and therefore, only three out of five columns in **P**, that is, those containing partial derivatives of **f** with respect to $(a_1, a_2, a_3, b_1, b_2)$, are linearly independent. Because **P** is a rank deficient matrix (rank(**P**) = 4), a non-zero damping value (k) must be used for $\mathbf{P}^T\mathbf{P}$ to be invertible. We have found from trial and error that $k \sim 1.0\times10^{-10}$ performs well. Multiple solutions of $(a_1, a_2, a_3, b_1, b_2)$ give the same $(\mathbf{e_1}, \mathbf{e_2})$, and four combinations of $\mathbf{e_1}$ and $\mathbf{e_2}$ $(\pm\mathbf{e_1}, \pm\mathbf{e_2})$ give the same MT elements and therefore, the same waveform fits. Depending on the initial values, the inversion proceeds towards any of these solutions, minimizing the LS error between observed and predicted waveforms. With successive iterations, linearly independent MT elements (which are functions of model parameters and fixed $\boldsymbol{\lambda}$) converge towards their best-fitting values. We terminate the inversion if VR changes less than 0.01% over 2 successive iterations.

3.4 Tests on synthetic waveforms

We use synthetic waveforms to evaluate the effectiveness of the inversion procedure. We forward model synthetic three-component displacement waveforms at seismic stations in northern California using equation 3.8 with 100 randomly generated MTs, assuming random eigenvectors and random values of m_0 (between 10^{-2} and 10^{+2}) for each of four source types: (1) pure DC ($\boldsymbol{\lambda}$ =[0.7071, 0, –0.7071]), (2) a tensile crack in Poisson's solid (Poisson's ratio v = 0.25; $\boldsymbol{\lambda}$ = [0.9045, 0.3015, 0.3015]), (3) explosion ($\boldsymbol{\lambda}$ =[0.5774, 0.5774, 0.5774]), and (4) a pure Compensated Linear Vector Dipole (CLVD; $\boldsymbol{\lambda}$ = [0.8165, –0.4082, –0.4082]). Figure 3.1a shows the recording stations for synthetic test events located at 8 km depth and one example source mechanism. For these hypothetical events and the real seismic events described in the subsequent sections, the GFs were computed using appropriate velocity and density models for each region and the frequency–wavenumber integration method based on Haskell (1964) and Wang & Herrmann (1980), as provided in Herrmann (2013a). The frequency-wavenumber integration method computes complete three-component seismograms (including near-field and intermediate-field terms) consisting of all body-wave and surface-wave phases for isotropic 1D layered velocity models.

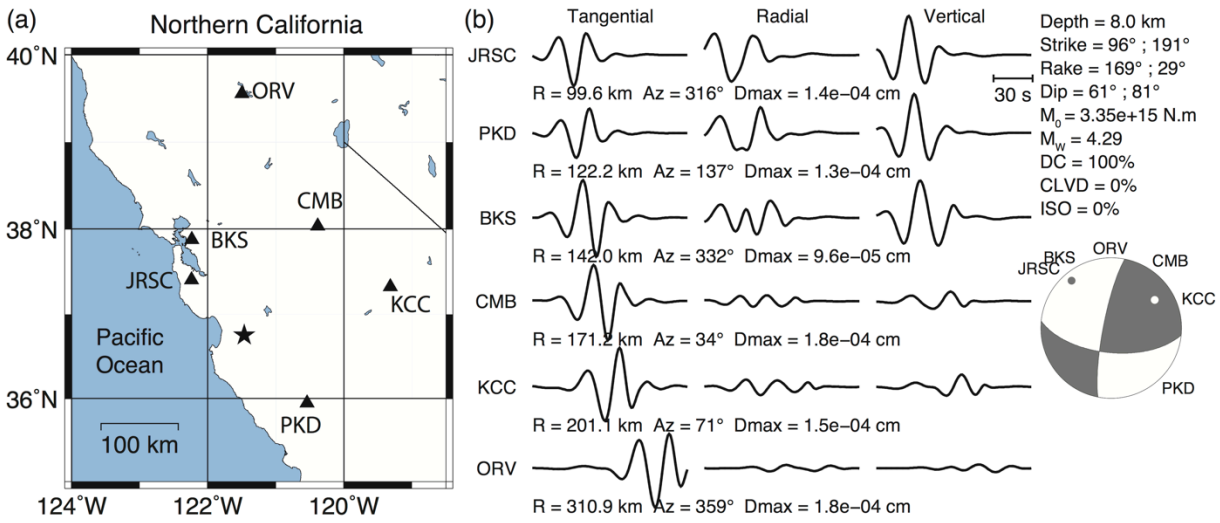

Figure 3.1: (a) Location of the epicenter (black star) of the hypothetical seismic event placed in the northern California network, from which the synthetic waveforms at Berkeley Digital Seismic Network stations (black triangles) were used for the evaluation of the inversion procedure proposed in this study, assuming different source types. (b) Three-component synthetic displacement waveforms (0.02-0.05 Hz) for one example random MT solution, assuming a DC source type. *R* = epicentral distance, Az = azimuth (°), and *D*max = maximum displacement amplitude at a station. The focal mechanism plot shows the lower hemisphere *P*-wave radiation pattern.

Table 3.1 shows the basic information on the seismic events in this study. For the randomly oriented hypothetical seismic events, filtered GFs were used to compute synthetic waveforms with the randomly generated MTs. The same GFs were used for inversion to investigate convergence properties of the linearized inversion. In this study, we decompose all MTs into a combination of isotropic (ISO), DC, and CLVD MTs, assuming the same principal stress orientations for DC and CLVD MTs (e.g. Jost & Herrmann 1989), and compute their relative contribution to the total M_0 (DC, CLVD and ISO are expressed in percentage in Fig. 3.1b). For all the four source types, all respective 100 iterative inversions, MTs were recovered correctly with all moment tensor variance reduction (MTVR; the model goodness of fit comparing the inverted MT solution with the actual MT used to compute synthetic data) and waveform VR greater than 99.5% and 99.7%, respectively.

Table 3.1: Event information and parameters of MT inversion for the three events in this study. MT, moment tensor; NSD, Napoleonville salt dome. p and n are number of passes (1 = causal; 2 = acausal) and number of poles of the Butterworth filter, respectively.

	Hypothetical Events	Event TE1, NSD Sinkhole	Event TE2, HUMMING ALBATROSS	Event TE3, The Geysers, Northern California
Reference	-	Nayak & Dreger (2014); this study	Chiang *et al.* (2016)	Boyd *et al.* (2015)
Date (yyyymmdd)	-	20120801	-	20110301
Origin time (hh:mm:ss.ss)	-	20:52:38.50	-	02:19:47.01
Hypocenter-Longitude (°E), Latitude (°N), Depth (km)	-121.464, 36.755, 8.0	-91.1422, 30.0112, 0.47	- Depth = 9 m	-122.8200, 38.8153, 3.5
M_W	-	1.36	1.89	4.50
Type of waveforms used	Displacement	Displacement	Velocity	Displacement
Filter (Butterworth)	0.02-0.05 Hz, p 2 n 2	0.1-0.2, or 0.1-0.3 Hz, p 1 n 4	1.2-2.0 Hz p 2 n 2	0.02-0.05 Hz, p 2 n 4
Recording network	Berkeley Digital Seismic Network	US Geological Survey Temporary Network	Temporary broadband and short period seismometers	Berkeley Digital Seismic Network, Northern California Seismic Network, Lawrence Berkeley National Laboratory Short Period Network at The Geysers
Velocity model	GIL7 (Stidham *et al.* 1996)	Fig. 3.2a	Saikia *et al.* (1990)	GIL7, SoCal (Dreger & Helmberger 1993)
Number of stations used for waveform inversion	6	5	5	11
Distance range of stations for waveform inversion (km)	100-311	0.4-1.4	1.2-4.3	61-230
Number of first-motion *P*-wave polarities	-	6	16	173
Inverse distance weights for waveforms	Yes	no; inverse sum-of-squares weights used for each station	Yes	Yes

3.5 Tests on a real event

Numerous seismic events were associated with the development of a sinkhole at the western edge of the Napoleonville salt dome (NSD), Louisiana in 2012. MT inversion of these events using a grid-search approach and separate preliminary 1D velocity models for the salt dome and the surrounding sediment sequence yielded large isotropic volume-increase components in the MT solutions (Nayak & Dreger 2014; **hereinafter referred to as ND14**; **content in ND14 is the same as Chapter 2 in this thesis**). The centroid locations of these events were found to be at the western edge of the salt dome at ~470 m depth.

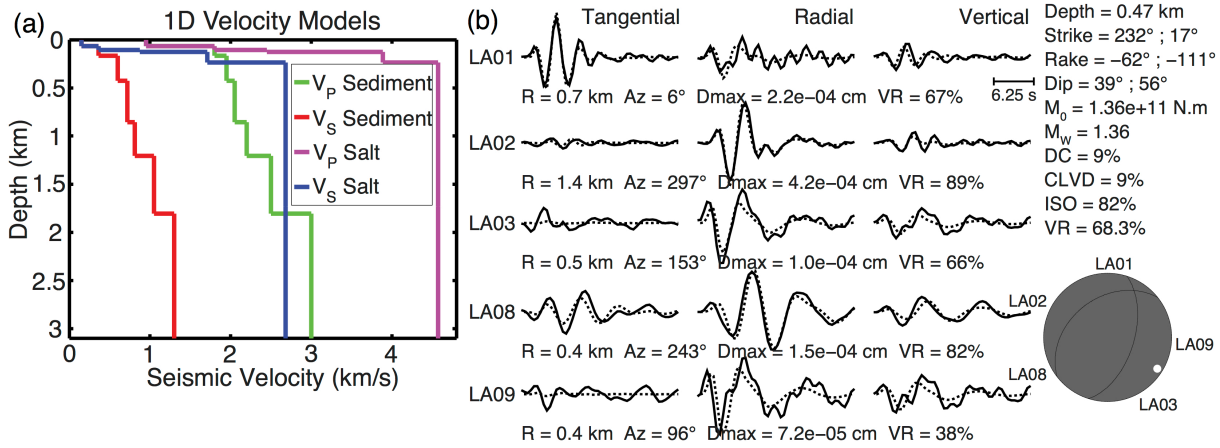

Figure 3.2: (a) Revised 1D velocity models used to compute Green's Functions (GFs) for MT inversion of event TE1. 'Salt' model was used for LA03 and LA09. 'Sediment' model was used for LA01, LA02 and LA08. (b) Observed (solid lines) and synthetic (dashed lines) displacement waveforms and the revised full MT solution for event TE1. The meanings of other symbols are the same as in Fig. 3.1b. Waveforms were filtered in the pass band 0.1-0.3 Hz for stations LA01, LA02, LA03 and LA09, and in 0.1-0.2 Hz for station LA08.

Here we use our iterative damped LS inversion scheme to estimate the MT solution of one of these events (event TE1 in ND14, **Chapter 2**) assuming various source types. Since the publication of ND14, we have updated the MT solution of event TE1 using revised 1D velocity models for the salt dome and the sediment layers surrounding the salt dome (Fig. 3.2a) and a broader frequency range of the waveforms (0.1–0.3 Hz used for LA01, LA02, LA03 and LA09 instead of 0.1–0.2 Hz used for all five stations previously). The details of the revised full MT solution and waveform fits are shown in Fig. 3.2b.

In this study, we consider pure opening cracks assuming sources in soft sediments ($\nu \sim 0.43$) and salt ($\nu \sim 0.24$), a pure DC source and a pure explosion for event TE1. $\boldsymbol{\lambda}$ corresponding to these four sources are indicated in Fig. 3.3. For the MT inversion of this event and other seismic events described subsequently, three-component broadband velocity waveforms were first corrected for instrument response, integrated to displacement, and then filtered in a low-frequency pass band appropriate for each seismic event. The horizontal, east-west and north-

south components were rotated to radial and transverse components. GFs were filtered in the same pass band as the observed waveforms.

The best-fitting MT solutions and waveform fits for various source types for event TE1 are shown in Fig. 3.3. A DC source, an explosion and a pure crack in salt fit the waveforms poorly at VR 31.5%, 32.3% and 45.7%, respectively. However, a pure crack in sediments fits the waveforms well at 66.6%, which is slightly lower than VR for the full MT solution, 68.3% (Fig. 3.2b). The uniform-phase nature of long-period *S* waves observed in radial components at all stations favors a volumetric source, whereas the strong variation of amplitudes with azimuth and the presence of SH waves favor a tensile-crack-type source rather than a spherically symmetric explosion. The strike of the tensile-crack plane for a crack in sediments (30° or 208°) agrees very well with the strike of the DC component in the full MT solution (17° or 232° in Fig. 3.2b) and with the strike of a shear-tensile source (crack + DC) in sediments (23° or 225°) estimated in ND14, **Chapter 2**.

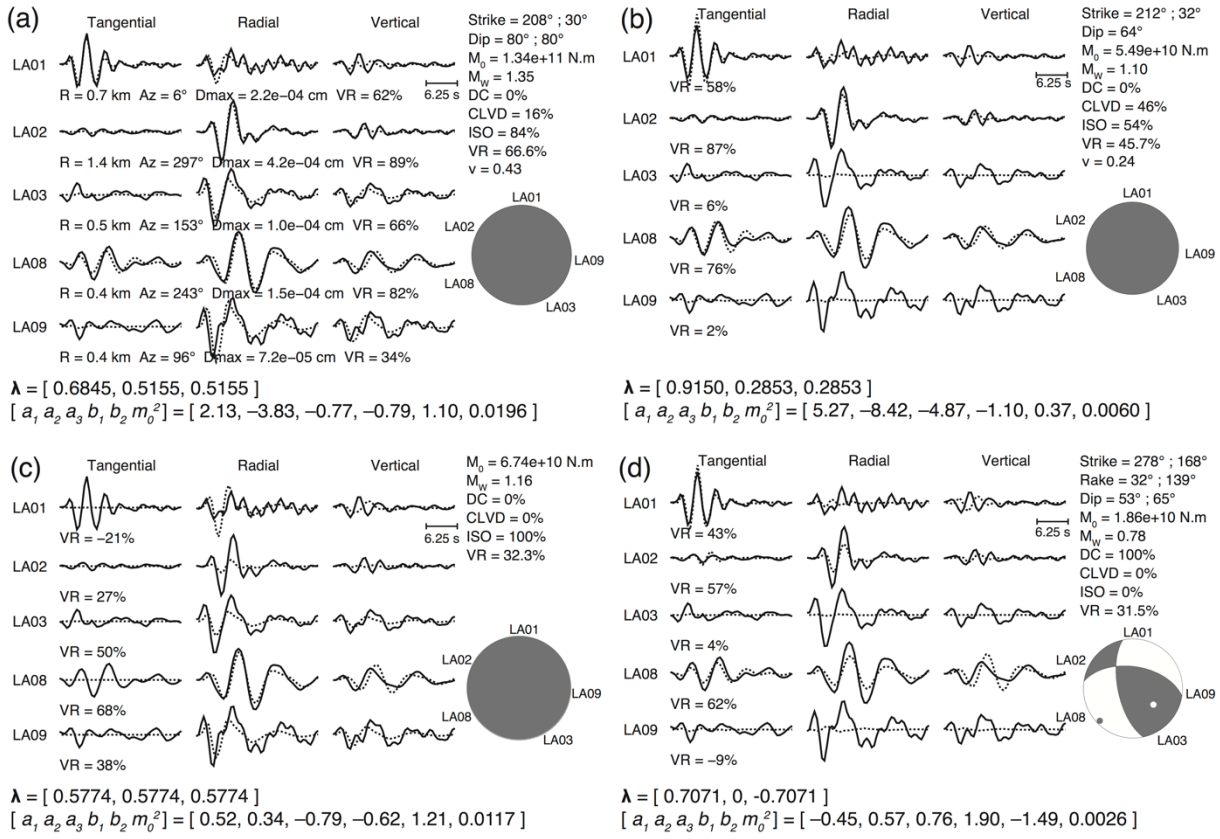

Figure 3.3: Best-fitting MT solutions of event TE1 described by normalized eigenvalues (**λ**), eigenvector parameters $(a_1, a_2, a_3, b_1, b_2)$ and seismic moment scale factor (m_0^2) for various source types: (a) tensile crack in sediment, (b) tensile crack in salt, (c) pure explosion and (d) a DC. The solid and dashed lines are observed and synthetic displacement waveforms, respectively. The meaning of other symbols are the same as in Fig. 3.1b. Station-specific *R*, Az and *D*max are the same in all subplots. Waveforms were filtered in the pass band 0.1-0.3 Hz for stations LA01, LA02, LA03 and LA09, and in 0.1-0.2 Hz for station LA08. Final values of $(a_1, a_2, a_3, b_1, b_2)$ are non-unique (see Fig. 3.A.2).

To verify our results, we estimated best-fitting MT solutions for these source types using a grid search and found the results agreed very well with our inversion results. With this method, separate constrained and linearized LS inversion formulations or grid-search formulations for common source types like explosions (Ford *et al.* 2009b), DC (Herrmann *et al.* 2011), and crack and pipe (Nakano & Kumagai 2005; Minson *et al.* 2007) sources can be replaced by a single mathematical formulation and inversion procedure where the user is required to only specify appropriate normalized eigenvalues for a particular source type. Moreover, the grid-search approach to estimate the best-fitting values of M_0 and fault-plane parameters (e.g., ϕ [strike], ζ [rake] and δ [dip] for pure DC MT solutions) is generally time consuming (Herrmann *et al.* 2011).

3.6 Application to maximum fit surfaces in source-type space

The maximum fit surface in source-type space has been called the Network Sensitivity Solution (NSS) in Ford *et al.* (2010) due to its ability to assess recovery of source-type information under changing network topology. The NSS is also used to assess confidence in source mechanisms of seismic events that are obtained from MT inversion with respect to its source type (or normalized eigenvalues). The NSS compares fits between observed and synthetic waveforms for a large population (usually on the order of tens of millions) of MTs covering the entire source-type space (Ford *et al.* 2010). MTs are assembled from random populations of eigenvalues and orthonormal eigenvectors. The eigenvalues are randomly drawn from a population of real numbers uniformly distributed between $-nL$ and nL where $L = \frac{\|\mathbf{u}_{\mathbf{T,R,Z}}\|}{\|\mathbf{G}\|}$ is a factor representing absolute size of the eigenvalues and the value of n (usually > 7) specifies the range of the eigenvalues with respect to L. Since the NSS depends on $\mathbf{u}_{\mathbf{T,R,Z}}$ and $\mathbf{G}$, it takes into account the station distribution, frequency content of waveforms, and data quality and quantity for a given MT inversion scenario. It generates a distribution of VR in source-type space that allows us to identify the uniqueness of the source type obtained from MT inversion, and the existence of possible trade-offs such as the explosion-negative CLVD trade-off commonly observed in nuclear explosions (Ford *et al.* 2010; Chiang *et al.* 2014). The eigenvalues are used to compute the two source-type parameters: ε and k (Hudson *et al.* 1989). In the Hudson plot (Hudson *et al.* 1989) the horizontal axis plots the ratio of the deviatoric eigenvalues (ε) and the vertical axis plots the relative isotropic component (k). For each coordinate (ε, k), the best VR value from all MTs corresponding to a small area around that coordinate is selected and plotted to generate the NSS (Ford *et al.* 2010).

The forward modeling of synthetic waveforms for millions of MTs required to produce the NSS is computationally intensive and time consuming. Moreover, considering a 6D parameter space, the population of random MTs needs to be very large in order to get some of the MTs close to the true best-fitting solutions for a particular source type, which, at best, can be approximate. However, we can use our source-type-specific MT inversion method to compute the NSS with greater accuracy and efficiency. We first construct a grid on the fundamental Lune of the normalized eigenvalue sphere using equation 20 of Tape & Tape (2012a), which

is reproduced in equation 3.15 with the radial coordinate set to unity.

$$\begin{bmatrix}\lambda_1\\ \lambda_2\\ \lambda_3\end{bmatrix} = \mathbf{U}^T \begin{bmatrix}\cos\gamma \sin\beta\\ \sin\gamma \sin\beta\\ \cos\beta\end{bmatrix}, in\ which\ \mathbf{U} = \frac{1}{\sqrt{6}}\begin{bmatrix}\sqrt{3} & 0 & -\sqrt{3}\\ -1 & 2 & -1\\ \sqrt{2} & \sqrt{2} & \sqrt{2}\end{bmatrix} \tag{3.15}$$

We keep the grid spacing in co-latitude β fixed at 1.8° and decrease the grid spacing in longitude γ linearly from ~ 1° at the poles to ~ 0.6° at latitudes ± 65°, keeping it fixed at ~ 0.6° around the equatorial region (Fig. 3.4a). This grid, comprising of 7457 unique coordinates, representing unique sets of normalized eigenvalues or unique source-types ($\boldsymbol{\lambda}$), is projected on the Hudson plot (Fig. 3.4b). The eigenvalue sets are arranged in a sequence having continuity in source-type space. For each $\boldsymbol{\lambda}$, we apply our iterative damped LS inversion scheme to estimate best-fitting values of m_0, a_1, a_2, a_3, b_1 and b_2. To estimate initial model parameter values for each $\boldsymbol{\lambda}$, we construct an initial population of ~50 solutions of m_0, a_1, a_2, a_3, b_1 and b_2 using values from inversion results of the previous $\boldsymbol{\lambda}$ (thus exploiting continuity of MT solutions in source-type space) and additional values of m_0 logarithmically distributed over two orders of magnitude. This set of solutions is used to forward model synthetic waveforms, and the solution that returns the best VR is used as the initial model. Sequentially repeating this process for all $\boldsymbol{\lambda}$ in the grid generates best-fitting eigenvectors and moment scale factors for all $\boldsymbol{\lambda}$, yielding the best-fitting VR surface covering the fundamental Lune or the Hudson space. We also skip over one or two eigenvalue sets in the grid if VR at the previous $\boldsymbol{\lambda}$ is between ~20% and ~30%, or less than ~20%, respectively. This increases the overall speed at the cost of source-type and VR resolution in those regions of the source-type grid that fit the waveforms poorly.

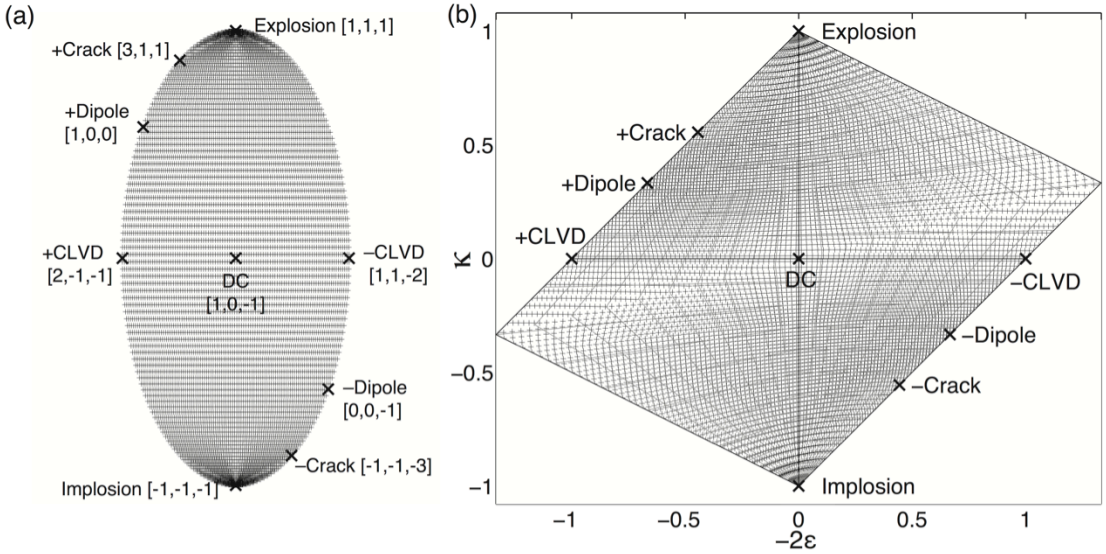

Figure 3.4: Grid of 7457 unique normalized eigenvalues (black '+' signs) or unique source types on (a) the fundamental Lune (Tape & Tape 2012a,b), and (b) on the Hudson source-type plot (Hudson *et al.* 1989). Black crosses are positions of major theoretical source types shown with their unnormalized eigenvalues.

We compute NSS for: (1) event TE1 of the NSD sinkhole sequence (ND14) described above, (2) event TE2, a chemical explosion for industrial applications (Chiang *et al.* 2016), and (3) event TE3, an earthquake at The Geysers geothermal field, northern California (Table 3.1).

TE2 is shot 800 in HUMMING ALBATROSS, an industrial quarry blast experiment involving a set of chemical explosions at very shallow depths (~10 to 15 m) and recorded at distances up to several kilometers away (Chiang *et al.* 2016). Data from these explosions have been analyzed in detail to study MT solutions in different frequency bands, depth dependence of MT solutions and source-type discrimination using both waveforms and FM polarities (Chiang *et al.* 2016). For event TE2, we used velocity waveforms and velocity GFs.

TE3 is an earthquake at The Geysers geothermal field in northern California that has witnessed a considerable increase in number of small-magnitude earthquakes (M_W 1.5–4.0) in response to steam production and water injection for reservoir recharge since the 1960s. Anomalous isotropic components have been detected in full MT solutions of many $M_W > 3.5$ earthquakes at The Geysers. The event we study (TE3) is a M_W 4.5 earthquake on 1 March 2011, which has a well-constrained 30% isotropic volume-increase component in its full MT solution (Boyd *et al.* 2015).

The NSS results for the three events are shown in Fig. 3.5. MT solutions that produce the best fits for the sinkhole event TE1 are tightly clustered in a region between theoretical explosions and tensile cracks, quite far away from theoretical deviatoric mechanisms and the expected closing cracks for a collapse process, which produce fits only up to VR ≤ 35% (Fig. 3.5a). Comparison of the shape of the NSS in Fig. 3.5a (computed using ~0.1-0.3 Hz waveforms), with NSS in Fig. 14a in ND14, Fig. 2.15b in **Chapter 2** (computed using 0.1-0.2 Hz waveforms) demonstrates that the constraints on source type are stronger for NSS computed using waveforms in a broader frequency pass band.

For event TE2, which is a chemical explosion, we observe that both DC and crack-like volume–increase MT solutions produce similar quality of waveform fits at VR ~82%-85% (Fig. 3.5b), which differs from common behavior of the explosion NSS. Usually CLVD sources with the vertical axis in compression provide similar quality of fits to explosion waveforms because an isotropic volume-increase MT solution and the vertically oriented negative CLVD both have an isotropic Rayleigh-wave excitation and no Love-wave excitation (Ford *et al.* 2009b, 2010, 2012). The very shallow depth of event TE2 (~ 9 m) causes the tangential (TDS), radial (RDS), and vertical (ZDS) GFs of the vertical dip-slip (DS) fundamental fault (Minson & Dreger 2008) to be vanishingly small due to free-surface vanishing traction. This, coupled with the fact that the source process also excited significant *SH* waves, introduces spurious M_{yz} and M_{xz} components in the MT solution leading to the vertical DS nature of best-fitting solutions near the DC region (Chiang *et al.* 2016). This is further confirmed by inverting waveforms of event TE2, assuming a pure DC source, which returns a vertical DS MT solution with M_W ~1.41, VR ~82.7%, and ϕ~ 34°, ζ~ 95°, and δ~ 86°, for one of the fault planes.

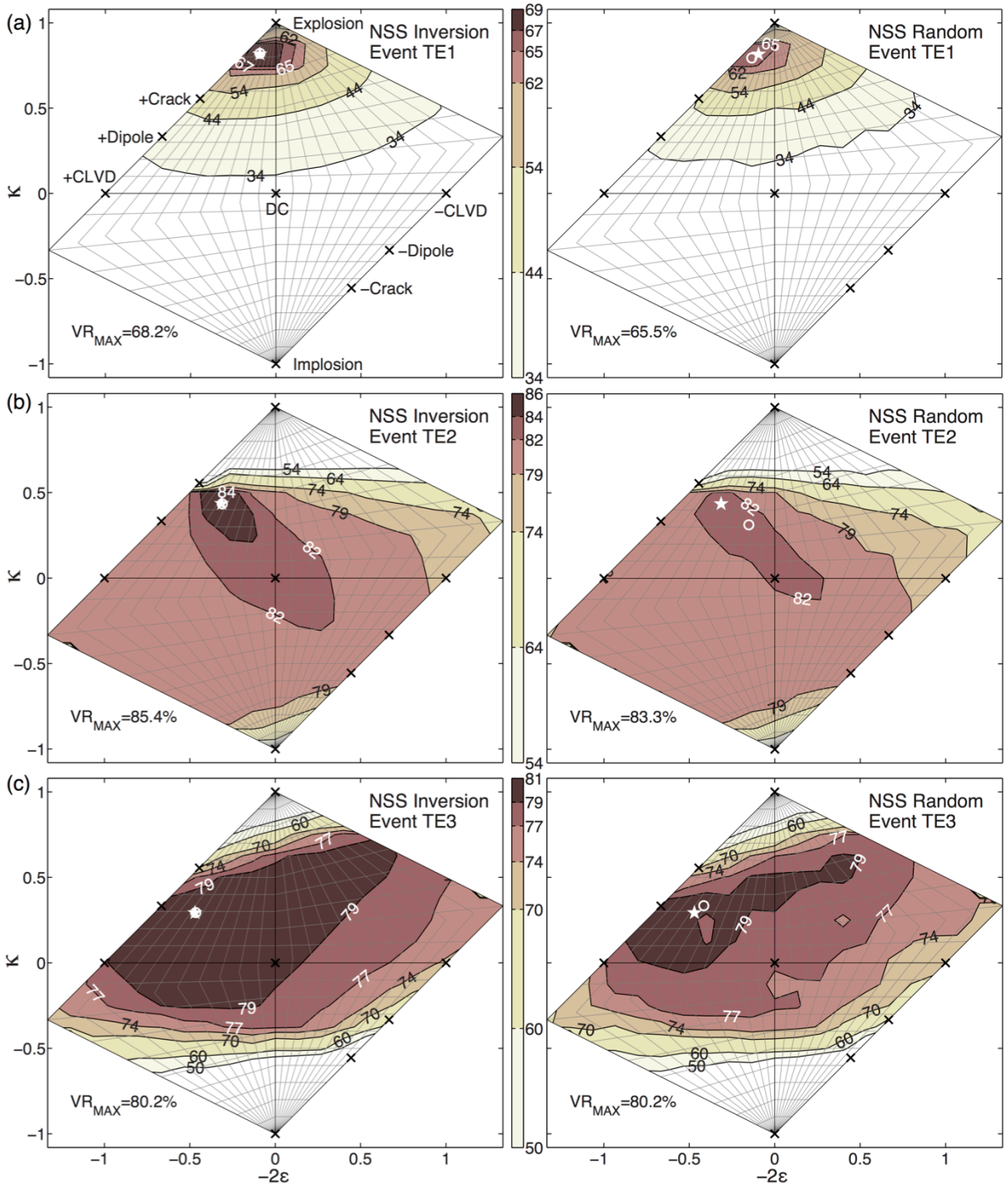

Figure 3.5: Network Sensitivity Solution (NSS) of the three events using low-frequency waveforms: (a) TE1, (b) TE2 and (c) TE3. Left panels (NSS Inversion) show NSS computed using the inversion approach in this study. Right panels (NSS Random) show NSS computed using randomly generated 80 million MTs. The contours and colors represent absolute values of variance reduction (VR; in %) whereas NSS plots in other studies usually show normalized VR (e.g., Guilhem *et al.* 2014; ND14; Chiang *et al.* 2014; Boyd *et al.* 2015). For each event, the VR scale is the same for both NSS plots (left and right) to enable better comparison. Black crosses are positions of major theoretical source types. For each event, the white star is

the position of the best-fitting full MT solution from a time-domain full MT inversion of waveforms. In each plot, the white circle is the source type corresponding to the maximum VR recovered by each NSS (VR_{MAX} in the lower left corner).

The best-fitting region of MT solutions for event TE3 (VR > 79%) covers a large area on the Hudson plot (Fig. 3.5c), and therefore its source type is poorly constrained by the NSS computed using low-frequency displacement waveforms alone. Its shape is different from that of a typical earthquake NSS (Ford *et al.* 2010; Chiang *et al.* 2014), which can be used to flag unusual events that warrant further investigation. Like many other events at The Geysers geothermal field, the best-fitting full MT solutions of event TE3 show primarily positive isotropic components (Boyd *et al.* 2015).

For comparison, we also compute the NSS for events TE1, TE2 and TE3 using the forward-modeling approach (e.g. Ford *et al.* 2010) with a population of 80 million MTs (n = 8) for each event (right panels in Fig. 3.5). For the three events, we compare: (1) the VR for the best-fitting randomly generated MT solution (VR_{MAX} in the NSS Random plots in Fig. 3.5), (2) the VR for the best-fitting MT solution obtained using our iterative damped LS inversion method (VR_{MAX} in NSS Inversion plots in Fig. 3.5), and (3) the VR of the best-fitting full MT solution computed from time-domain full MT inversion of waveforms (Minson & Dreger 2008). For the three events, the best-fitting random NSS VR are ~ 65.5%, 83.3%, and 80.2%, respectively. For the NSS-inversion method, they are ~ 68.2%, 85.4%, and 80.2%, respectively. The best-fitting full MT solution (Fig. 3.2b; Chiang *et al.* 2016; Boyd *et al.* 2015) VR are ~ 68.3%, 85.4% and 80.2%, respectively. The white circles and stars in Fig. 3.5 show the respective best-fit solutions.

Even with 80 million MTs, the best-fitting randomly generated MT solutions for events TE1 and TE2 fit their respective waveforms at VR lower than the VR of the best-fitting full MT solutions. The best values of VR recovered by the NSS computed using our iterative damped LS inversion approach are close to or the same VR as the best-fitting full MT solutions for all three events. We are also able to recover the source type of the best-fitting full MT solution, as seen in the overlap of the white star and the white circle on the NSS Inversion plots for all three events. Overall, we observe that our inversion-based MT solutions produce better waveform fits than MT solutions from a population of randomly generated solutions by VR ~ 0%–3% over a substantial area on the Hudson plot for all three events.

Computing the NSS by estimating the best-fitting MT solution at each grid point on the Hudson plot also gives us the flexibility to make the grid coarser or finer, depending on the purpose of our analysis, since the number of grid points affects the computation time. We can also choose to evaluate only a portion of the source-type space. For example, we can compute the NSS only for source types with positive sum of eigenvalues for the purpose of explosion monitoring. For event TE2, which has a total number of 7500 waveform samples (5 stations x 3 components x 500 samples per time series), a Fortran 90 code supported by LAPACK running in Mac OS X v.10.8.5 on a third-generation Intel 2.6 GHz i7-3720QM processor took little over 3 min in computing the NSS using the inversion-based approach. This opens up the possibility of near-real time source-type confidence analysis of seismic events after a general

MT solution has been computed (and possibly reviewed by an analyst), using minimal computational resources. In comparison, the same computer took ~60 minutes for forward modeling waveforms with 80 million random MTs.

The method to determine the NSS from a random population of eigenvectors and eigenvalues requires using a uniform distribution. Vavryčuk (2015) has shown that care is needed in the use of various MT norms applied to solution distributions in different source-type projections because a uniform distribution in one projection may not be uniform in a different projection. Moreover, distributions and uncertainties in MT elements are projected on source-type plots in complicated ways on different sections of the plots (Vavryčuk 2015). However, the NSS-inversion approach does not depend on any assumption on the distribution of MT eigenvalues. Instead the NSS-inversion systematically finds the best-fitting MT solution corresponding to each source type (normalized eigenvalues) on a predefined source-type grid sufficiently covering the entire source-type space or a specific section under investigation, for any source-type projection.

3.7 Incorporating first motions in the NSS

To better constrain the source radiation patterns of shallow explosion events, Ford *et al.* (2012) introduced the inclusion of teleseismic *P*-wave FM polarities in the NSS approach for better sampling of the entire focal sphere. Since waveforms used in MT inversion are usually of a low-frequency nature, inclusion of *P*-wave FM polarities from regional or teleseismic distance stations provides independent high frequency information. Inversion of MT solutions from *P*-wave FM polarities using the derivative-based scheme that we have implemented for waveforms is problematic, because the sign function is not differentiable at one point and its derivatives are zero everywhere else in the domain. Therefore, we employ a continuous function to approximate the sign function.

P-wave FM polarity data, u_{FM}, which is –1 (down or dilation), 0 (zero), or +1 (up or compression), can be written as

$$u_{FM} = \frac{u_{0Z}}{|u_{0Z}|} \text{ for } u_{0Z} \neq 0, \text{ and } u_{FM} = 0 \text{ otherwise} \tag{3.16}$$

in which $u_{0Z}$is first arriving *P*-wave vertical-component displacement amplitude that depends on MT elements, as well as azimuths and takeoff angles to individual stations (expression for far-field *P*-wave radiation in equation 4.29 in Aki & Richards 2002). u_{FM} can be approximated as

$$u_{FM} = \frac{u_{0Z}}{\sqrt{\epsilon + {u_{0Z}}^2}} \tag{3.17}$$

in which ϵ is a small positive number. Fig. 3.6 compares the sign function and its

approximation with $\epsilon = 1\text{x}10^{-4}$ used in this study, which makes it continuous and differentiable. u_{0Z} can be expressed as

$$\mathbf{u_{0Z}} = \mathbf{G'm'} = \mathbf{G'}\,\mathbf{f}(m_0^2, \boldsymbol{\lambda}, \mathbf{e_1}, \mathbf{e_2}, \mathbf{e_3}) = \mathbf{G'}\,\mathbf{g}(\boldsymbol{\lambda}, a_1, a_2, a_3, b_1, b_2) \qquad (3.18)$$

in which $\mathbf{G'}$ is a function of takeoff angles and azimuths. Because we are considering only the polarities of the displacement, we can drop the moment scale factor, m_0^2 as a variable (or $\mathbf{g} = \mathbf{f}/m_0^2$). Therefore, for constant and known source type $\boldsymbol{\lambda}$, FM polarity information can be expressed as an approximate scalar function of five independent parameters. Similar to the procedure applied to waveforms, we can set up an iterative damped LS inversion scheme to estimate best-fitting values of $(a_1, a_2, a_3, b_1, b_2)$ for a given $\boldsymbol{\lambda}$ with $\mathbf{du_{T,R,Z}}$ and $\mathbf{P}$ in equations 3.10–3.14 replaced by $\mathbf{du_{FM}}$ and $\frac{\partial \mathbf{u_{FM}}}{\partial \mathbf{u_{0Z}}}\mathbf{G'}\left[\frac{\partial \mathbf{g}}{\partial a_1}\ \frac{\partial \mathbf{g}}{\partial a_2}\ \frac{\partial \mathbf{g}}{\partial a_3}\ \frac{\partial \mathbf{g}}{\partial b_1}\ \frac{\partial \mathbf{g}}{\partial b_2}\right]$, respectively, with a different damping parameter k'.

The derivatives $\frac{\partial \mathbf{u_{FM}}}{\partial \mathbf{u_{0Z}}}$ are specific to each polarity data point. From Fig. 3.6, it is obvious that the derivatives will be non-zero only for data points close to the *P*-wave nodes. Therefore, for the FM polarity based inversion to proceed, there must be a sufficient amount of data such that some data points are always close to zero and their derivatives are non-zero. So, this derivative-based scheme for inversion of MT solutions works best on large FM polarity datasets. The quantity of FM polarity data required will depend on the takeoff angles, azimuths and the source mechanism itself. We fixed the value of ϵ at 10^{-4} from trial and error. Greater values of ϵ make the inversion more stable, but the derivatives are more approximate, making the final solution deviate from the true solution.

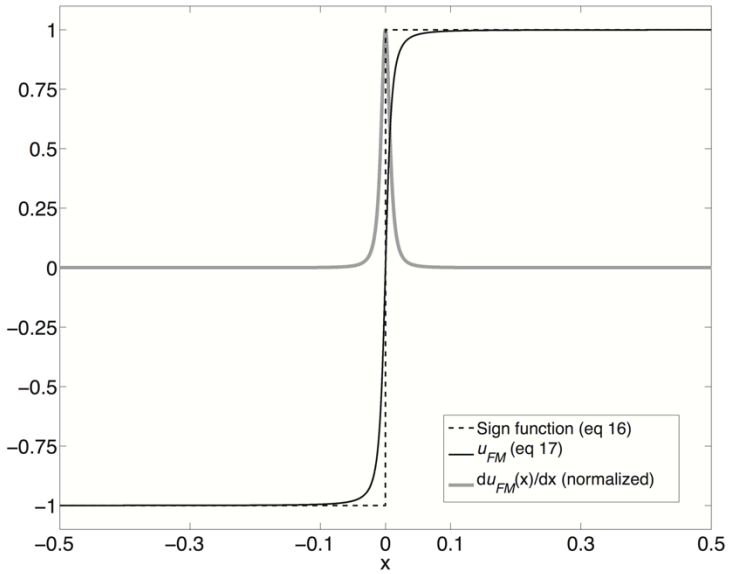

Figure 3.6: Figure showing the true sign function $sign(x)$ (equation 3.16), its approximation used in this study, $u_{FM}(x)$ (equation 3.17), and its normalized derivative $\frac{du_{FM}(x)}{dx}$, in which $x = u_{0Z}$.

We use this inversion scheme to construct an FM polarity-based NSS similar to that implemented for waveforms. We apply this scheme on FM polarities of event TE3 that has the largest amount of FM data among the three events (173 FM polarities collected from the stations of three networks in northern California). For all events in this study, FM polarities were picked by analysts and assigned weights on a scale of 1 to 3, based on their quality. We also increase number of initial models for each **λ**-specific inversion to 100 and we proceed with the inversion with 20 best initial models after comparing the initial fits. From trial and error, $k' = 10^{-2}$.

Prior to inversion of event TE3 polarity data, the inversion scheme was applied to synthetic *P*-wave FM polarity data sets for the 100 random MTs of pure DC and pure CLVD sources that were used in the synthetic waveform tests. The azimuths and takeoff angles in event TE3 dataset were used to generate synthetic *P*-wave FM polarities. For both source types, the inverted MT solutions were able to fit the polarity data perfectly (VR = 100%) for almost all (98 out of 100) random MTs, whereas the final data VR for the remaining MTs is > 98%. Because there can be multiple similar eigenvectors or orientations that fit a polarity dataset equally, the MTVR corrected for m_0^2 varies from ~91% to 99.9%.

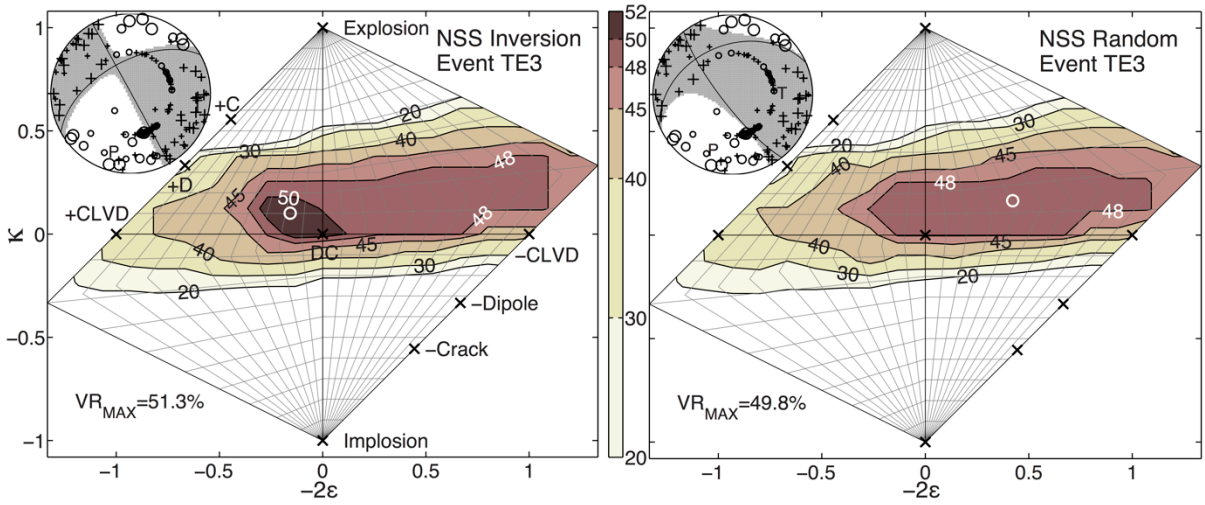

Figure 3.7: NSS of event TE3 using *P*-wave first motion polarities. '+Dipole' and '+Crack' are abbreviated to '+D' and '+C', respectively in the left panel. Focal mechanism plots show *P*-wave radiation pattern predicted by the MT solution corresponding to the maximum VR recovered by each NSS (white circle). Plotted against the predicted radiation patterns, black crosses and circles represent observed positive and negative *P*-wave FM polarities, respectively; the size of the polarity symbols is scaled by their quality weight (1, 2 or 3). 'P' and 'T' indicate pressure and tension axes, respectively. Explanation of other symbols, colors and contours in the NSS plots is same as in Fig. 3.5.

The results for event TE3 are shown in Fig. 3.7. Although the FM NSS constrains the mostly likely source type to be close to DC or deviatoric, the maximum VR is only ~51% indicating that there are no source types that fit all of event TE3 FM data well. This might be indicative of a complicated initial rupture process, errors in FM picks, or possible errors in depth or

takeoff angles. The misfit between observed and predicted polarities (focal mechanism in Fig. 3.7) is largely contributed by: (1) the anomalous polarities of Pn waves (polarities with steep equal takeoff angles in northeast and southeast quadrants) that are usually associated with uncertainties owing to their emergent nature, and (2) the section of the focal sphere towards south-southeast with both positive and negative polarities. Fig. 3.7 also shows the NSS computed from forward modeling FM polarities using a population of 80 million randomly generated MTs. Comparison of the two NSS plots in Fig. 3.7 shows that our approximate inversion method works well on large FM polarity datasets. It can possibly be used along with FM polarity analysis software like FPFIT (Reasenberg & Oppenheimer 1985) and HASH (Hardebeck & Shearer 2002) to identify anomalous events in near-real time. The approximation to the sign function (equation 3.17) doesn't affect the values of VR because the approximation is used to only compute the derivatives, whereas the actual sign function is used to forward model synthetic FM polarities to compute VR.

In order to test if the inversion-based NSS approach works for a smaller quantity of FM polarity data, we randomly selected two subpopulations containing only 30 and 7 FM polarities, out of the original TE3 dataset containing 173 *P*-wave FM polarities. The analysis was repeated on the smaller datasets, and the results are shown in Fig. 3.8. For both data subsets, our inversion scheme can compute an NSS nearly equivalent to one estimated by the forwarding modeling approach. Fig. 3.8 also shows that, ideally, a large quantity of FM polarity data is required to reliably constrain the source type of any seismic event. However, it is noted that the greatest benefit of our approach is the combination of waveforms and FM polarities, for which, as shown in previous studies (Ford *et al.* 2012; Chiang *et al.* 2014), only a few (~3 to 10) FM polarity observations can greatly enhance the recovery of the source type of events like nuclear explosions in sparse monitoring conditions.

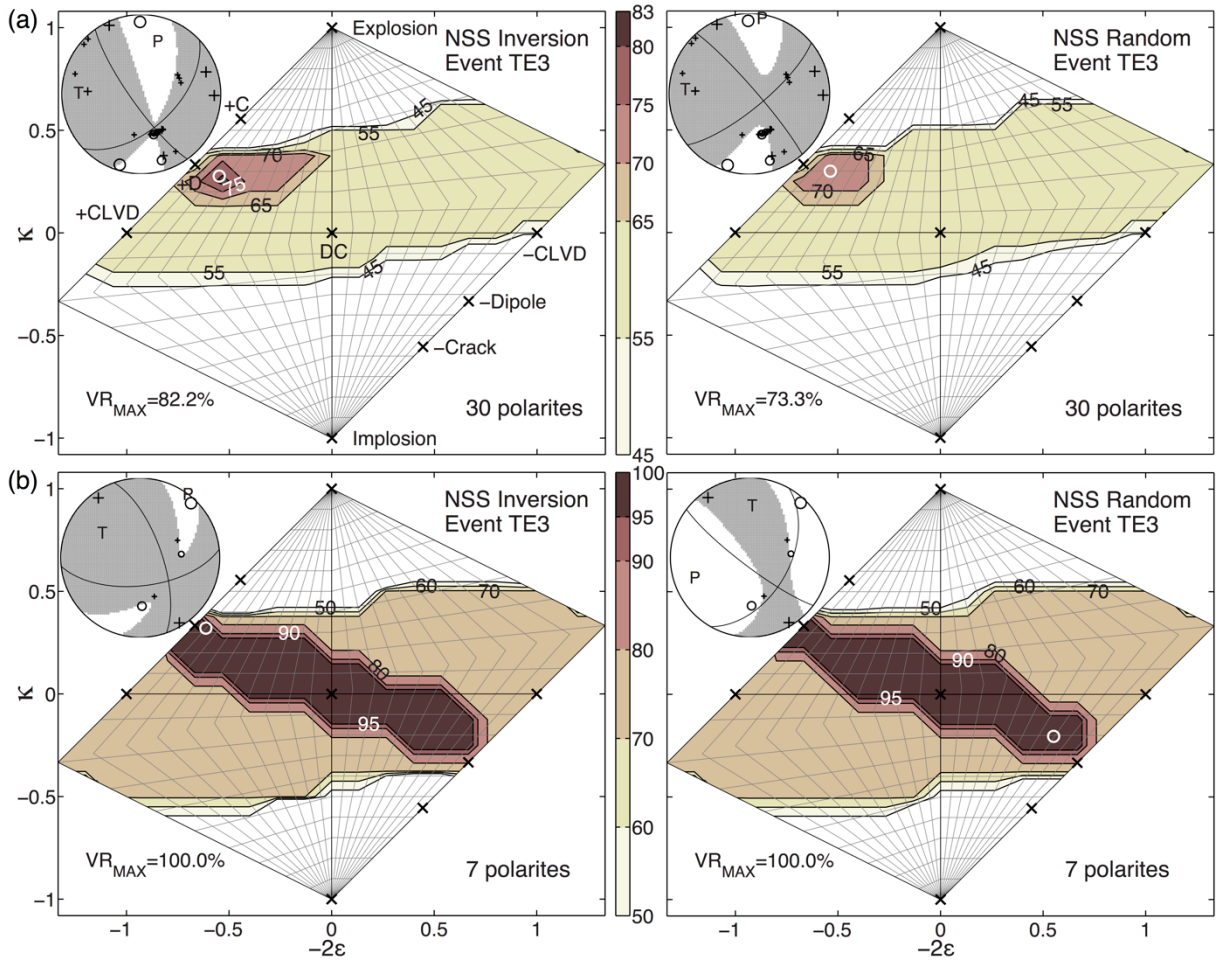

Figure 3.8: NSS of event TE3 using (a) 30 and (b) 7 P-wave first motion polarities randomly selected from the original dataset of 173 polarities. Explanation of features, symbols, colors and contours in the NSS plots is same as in Fig. 3.7.

3.8 Joint waveform and first-motion NSS-inversion

With the waveform and first-motion approaches it is now possible to perform a joint NSS inversion of waveform and FM polarity data for events TE1, TE2 and TE3. The two types of data are first inverse-weighted by their sum of squares to account for the difference between their amplitudes. We use 100 random initial models for each **λ**-specific inversion and test them against the data. Three models with the best fits are then used as starting models in the inversion. The damping parameter from trial and error is set to 10. Fig. 3.9 compares NSS computed using waveform and FM polarity data by joint inversion and forward modeling 80 million MTs, which are very similar. For events TE1 and TE2 (Fig. 3.9a,b), all FM polarities are positive, and the inclusion of FM polarities in the NSS constrains the best-fitting source type to be dominantly volume increase. The maximum VR recovered from the NSS computed using the joint inversion of waveforms and FM polarities for events TE1 and TE2 (~84.0%

and ~91.9%, respectively) are very close to the mean of separate maximum VR values for FM polarity data (100% for both events) and waveforms (~ 68.2% and 85.4%, respectively) which demonstrates the success of the joint inversion scheme proposed in this study.

For event TE3 (Fig 3.9c), the maximum VR recovered from NSS computed using the joint inversion of waveforms and FM polarities (~59.4%) is less than mean of maximum VR values (~65.8%) for separate waveform (~80.2%) and FM polarity (~51.3%) NSS. Assuming NSS converged to the best-fitting solution, this suggests that MT solutions or source types that best fit the low-frequency displacement waveforms and high-frequency *P*-wave FM polarities separately are not in perfect agreement with each other.

While FM polarities reflect the source mechanism at the beginning of the source-time history of an earthquake, low-frequency waveforms reflect the average source mechanism of the event under a point source assumption in time and space, which might lead to disagreement between best-fitting MT solutions for the two data types in the case of complex events. For example, initial radiated energy in explosions is expected to be isotropic and explosive, leading to all compressive FM polarities, whereas tectonic release during the later part of the time history might lead to deviatoric components in the point source MT solution obtained from waveform inversion. Man-made explosions are suitable for joint analysis of waveforms and FM polarity data, because the initial mechanism must be explosive and volume increase, leading to positive FMs irrespective of the nature of secondary mechanism responsible for non-isotropic components that are commonly found in MT solutions of explosions. For events in geothermal and volcanic environments, source-time functions could be complex and composite mechanisms could be diverse, and therefore, it might be difficult to reconcile FM polarity data with composite point source MT solutions. It is therefore expected that joint inversion of polarity data and low-frequency waveforms works best for small events with short-duration impulsive source-time functions. Nevertheless, the analysis can identify potential discrepancies between the two datasets, thereby raising caution and a need for further analysis.

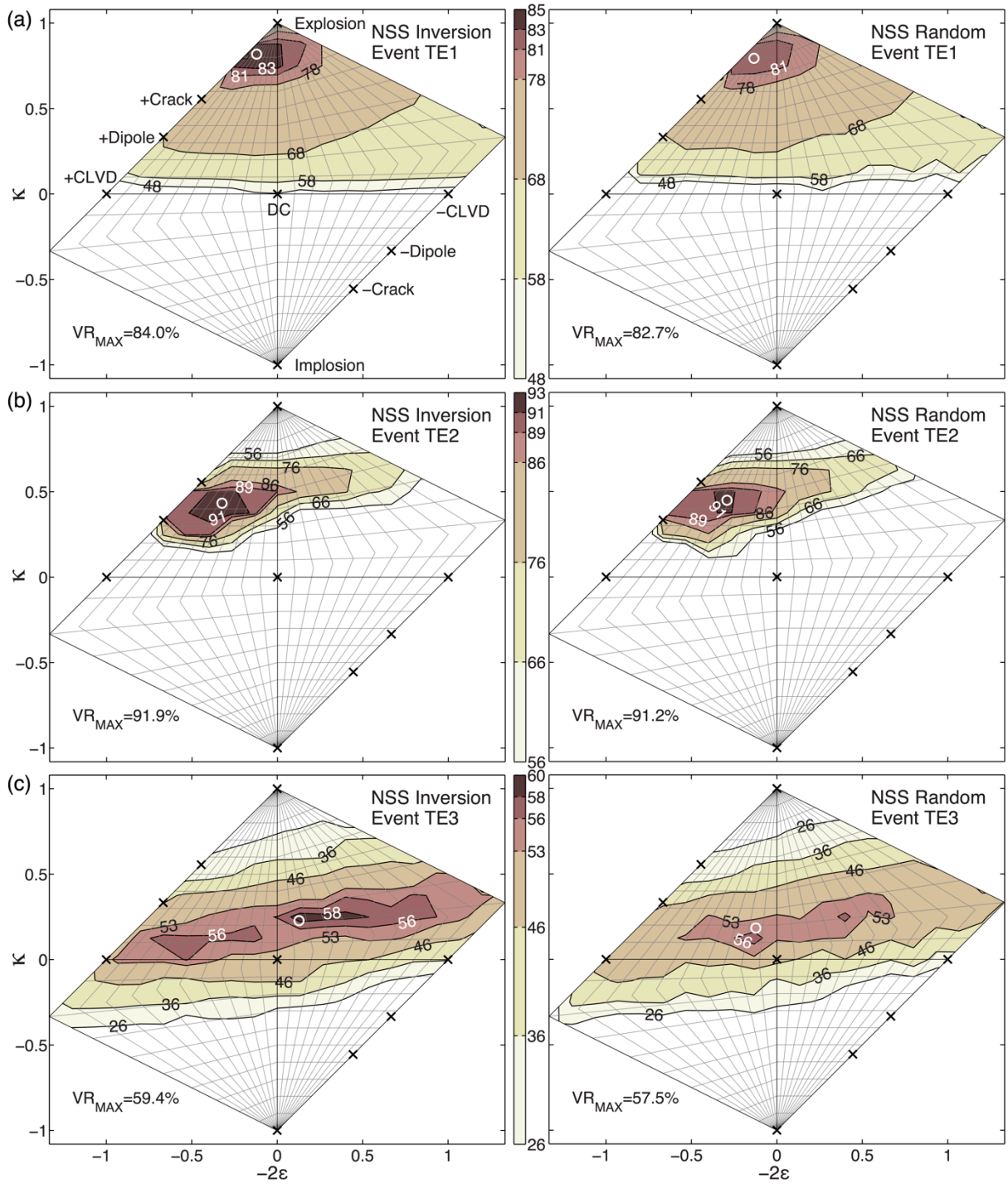

Figure 3.9: NSS of the three events using both low-frequency waveforms and FM polarity data: (a) TE1, (b) TE2 and (c) TE3. Explanation of symbols, colors and contours is same as in Fig. 3.5.

For all events and all types of NSS, the maximum VR, as well the size of the region of best-fitting MT solutions (highest contour levels in Figs 3.5, 3.7 and 3.9) recovered by the NSS-inversion approach, are either same as or greater than those recovered by forward modeling

80 million random MTs. For the waveform-only NSS, the VR recovered by the NSS-inversion approach are the either same as or greater than those recovered by forward modeling random MTs for almost all source types (Fig. 3.5). For the NSS computed using waveform and polarity data simultaneously, we recognize there are few eigenvalue sets for which VR values of the best-fitting MT solutions recovered by our inversion method are not as good as those from the large population of random MT solutions (e.g., see outermost contours of Fig. 3.9b). These differences are possibly caused by the inability of the inversion to converge further towards the true solutions on account of the derivatives of polarity data having near-zero values (see Fig. 3.6 and its explanation earlier in the previous section).

Comparing the results of multiple runs of joint waveform and FM polarity NSS inversion, we have observed that, while the shape of VR contours in NSS are similar, the maximum VR recovered can vary by ~1%–2%. Further work is required to design an improved inversion scheme with a better way of incorporating polarities that converges to the true global VR maximum at each instance. The computation of NSS by joint inversion of waveforms and polarity data also takes ~2-4 times longer than the computation when inverting waveforms alone. However, this increase in computation time can be remedied by not inverting at source-type grid points where the waveform-only VR is less than a particular threshold (e.g., 40%).

3.9 Conclusions

In this study, we define elements of the general MT in terms of: (1) its normalized eigenvalues that characterize its source type, (2) a seismic moment scale factor that scales the normalized eigenvalues to appropriate size or scalar moment, and (3) its eigenvectors that specify its orientation. We utilize this formulation to implement an iterative damped LS inversion scheme to invert displacement waveforms for best-fitting eigenvectors and the moment scale factor for specific eigenvalues, which results in the best-fitting MT solution for a specific source type. However, the expressions are general and can be used with other appropriate inversion techniques as well.

Our technique is successfully demonstrated by estimating best fitting MT solutions for synthetic data assuming various source types: cracks, explosion and DC. For low-frequency displacement waveforms of the three example events, we find the NSS computed using the inversion approach to be faster and more accurate by VR ~ 0%–3% compared to NSS computed by forward modeling 80 million randomly generated MTs. To better constrain the source types of these seismic events, we employ an approximation of the sign function in order to invert FM polarity data along with displacement waveforms using our derivative-based inversion scheme. We find that our inversion method is more successful than the random search approach in recovering the MT solution with the maximum VR, as well as the region of best-fitting MT solutions or source types for NSS computed using low-frequency displacement waveforms and *P*-wave FM polarities, both separately and jointly. The inclusion of *P*-wave FM observations with long-period waveforms narrows the range of possible MT solutions in the source-type space, leading to improved source-type discrimination. It would

be straightforward to also incorporate body-wave amplitude ratios, and such a combination of data types could be useful in cases in which the individual data sets are very sparse, such as for small-magnitude induced earthquakes.

3.10 Data and Software

The data for event TE1 were recorded by a U.S. Geological Survey temporary network (network code - GS) and downloaded through the Incorporated Research Institutions in Seismology Data Management Center (http://www.iris.edu/dms/nodes/dmc/; last accessed August 2013). Event TE2 was a part of the HUMMING ALBATROSS industrial quarry blast experiment whose data were provided by Weston Geophysical. Data for event TE3 come from Berkeley Digital Seismic Network (BDSN), doi:10.7932/BDSN, operated by the UC Berkeley Seismological Laboratory, Northern California Seismic Network (NCSN), and Lawrence Berkeley National Laboratory (LBNL) Short Period network at the Geysers, which are archived at the Northern California Earthquake Data Center (NCEDC), doi:10.7932/NCEDC. The Matlab versions of the inversion codes used in this study and Fortran 90 version of the waveform-only NSS inversion code are available with A.N.

3.11 Acknowledgements

We would like to thank Václav Vavryčuk (Institute of Geophysics, AS CR) for pointing out the equation used to compute P-wave FM polarities for a general MT and for his careful review of the manuscript submitted to *Bulletin of Seismological Society of America*. We are grateful to Václav Vavryčuk, an anonymous reviewer, Andrea Chiang (BSL), Sean Ford (LLNL) and Associate Editor of BSSA Michel Bouchon for their comments and suggestions, which greatly helped in improving this study. We also thank Andrea Chiang for providing the full MT solution, processed waveform and FM polarity data of event TE2, and for helpful discussions. We thank Sierra Boyd (BSL) and Voon Hui Lai (BSL) for providing the full MT solution, processed waveform and FM polarity data of event TE3.

3.12 Appendix

3.A.1 Partial derivatives of MT elements with respect to $(\boldsymbol{m_0, a_1, a_2, a_3, b_1, b_2})$

For partial derivatives of a quantity y with respect to $\mathbf{x} = [a_1, a_2, a_3, b_1, b_2]$, we will follow the convention

$$\frac{\partial y}{\partial \mathbf{x}} = \left[\frac{\partial y}{\partial a_1}, \frac{\partial y}{\partial a_2}, \frac{\partial y}{\partial a_3}, \frac{\partial y}{\partial b_1}, \frac{\partial y}{\partial b_2}\right] \tag{3.A.1}$$

Partial derivatives of r_1 and r_2:

$$\frac{\partial r_1}{\partial a_i} = \frac{a_i}{r_1} \; and \; \frac{\partial r_1}{\partial b_j} = 0 \text{ for } i = 1, 2, 3 \text{ and } j = 1, 2 \tag{3.A.2}$$

$$\frac{\partial r_2}{\partial \mathbf{x}} = [-b_1 e_{23}, -b_2 e_{23}, (b_1 e_{21} + b_2 e_{22}), (a_3 e_{21} - a_1 e_{23}), (a_3 e_{22} - a_2 e_{23})]$$

Partial derivatives of $\mathbf{e_1}$:

$$\frac{\partial e_{1i}}{\partial a_j} = \frac{\delta_{ij}}{r_1} - \frac{a_i a_j}{{r_1}^3} \text{ for } i = 1, 2, 3 \text{ and } j = 1, 2, 3 \tag{3.A.3}$$

$$\frac{\partial e_{1i}}{\partial b_j} = 0 \text{ for } i = 1, 2, 3 \text{ and } j = 1, 2$$

Partial derivatives of $\mathbf{e_2}$:

$$E = \begin{bmatrix} 0 & 0 & b_1 \\ 0 & 0 & b_2 \\ -b_1 & -b_2 & 0 \end{bmatrix}, \frac{\partial e_{2i}}{\partial a_j} = -\frac{e_{2i}}{r_2}\left(\frac{\partial r_2}{\partial a_j}\right) + \frac{E_{ij}}{r_2} \text{ for } i = 1, 2, 3 \text{ and } j = 1, 2, 3 \tag{3.A.4}$$

$$F = \begin{bmatrix} a_3 & 0 \\ 0 & a_3 \\ -a_1 & -a_2 \end{bmatrix}, \frac{\partial e_{2i}}{\partial b_j} = -\frac{e_{2i}}{r_2}\left(\frac{\partial r_2}{\partial b_j}\right) + \frac{F_{ij}}{r_2} \text{ for } i = 1, 2, 3 \text{ and } j = 1, 2$$

Partial derivatives of $\mathbf{e_3}$ with respect to $[a_1, a_2, a_3, b_1, b_2]$ can be computed using partial derivatives of $\mathbf{e_1}$ and $\mathbf{e_2}$ by simple chain rule. For example,

$$e_{31} = e_{12} e_{23} - e_{13} e_{22} \tag{3.A.5}$$

$$\frac{\partial e_{31}}{\partial \mathbf{x}} = e_{12}\frac{\partial e_{23}}{\partial \mathbf{x}} + e_{23}\frac{\partial e_{12}}{\partial \mathbf{x}} - e_{13}\frac{\partial e_{22}}{\partial \mathbf{x}} - e_{22}\frac{\partial e_{13}}{\partial \mathbf{x}}$$

Partial derivatives of M_{ij} with respect to $[a_1, a_2, a_3, b_1, b_2]$ can be computed using partial derivatives of $\mathbf{e_1}, \mathbf{e_2}$ and $\mathbf{e_3}$ with respect to $[a_1, a_2, a_3, b_1, b_2]$ by chain rule.

$$\frac{\partial M_{ij}}{\partial \mathbf{x}} = m_0^2\left[\lambda_1\left(e_{1i}\frac{\partial e_{1j}}{\partial \mathbf{x}} + e_{1j}\frac{\partial e_{1i}}{\partial \mathbf{x}}\right) + \lambda_2\left(e_{2i}\frac{\partial e_{2j}}{\partial \mathbf{x}} + e_{2j}\frac{\partial e_{2i}}{\partial \mathbf{x}}\right) + \lambda_3\left(e_{3i}\frac{\partial e_{3j}}{\partial \mathbf{x}} + e_{3j}\frac{\partial e_{3i}}{\partial \mathbf{x}}\right)\right] \quad \text{for } i = 1, 2, 3 \text{ and } j = 1, 2, 3 \tag{3.A.6}$$

The partial derivatives with respect to the moment scale factor are straightforward.

$$\frac{\partial M_{ij}}{\partial m_0} = \frac{2M_{ij}}{m_0} \text{ for } i = 1, 2, 3 \text{ and } j = 1, 2, 3 \tag{3.A.7}$$

3.A.2 Comparison between results of inversions using spherical and Cartesian eigenvector parameterizations

Assuming three independent trigonometric angles θ_1, θ_2 and θ_3 with domains $[-\pi, \pi]$, $[-\pi/2, \pi/2]$ and $[-\pi, \pi]$ respectively, we can define $\mathbf{e_1}$ and $\mathbf{e_2}$ in spherical coordinates as

$$\mathbf{e_1} = [\cos\theta_1 \cos\theta_2\,, \sin\theta_1 \cos\theta_2\,, \sin\theta_2] \tag{3.A.8}$$

$$\mathbf{e_2} = \frac{[\cos\theta_3 \sin\theta_2\,, \sin\theta_3 \sin\theta_2\,, -\cos\theta_2\,(\cos\theta_1 \cos\theta_3 + \sin\theta_1 \sin\theta_3)]}{r_0}$$

$$r_0 = \sqrt{\left(\cos\theta_2\,(\cos\theta_1 \cos\theta_3 + \sin\theta_1 \sin\theta_3)\right)^2 + (\sin\theta_2)^2}$$

$$\mathbf{e_3} = \mathbf{e_1} \times \mathbf{e_2}$$

The partial derivatives of MT elements with respect to $(\theta_1, \theta_2, \theta_3)$ can be easily derived as for the Cartesian parameters in section **3.A.1**. Following the procedure in section **3.4 Test on synthetic waveforms**, synthetic waveforms were computed for a hypothetical event assuming a pure DC MT solution ($\boldsymbol{\lambda} = [0.7071,\ 0,\ -0.7071]$), M_0 = 1x10^{15} N.m, $\phi = 325°$, $\delta = 60°$, $\zeta = 112°$) for the same depth and station configuration. We use the damped LS inversion procedure established in section **3.3.4 Inversion parameters** to compare results assuming both Cartesian $(a_1, a_2, a_3, b_1, b_2)$ and spherical $(\theta_1, \theta_2, \theta_3)$ parameterizations. We randomly generate 200 sets of orthonormal eigenvectors and m_0 values (between 1.0 and 10), and use them as initial values for both sets of inversions. For the spherical parameterization, the damping parameter was fixed at 10^{-7} from trial and error.

Figs 3.A.1 and 3.A.2 show the evolution of all parameters from their initial to final values as a function of number of iterations, for all 200 initial models and inversions with both

parameterizations. Fig. 3.A.1 shows that most of the initial models (197 out of 200) converge to the final correct MT solution as indicated by the final VR (> 99.9%) for most VR trajectories. For our choice of damping parameters, the inversions with spherical parameterization required more iterations (50–200) to converge to the correct solution compared to inversions with Cartesian parameterization (10–25). The final eigenvectors are one of the four combinations of $(\pm\mathbf{e_1}, \pm\mathbf{e_2})$ where the eigenvectors of the correct MT are $\mathbf{e_1}$ = [0.3222, 0.924, 0.206], $\mathbf{e_2}$ = [0.868, –0.3752, 0.3252] and $\mathbf{e_3}$ = [–0.3778, –0.074, 0.9229].

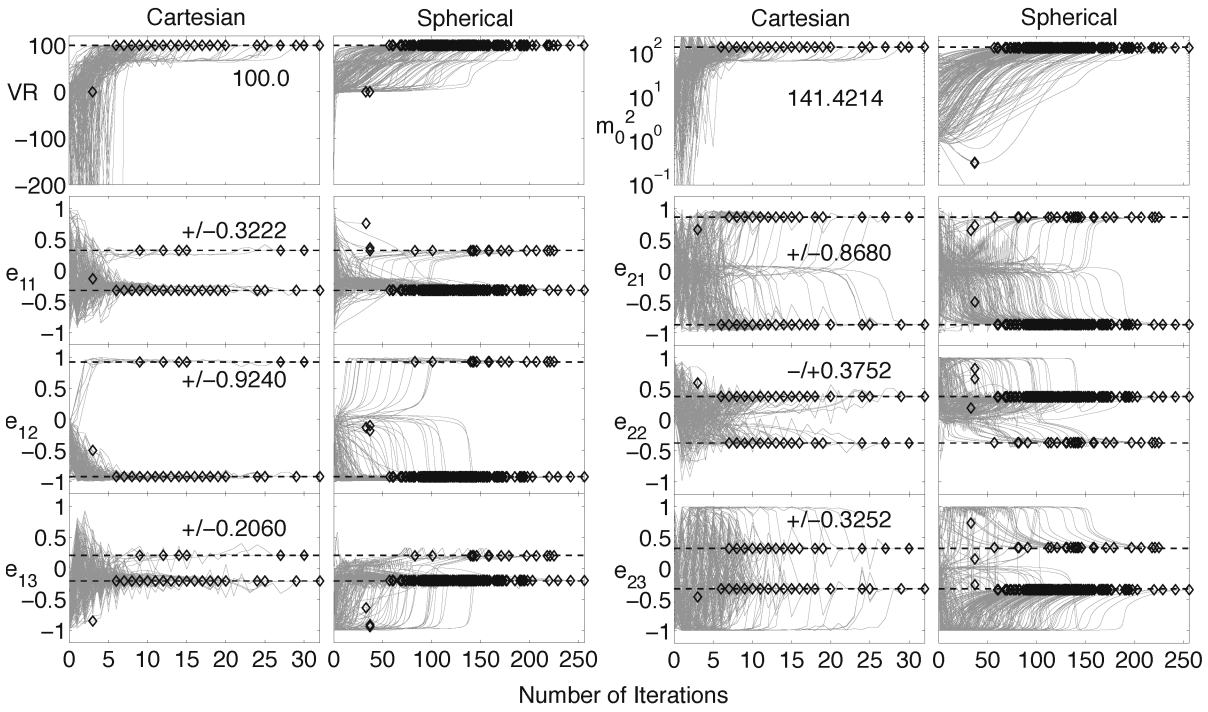

Figure 3.A.1: Comparison of values of various quantities as they change during the course of the iterative inversions, assuming Cartesian (left) and spherical (right) eigenvector parameterization. e_{ij} is the j^{th} component of eigenvector $\mathbf{e_i}$, m_0^2 is the moment scale factor and VR is variance reduction. Each gray line is a parameter trajectory that shows the path of that parameter from initial value at the beginning of the inversion (at iteration 0) to the final value at the end of that inversion (ending in a black diamond). Because there are 200 separate initial models, there are 200 parameter trajectories or 200 gray curves in each subplot. Dashed black lines indicate the theoretical values of the parameter at convergence to the correct MT solution. If an inversion has converged correctly to the true MT solution, its corresponding gray curve should meet a dashed black line at some iteration number (black diamond).

Fig. 3.A.2 shows that different initial values of $(a_1, a_2, a_3, b_1, b_2)$ can lead to different final values during the course of the iterative inversion, and multiple final combinations of $(a_1, a_2, a_3, b_1, b_2)$ can give the same MT elements and hence the same VR. Inverting for eigenvectors using spherical parameters (Fig. 3.A.2) also suffers from the issue of non-

uniqueness in final values as phase shifts in $(\theta_1, \theta_2, \theta_3)$ by $\pm\pi$ can also lead to the same MT elements.

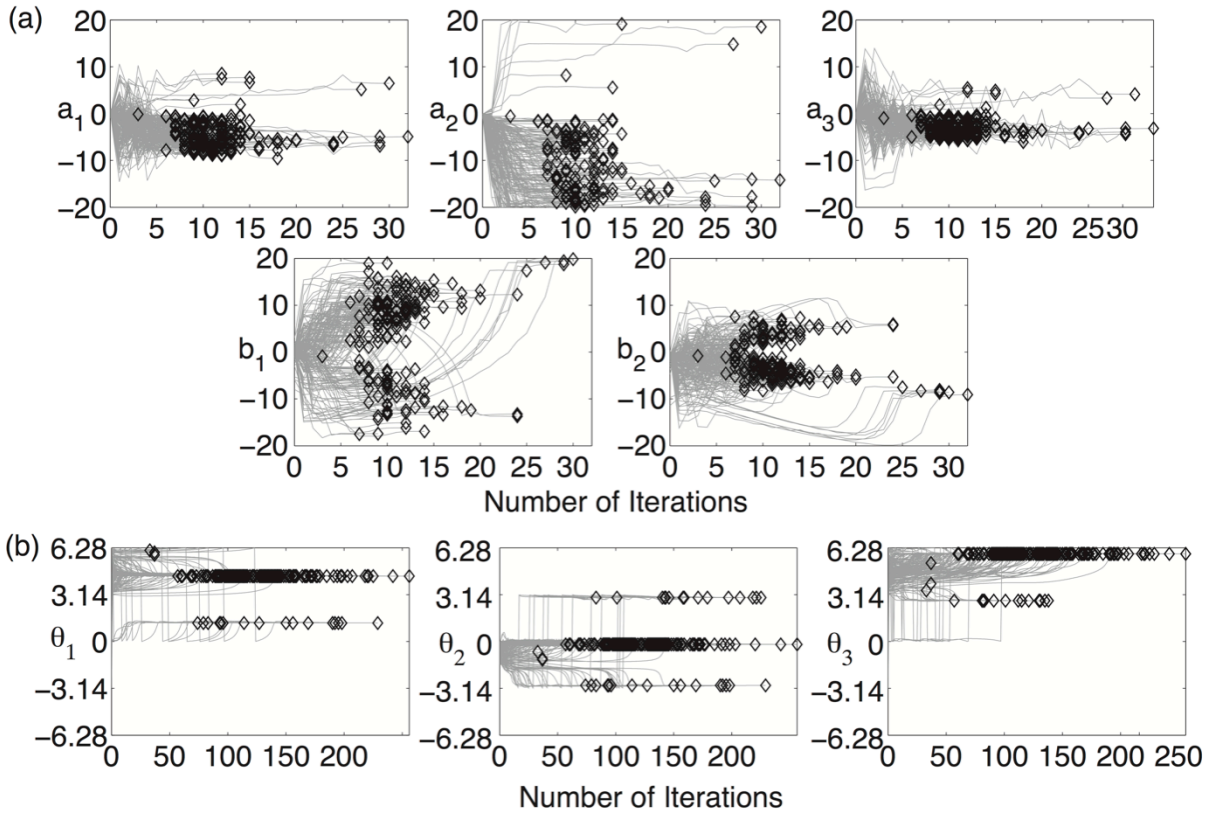

Figure 3.A.2: Similar to Fig. 3.A.1 but showing change in eigenvector model parameters for (a) Cartesian $(a_1, a_2, a_3, b_1, b_2)$, and (b) spherical $(\theta_1, \theta_2, \theta_3)$ parameterization. The final solutions in (a) are non-unique and widely varying but give the same MT solution (Fig. 3.A.1).

Fig. 3.A.3 shows the NSS for the three events in this study, computed from waveform inversion using spherical parameterization for describing the eigenvectors. They are similar to those in Fig. 3.5, computed using Cartesian parameterization, demonstrating that either parameterization can be used.

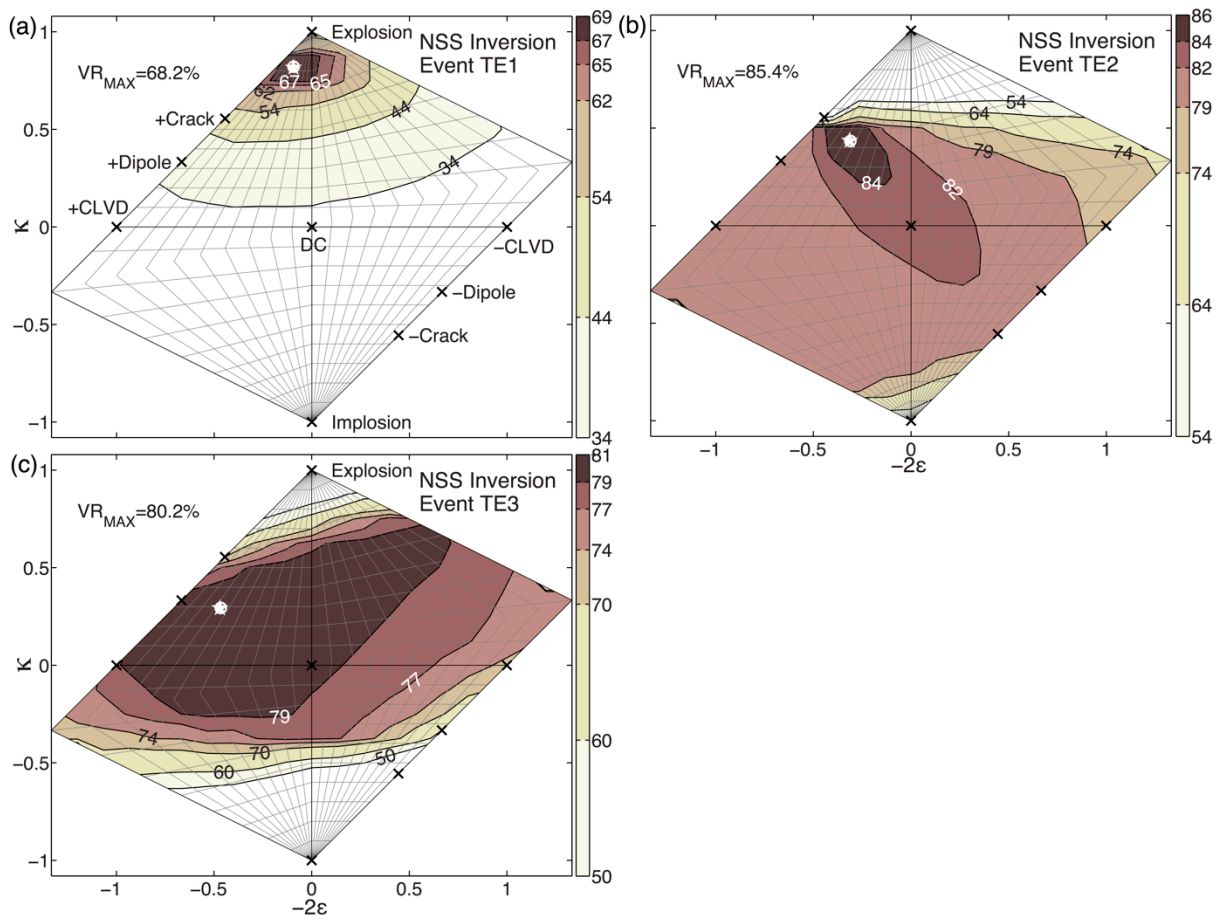

Figure 3.A.3: NSS of the 3 events in this study computed from inversion of low-frequency waveforms using spherical parameterization for describing eigenvectors: (a) TE1, (b) TE2 and (c) TE3. Explanation of features, symbols, colors and contours in the NSS plots is same as in Fig. 3.5. These plots are same as NSS in left panels of Fig. 3.5 that were computed using Cartesian parameterization of eigenvectors.

Chapter 4

Source Inversion of Seismic Events Associated with the Sinkhole at Napoleonville Salt Dome, Louisiana in the 0.1-0.3 Hz Frequency Band using a 3D Velocity Model

4.1 Chapter Abstract

The formation of a large sinkhole at the Napoleonville salt dome (NSD), Assumption Parish, Louisiana, caused by the collapse of a brine cavern, was accompanied by an intense and complex sequence of seismic events. We implement a grid-search approach to compute centroid locations and point-source moment tensor (MT) solutions of these seismic events using ~0.1-0.3 Hz displacement waveforms and synthetic Green's functions (GFs) computed using a 3D velocity model of the western edge of the NSD. The 3D model incorporates the currently known approximate geometry of the salt dome and the overlying anhydrite-gypsum cap rock, and features a large velocity contrast between the high velocity salt dome and low velocity sediments overlying and surrounding it. For each possible location on the source grid, Green's functions to each station were computed using source-receiver reciprocity and the finite-difference seismic wave propagation software SW4. We also establish an empirical method to rigorously assess uncertainties in the centroid location, M_W and source type of these events under evolving network geometry, using the results of synthetic tests with hypothetical events and real seismic noise. We apply the methods on the entire duration of data (~6 months) recorded by the temporary US Geological Survey network. During an energetic phase of the sequence from 24-31 July 2012 when 4 stations were operational, the events with the best waveform fits are primarily located at the western edge of the salt dome at most probable depths of ~0.3-0.85 km, close to the horizontal positions of the cavern and the future sinkhole. The data are fit nearly equally well by opening crack MTs in the high velocity salt medium or by isotropic volume-increase MTs in the low velocity sediment layers. The addition of more stations further constrains the events to slightly shallower depths. We find that data recorded by 6 stations during 1-2 August 2012, right before the appearance of the sinkhole, indicate that some events are likely located in the lower velocity media just outside the salt dome at depths ~0.35-0.65 km, with preferred isotropic volume-increase MT solutions. We find that GFs computed using the 3D velocity model generally result in better fits to the data than GFs computed using 1D velocity models, especially for the smaller amplitude tangential and vertical components, and result in better resolution of event locations and event source type. The dominant seismicity during 24-31 July 2012 is characterized by steady occurrence of seismic events with similar locations and MT solutions at a near-characteristic inter-event time. The steady activity is sometimes interrupted by tremor-like sequences of multiple events in rapid succession, followed by quiet periods of little of no seismic activity, in turn followed by the resumption of seismicity with a reduced seismic moment-release rate. The dominant volume-increase MT solutions and the steady features of

the seismicity indicate a crack-valve-type source mechanism possibly driven by pressurized natural gas.

4.2 Introduction

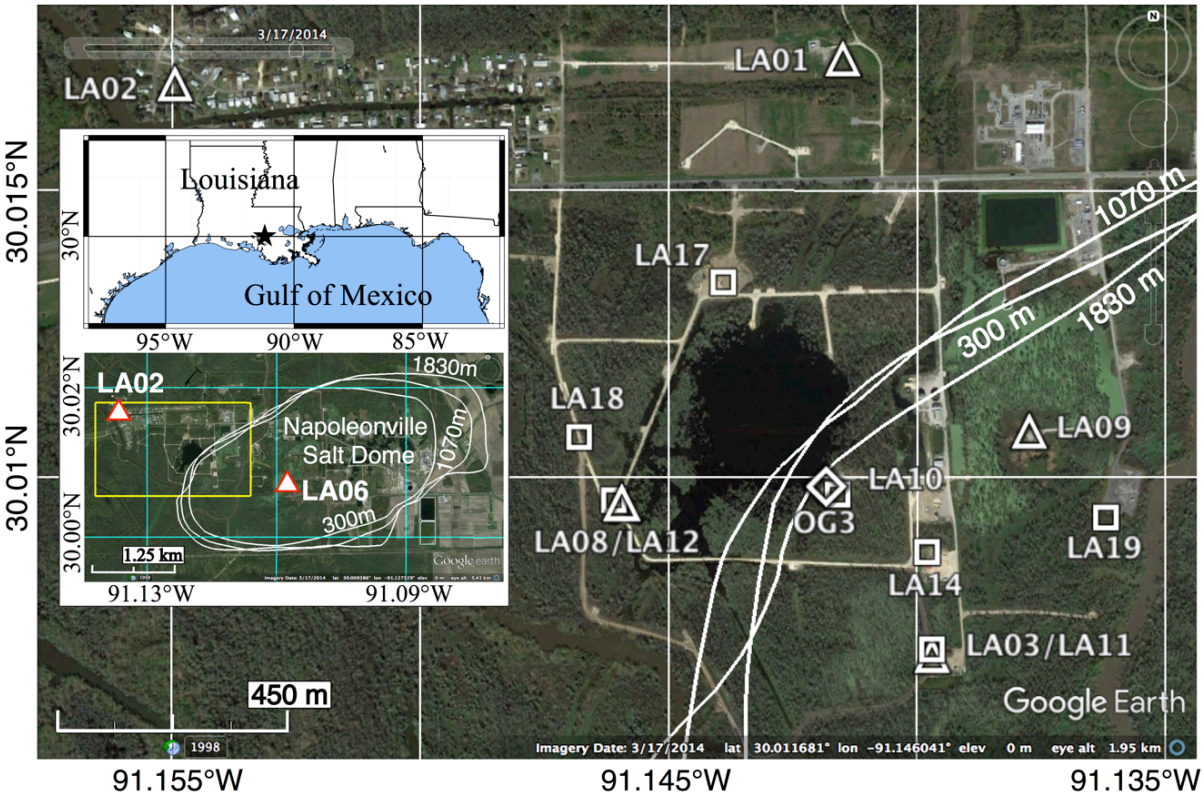

Figure 4.1: Top inset shows the location of the study region (black star) relative to the state of Louisiana (southeastern United States). Google Earth image in the bottom inset shows the study region, indicated by the rectangle and expanded in the main figure, at the western edge of the Napoleonville salt dome (NSD), with the depth contours of the salt dome indicated by white lines. The main plot shows locations of the U.S. Geological Survey (USGS) broadband stations (white triangles), the approximate location of the Oxy Geismar 3 cavern (white diamond) and station locations of the Texas Brine Corporation Louisiana Seismic Network (TBLSN; white squares) that replaced the USGS temporary network in January 2013. The USGS station LA06 shown in the bottom inset, located ~1.4 km east-southeast of the sinkhole, was not used in ND14. The Google Earth images are dated March 2014.

The formation of a large sinkhole at the Napoleonville salt dome (NSD), Assumption Parish, Louisiana (Fig. 4.1) in August 2012, associated with the sidewall collapse of an abandoned brine cavern Oxy Geismar 3 (OG3), was accompanied by a rich sequence of unusual and complex seismic events (Nayak & Dreger 2014 and references therein; Louisiana Department of Natural Resources, Office of Conservation [LADNR, OOC] 2013). OG3 was situated at the western edge of the salt dome very close to the present location of the sinkhole projected at depth, and extended from ~1.0 km to ~1.7 km below the surface (Figs 4.2, 4.3b-d). An exploratory well (Oxy Geismar 3A) drilled to the top of the cavern after the appearance of the

sinkhole revealed that the top of the cavern was intact and indicated a sidewall collapse (LADNR, OOC 2013). The cavern was partly filled with crude oil, natural gas and sedimentary material that established links to the bubbling of natural gas in the surface water bodies and crude oil found in the sinkhole. A funnel-shaped Disturbed Rock Zone (DRZ) from the base of the sinkhole down to a depth of ~360 m has been inferred from 3D seismic reflection surveys. The DRZ grows thinner adjacent to the salt dome with possible pinching in the strong limestone layers, and possibly has broad base adjacent to OG3 (LADNR, OOC & Chicago Bridge & Iron Company [CB&I] 2013). The DRZ is believed to be a pathway for the intense natural gas influx and crude oil accumulation observed at the surface.

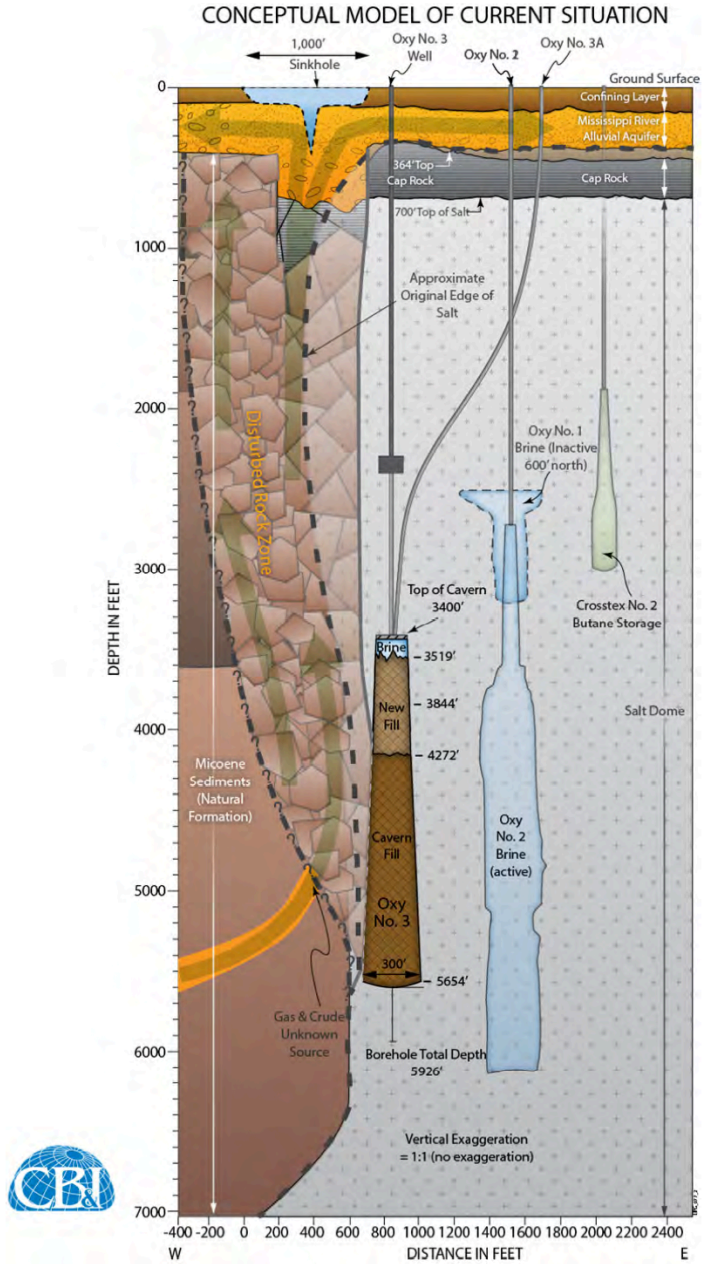

Figure 4.2: An illustration of the subsurface situation along an east-west profile (reproduced from CB&I 2013b).

Due to the large uncertainties in travel-time locations and the large number of events, Nayak & Dreger (2014) (hereinafter referred to as ND14; **content in ND14 is the same as Chapter 2 in this thesis**) implemented a grid-search based technique for autonomous detection, location and full moment tensor (MT) inversion (GRiD MT; Kawakatsu 1998; Tsuruoka *et al.* 2009) to investigate their source mechanisms. In this method, a 3D source grid is established around the probable source region of the seismic events under investigation. Segments of streaming low frequency waveform data are inverted for point source MT solutions at each location on the source grid using pre-computed Green's Functions (GFs) to the receivers. A real seismic event is inferred if the goodness-of-fit between the observed waveforms and the predicted waveforms based on the estimated MTs exceeds a particular threshold, and the best-fitting location and the associated MT solution are inferred to be the most appropriate centroid location and MT for that event. Applying this method, ND14 constrained the locations of ~60 events in a day prior to the appearance of the sinkhole to the western edge of the salt dome and found significant isotropic volume-increase moments in their MT solutions. ND14 attributed the events to high-pressure flow of natural gas or water–gas mixture through voids or pre-existing zones of weaknesses, such as cracks, fractures or faults at the edge of the salt dome, by volumetric expansion or tensile failure mechanisms similar to those observed in geothermal or volcanic environments.

The seismic velocity structure in the study region encompassing the recording stations and the source region of these events is strongly inhomogeneous, with a large seismic impedance contrast at the surface of the dome-shaped high velocity salt body, which is surrounded and overlain by weak, low velocity sediments. The effect of the 3D velocity structure is easily reflected in the differences between the broadband waveforms recorded at the stations on the sedimentary strata surrounding the salt dome (LA01, LA02 and LA08) and at the stations on the sediments overlying the salt dome (LA03 and LA09) as shown in fig. 4 in ND14, Fig. 2.4 in **chapter 2**. To compute the Green's Functions for MT inversion of these events, ND14 assumed two separate 1D velocity models, a sediment model and a salt dome model for paths to these two groups of stations, respectively and employed displacement waveforms filtered in a low-frequency passband 0.1-0.2 Hz that justified the assumption of simplified velocity models and treatment of the seismic events as point sources. However, employing low-frequency waveforms and different 1D models for different paths also reduced the accuracy and precision of the centroid location and it was unclear whether the events were located inside the salt dome or in the adjacent sediments. As a component of a separate study, Nayak & Dreger (2015) (hereinafter referred to as ND15; **content in ND15 is the same as Chapter 3 in this thesis**) presented revised results for one event (event TE1 in ND14) using higher frequency waveforms (0.1-0.3 Hz) for 4 stations and updated 1D velocity models. While the isotropic volume-increase component in the revised MT solution was found to be stable at ~82%, the Variance Reduction (VR), a measure of normalized goodness-of-fit between observed and synthetic waveforms (Minson & Dreger 2008), decreased from ~84% (ND14) to ~68% (ND15) reflecting poorer fits to the higher frequency waveforms especially in the smaller amplitude tangential components. In this study, we build upon and expand the work done by ND14 and ND15 by applying GRiD MT with GFs computed for a 3D velocity model of the western edge of the NSD that incorporates the currently known approximate geometry of the salt dome and the overlying anhydrite-gypsum cap rock.

In some source inversion studies of earthquakes at regional distances, GFs of properly calibrated 3D velocity models have been found to be helpful in improving fits to higher frequency waveforms (e.g., Covellone & Savage 2012; Zhu & Zhou 2016). Covellone & Savage (2012) also reported an increase in the percentage of the recovered double-couple (DC) moment in MT solutions of earthquakes that were obtained using a 3D velocity model GFs (3DGFs). This supports the idea that small non-double-couple (NDC) components commonly found in MT solutions of earthquakes estimated assuming GFs for 1D velocity models (1DGFs) can be caused by unaccounted path effects resulting from the real 3D velocity structure (Panning *et al.* 2001), in addition to other possible reasons such as noise or complexities in source processes (Julian *et al.* 1998). While it is unlikely that the large dominant volume-increase components in the MT solutions of events at the NSD are solely a consequence of the 1D velocity model assumption (ND14; Panning *et al.* 2001), the significant 3D nature of the velocity structure in the study region warrants source inversion of these events using GFs for a realistic 3D velocity model. In addition to the effects of large impedance contrasts, focusing or de-focusing of seismic waves caused by geometrically non-planar or irregular interfaces of geologic structures can significantly modify the seismic wavefield recorded at the earth's surface (Shani-Kadmiel *et al.* 2014 and references therein). By using GFs for a more appropriate and realistic 3D velocity model in the MT inversion framework, we improve fits to the higher frequency waveforms (0.1-0.3 Hz), gain more confidence in the centroid locations and better resolve the source-types of the seismic events. We obtain centroid locations and MT solutions of ~1567 seismic events at NSD during the entire duration (15 June 2012 to 27 January 2013) of the deployment of the temporary network of broadband stations by the United States Geological Survey (USGS) and describe the temporal evolution of the detected events.

4.3 Methodology

The basic details of the methodology and preliminary application of GRiD MT to the seismicity at NSD are described in ND14. In this section, we describe the 3D velocity model, methods used to compute GFs for the velocity models, and a modified version of the GRiD MT procedure employed in ND14.

4.3.1 Velocity model

The 3D velocity model, as described below, was assembled from results of various geophysical surveys, and analysis and interpretation of multiple datasets (Julie Shemeta, personal communication; Mark Leidig, personal communication). The sediment strata surrounding the NSD are part of the Mississippi River Valley alluvial aquifer (MRAA) zone, which is primarily composed of weak sediments of upper Pleistocene–Holocene age, trending towards older (~Miocene) and thicker units at greater depths. The inter-bedded salt, silt and clay layers are represented by a layered velocity model with P-wave velocity (V_P) and S-wave velocity (V_S) gradually increasing from ~950 m/s and ~150 m/s, respectively, at the surface to ~3.0 km/s and 1.3 km/s, respectively, at ~1.9 km depth (Fig. 4.3a). The very shallow V_S

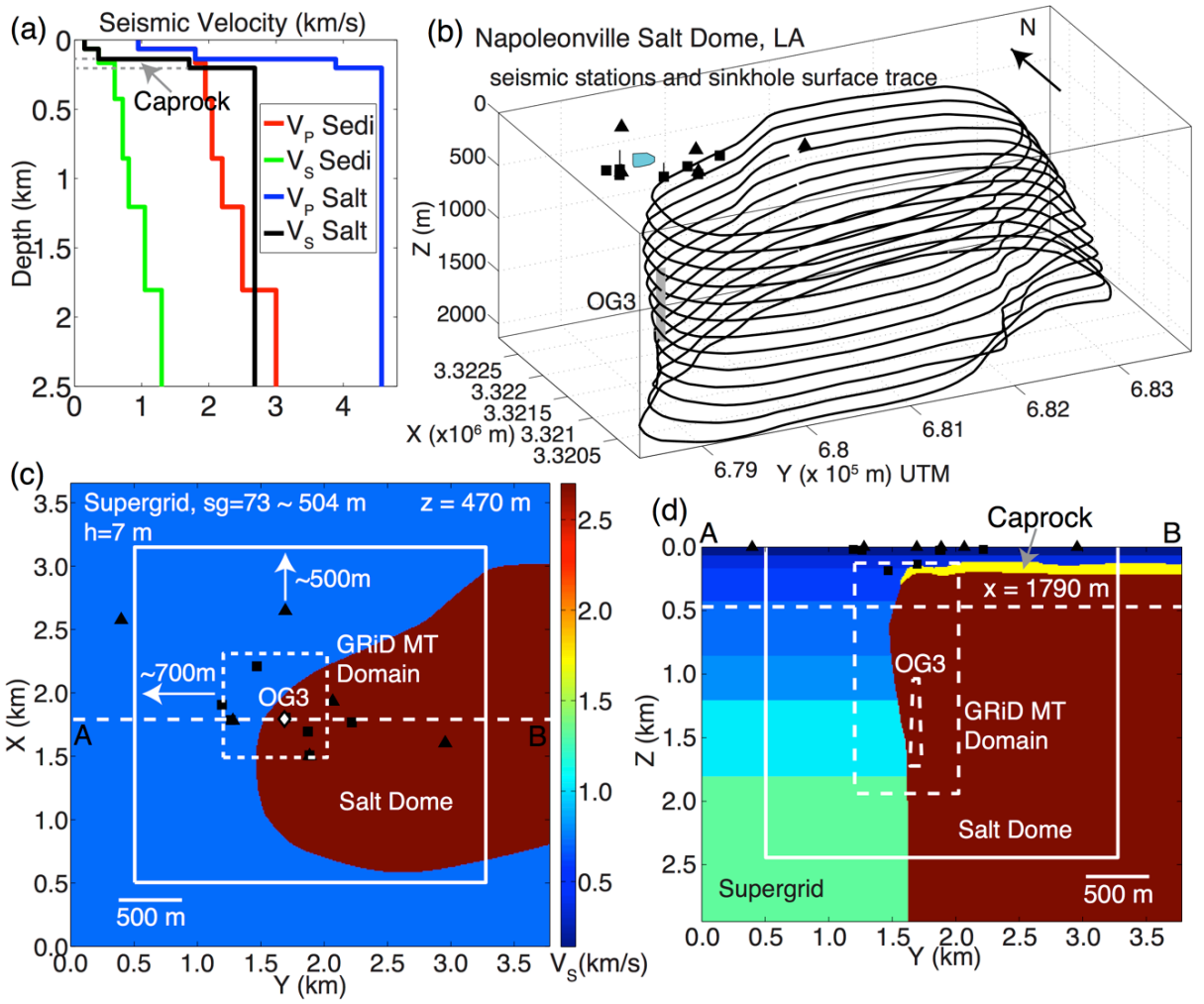

Figure 4.3: (a) 1D velocity profiles used in this study for stations over the salt dome (Salt) and over the sediment layers (Sedi). For the salt profile, the cap rock layer is delineated by gray dashed lines, sandwiched between the sediment layers (top) and the salt (bottom). Q_P, Q_S and ρ values adopted for the 1D models are similar to those for the 3D model. (b) Shape of NSD indicated by depth contours from ~300 m to ~2.1 km at ~152 m interval. Black triangles and squares are USGS and TBLSN stations, respectively. Blue polygon delineates the approximate surface extent of the sinkhole in ~2014. The vertical gray bar marks the approximate location of the cavern OG3 in 3D space. The coordinates are in UTM system (X, Y, Z positive towards north, east and down). (c) and (d) are XY and YZ slices through the computation domain with the color indicating V_S (same color scale for both plots). This domain was used for computing GFs for station LA01. (c) is a slice at depth ~470 m, marked by a dashed white line in (d) and (d) is a depth section across the profile AB (x=1790 km) shown in (c). In (c) and (d), the white rectangle delineates the extent of the supergrid domain at the sides and the bottom of the computation grid (~504 m thick), the dashed white rectangle delineates the extent of the GRiD MT grid and the black triangles and squares are USGS and TBLSN stations, respectively. In (d), the innermost dashed white polygon is an approximate outline of the OG3 cavern. A white diamond marks the approximate surface project of its horizontal location in (c).

structure (depth ~0-90 m) was constrained with Spectral Analysis of Surface Waves (SASW) tests at ~3 sites near the surface location of OG3. V_S ~150 m/s of the shallowest ~65 m thick layer in our velocity model is an approximate average of linearly increasing velocities from ~100 m/s at the surface to ~250 m/s at ~60 m depth. The high frequency Rayleigh wave phase velocity dispersion measurements in the SASW analysis are not very sensitive to P-wave velocities (V_P). Therefore, V_P for this layer is assumed to be ~950 m/s (Poisson's ratio ν~0.49). The salt dome and the overlying cap rock are treated as homogenous 3D volumes in the velocity model with V_P ~4.6 km/s, V_S ~2.68 km/s and V_P~3.8 km/s, V_S ~1.71 km/s, respectively, overlain and surrounded by sediments represented by the 1D sediment velocity profile in Fig. 4.3a. Fig. 4.3b shows the surface geometry of NSD with an average 1D velocity profile for locations over the salt dome in our area of interest shown in Fig. 4.3a. The salt in salt domes consists of interlocking halite crystals with seismic velocities that are nearly constant or increase very slowly with depth (Ezersky 2006; Zong 2014). The surface geometries of the salt dome and the cap rock at the western edge of the NSD were mapped in detail by extensive 3D seismic reflection surveys conducted in 2013 (Fig. 4.3a). Additionally, salt penetration data in the NSD salt structure map (New Orleans Geological Society, 1963), data collected during previous 3D seismic surveys in 2007 and a Vertical Seismic Profiling (VSP) survey in 2011 were utilized in building the models (Ratigan & Hill 2013). The velocity structure above the salt dome and absolute velocities in the salt are also constrained by zero-offset VSP surveys at ~3 sites within ~300 m of the surface location of OG3. The salt and the anhydrite-gypsum cap rock velocities in our model are generally consistent with corresponding material velocities in other studies (e.g. Zong [2014], Ezersky [2006] and references therein; CB&I 2013a). Zong (2014) obtained lab measurements of V_P ~ 4.4-4.8 km/s and V_S ~ 2.5-2.8 at confining pressures of ~0-27 MPa for salt cores from the NSD. The salt dome intrudes the sediment layers from below at depths of ~200-300 m below the Earth's surface and is believed to extend down to its source, the mid-Jurassic period Louann salt layer, at depth ~12 km. Contours of the salt dome are available down to a depth of ~2.2 km and show that the flanks are steeply dipping or almost vertical. The cap rock layer covers the crest of the salt dome with varying thickness (~50-70 m). We slightly modified the crest of the salt dome in the velocity model taking into account the salt penetration depths available at numerous wells and caverns in the NSD (Ratigan & Hill 2013). The velocity model contains sharp velocity contrasts between the sediment layers, and the cap rock and the salt volumes – V_S ratios (kms^{-1}/kms^{-1}) 1.7/0.36 ~ 4.7, ~1.7/0.6 ~ 2.8, ~2.7/0.6 ~ 4.5, ~2.7/0.7 ~ 3.75 and ~2.7/0.8 ~ 3.3.

The amplitude characteristics of elastic wave propagation are also controlled by the density and attenuation structure of the medium. The S-wave quality factor, Q_S is adopted following the V_S-Q_S relationship of Brocher (2008) [Q_S ~13–240 for V_S ~ 0.15–2.68 km/s in our model] and the P-wave quality factor, Q_P is assumed to be 2 x Q_S. For the adopted Q_S values, distances and wavelengths in this study, there is negligible anelastic attenuation of seismic waves through the salt body. This was also observed in the VSP studies. Cap rock and salt density were fixed at ~2.4 g/cm^3 and ~2.16 g/cm^3, respectively (e.g. Zong 2014). The density values (ρ) for sedimentary layers are derived from V_P values using Gardener's rule, $\rho = 1.75V_P^{0.25}$ (Gardener *et al.* 1974) with upper and lower bounds of ~1.93 g/cm^3 and ~2.4 g/cm^3, respectively. The adopted ρ values for the shallow structure over the salt dome are not very different from values obtained from density logging at one of the VSP sites. Figs 4.3c,d

show slices through the velocity model in the framework of the seismic wave propagation computation domain (described in the following).

4.3.2 Seismic wave propagation in the 3D model

To compute 3DGFs in our 3D velocity model, we use the software SW4 (Seismic Waves, 4^{th} order; version 1.19) developed at the Lawrence Livermore National Laboratory (LLNL), and invoke source-receiver reciprocity (Eisner & Clayton 2001) which greatly reduces the number of necessary finite-difference calculations.

SW4 is a node based finite difference seismic wave propagation code that solves the elastic wave equation in displacement formulation in 3D domains with 4^{th} order accuracy in space and time (Sjögreen & Petersson 2012; Petersson & Sjögreen 2015). The formulation satisfies the principle of summation by parts that guarantees energy stability of the numerical solution. Absorbing supergrid boundary conditions are used at the far-field boundaries and anelastic attenuation is also allowed (Petersson & Sjögreen 2012, 2014b). Since our stations lie at a wide range of distances from the source grid, we use different computational domains for different stations to reduce the computational effort. The basic grid used for computation of the 3DGFs spans ~1.8 km from the western tip of the NSD to the east and includes the southernmost extent of the NSD. This extent is likely to include the primary and all the major secondary interactions (reflections, etc.) of the wavefield with the salt dome for sources close to its western edge. In the horizontal plane, the computational grid is further extended such that it is always ~500 m away from the station locations and ~700 m away from the GRiD MT source grid. In depth, it extends to ~2.44 km, which is ~500 m deeper than the depth extent of the GRiD MT source grid. Since our knowledge of the geometry of the NSD is limited to ~2.2 km depth, the ~2.2 km depth contour of the NSD is extended to deeper depths as well in the 3D velocity model. We pad the computational grid with a supergrid of additional 73 grid points (~500 m). Figs. 4.3c,d show slices through our computation grid used to compute GFs for station LA01. For computation of 3DGFs with SW4, we use a grid spacing h = 7 m that allows ~21 grid points per shortest wavelength for the minimum V_S ~150 m/s in our model and the maximum frequency of our interest ~1.0 Hz. The corresponding time step is fixed at ~ 1.518e-3 s to for the maximum V_P ~ 4.6 km/s in our model. We compute waveforms up to ~37.7 s in time with origin time 0.7 s.

Our source grid for GRiD MT at the western edge of the NSD comprises of 14 (NS) x 14 (EW) x 33 (Z) ~ 6400 grid points with horizontal spacing of ~63 m and the vertical spacing that increases from ~49 m at the surface to ~70 m at ~1.94 km depth (Figs 4.3c,d). This source grid spans the 3D extent of the sinkhole, DRZ and OG3. All locations in our analysis are grid point locations unless stated otherwise.

As an example of the finite-difference calculation and to illustrate the effect of the strong 3D structure on the seismic wavefield, Fig. 4.4 shows the vertical component velocity wavefield for an isotropic moment tensor source ($M_{XX}=M_{YY}=M_{ZZ}=10^{11}$ Nm) placed just 160 m away from the salt dome. A Gaussian source time function with fundamental frequency f_0 ~ 0.5 Hz (*freq* parameter = 3.1416 and f_{max} ~ 1.25 Hz in SW4) was used for this particular wavefield. The seismic wavefield should be radially symmetric for an isotropic source in an isotropic 1D

velocity model, with zero amplitudes in the tangential component waveforms. At both long and short wavelengths at depth ~370 m and at the surface respectively (Figs 4.4a,b), the amplitudes in the sediment layers are larger than the amplitudes within and over the salt dome. Significant energy is reflected back into the sediment layers from the walls of the salt dome on account of the significantly higher velocity in the salt. The difference in amplitudes can also be visualized in synthetic waveforms at stations LA03 and LA09 that are located at similar distances from the isotropic source (Fig. 4.4c). Note the absence of any significant reflections from the boundaries of the domain showing the effectiveness of the supergrid absorbing boundary conditions. Thus the complex 3D wave propagation is likely to have an effect on both the estimation of event locations and the source mechanisms.

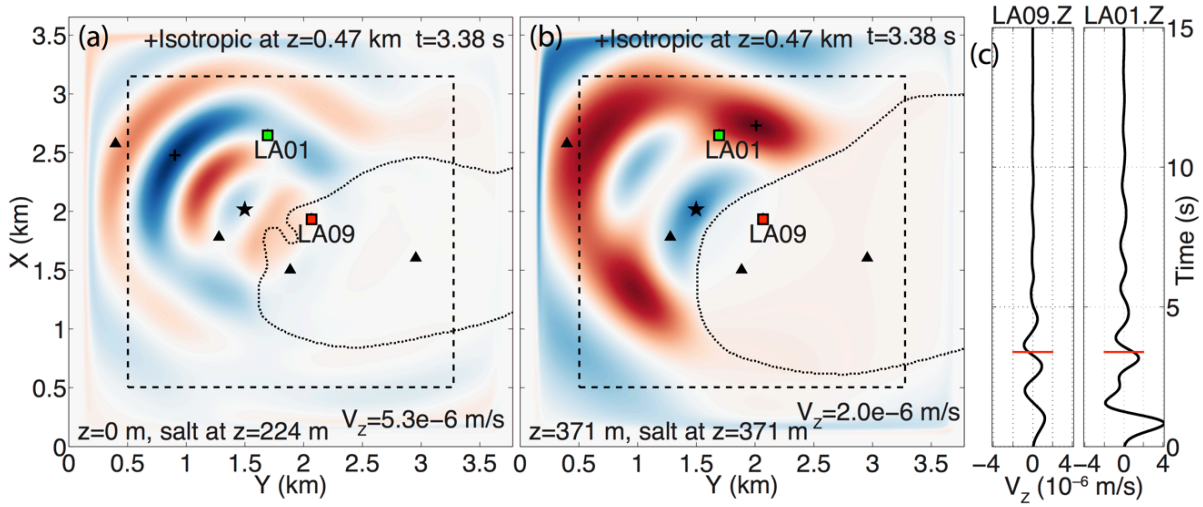

Figure 4.4: (a) and (b) are snapshots of the vertical component velocity wavefield at time t=3.38 s, at depths z=0 m (surface) and z=371 m, respectively (indicated at bottom left corner), in response to an isotropic MT source (black star) placed at z=470 m. The amplitudes of the wavefield are normalized by the instantaneous peak absolute amplitude (indicated at bottom right corner) and are plotted on a red (-1) to blue (+1) color scale. The domain shown here corresponds to the computation domain and the dashed rectangle marks the supergrid boundary (Figs 4.3c,d). The dotted line is the closest depth contour of the salt dome (depth indicated at the bottom of the plot: "salt at"), black triangles are USGS stations and the black '+' mark shows the location for the peak amplitude. (c) Time history of the same wavefield at stations LA09 and LA01 (red and green square, respectively, in [a] and [b]). The red tick is the instant corresponding to the snapshot shown in (a) and (b).

4.3.3 Reciprocal 3D model Green's functions for GRiD MT

GRiD MT requires force-couple GFs from each of the ~6400 grid points in the GRiD MT source grid to all stations. Instead of computing the required 3DGFs directly for the 3D velocity model, we use the reciprocity theorem and compute the spatial derivatives of the single-force 3DGFs from the stations to all grid points in the source grid (Graves & Wald

2001; Eisner & Clayton 2001; Aki & Richards 2002). This considerably reduces the amount of computational effort required.

The reciprocal formulation is briefly described. Let $G_{ij}(\mathbf{x}', \mathbf{x}; t)$ be a single-force GF from the source at position $\mathbf{x}$ on the GRiD MT source grid to a station at position $\mathbf{x}'$ where i is the direction along which the single force is applied at the source, j is the displacement direction at the station and t is time. Here i, j and k are along any of the orthogonal axis directions of our cartesian reference frame. Following the spatial reciprocity theorem (equation 2.39 in Aki & Richards 2002),

$$G_{ij}(\mathbf{x}',\ \mathbf{x};\ t) = \overline{G}_{ji}(\mathbf{x},\ \mathbf{x}';\ t) \tag{4.1}$$

We denote the reciprocal GFs from the station positions ($\mathbf{x}'$) to the source positions ($\mathbf{x}$) by $\overline{G}$. Assuming two equal and opposite forces along direction i and separated by an infinitesimally small distance along direction k, the force-couple GF $G_{ij,k}(\mathbf{x}', \mathbf{x}; t)$ from $\mathbf{x}$ to $\mathbf{x}'$ is given by

$$G_{ij,k}(\mathbf{x}', \mathbf{x}; t) = \frac{\partial G_{ij}(\mathbf{x}',\ \mathbf{x}; t)}{\partial x_k} = \frac{\partial \overline{G}_{ji}(\mathbf{x},\ \mathbf{x}'; t)}{\partial x_k} \tag{4.2}$$

$\frac{\partial \overline{G}_{ji}(\mathbf{x},\ \mathbf{x}'; t)}{\partial x_k}$ are the spatial derivatives of the reciprocal single-force GFs from the station positions $\mathbf{x}'$ at the source locations $\mathbf{x}$ on the GRiD MT source grid. For a seismic source at $\mathbf{x}$ with MT elements M_{ik}, the displacement u_j along direction j at station position $\mathbf{x}'$ is given by

$$u_j = M_{ik} G_{ij,k}(\mathbf{x}', \mathbf{x}; t) = M_{ik} \frac{\partial \overline{G}_{ji}(\mathbf{x},\ \mathbf{x}'; t)}{\partial x_k} \tag{4.3}$$

Repeated indices imply summation. In our implementation, the spatial derivatives are calculated by a 4th order accurate central-difference formula.

$$\frac{\partial \overline{G}_{ji}(\mathbf{x},\ \mathbf{x}'; t)}{\partial x_k} = \frac{-\overline{G}_{ji}(\mathbf{x}+2h\hat{\mathbf{e}}_\mathbf{k},\ \mathbf{x}'; t)+8\overline{G}_{ji}(\mathbf{x}+h\hat{\mathbf{e}}_\mathbf{k},\ \mathbf{x}'; t)-8\overline{G}_{ji}(\mathbf{x}-h\hat{\mathbf{e}}_\mathbf{k},\ \mathbf{x}'; t)+\overline{G}_{ji}(\mathbf{x}+2h\hat{\mathbf{e}}_\mathbf{k},\ \mathbf{x}'; t)}{12h} \tag{4.4}$$

where $\hat{\mathbf{e}}_\mathbf{k}$ is the unit vector along axis k and h is grid spacing (=7 m). Therefore, we require $\overline{G}_{ji}$ at 4 grid points on the computation grid for spatial derivatives with respect to one direction and at 4x3=12 grid points on the computation grid for a complete description of $G_{ij,k}(\mathbf{x}', \mathbf{x}; t)$ at one grid point $\mathbf{x}$ on the GRiD MT source grid. The spatial derivatives can also be directly obtained from SW4, which implements a 2nd order accurate central difference formula.

4.3.4 GRiD MT

For computation of all GFs (both 1DGFs and 3DGFs) in this study, we use impulse or Dirac source-time function for numerical stability. The ground motions thus obtained are displacement responses for an input impulse source-time function or effectively velocity

responses for an input step source-time function. The responses are integrated and filtered in appropriate passbands: 0.1-0.2 Hz for LA08 and 0.1-0.3 Hz for all other stations using a causal 4-pole Butterworth bandpass filter. The filtered responses are decimated (after applying an anti-aliasing filter) and resampled to 0.25 s sampling interval and then used in GRiD MT. The observed broadband velocity waveforms are integrated to displacement, filtered in the same frequency passbands as the GFs and decimated to 0.25 s sampling interval. In this study, we also use a 6th station LA06 situated over the salt dome ~1.3 km away from the sinkhole (Fig. 4.1). While LA06 is the farthest station from the sinkhole and its records are of ~poorer signal-to-noise ratio (SNR, defined in the section **4.3.6 Location Uncertainties**) compared to the records at other stations, it is a crucial station for constraints on seismic events early into the sequence prior to the installation of stations LA08 and LA09 close to the probable source region (on ~31 July and 01 August 2012, respectively). We also slightly modify the GRiD MT procedure in this study. First, we apply GRiD MT using coarsely sampled GFs on coarsely sampled observed waveforms (at 0.5 s) without any weighting. Thereafter, GRiD MT with GFs and observed waveforms sampled at 0.25 s is applied to the temporal neighborhood (±5 samples) of centroid origin times that returned best-fitting VR > 40%. A real event is inferred if the final VR has a local maximum over 5 consecutive samples and peak VR exceeds 40%. Waveforms at each station are also inversely weighted by the variance of the waveforms of the three components to reduce bias from any particular station. However, this requires that the generalized inversion kernels to be calculated for each grid location and origin time separately. For all detections, we visually examine the data to remove false detections from our catalog. Sometimes, we also remove the data of the noisier station LA06 from solutions of smaller events. We calculate the scalar seismic moment (M_0) using the definition of Bowers & Hudson (1999). We decompose all MTs into a combination of isotropic (ISO), double-couple (DC), and compensated linear vector dipole (CLVD) MTs, assuming the same principal stress orientations for DC and CLVD MTs (e.g. Jost & Herrmann 1989), and compute their relative contribution to the total M_0 (DC, CLVD, and ISO contributions are expressed in percentage).

4.3.5 GRiD MT results

ND14 and ND15 discussed results for event TE1 in great detail. In this study, we discuss another event TE2 that occurred ~125 min after event TE1 as event TE1 waveforms at station LA06 were found to be significantly contaminated by noise. For seismic events in this time window around ~1 day before the appearance of the sinkhole, ND14 reported very similar waveforms indicating closely spaced hypocenters and a repetitive source process, which reflected in very similar GRiD MT solutions. Therefore, we expect results for TE2 to be similar to TE1. Using 3DGFs and the 6 USGS stations, we locate event TE2 at grid point –91.1428°E, 30.0114°N, depth 518 m (Figs 4.5a,b), with the centroid origin time 22:57:48.75 UTC on 01 August 2012. The centroid location is well constrained, immediately outside the salt dome (Figs 4.5a,b). The details of the full MT solution and the waveform fits are shown in Fig. 4.6a. While the best-fitting depth (z_{MAX}) is similar to the depth of event TE1 estimated by ND14 and ND15, we find a slightly larger volume-increase moment in the full MT solution (ISO 88% compared to 72%-82% in the other 2 studies). The 3DGFs provide excellent fits to all components of observed displacement especially to the small-amplitude tangential and vertical components with the maximum VR of the best-fitting MT solution

(VR_{MAX}) up to ~73.5%. Figs 4.5c and 4.5b show the centroid location in XY space and waveform fits, respectively, for event TE2 obtained with 1DGFs (velocity models shown in Fig 4.3a) computed using the frequency-wavenumber integration method based on Haskell (1964) and Wang & Herrmann (1980), as provided in Herrmann (2013a). The 3D velocity model provides significant improvement in waveform fits over the 1DGFs in the very small tangential components at the stations over the salt dome (LA03, LA06 and LA09). VR_{MAX} obtained with 3DGFs (~73.5%) is substantially larger than VR_{MAX} obtained with 1DGFs (~64.3%). The source mechanism recovered using 1DGFs is not very different from the one obtained with 3DGFs (both are dominantly isotropic volume-increase mechanisms) except for a slight increase in M_W. The 1DGF GRiD MT results locate event TE2 to the western edge of the salt dome but pinpointing the location exactly to the salt dome or the adjacent sediments is impossible because we use multiple 1D models. The 1DGF results are similar to the results obtained by ND14 and ND15 using one fewer station, slightly different 1D models, and/or different passbands.

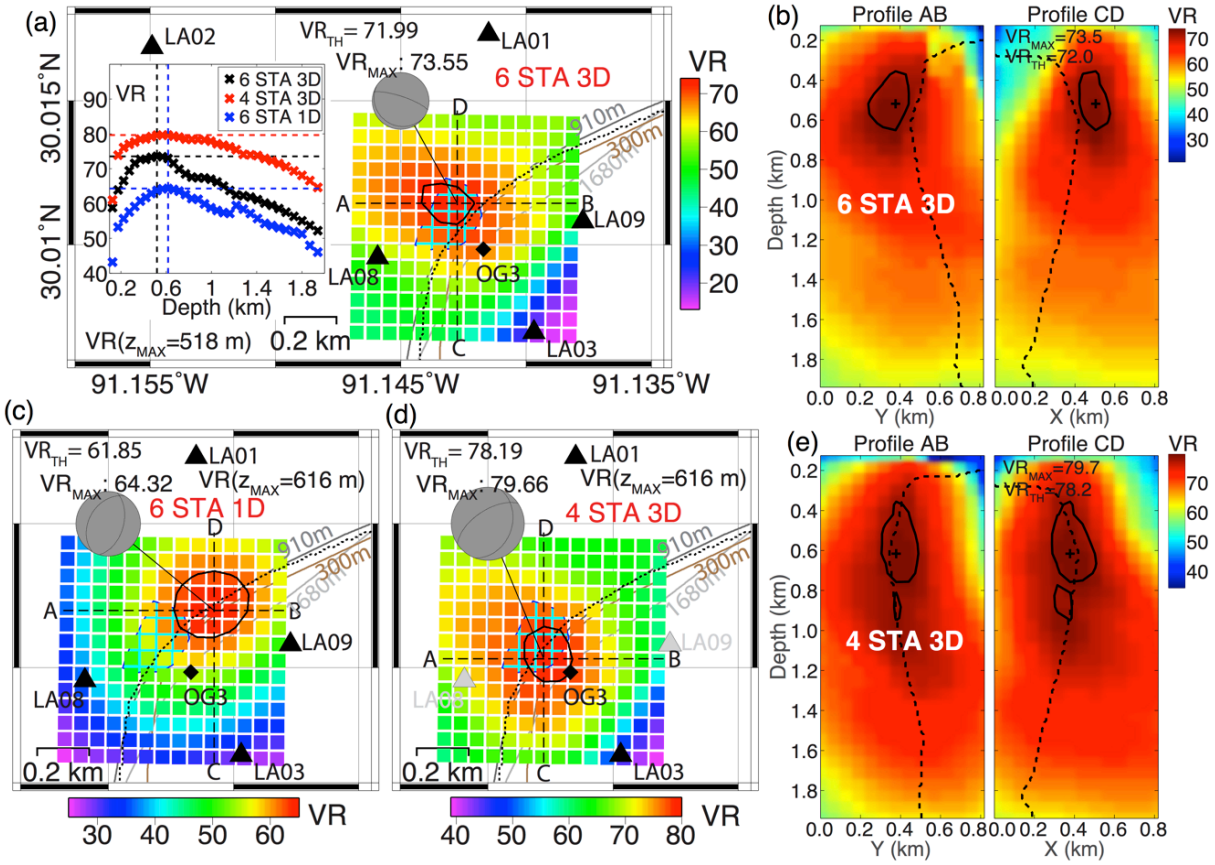

Figure 4.5: GRiD MT results for event TE2 (a) Spatial distribution of VR at grid points (colored squares) at the best-fitting grid point depth, z_{MAX} = 518 m [shown on the map as "VR(z_{MAX} =518 m)"]. This GRiD MT solution uses all 6 stations and 3DGFs ("6 STA 3D"). The dotted black line is NSD's depth contour at the best-fitting depth. Salt dome contours at 300 m, 910 m and 1680 m, color-coded by depth, are also shown as solid curves. Black triangles are USGS stations and black diamond is the approximate XY location of OG3. The blue polygon (under the grid) shows the approximate surface extent of the sinkhole in ~July

2013. Focal mechanism plot, representing lower hemisphere P-wave radiation pattern for the best-fitting MT solution, along with the best-fitting VR above it ("VR_{MAX}: 73.55%"), points to the best-fitting centroid location on the grid. The depth section of VR across profiles A–B and C–D (black dashed lines) through the centroid location are shown in (b). The waveform fits for the best-fitting solution are in Fig. 4.6a. Black closed polygon is the VR=VR_{TH} contour and delineates the extent of grid points with VR ≥ VR_{TH} [indicated on the map as "VR_{TH}=71.79"]. This area has a strong likelihood of containing event TE2's centroid location (see section **4.3.6 Location Uncertainties**). Inset shows the best VR vs. grid point depth for different GRiD MT implementations applied on event TE2 (6 stations with 3DGFs, 4 stations with 3DGFs, 6 stations with 1DGFs). Color-coded dashed lines indicate the maximum VR and the corresponding depth; (b) Depth sections across profiles A–B and C–D in (a) show depth distribution of VR. Meanings of the black closed polygon, VR_{MAX} and VR_{TH} are the same as in (a). Black '+' sign indicates the best-fitting centroid location and the black dashed line is the outline of NSD; (c) same as (a) but using 1DGFs ("6 STA 1D"). The waveform fits for the best-fitting solution are in Fig. 4.6b; (d) same as (a) but for the 4-station solution without the two closest stations, LA08 and LA09, which are grayed out ("4 STA 3D"). The waveform fits for the best-fitting solution are in Fig. 4.6c; (e) same as (b) but for the 4-station solution with 3DGFs in (d).

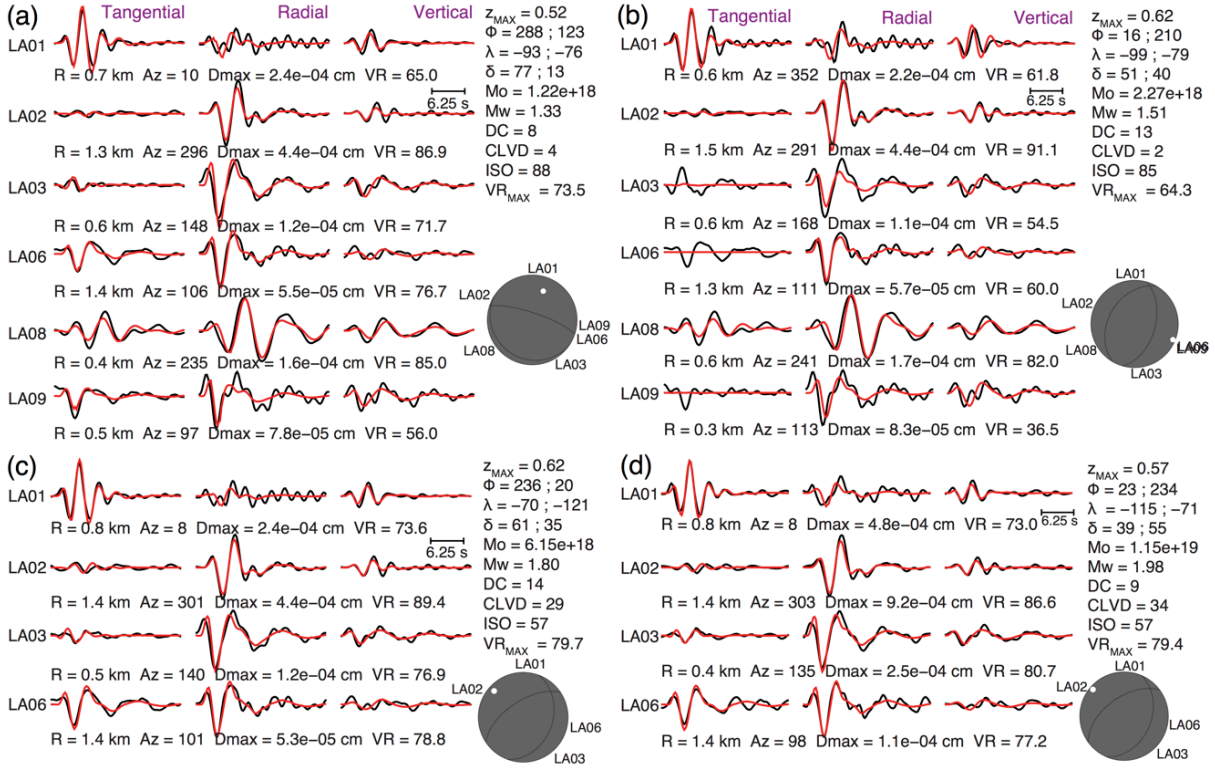

Figure 4.6: (a) Observed displacement waveforms (black traces), the best-fitting full MT solution for event TE2 obtained using 6 stations and 3DGFs (best-fitting centroid location is shown in Figs 4.5a,b) and the corresponding synthetic displacement waveforms (red traces). Beach-ball represents the lower hemisphere P-wave radiation pattern. R= epicentral distance, Az= azimuth (°), *D*max = maximum displacement amplitude and VR=Variance Reduction at a station. VR_{MAX} (%), ISO (%), CLVD (%) and DC (%) components in the MT solution, M_W,

M_0 (dyne.cm), z_{MAX} (km) and the fault-plane solutions of the DC component of the MT solution in terms of strike Φ (°), rake λ (°) and dip δ (°) are indicated; (b) same as (a) but using 1DGFs (Fig. 4.5c); (c) same as (a) but using 4 stations only (without LA08 and LA09, Figs 4.5d,e); (d) same as (c) but for a different event on 00:12:46, 27 July 2012.

We also analyze GRiD MT results of event TE2 in absence the nearest stations LA08 and LA09. For the majority of the seismic sequence, before the appearance of the sinkhole, only 4 stations were operational (before 31 July 2012). Therefore, it is important to check if the absence of the two closest stations introduces any significant bias or significantly inhibits our ability to precisely determine the location and source mechanism of events earlier into the seismic sequence. Figs 4.5d,e show the 4-station results for event TE2. The best-fitting centroid location shifts into the salt dome at a similar depth of 0.62 km. The best-fitting MT solution has reduced positive isotropic moment (ISO ~57%; Fig. 4.6c) compared to the best-fitting 6-station solution, which was dominantly isotropic (ISO ~88%). Waveforms at LA09 generally exhibit lower SNR and poorer waveform fits, and its removal leads to higher overall VR_{MAX} (~79.7%). The location uncertainties are further discussed in the following subsection.

4.3.6 Location Uncertainties

Our inability to fit the observed waveforms to 100% could be due to multiple factors, the most important of which are contamination of data from ambient seismic noise (measurement error), inaccuracy of the velocity model, and possible incompatibility of the seismic events with the assumed point-source MT model (modeling errors). GRiD MT provides a spatiotemporal distribution of the goodness-of-fit measure (VR), and the true centroid location and the MT solution likely exist in some neighborhood of the best-fitting grid point and the MT solution corresponding to the maximum VR (VR_{MAX}) in the parameter space. In order to assess the uncertainties in the location, origin time and the MT solution, we need to establish an appropriate VR threshold (VR_{TH}) such that all possible solutions with VR $\gtrsim$ VR_{TH} can be accepted as likely solutions. VR_{TH} should take into account the quality of waveform fits and the location of the event with respect to the network geometry. Almendros & Chouet (2003) used an empirical approach based on synthetic tests to choose radial semblance thresholds for defining probable source regions of Very Long Period (VLP; ~0.01-0.5 Hz) events in volcanoes. We follow a modified version of their approach for estimating VR_{TH} in our study.

We first assume a range of semi-evenly spaced locations for the synthetic tests– grid point numbers (3, 7, 11), (4, 8, 12) and (1, 3, 5, 7, 9, 11, 15, 17, 21, 25, 29, 33) in X, Y and Z directions, respectively, leading to a total of 3x3x12 = 108 locations that approximately cover the entire GRiD MT grid. For each location, we compute synthetic waveforms assuming MTs of 17 different sources: isotropic, 45°-dipping and vertical dip-slip faults (DC MTs; strike, ϕ = –45°, 0°, 45°, 90°) and 45°-dipping and vertical cracks (ϕ = –45°, 0°, 45°, 90°). For the crack MTs, we use the value of ν from the 3D velocity model for each specific source location. For each source mechanism at each location, we compute synthetic waveforms and add 20 different realizations of noise at 5 different levels of the average signal-to-noise ratio (SNR): 2.8, 4.6, 7.5, 12.2 and 20.0. For the observed waveforms, we define SNR as ratio of

the maximum of absolute amplitudes in a waveform segment containing a seismic event to root-mean-square amplitude of the preceding waveform segment. For calculation of SNR for synthetic waveforms of hypothetical events, the peak amplitude used is the maximum absolute amplitude of the noise-free synthetic waveform prior to adding noise. The average SNR is the mean SNR of all components available for an event (e.g., mean value of individual SNRs of = 5 x 3 = 15 components for 5 stations). GRiD MT is applied on these synthetic noise-contaminated hypothetical event waveforms. The difference between the highest VR obtained (VR_{MAX}) and the VR at the correct centroid location (VR_0) in the synthetic tests guides our choice of VR_{TH} for real events. For example, assume that VR_{MAX} and VR_0 for a synthetic event are x and $0.95x$, respectively. Assuming this synthetic event is a real event, if we choose the volume of locations with VR $\geq 0.95x$ ($=VR_{TH}$), the actual location is likely to be present within this volume (certainly present if $VR_{TH}=V_0$). Using VR_{MAX} and VR_0 values from synthetic tests over a wide range of possible scenarios, we seek to quantify an average reasonable estimate of VR_{TH} for a given value of VR_{MAX}.

The characteristics of noise added to the synthetic waveforms are important for generating realistic hypothetical event waveforms. Alemendros & Chouet (2003) assumed independent random noise in the VLP passband (~5-50 s) for different stations and components because they observed little coherence in noise recorded at stations just a few kms apart, which suggested that the noise was primarily composed of thermal and electrical noise originating within the sensors. Among probabilistic source inversion studies, Duputel *et al.* (2012) and Mustać & Tkalčić (2016) have accounted for correlations between the samples of each filtered noise waveform but they assumed no correlation between waveforms recorded at different components of a station or between waveforms recorded at different stations. Neglecting correlation between waveforms at different stations is easily justified in case the stations are far apart with respect to the seismic wavelengths employed. Fig. 4.A.1 in the **Appendix** shows filtered noise segments (0.1-0.3 Hz) recorded at stations in our study area for a randomly chosen instance of time. The noise in the secondary microseism passband is highly correlated at the salt dome stations, as they are less than one wavelength away from each other (Longuet-Higgins 1950; Rayleigh wave phase velocity is ~2.4 km/s at frequencies ~0.1-0.3 Hz for the 1D salt dome model, calculated using Computer Programs in Seismology [Herrmann 2013a]). It is also likely that the low velocity layers over the salt dome act as a waveguide and trap seismic energy. As Rayleigh waves constitute a major part of secondary microseism energy, some correlation between the horizontal and the vertical components of seismic noise is also expected (Friedrich *et al.* 1998). Therefore, instead of assuming independent random noise at different components and stations, we use real ambient noise recorded at stations in our study area to simulate real-world conditions in which noise recorded at different stations or components can be correlated (e.g., Ford *et al.* 2009a). We use all data recorded between 16 June 2012 and 2 Aug 2012, filter the waveforms in appropriate passbands and remove the 25 s segments corresponding to events detected by GRiD MT. The remainder of the data is treated as noise. 25.75 s long (104 samples) noise waveform segments are extracted at randomly chosen times for the synthetic tests. However, the amplitudes of each component are rescaled such that its root-mean-square (RMS) amplitude is equal to its average RMS value over the entire time period (Table 4.A.1). The 24.75 s long (100 samples) noise-free synthetic waveforms of all components are scaled up by a single scalar factor to get the desired average SNR and added to the noise waveforms 3rd

sample onwards, which allows for possible origin time error up to ± 2 samples (0.5 s) in the synthetic tests.

Figs 4.7a,b demonstrate the procedure for obtaining VR_{MAX} vs. VR_{TH} relationship from synthetic tests for two different best-fitting depths (z_{MAX}), ~0.52 km and ~1.16 km, respectively, for 6-station GRiD MT solutions. In Fig. 4.7a, we show the distribution of z_{MAX} for actual source depths (z_0) at ~0.52 km (subplot 1) and the distribution of z_0 for all results with 0.44 km < z_{MAX} < 0.59 km (subplot 2). We bin the results of synthetic tests as a function of z_{MAX} with the bins centered on depths at which synthetic sources were placed and bin half-width of ± 1 or 2 depth grid points. Subplot 3 in Fig. 4.7a shows VR_{MAX} vs. VR_0 for all synthetic tests in which 0.44 km < z_{MAX} < 0.59 km. This plot is an average of results for different sources with different SNRs placed at different epicenters. For each 2%-wide VR_{MAX} bin (e.g., VR_{MAX} bin 68%–70% in subplot 3 delineated by dashed vertical lines), we choose 4.5% cumulative probability quantile of VR_0 values (~67.0% for this bin, shown as red '+' symbol) as VR_{TH} value for the center-point VR_{MAX} of that bin (69%, shown as black '+' symbol). It implies that if VR_{MAX} of an event at z_{MAX} ~0.52 km is 69%, if we choose a volume of grid points with VR ≥ VR_{TH} ~ 67.0%, there is a 95.5% likelihood (not in a strict statistical sense) that the true location of that event is present within this volume. In the rest of the article, we refer to the volume of these grid points at which VR ≥ VR_{TH} (example Figs 4.5a,b,d,e) as "probable source volume" and it represents the uncertainty in the centroid location of an event in 3D space. Similarly, the depth extent of grid points at which VR ≥ VR_{TH} is referred to as "probable source depths" and it represents the uncertainty in centroid depth of an event. We consider the assumed threshold of 95.5% probability to be reasonable because results are commonly reported as mean ± 2 standard deviations, which covers 95.5% of a normal probability distribution. It is important to note that the volume of probable locations will be larger for a stronger probability (e.g., 98%). We compute VR_{TH} for each bin from the minimum VR_{MAX} =40% to the bin (74%–76%) succeeding the bin containing the maximum VR achieved for a real event (73.5% for 6 stations) and fit a straight line to all values of VR_{TH}. This provides us a general VR_{MAX} vs. VR_{TH} relationship (red line in subplot 3) for real seismic events with z_{MAX} at grid point depth 0.52 km. The difference between VR_{MAX} and VR_{TH} increases with decreasing VR_{MAX} resulting in a generally larger volume of likely locations and hence greater location uncertainties with poorer waveform fits. Subplot 4 in Fig. 4.7a shows a histogram of VR_{MAX} values in 2% bins for synthetic tests in this depth range and demonstrates that our synthetic tests cover the entire VR_{MAX} range and there are ≳ 200 data points in each bin, thereby providing statistically meaningful quantile estimates for each bin.

Almendros & Chouet (2003) assume a single empirical relationship for determining the threshold semblance irrespective of the best-fitting location of the seismic events. Due to limited aperture of our surface seismic network, location uncertainties for deeper events are likely to be greater than location uncertainties for shallower events. Fig. 4.7b shows plots similar to those in Fig. 4.7a but for z_{MAX} ~ 1.16 km. Generally, VR_{TH} values are lower at z_{MAX} ~ 1.16 km compared to VR_{TH} values at z_{MAX} ~ 0.52 km (Fig. 4.7a). For example, for VR_{MAX} =69%, VR_{TH} ~66.3% at z_{MAX} ~1.16 km. We form separate empirical VR_{MAX} vs. VR_{TH} relationships as a function of z_{MAX}. The relationships for the grid point depths at which we did

not place hypothetical events for synthetic tests were interpolated from relationships at other grid point depths.

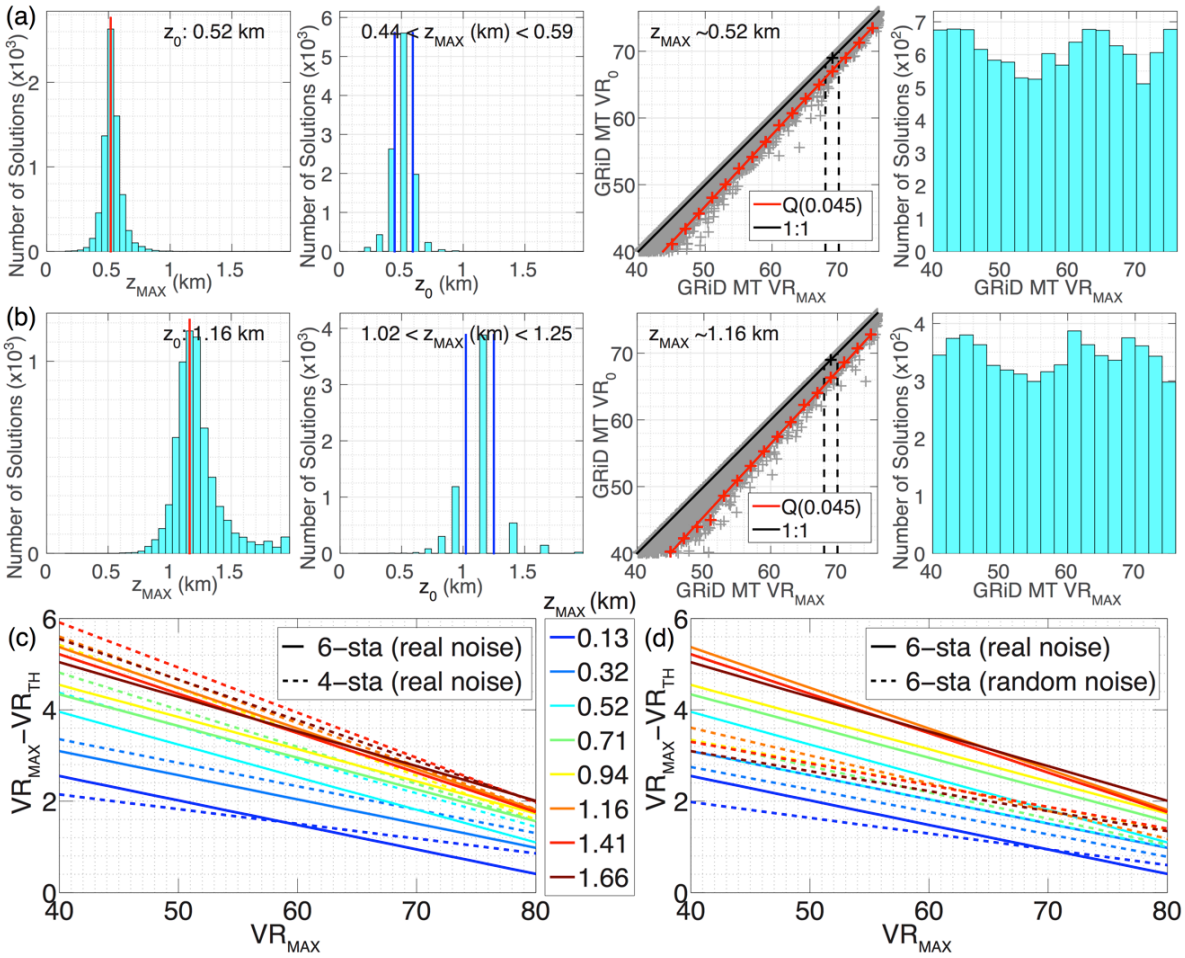

Figure 4.7: (a) 6-station synthetic test results: 1st subplot (from left to right) shows the histogram of best-fitting depths (z_{MAX}) obtained for sources placed at 0.52 km depth (vertical red bar) and synthetic waveforms contaminated with difference instances and levels of noise. 2nd subplot shows the combined distribution (histogram) of actual source depths (z_0) for all z_{MAX} between ~0.44 km and ~0.59 km (two vertical blue bars; all results at ±1 depth grid point from 0.52 km depth are combined together). The distribution looks discrete because we place synthetic sources only at some specific depths (see section **4.3.6 Location Uncertainties**). 3rd subplot shows VR_{MAX} vs. VR_0 (data points denoted with gray '+' symbol) for all results with z_{MAX} between ~0.44 km and ~0.59 km combined together. Red '+' symbols denote the 4.5% cumulative probability quantiles (VR_{TH}) of VR_0 values in 2% VR_{MAX} bins for the center VR_{MAX} value of each bin. The two vertical dashed lines delineate the VR_{MAX} 68%-70% bin discussed in the text. The red line is a straight-line fit through the VR_{TH} values of all bins (red '+') and provides an average VR_{MAX}–VR_{TH} relation for real events with z_{MAX} ~0.52 km. 4th subplot shows a histogram of VR_{MAX} values in 2% bins. (b) Same as (a) but for average VR_{MAX}–VR_{TH} relation for z_{MAX} ~1.16 km. For any VR_{MAX}, VR_{TH} at 1.16 km depth is smaller than VR_{TH} at 0.52 km. (c) A comparison of (VR_{MAX} – VR_{TH}) vs.

VR_{MAX} relationships at different depths (different colors) using 6 stations (solid lines) and 4 stations (dashed lines; LA08 and LA09 omitted). For any particular color, the dashed line is generally above the solid line. (d) A comparison of ($VR_{MAX} - VR_{TH}$) vs. VR_{MAX} relationships at different depths (different colors) for 6-station synthetic tests using real noise (solid lines) and random noise (dashed lines) generated separately for each different component. For any particular color, the dashed line is generally below the solid line.

The uncertainties are also expected to depend on the presence or absence of better or poorer quality stations in the GRiD MT implementation. The waveform fits at each station depend on both ambient noise level at that station and the applicability of the velocity model for the path between the source and that particular station. VR_{TH} can be expected to be generally lower (i.e., greater uncertainties) in case we have fewer good quality stations, as our spatial resolution becomes poorer. The depth resolution is especially poorer in the absence of the two stations closest to the source region (LA08 and LA09). Fig. 4.7c shows a summary of ($VR_{MAX} - VR_{TH}$) vs. VR_{MAX} relationships for different depths for GRiD MT implementations using 4 (LA08 and LA09 omitted) and 6 stations. Except for the shallowest depth (z_{MAX}~0.13 km), VR_{TH} for 6-station GRiD MT is greater than VR_{TH} for 4-station GRiD MT for the same values of VR_{MAX} at all depths, implying generally smaller probable source volume or smaller location uncertainties if we are using the two closest stations LA08 and LA09. We perform similar synthetic tests and obtain VR_{MAX}-VR_{TH} relationships for all 3-station, 4-station and 5-station GRiD MT implementations.

While Almendros & Chouet (2003) related their radial semblance thresholds to SNR, we relate VR_{TH} to the goodness-of-fit itself (VR_{MAX}) instead of the SNR. This accounts for uncertainties due to modeling errors to some extent. For example, if VR_{TH} was related to SNR, we will obtain high misleading values of VR_{TH} very close to VR_{MAX} in the case of large amplitude events with very high SNR, resulting in small probable source volumes. This ignores the possibility of errors in the velocity model or in the assumed source model (modeling errors) that will result in poor waveform fits irrespective of the SNR of the event. Some penalty or uncertainties must result from our inability to explain or fit waveforms to 100% VR. Fig. 4.7d shows a comparison of ($VR_{MAX} - VR_{TH}$) vs. VR_{MAX} relationships obtained from synthetic tests using real noise (which is strongly correlated at salt dome stations) and random noise generated separately for each different component (i.e., no correlation between different components). Except for the shallowest depth (z_{MAX}~0.13 km), VR_{TH} for synthetic data contaminated with real noise is lower than VR_{TH} for synthetic data contaminated with completely random and uncorrelated noise at all depths. While random noise is expected to reduce the quality of waveform fits without generating any strong systematic bias in the centroid location and MT solution, noise correlated across stations or components can lead to systematic bias in waveforms and the resulting MT solutions. The results of our synthetic tests imply generally larger probable source volume and greater location uncertainties in presence of real world noise. In MT uncertainty analysis, the correlation between residuals at different stations has been usually ignored in bootstrap analyses in previous studies (e.g., ND14) and needs to be critically investigated.

For event TE2, VR_{TH} for 6-station and 4-station solutions are ~72.0% and ~78.2%, respectively (VR_{MAX} 73.5% and 77.9% at z_{MAX} 0.52 km and 0.62 km, respectively). While the

6-station GRiD MT solution indicates that event TE2 is likely located outside the salt dome within uncertainties, the volume of the best locations for the 4-station GRiD MT solution is slightly larger and encompasses both the salt dome and the sediment layers adjacent to it. While MT solutions at grid points both inside and outside the salt dome fit the waveforms at 4 stations to a similar level, 4-station GRiD MT preferentially places the best-fitting location inside the high velocity salt medium. As expected, including nearer stations LA08 and LA09 better constrains the centroid location in both the horizontal plane and in depth. However, in both cases, the most probable depths ($\lesssim$ 0.62 km and $\lesssim$ 0.94 km for 6-station and 4-station solutions, respectively) are well above the cavern depth (~1.0-1.7 km).

4.3.7 Uncertainty in Source Type and Seismic Moment

While the best-fitting MT solutions of event TE2 for both the 4-station and the 6-station scenarios are dominantly isotropic volume increase, it is necessary to examine the range of source types that can fit TE2 waveforms to an acceptable degree of goodness-of-fit. ND15 refined the method to construct the maximum fit surface in the source-type space, which is called the Network Sensitivity Solution (NSS; Ford *et al.* 2010) due to its ability to assess recovery of source-type information under changing network topology. The NSS can be useful in assessing the confidence in our ability to constrain the source type of seismic events. Similar to the best-fitting MT solution, the distribution of best-fitting source types in the source-type space is also a function of the centroid location. We build a composite NSS for our seismic events taking into account the uncertainty in centroid location obtained from GRiD MT. We compute NSS using the method of ND15 at each grid point location at which $VR \geq VR_{TH}$. For each location, we also allow an uncertainty up to ±0.5 s (2 samples) in the centroid origin time. In the composite NSS, the overall VR for a source-type is the maximum of VR for that source-type obtained at all centroid locations and all origin times with $VR \geq VR_{TH}$ for the full MT solution. Fig. 4.8a shows distribution of VR for the 6-station GRiD MT solutions of event TE2 with respect to source types plotted on the Hudson plot (Hudson *et al.* 1989) in which the horizontal axis plots the ratio of the deviatoric eigenvalues (ε) and the vertical axis plots the relative isotropic component (κ). For event TE2, we constrain the best-fitting source types ($VR \geq VR_{TH}$) to be dominantly isotropic volume increase (ISO ~ 71–92%) for a range of centroid locations in the probable source volume outside the salt dome. In the source-type plot, we also point out the positions of cracks for various values of ν in our 3D velocity model: ~0.48 (sediments at depth ~0-160 m, 0-120 m over the salt dome), ~0.45 (sediments ~160-420 m), ~0.43 (sediments ~ 420 m-1.2 km), ~0.39 (sediments $\gtrsim$ 1.2 km depth and the cap rock) and ~0.24 (salt). Opening crack source types assuming ν corresponding to the shallow sediment layers (ν ~0.43 at z_{MAX}) also fit event TE2 waveforms quite well. For a uniform parameterization of source types, it is also possible to compute probabilistic estimates of the best-fitting source types or a confidence estimate in source-type determination (Tape & Tape 2012a, 2015) taking into account the range centroid locations, similar to estimates made for focal mechanisms in recent earthquake MT studies (e.g., Silwal & Tape 2016).

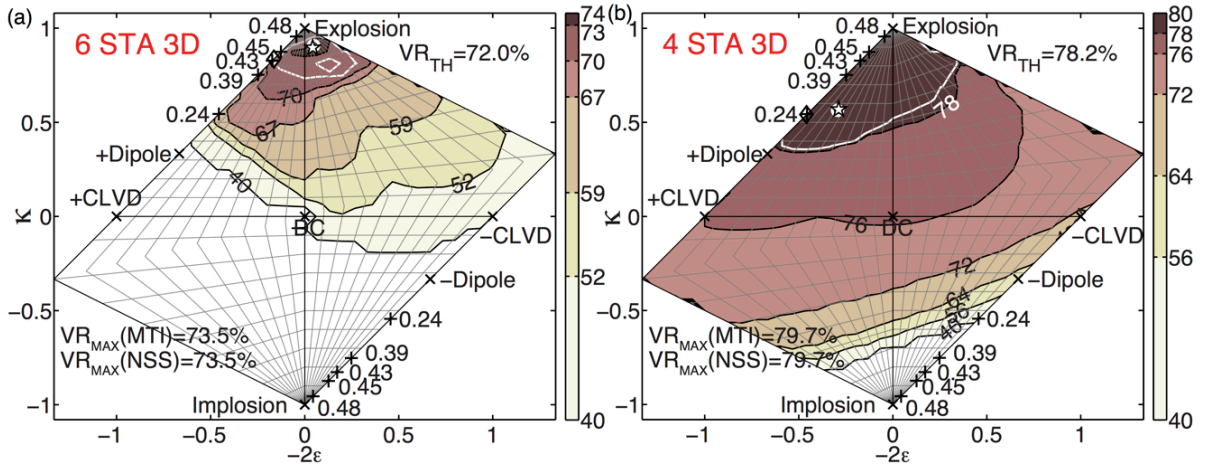

Figure 4.8: Composite NSS of event TE2 using (a) 6 stations and (b) 4 stations. The black contours and colors represent absolute values of VR and the white contour corresponds to VR=VR_{TH} (value at upper right corner). The white star is the position of the best-fitting full MT solution from GRiD MT (MTI), the white circle is the source type corresponding to the maximum VR recovered by source-type-specific MT inversion (NSS); the corresponding VR_{MAX} values are mentioned in the lower left corner. Black crosses are the positions of major theoretical source types. Black '+' signs are positions of crack source types with corresponding values of ν indicated next to the signs. Black diamond corresponds to the crack MT source type for the value of ν at the best-fitting centroid location.

Fig. 4.8b shows the composite NSS for event TE2 using the 4-station GRiD MT results. The absence of the 2 closest stations increases the uncertainties in the source-type of event TE2 as the region of the probable source types (VR ≥ VR_{TH}) is significantly broader that for the 6-station composite NSS and encompasses the regions of high isotropic volume-increase sources (ISO ≳ 70%) and of opening crack-type sources with ν as low as ~0.24. The inability of 4-station GRiD MT to restrict event TE2 to a single medium (salt or a sediment layer) strongly contributes to the uncertainty in source type and M_0. Spatial derivatives of Green's functions can be discontinuous across material interfaces (i.e., contact of two media with non-zero velocity or density contrasts) and consequently, moment tensors, that represent equivalent body forces, display jumps when the source position crosses the interface (Vavryčuk 2013). Fig. 4.9a shows the distribution of the source types for the MT solutions in terms of ν at the centroid locations within the probable source volume. Event TE2 waveforms at 4 stations are fit equally well by a dominantly isotropic volume-increase source or an opening crack-type source in the sediment layer (ISO ≳ 70%; ν~0.43) or by an opening crack-type source within the salt medium (ν~0.24-0.3). 4-station GRiD MT preferentially places the source with the salt medium and returns an opening-crack MT solution with ISO ~60% as the best-fitting MT solution. However, it is important to note that even for a wide range of centroid locations, the best-fitting source types for both 4-station and 6-station GRiD MT solutions are far away from the DC region on the Hudson plot (Fig. 4.8), indicating that event TE2 is very different from naturally occurring tectonic earthquakes for which we would expect a high DC MT solution (Ford *et al.* 2010). The large velocity contrast between the sediment layers and the salt (V_S ratio ~ 3.3–4.5 with greater V_S for the salt) also leads to large differences in M_0 (by factor of ~2.8-4.7) and M_W (~0.3-0.45 units) estimates for adjacent

probable centroid locations in the two media at depth z_{MAX}, with M_0 greater for sources placed in the salt (Figs 4.9b,c). The M_W and M_0 differences between adjacent centroid locations can be as large as ~0.55 units or factor of ~6.7 at shallower depths. Within the population of the best-fitting source locations and source types ($VR \geq VR_{TH}$), M_W varies between ~1.05–1.95 and ~1.16–1.61 for 4-station and 6-station GRiD MT results, respectively.

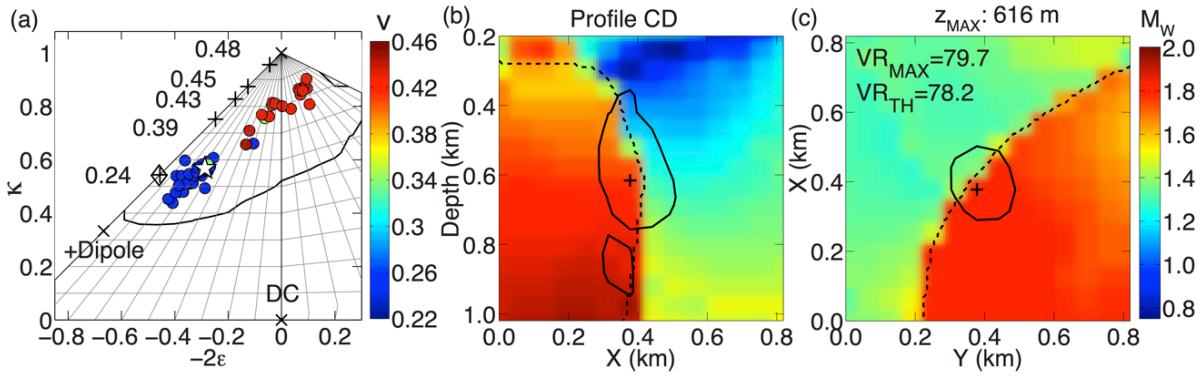

Figure 4.9: (a) Source-type distribution of MT solutions of event TE2 at different probable source locations ($VR \geq VR_{TH}$) obtained from 4-station GRiD MT. The points are color-coded by the local value of ν from the 3D velocity model. The black curve is the $VR=VR_{TH}$ contour from Fig. 4.8b. Explanation of other symbols is the same as in Fig. 4.8b. (b) Spatial distribution of M_W for the MT solutions of TE2 obtained from 4-station GRiD MT along profile CD in Fig. 4.5d. Explanation of other symbols is the same as in Fig. 4.5e. (c) Same as (b) but for an XY slice through z_{MAX}. '+' sign is the location of the best-fitting full MT solution. Explanation of other symbols is the same as in Fig. 4.5d. The VR distributions corresponding to sections in (b) and (c) can be seen in Figs 4.5e and 4.5d, respectively.

Seismic sources can be alternatively parameterized using a potency tensor, P_{kl}, which is defined as the integral of transformational strain over the source volume and is related to the moment tensor as, $M_{ij} = c_{ijkl}P_{kl}$ (Ben-Zion 2003; Zhu & Ben-Zion 2013), where c_{ijkl} are the elastic constants. Seismic potency tensor is independent of the elastic constants and changes smoothly across material interfaces (Vavryčuk 2013). Here we examine the variability in seismic scalar potency P_0 within the probable source volume containing two different media. We first compute seismic scalar moment, $M_0' = \sqrt{(\sum_{i,j} {M_{ij}}^2)/2}$ for the full MT solution at each grid point using the definition (eq. 21) of Zhu & Ben-Zion (2013); here we use a different symbol M_0' to distinguish it from the Bowers & Hudson (1999)'s definition of M_0 that we have used at all other places in our study. Using the local values of V_S, ρ and ν at each grid point, we convert M_0' to P_0 through equations 22, 28 and 29 of Zhu & Ben-Zion (2013). Fig. 4.10 shows the distribution of P_0 across the same sections as in Figs 4.9b,c. It is interesting that P_0 varies by only a factor of $\lesssim 2$ over adjacent grid points across the salt interface within the probable source volume. P_0 can be potentially useful in quantifying magnitude of seismic events in cases where uncertainty in location close to a material interface results in large uncertainties in M_0 (Vavryčuk 2013). We leave the detailed inversion and source-type analysis of potency tensors for future studies.

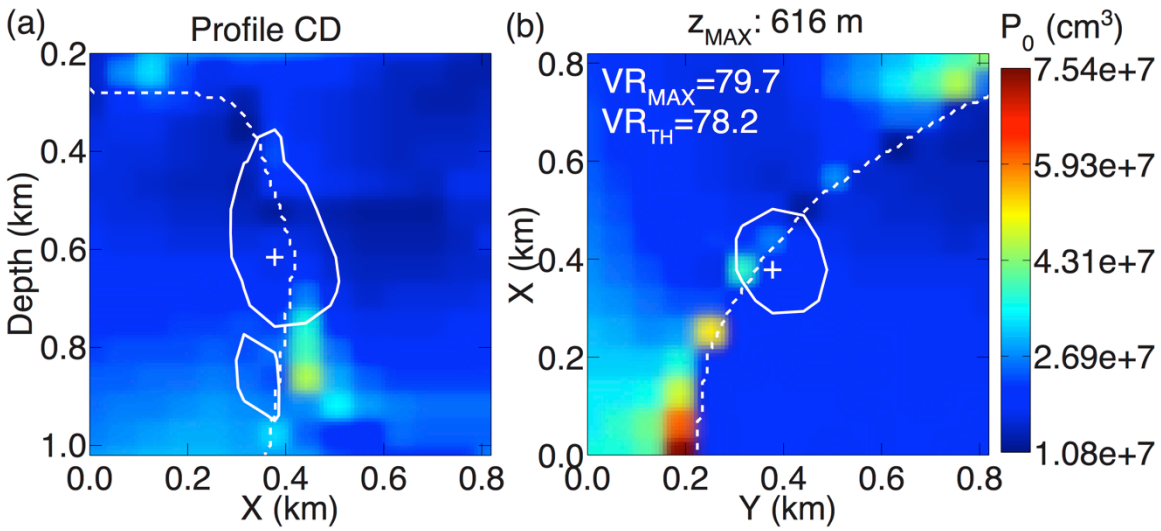

Figure 4.10: (a) Spatial distribution of P_0 for the MT solutions of event TE2 obtained from 4-station GRiD MT along profile CD in Fig. 4.5d. Explanation of other symbols is the same as in Fig. 4.5e (in black instead of white). (c) Same as (b) but for an XY slice through z_{MAX}. '+' sign is the location of the best-fitting full MT solution. Explanation of other symbols is the same as in Fig. 4.5d (in black instead of white). The VR distributions corresponding to sections in (b) and (c) can be seen in Figs 4.5e and 4.5d, respectively.

4.4 Description of the Seismic Sequence

Methodologies described above are applied to all the seismic data collected by the temporary USGS network at NSD. In this section, we describe the evolution of the seismic sequence in terms of the best-fitting centroid locations (easting (Y), northing (X) on the source grid with the southwest corner assumed to be [0,0], and z_{MAX}), M_W, the contribution of the isotropic moment represented by the Hudson parameter (κ) and VR_{MAX} (Fig. 4.11). We also plot the 3D extent of the spatial volume in which VR ≥ VR_{TH}, which is a measure of the uncertainty in the centroid location (error bars in Figs 4.11c-e). We quantify the M_W uncertainty (error bars in Fig. 4.11b) by the range of M_W of the MT solutions in the population of probable source types at the probable source locations (VR ≥ VR_{TH}) obtained from the composite NSS analysis. We discuss results and uncertainties only for events with generally good VR (≥ 75%, 75%, 70%, 60% for 3-, 4-, 5-, 6-station solutions, respectively). However, we make some exceptions for interesting events with lower VR_{MAX} values, which occurred at the beginning of the sequence or were larger events with waveforms contaminated by decaying amplitudes of immediately preceding events. Fig. 4.11a shows the evolution of peak displacement amplitudes (vector norm of 3 components) of the detected events at stations LA02 and the nearest Transportable Array (TA) station 544A (at distances ~1.3 km and ~11.3 km, and azimuths ~290° and ~350°,

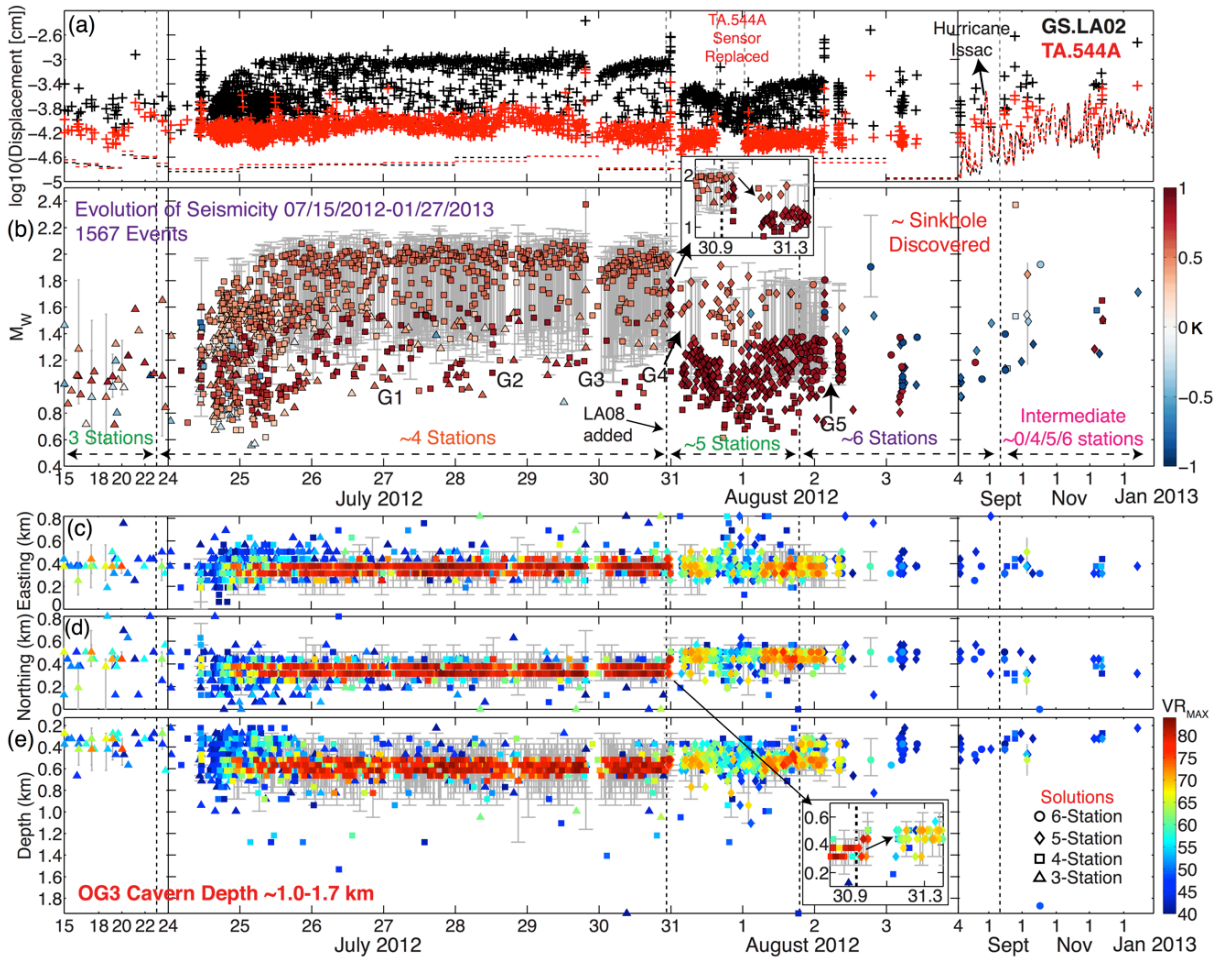

Figure 4.11: Evolution of the seismic sequence associated with the sinkhole at NSD. Major changes in seismic stations/network are indicated by vertical dashed lines (description in [a] and [b]). (a) Peak vector norm of displacement amplitudes at GS.LA02 (black) and TA.544A (red) in 0.1-0.3 Hz passband for all detected events; dashed horizontal lines indicate daily RMS noise levels; (b) M_W of detected events with time, color-coded by Hudson parameter κ. Different symbols indicate the number of stations used in GRiD MT (meaning of symbols described at lower right corner of [e]). Inset shows the drop in M_W of the detected events following the quiescence period after the large amplitude ground motions. The increase in the positive isotropic component and a fraction of the drop in M_W of the detected events can be attributed to the shift in the best-fitting centroid location from the salt to the sediment layers following the addition of LA08 to the network (vertical dashed line). Gaps "G*" are periods of relatively fewer seismic events detected after episodes of large amplitude semi-continuous ground motions. Centroid locations of the detected events indicated by (c) easting, (d) northing and (e) depth on the GRiD MT grid, color-coded by VR_{MAX}. Inset in (e) shows the shift in the best-fitting centroid location (its northing) primarily caused by addition of LA08 to the network.

respectively). The amplitudes at the distant station 544A should be relatively less sensitive to source depth and can be considered to be a proxy for event magnitudes assuming a compact source region and similar source mechanisms. Amplitudes at LA02 are also plotted for comparison. The same figure also shows daily RMS amplitudes at the 2 stations after excluding the 25 s-duration time windows that contain detected events. Fig. 4.11b shows the M_W of the detected events color-coded by κ. Fig. 4.11c-e show the spatial coordinates color-coded by VR_{MAX}.

Our GRiD MT analysis begins on 15 July 2012, the first day when 3 stations became operational (LA01, LA02 and LA03). However, felt events were reported in the area as early as 24 June 2012 (LADNR, OOC 2013). Going back further in time, analysis of events detected at the TA station 544A using a waveform cross-correlation approach revealed a noticeable increase in the seismicity rate on 12 May 2012, which may mark a significant growth in the process driving the seismicity (Dreger *et al.* 2015). Using UAVSAR (Uninhabited Aerial Vehicle Synthetic Aperture Radar) data, Jones & Blom (2014) estimated significant surface deformation up to a maximum of 2.6 cm, over an extended area above the western edge of the NSD between June 2011 and 02 July 2012. The sinkhole later formed in the area with the largest gradient in surface strain.

From 15 July–23 July, we observe intermittent low M_W (~ 0.7-1.3) seismicity at generally shallow depths ($z_{MAX} \lesssim 0.6$ km). Waveform fits for these events are generally poor, resulting in large uncertainties, as there were only 3 stations available before 23 July. MT solutions of these events are generally compound mechanisms with ~10%-60% ISO, CLVD and DC components. For 8 events in this period with relative better waveform fits ($VR_{MAX} > 60\%$), probable centroid depths from the uncertainty analysis are $\lesssim 0.65$ km. Probable source volumes of few of them are right outside the salt dome and the rest are at the edge of the salt dome (i.e., the volumes encompass parts of the salt dome and the adjacent sediment layers; Fig. 4.12a). The probable source volume, best-fitting MT solution, waveform fits and the composite NSS of the event with the highest VR_{MAX} in this time period (at 00:21:53.26 hours on 20 July 2012) are shown in Figs 4.12a and 4.13a,b. Except for another similar event, uncertainties in source type of all other events are very large ($VR=VR_{TH}$ contour on the composite NSS encloses $\gtrsim 40\%$ of the total area on the Hudson plot) and are not discussed here. Station LA06 started operating from 23 July 2012. On 24 July 2012, there was a rapid succession of events between ~10:00-13:00 hours. These events have generally compound source mechanisms and disproportionally large amplitudes at LA02 compared to events with similar M_W later in the sequence (Fig. 4.11a). Waveforms for many of these events are contaminated by decaying amplitudes of immediately preceding events leading to poor waveform fits despite large amplitudes. Two of these events with relatively better waveform fits (VR_{MAX} ~67%) have relatively larger DC (~40%) and ISO (~50%) components than CLVD (~10%) component and their probable depths are $\lesssim 0.8$ km. Results for one of these events (at 11:08:51.53 hours) are shown in Figs 4.13c,d. The waveforms are quite oscillatory at the sediment stations compared to the waveforms of the event in Fig. 4.13a. While its best-fitting centroid location is well outside the salt dome, the probable source volume intrudes into the salt. This sequence of events was followed by a rapid increase in the seismicity rate and an increase in magnitude of the events that is reflected in both the M_W estimated by GRiD MT and the amplitudes at LA02. Initially, the seismic events have diffused centroid locations

(possibly because of errors in centroid location), low M_W and low VR_{MAX} on 24-25 July. Many of these events have low SNR at LA06 and their GRiD MT solutions were calculated excluding LA06. However by the end of 25 July 2012, a steady opening crack-like source gradually emerges and becomes the dominant source in the seismic sequence until 30 July. The source can be easily distinguished by the steady maximum peak displacement amplitudes at LA02, steady $M_W \gtrsim 1.85$, high $VR_{MAX} \gtrsim 70\%$, $\kappa \sim 0.6$, and a steady centroid location in Fig. 4.11 between 25 - 30 July 2012. Fig. 4.5d shows waveform fits and the best-fitting MT solution of one example event (at 00:12:46, 27 July 2012), which are very similar to the 4-station solution for event TE2 in Fig. 4.5c except that the displacement amplitudes of event TE2 are smaller by ~50% (consistent with ~0.18 units difference in M_W). The source volumes of ~44 events of this population with $VR_{MAX} \geq 81\%$ are plotted in Fig. 4.12b. The best-fitting location is at the western edge of the salt dome, usually at a grid point in the high velocity salt medium, ~100-150 m E-NE of OG3 in the XY plane and under the southern section of the approximate surface extent of the sinkhole in ~2013. The best-fitting centroid depths are ~0.5-0.6 km and the probable depths from the uncertainty analyses are ~0.3-0.85 km. The probable source volume includes both areas of the salt dome and the sediment layers and the region of probable source types includes both dominantly isotropic volume-increase sources ($ISO \gtrsim 70\%$) and opening crack-type sources with ν as low as ~0.24, with a small DC component. 4-station GRiD MT implementation places the centroid location preferentially in the salt medium resulting in the best-fitting source type being close to an opening crack with $\nu \sim 0.24$-0.3. These characteristics strongly indicate these events during 25-30 July 2012 are similar to event TE2 on 01 August 2012 except for a difference in magnitude. The DC, CLVD and ISO components in the best-fitting opening crack-like solutions for ~318 events ($VR_{MAX} \geq 70\%$; $M_W \geq 1.7$) are 11±4 %, 32±5% and 57±3%, respectively. During this time period, there are also intermittent smaller magnitude events ($M_W \lesssim 1.5$) with lower VR_{MAX} and lower amplitudes at LA02 (Figs 4.11a,b).

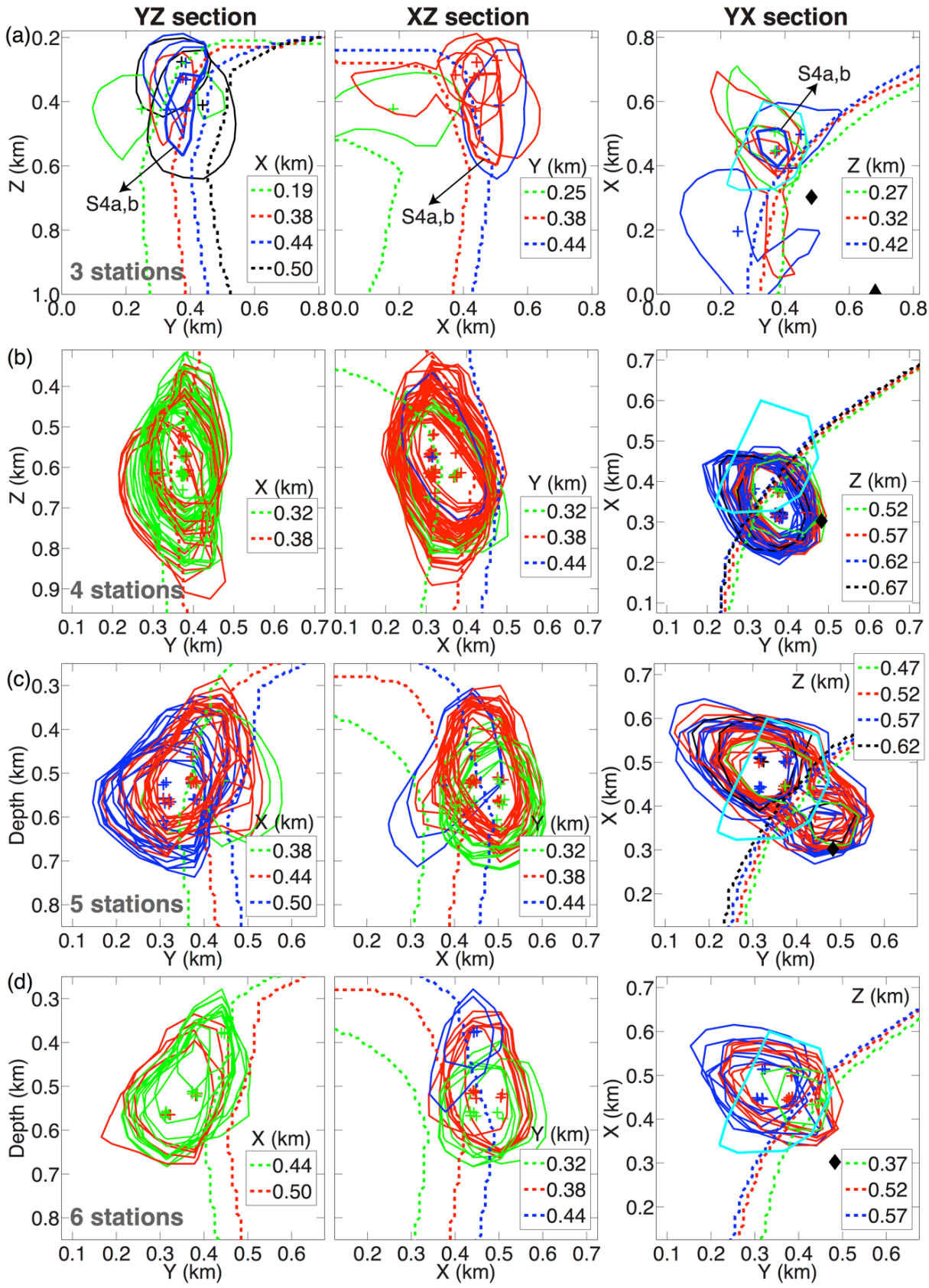
YZ section
XZ section
YX section
(a)
Z (km)
Y (km)
X (km)
S4a,b
3 stations
X (km)
0.19
0.38
0.44
0.50
Y (km)
0.25
0.38
0.44
X (km)
Z (km)
0.27
0.32
0.42
(b)
4 stations
0.32
0.38
0.32
0.38
0.44
0.52
0.57
0.62
0.67
(c)
Depth (km)
5 stations
0.38
0.44
0.50
0.32
0.38
0.44
0.47
0.52
0.57
0.62
(d)
6 stations
0.44
0.50
0.32
0.38
0.44
0.37
0.52
0.57

Figure 4.12: From the left to the right in each row of subplots, parallel cross-sections across the GRiD MT grid in the YZ plane (1st subplot, left), XZ plane (2nd subplot, center) and XY plane (3rd subplot, right). X, Y and Z directions are northing, easting and depth (all km). In the 1st subplot of each row (left), the closed polygons are VR = VR_{TH} contours of VR distribution on the YZ plane for different events and delineate the probable source volume color-coded by the X value of the best-fitting centroid MT solution. Similarly color-coded contours of the salt dome (dashed lines) and best-fitting centroid location ('+' signs) are also plotted for corresponding values of X. Random noise (up to ± 10 m) is added to the centroid locations to distinguish them from one another (otherwise many discrete grid point locations will be on top of each other). This subplot is similar to the one for profile AB in Fig. 4.5b except that we plot source volumes of multiple events and show their position with respect to the salt dome in the same subplot and don't show the VR distribution. 2nd subplot in each row (center) is similar to the 1st subplot but shows parallel XZ sections at different values of Y (similar to profile CD in Fig. 4.5b). 3rd subplot in each row (right) is similar to the 1st subplot but shows parallel YX sections at different depths, Z (similar to the depth slice in Fig. 4.5a). The locations of OG3 on the XY plane and the USGS stations are shown as black diamond and black triangles, respectively. Cyan polygon shows the approximate surface extent of the sinkhole in ~July 2013. Different rows of the figures are of different groups of events in the sequence at different time periods with their GRiD MT solutions computed with different number of stations: (a) 8 events with $VR_{MAX} \geq 60\%$ till end of 23 July 2012 (3-station solutions). Contours corresponding to the event on 20 July 2012 discussed in the text and in Figs 4.13a,b are thickened and marked with arrows. (b) 44 events with $VR_{MAX} \geq 81\%$ from the initiation of the steady phase of the seismicity on 24 July 2012 till the installation of LA08 on 30 July 2012 (4-station solutions). (c) 31 events with $VR_{MAX} \geq 70\%$ from the resumption of the seismicity after the quiescence period G4 on 31 July 2012 till the installation of LA09 at 19:00 hours, 01 August 2012 (5-station solutions). (d) 15 events with $VR_{MAX} \geq 68\%$ from the time of installation of LA09 to the onset of final episode of continuous large amplitude ground motions at 03:21 hours on 02 August 2012 (6-station solutions). Note that axis limits and scales are different for each period of events.

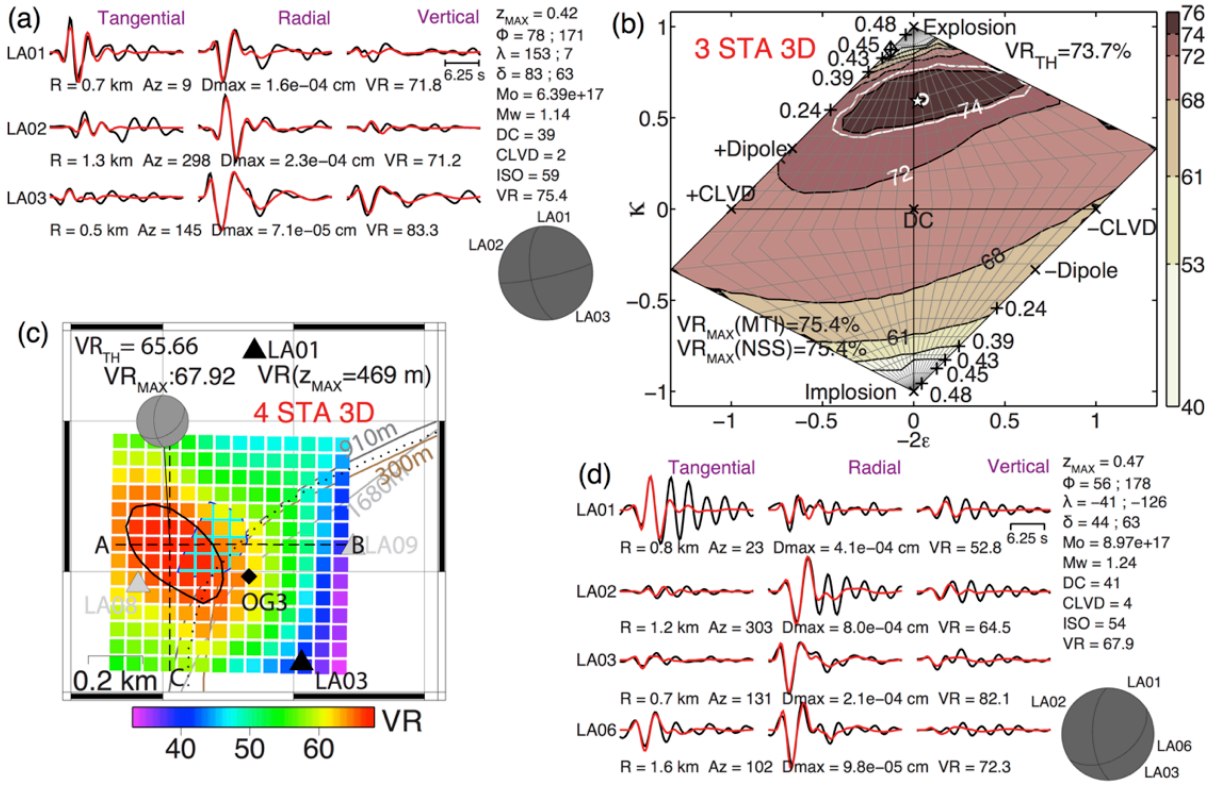

Figure 4.13: (a) Same as Fig. 4.6c but for an event on 20 July 2012 using 3 stations. (b) same as Fig. 4.8a but for the event shown in (a). (c) same as Fig. 4.5d but for an event on 24 July 2012. (d) same as Fig. 4.6c but for the event shown in (c).

This steady sequence was interrupted by an episode of a few closely timed larger magnitude events or semi-continuous large amplitude ground motions at ~19:34 hours, 29 July that lasted ~142 s. We refer to this episode and other similar episodes of closely timed relatively larger magnitude events or semi-continuous ground motions as "tremor-like" episodes (not to be confused with tectonic tremor). GRiD MT could detect only one event buried in these ground motions and it is one of the largest events detected prior to the appearance of the sinkhole. While its amplitudes are ~5 times larger than amplitudes of M_W ~2.0 events during July 25-29 at all stations, its waveforms are contaminated by preceding event ground motions leading to poor waveform fits (VR_{MAX} ~56%) and rather large uncertainties in source location, source type and M_W (best-fitting M_W ~2.37 and probable M_W ~1.8-2.7 from the composite NSS analysis). This episode was immediately followed by a pronounced quiescence in the detected seismicity with only ~2 events detected in the next ~3.93 hours (Gap G3 in Fig. 4.11b). There are multiple relatively smaller magnitude events visible in the raw data during this period of relative inactivity, but they are likely too small to be detected in our passband. The record section in Fig. 4.14a shows the steady seismicity with opening crack-like source type being interrupted by the tremor-like and the following quiet period G3 on 29 July, with an expanded view in Fig. 4.14b. Figs 4.14c shows a detailed picture of the observed long period displacement and the synthetic displacements from GRiD MT for the M_W 2.37 event buried in the semi-continuous ground motions (ev281943) along with an immediately preceding opening crack-like event from the steady part of the seismic sequence

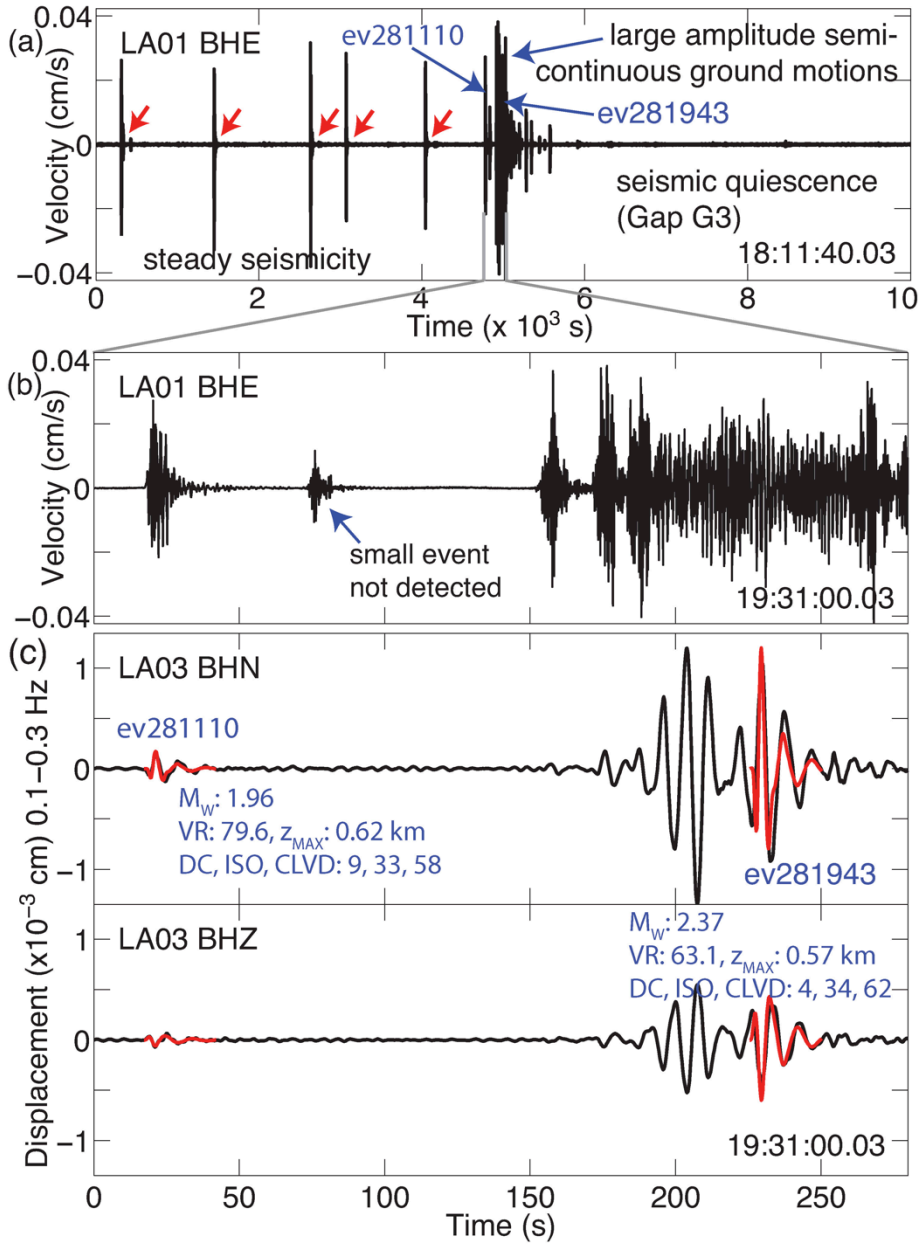

Figure 4.14: (a) Record section (velocity) on 29 July 2012 showing the steady seismicity being interrupted by a tremor-like episode, followed by a period of inactivity (Gap G3). Two of the events detected by GRiD MT are indicated ("ev*"). The vertical gray lines mark the time window expanded in (b) and (c). Other events detected by GRiD before the tremor-like episode are marked by red arrows. (b) Expanded view of the record between the two gray lines in (a). (c) Same time window as (b) showing low frequency displacement waveforms (black) along with synthetic waveforms (red) for best-fitting MT solutions (M_W, z_{MAX}, DC, ISO and CLVD components and station VR are indicated) of the two events detected by GRiD MT. ev281110 is a regular opening crack-type event located in the salt whereas ev281943 is a large magnitude event (notice the factor of 5 difference in amplitudes of the two events) buried in the continuous ground motions between 180-260 s. For all subplots, the station name and component, and the absolute start time of the record are indicated in the upper left and the lower right corners, respectively.

(ev281110). The steady sequence of the opening crack-like sources resumed at 00:12 hours on July 30 with a small but clearly noticeable reduction in magnitudes (average M_W ~1.98 ± 0.05 for 8 events before the large event and average M_W ~1.83± 0.05 for the first 8 events after gap G3, M_W difference ~0.15 units; Figs 4.11a,b). The M_W and the displacement amplitudes steadily increased back to close to prior levels within a day before the sequence was interrupted by another tremor-like episode (before Gap G4 in Fig. 4.11b). There are also 2 other smaller periods of seismic quiescence (periods of relatively fewer events detected by GRiD MT) of durations ~1.12 hours and ~2.15 hours following tremor-like episodes with durations ~134 s and ~118 s at ~01:35 hours on 27 July and at ~16:36 hours on 28 July, respectively (Gaps G1 and G2 in Fig. 4.11b). G2 was followed by an interesting reduction in displacement amplitudes of the detected events at the TA station (Fig. 4.11a).

Fig. 4.15 shows the 5-station GRiD MT solution, waveform fits, VR distribution at z_{MAX}, and composite NSS of event TE2 (excluding LA09). The installation of the closest station to the source region, LA08, at ~22:33 hours on July 30, greatly improved the constraints on the centroid depth of the events (probable source depth for event TE2 $\lesssim$ 0.62 km). The probable source volume still includes sections of both sediment and salt media as before, resulting in similar VR for alternative isotropic volume-increase sources and opening crack-type sources in the two media. However, the 5-station GRiD MT implementation preferentially places the best-fitting centroid location in the sediment layer and returns a lower M_W (~1.37 for TE2 instead of ~1.8 from 4 stations; Fig. 4.6c), and a dominantly isotropic volume-increase MT solution as the best-fitting solution. Immediately after the installation of LA08, another tremor-like episode began at ~23:59 hours and continued for ~389 s. We were able to detect 3 discrete M_W ~1.73-1.79 events with high ISO (~87-91%) components in this period and their amplitudes are ~2 times the amplitudes of previous crack-like events. Contamination of waveforms from preceding events again leads to low values of VR_{MAX}. This episode of large ground motions was followed by a period of ~3.13 hours in which no events were detected (Gap G4).

The seismicity resumed at 03:13 hours on July 31 with a pronounced reduction in M_W, which is reflected in the decrease in VR_{MAX} and displacement amplitudes at both LA02 and TA.544A. The apparent large M_W drop (~0.82 units) across the quiescence period G4 (from average M_W ~1.95±0.05 to average M_W ~1.13±0.11 for ~20 representative events before and after G4) shown in the inset in Fig. 4.11b is partially caused by the shift of the preferred best-fitting centroid location from the salt medium to the adjacent sediment layer following the addition of LA08 to the network (see the change in northing in the inset in Fig. 4.11e). Crudely assuming a bias of ~0.45 units in M_W between MT solutions at adjacent centroid locations in the salt and sediment layers (from event TE2 results in Figs 4.6a,b, 4.15a), the true M_W decrease is likely to be around ~0.37 units. This value is close to the drop of ~0.25 units in M_W error bars across G4 in Fig. 4.15b (upper bounds change from ~2.07±0.05 [average of 20 specific events] to ~1.81±0.07 [average of 8 specific events]; lower bounds change from ~1.34±0.07 to ~1.09±0.06). We further confirm this by recalculating best-fitting centroid locations and MT solutions for events during July 31-August 1 using the original 4 stations (Fig. 4.A.2 in the **Appendix**). Assuming the preferred best-fitting centroid locations in salt with opening crack-type MT solutions, the average decrease in M_W across G4 is ~0.28

units (from average M_W ~1.95±0.05 to average M_W ~1.67±0.07 for ~20 events before and after G4).

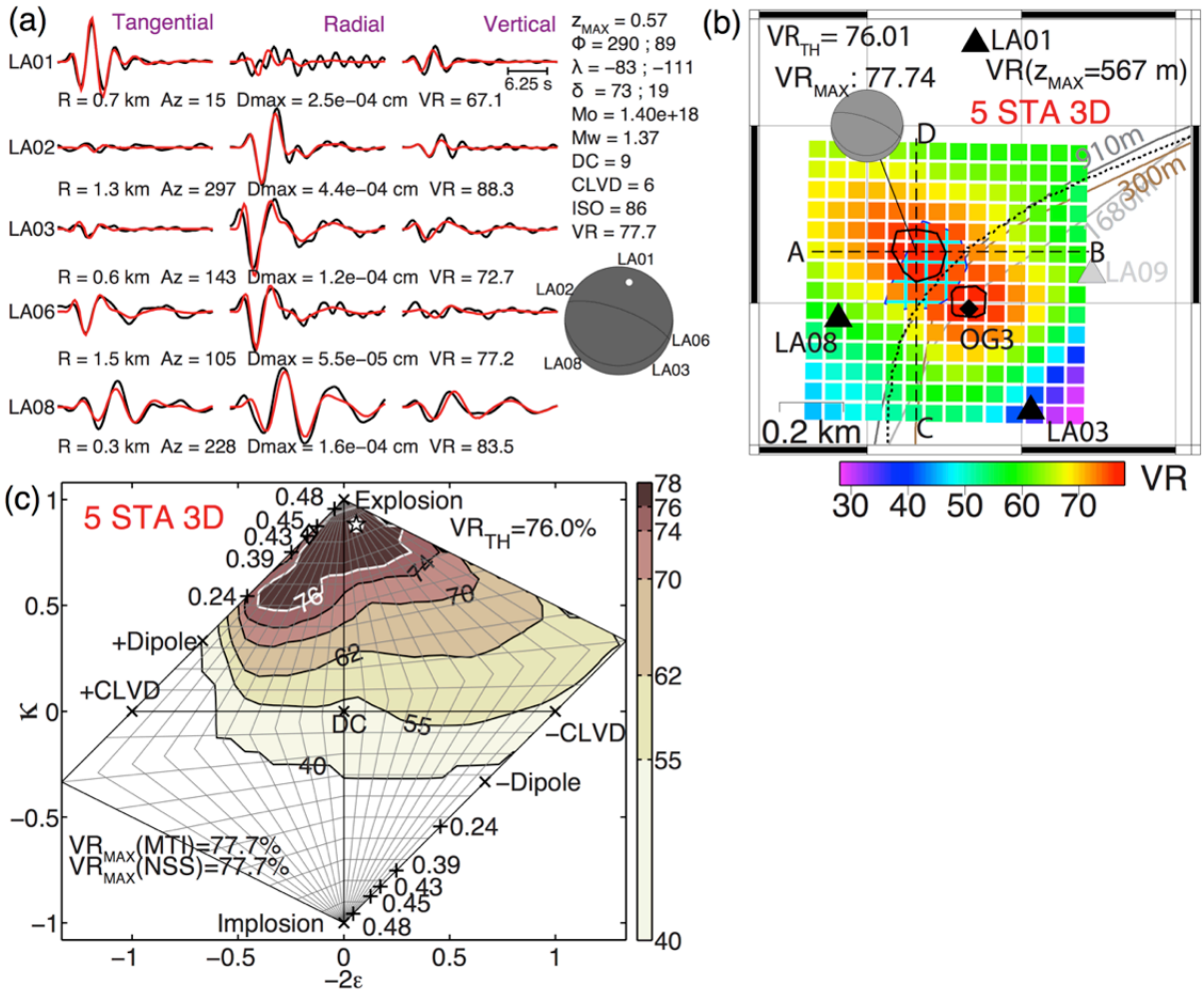

Figure 4.15: (a) same as Fig. 4.6a but for 5-station GRiD MT (excluding station LA09). (b) same as Fig. 4.5d but for 5 stations. (c) same as Fig. 4.8a but for 5-stations.

While the VR_{MAX} values are low for the smaller events during July 31-August 01, the probable source depths are generally well constrained to $\lesssim$ 0.75 km (Figs 4.11e, 4.12c). However, the probable source volumes are generally wider in ~NW-SE direction (Fig. 4.12c) compared to those in Fig. 4.12b, possibly reflecting the increase in uncertainties due to lower VR_{MAX} in this period or possibly because of longer wavelengths introduced by LA08, as we are using lower frequencies (0.1-0.2 Hz) for LA08 compared to 0.1-0.3 Hz for all other stations. The preferred best-fitting centroid locations are generally in the sediment layers and consequently the best-fitting GRiD MT solutions are strongly isotropic (Fig. 4.11b). The scatter in the centroid locations could be due to loss of localization and broadening of the source area or could be a manifestation of larger errors in the solutions of smaller magnitude

events. There is a subtle decrease in M_W followed by an increase, also reflected in the amplitudes at LA02 and in changes in VR_{MAX} (Figs 4.11a-c).

The addition of the last station, LA09, at 19:00 hours on 01 August leads to a further tightening of constraints on the centroid location (Fig. 4.12d). The probable depths for events with good waveform fits are $\lesssim$ 0.7 km. The probable source volumes are either completely outside the salt medium or slightly intrude into it. Consequently, for at least a few events, we can constrain the most probable source types to be dominantly isotropic volume increase (ISO $\gtrsim$ 70%) or opening cracks with $\nu \gtrsim 0.43$ from the composite NSS analysis, similar to the 6-station result for event TE2 (Fig. 4.8a).

The final tremor-like episode occurred at ~03:21 hours on 02 August and lasted ~303 s, followed by a ~3.67 hours long quiescence period. VR_{MAX}, M_W, probable depths, and ISO contribution in the MT solution for one of the large events during this episode are ~60.6%, ~1.81 (the large M_W is supported by the displacement amplitudes), $\lesssim$ 0.7 km and ~91% (volume increase), respectively (Fig. 4.16a). The probable source volume is predominantly in the sediment layer, which is reflected in the composite NSS (Figs 4.17a,b). The sequence of the final small amplitude seismic events detected by GRiD MT ended at ~09:24 hours and was followed by a ~9.41 hours long relatively quiet period with very few detected events. A large magnitude event (M_W ~ 1.90 for the best-fitting solution and M_W ~1.68-2.29 from the composite NSS analysis) at ~18:48 hours was the final event detected on 02 August. Despite poor waveform fits (VR_{MAX} ~ 56.8%; Fig. 4.16b) owing to contamination from decaying amplitudes of a preceding event, the probable source volume is mostly outside the salt dome, in the sediment layers at depths $\lesssim$ 0.7 km (Fig. 4.17c). The NSS clearly indicates that this event involved a collapse mechanism, and its waveforms are fit well by closing crack MTs or an implosion (Fig 4.17d). This event probably caused permanent damage to the source region or the driving mechanism of the seismic events.

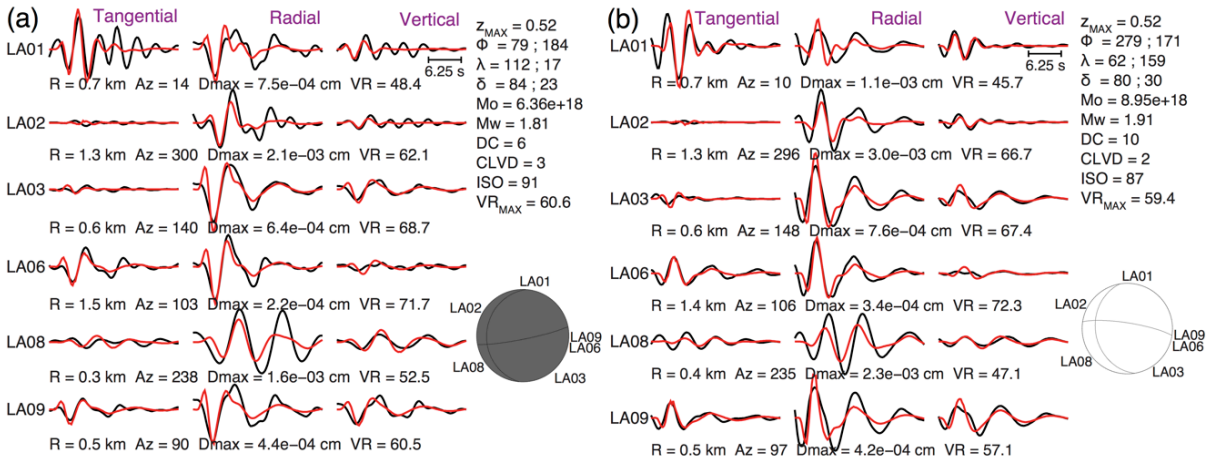

Figure 4.16: (a) Same as Fig. 4.6a but for one of the large events detected during the continuous shaking episode on 03:21 hours, 02 August 2012. (b) Same as Fig. 4.6a but for the large event with negative ISO component at ~18:48 hours, 02 August 2012.

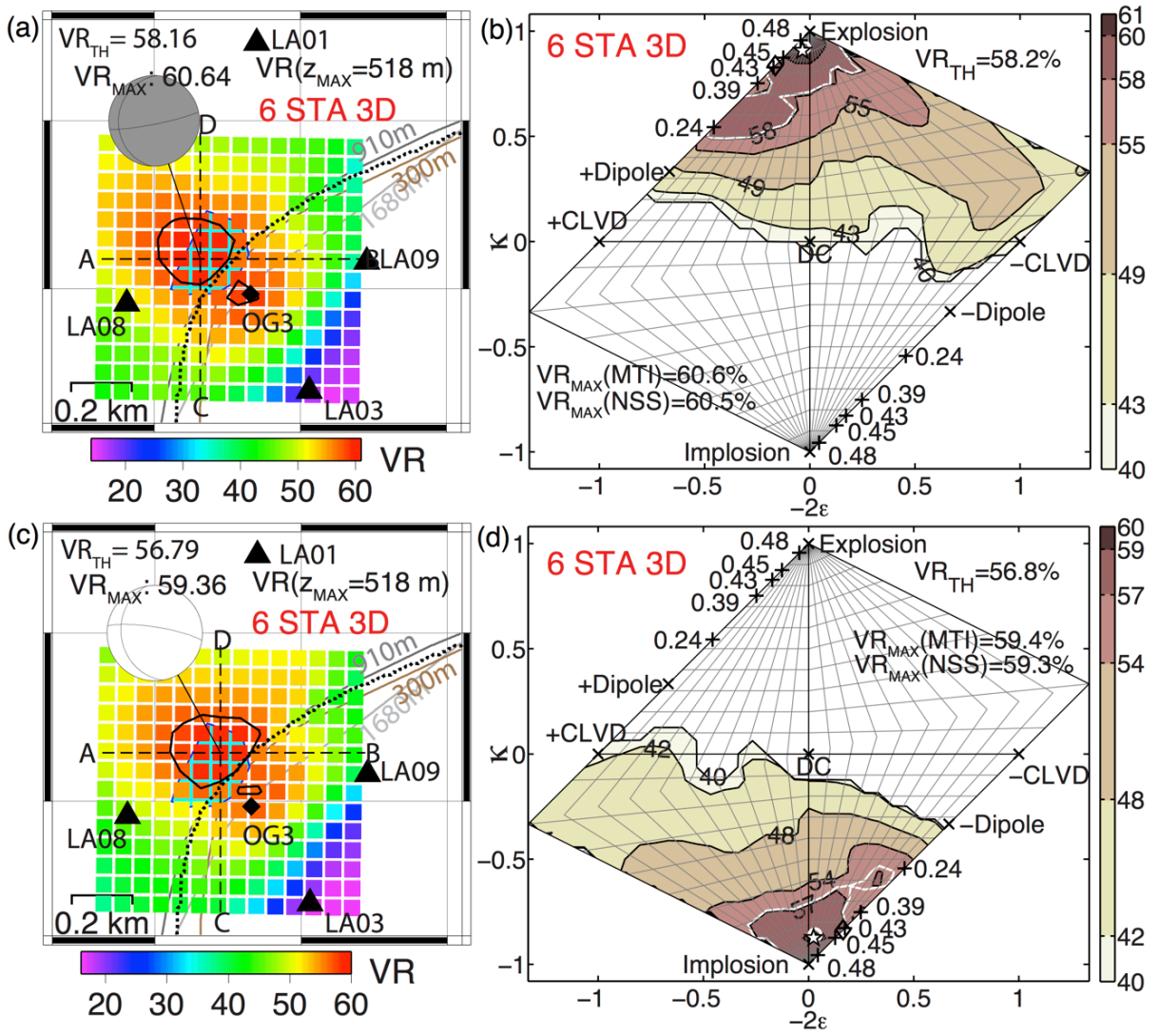

Figure 4.17: (a) Same as Fig. 4.5a but for one of the large events detected during the continuous shaking episode on 03:21 hours, 02 August 2012 (waveform fits in Fig. 4.16a). (b) Same as Fig. 4.8a but for the event in (a). (c) Same as Fig. 4.5a but for the large event with negative ISO component at ~18:48 hours, 02 August 2012 (waveform fits in Fig. 4.16b). (d) Same as Fig. 4.8a but for the event in (c).

The earliest reports of the sinkhole were received at morning hours (lagging UTC by 5 hours) on 03 August 2012 (LADNR, OOC 2013). However, residents reported smelling odors of hydrocarbons during the previous night (Julie Shemeta, personal communication), and therefore it is possible that the sinkhole could have appeared during the night itself (7 PM-7 AM ~ 03 August, 0-12 hours UTC). GRiD MT detected very few events after the formation of the sinkhole till the end of the deployment of the temporary USGS network on ~27 January 2013. VR_{MAX} for detected events during this period is very low, primarily due to a decrease in predominant frequencies of the seismic events. While micro-earthquakes and VLP events have been reported in the months following the formation of the sinkhole (CB&I 2013; LADNR, OOC 2013), they are unlikely to be detected in our passband (0.1-0.3 Hz). The increase in ambient noise levels in the secondary microseism passband during winter months

in 2012 is likely due to storm and hurricane activities near the eastern coast of US and/or Gulf of Mexico (Fig. 4.11a). Some episodes (but not all) of gradual increase in ambient noise levels followed by a gradual decrease over the course of a few days are correlated with the decrease and subsequent recovery in atmospheric pressure recorded by the pressure sensors installed at the regional Transportable Array stations (LDO channels of TA.544A, TA.645A, etc.), with one prominent episode during ~ 27 August-01 September 2012 coinciding with the passage of Hurricane Issac (https://www.weather.gov/mob/isaac, last accessed July 2017). From September 2012 till the end of the deployment, we restrict the GRiD MT analysis to lower number of stations or refrain from analyzing any data (for 5 days in January 2013) due to intermittent unavailability of some stations on some days.

For the analysis of the seismicity and moment-release rates during the most energetic section of the sequence (10:00 hours, 24 July – 03:21 hours, 02 August 2012), we constrain the seismic events to be preferentially located at the best location in the low-velocity sediment layers within their probable source volumes. This alleviates the uncertainty in M_0 resulting from the possibility of the centroid location being in either of the two media, sediment or salt. There were only 3, relatively poorer VR events (VR_{MAX} < 67%) for which the probable source volume was entirely inside the salt dome and we leave their locations unchanged. We also remove events detected during the tremor-like episodes and succeeding quiet periods G3, G4 and G5. Fig. 4.18a shows the number of detected events and M_0 released in 2-hour windows, shifted by 1 hour. Since it is difficult to identify and characterize all the individual events buried in the tremor-like episodes, we compare their relative size using the apparent seismic energy released over the entire duration of strong shaking (e.g. Kinscher *et al.* 2015). The seismic energy recorded at each station is calculated as, $= \sum_{j=1}^{3} \int_{t_1}^{t_2} \dot{u}_j(t)^2 dt$, where $\dot{u}_j$ is the j^{th} component of velocity filtered in the passband 0.1-0.3 Hz, and t_1 and t_2 are the start time and the end time of the tremor episode. For each station, the energy for each tremor-like episode is normalized by energy for the episode prior to Gap G3 (the one with the largest energy). We take the average of the relative energy estimated from multiple stations (LA01, LA02 and LA03) and compare against the duration of the period of relative inactivity following the tremor-like episodes (Fig. 4.18b). While we have only 5 data points, it seems that tremor-like episodes associated with greater seismic energy release were followed by longer quiet periods. The episodes prior to quiet periods G3, G4 and G5 can be interpreted as durations of rapid release of significant accumulated seismic strain leading to a period of inactivity until sufficient strain was built back up for new seismic events by the driving mechanism. We were able to locate few events embedded in the continuous ground motions of the tremor-like episodes to approximately the same source region as the dominant isolated events of the steady sequence, although the uncertainties are large due to poorer waveform fits (Figs 4.14c, 4.17a,b). The decrease in M_W and the moment-release rate (Figs 4.11a,b, 4.18a) following the tremor-like episodes indicate material damage at the source region and/or weakening of the mechanism driving the seismicity. The gradual increase in M_W and moment release-rate immediately after Gap G3 suggests that the source region healed with time and/or the driving mechanism recovered to earlier levels. However, there was a permanent drop in the moment release-rate following the tremor-like episode associated with Gap G4. To examine the time interval between successive events (inter-event time, T), we divide all the events until the tremor-like episode before Gap G4 into two sub-populations of events with relatively better waveform fits ($VR_{MAX} \geq 70\%$) and events with relatively poorer waveform

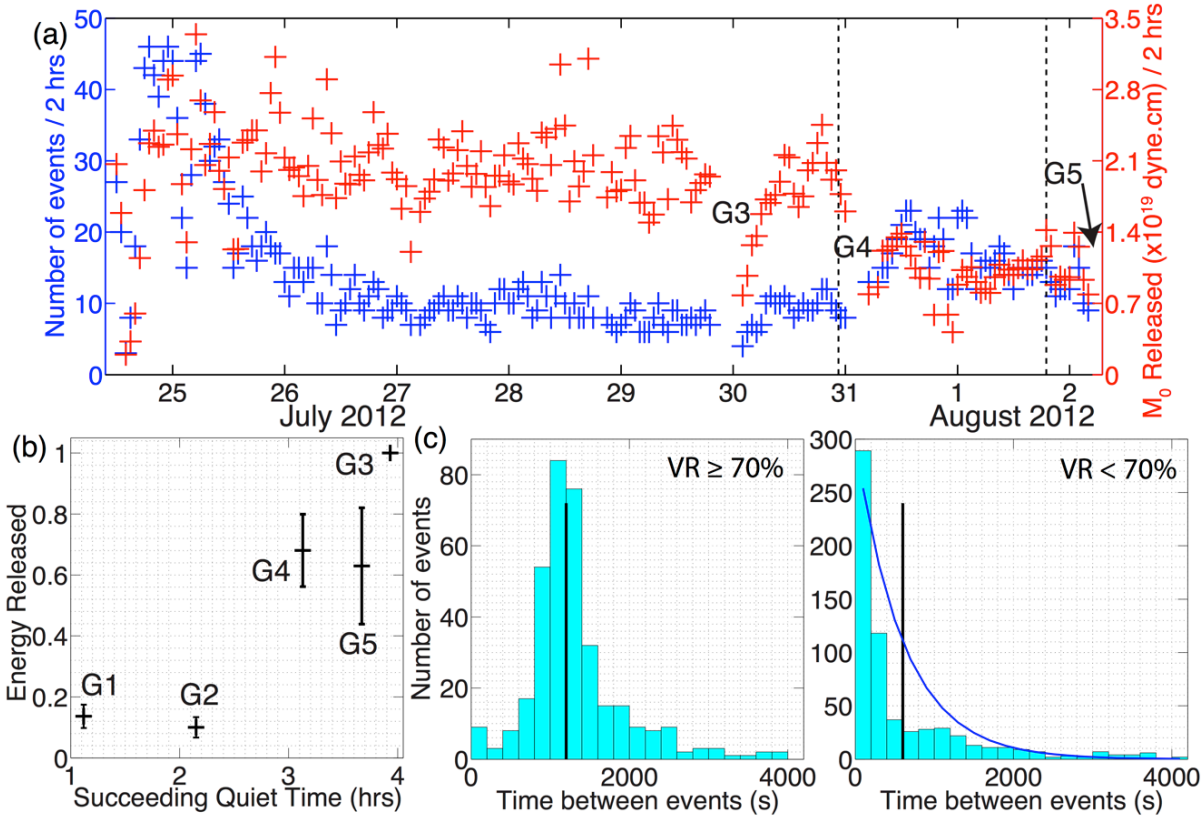

Figure 4.18: (a) Number of detected seismic events and total M_0 released through these events in 2-hour time windows, shifted by 1 hour, during the most energetic part of the sequence (10:00 hours, 24 July – 04:00 hours, 02 August 2012). For this plot, we preferentially assumed centroid locations in the sediment layers and excluded seismic events detected during tremor-like episodes preceding quiet periods G3, G4 and G5. Data points have been plotted for only those 2-hour windows in which seismic events span at-least 1.25 hours. (b) Energy released during tremor-like episodes prior to all the inferred quiet periods (numbers indicated on the plot) normalized by the energy released during the tremor episode preceding G3, plotted against the duration of the quiet periods (periods of relative seismic inactivity or fewer events detected). The error bars span the standard deviation of relative energy calculated for multiple stations. (c) Histograms of inter-event time (T) for events with generally good waveform fits ($VR_{MAX} \geq 70\%$: left subplot) and events with poorer waveform fits ($VR_{MAX} < 70\%$; right subplot) during the steady period of the sequence in 24-30 July 2012, excluding tremor-like episodes and the succeeding quiet periods G3 and G4. The bin width is 200 s; the vertical black line marks the median and mean of the distributions in the left and right subplots, respectively. In the right subplot, the blue curve is proportional to an exponential probability density function with mean inter-event time ~600 s (i.e., $\propto e^{-T/600}$), and is shown for reference.

fits ($VR_{MAX} < 70\%$; Fig. 4.18c). This crudely divides the seismic sequence into two populations: one population is composed of ~350 dominant opening crack-like events (steady $M_W \gtrsim 1.85$, κ ~0.6 and a steady centroid location in Fig. 4.11c-e) discussed previously and the other population is composed of relatively lower M_W events that show relatively scattered locations and source mechanisms, likely due to noisy waveforms. We remove outliers with T

> 4200 s (< 4% of the data). The distribution of *T* for the dominant opening crack-like events is strongly peaked at ~1200 s (median) with standard deviation of ~600 s. While our catalog is definitely incomplete for the second population of generally smaller M_W events, the number of these events in a given range of *T* generally decreases with increase in T. We assume that the scalar isotropic moment ($M_{0,ISO}$) of a seismic event is related to the coseismic volume change (dV) by $M_{0,ISO} = (\lambda+2\mu)dV$, where λ and μ are the Lame's parameters at the centroid location (Aki & Richards 2002). The cumulative volume increase inferred from the positive isotropic moments of all MT solutions until 2 August 2012 is ~1.29×10^4 m^3 (assuming preferred centroid locations in the sediment layers). This value is a lower bound because we are missing many events. Assuming the events are preferentially located in the salt, the volume increase is lower by ~30%. The cumulative volume decrease during this time period is significantly smaller (~300 m^3), however it is likely that the rapid volume increase of a given event is followed by a more gradual deflation of the volume that does not radiate seismically or does so below the noise floor.

4.5 Results for the 01 January 2015 Event

Following the decommissioning of the temporary USGS network in January 2013, a new seismic network (Texas Brine Corporation Louisiana Seismic Network [TBLSN]) composed of posthole and borehole Trillium Compact broadband sensors was installed near the sinkhole (Fig. 4.1). These sensors had the lower corner period at ~20 s (compared to ~120 s for the USGS broadband sensors) and most of them (5 out of 7) were installed at depths 18-25 m except 2 that were installed at depths 134 m and 185 m (LA10 and LA17). The new stations are located closer to surface location of OG3 (all stations are within ~0.55 km) compared to the USGS stations (LA02 and LA06 were at distances ~1.3-1.4 km, respectively). We applied GRiD MT to the data from the new network using the 3DGFs to verify if GRiD MT with the 3D velocity model is capable of detecting more recent deeper seismic events that are known to be occurring in the salt dome (Mousavi *et al.* 2016). We apply GRiD MT on 0.1-0.3 Hz displacement waveforms of an event on 01 January 2015 that was located to a depth of ~1.62 km inside the salt dome by a separate downhole string of geophones extending to ~915 m depth near the top of OG3, using body-wave arrival times (Mousavi *et al.* 2016). 3DGFs were calculated for paths to the new stations using methods similar to that described earlier for the USGS stations. For calculation of 1DGFs, the sensor depths were modified by a few meters because the numerical integration method used in the frequency-wavenumber integration requires a non-zero depth difference between the source and the receiver. Similar as before, we assume that paths to the stations over the sediment layers (LA12, LA17, LA18) and to stations over the salt dome (LA10, LA11, LA14, LA19) are satisfied by the 1D sediment and 1D salt dome models, respectively. The grid of possible source locations was extended by two grid points (126 m) to the east and shifted 63 m to the north and to the east. VR_{TH}-VR_{MAX} relationships were calculated with ~5 days of recorded noise using a similar procedure as before (Table 4.A.1).

Fig. 4.19 shows the spatial distribution of VR for this event obtained using 3DGFs, the probable source volume and the travel-time location. Unlike other events prior to the appearance of the sinkhole, the probable source volume constrains this event to be deeper than 1.25 km with z_{MAX} ~1.94 km (deepest grid point), close to the travel-time depth of ~1.62 km.

However, the constraints on the horizontal location are weak and the horizontal location is off the travel-time location by ~350 m. This is not surprising as the event is deep compared to the aperture of the network used for GRiD MT (see the surface distribution of stations in Fig. 4.19b), resulting in large uncertainties in the centroid location (the probable source volume is large). However, the travel-time location (corresponding to VR ~73.6%) is within the probable source volume (VR_{TH} ~72.9%) demonstrating that our empirical VR thresholds established from the analysis of noise contaminated-synthetic waveforms return realistic location uncertainty estimates. While GRiD MT with 1DGFs also returns a deep centroid location, the horizontal location is completely off, at the northwest corner of the grid. VR as a function of the centroid depth, the best-fitting MT solutions and waveforms fits for solutions

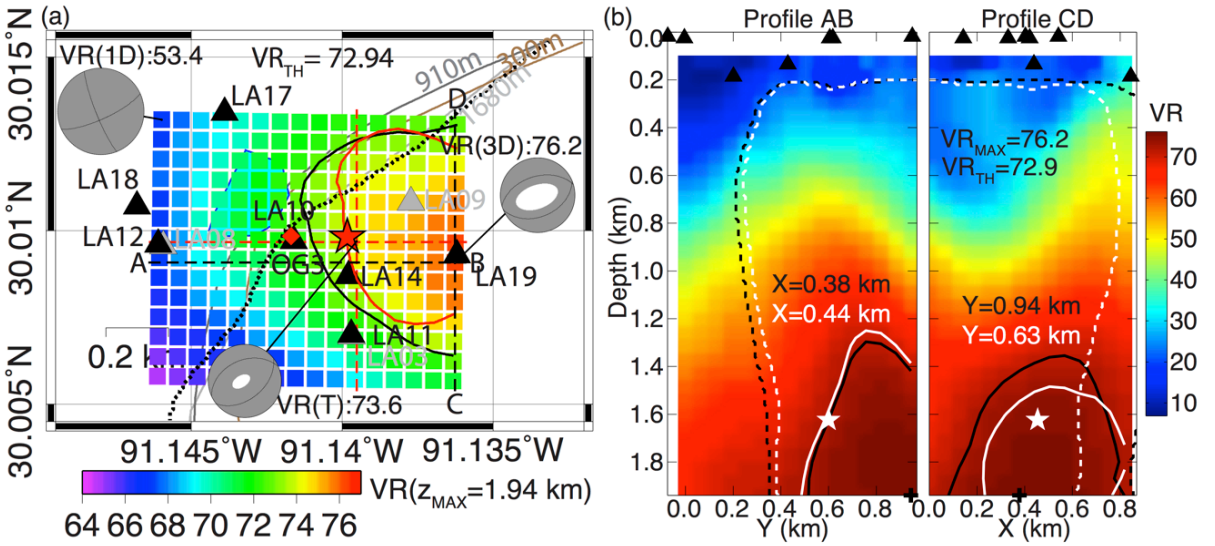

Figure 4.19: GRiD MT results for the 01 January 2015 event similar to Figs 4a,b that show results for event TE1. (a) Spatial distribution of VR at grid points at z_{MAX} = 1.94 m. The dotted black line is NSD's depth contour at z_{MAX}. Red triangle is the travel-time location in XY space. Black and red closed polygons are VR=VR_{TH} contours at z_{MAX} and the travel-time depth (~1.62 km), respectively. Black and gray triangles are locations of TBLSN and USGS stations (operating during 2012-13), respectively. Red diamond is the approximate XY location of OG3. Beach-balls representing upper hemisphere P-wave radiation pattern for the best-fitting MT solution computed using 3DGFs, MT solution at the travel-time location computed using 3DGFs and best-fitting MT solution computed using 1DGFs are shown and point to the corresponding centroid locations. The corresponding values of VR– VR(3D), VR(T) and VR(1D), respectively, are mentioned near the beach-balls. The depth sections of VR across profiles A-B and C-D through the best-fitting centroid location (black dashed lines) are shown in (b). We also plot VR=VR_{TH} contours on parallel profiles through the travel-time location (red dashed lines) in (b). The waveform fits for the best solutions computed using 3DGFs and 1DGFs are shown in Fig. 15. Meaning of other symbols is same as in Fig. 4a. (b) Depth sections across profiles A–B and C–D in (a) show depth distribution of VR. Black and white closed polygons are VR=VR_{TH} contours on sections through the best-fitting centroid location (thick black '+' sign) and the travel-time location (white star), respectively. Black and white dashed lines are outlines of NSD on the corresponding profiles. Black triangles are station locations. Color-coded X, Y values on the plot are positions of the profiles on the GRiD MT grid with the SW corner as the origin.

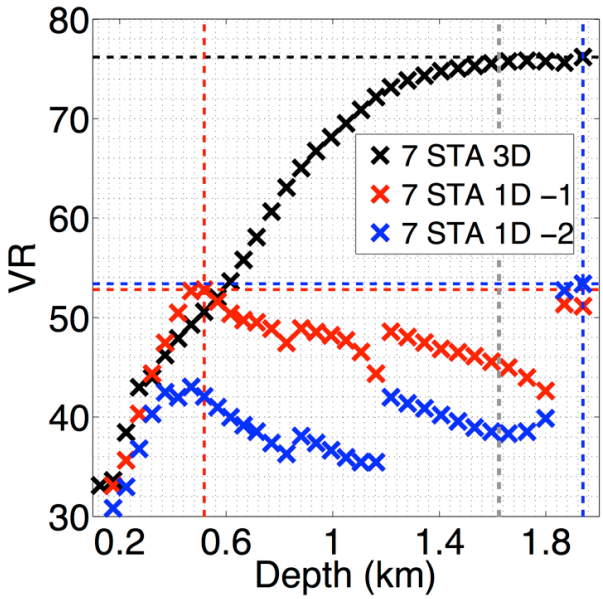

Figure 4.20: VR vs. grid point depth for the 01 January 2015 event for GRiD MT solutions obtained using 3DGFs ("3D") and 1DGFs ("1D"). For the 1DGFs, results for two cycle-shifted detections, separated by ~2.75 s in centroid origin time, are shown. Gray dashed line is the travel-time depth.

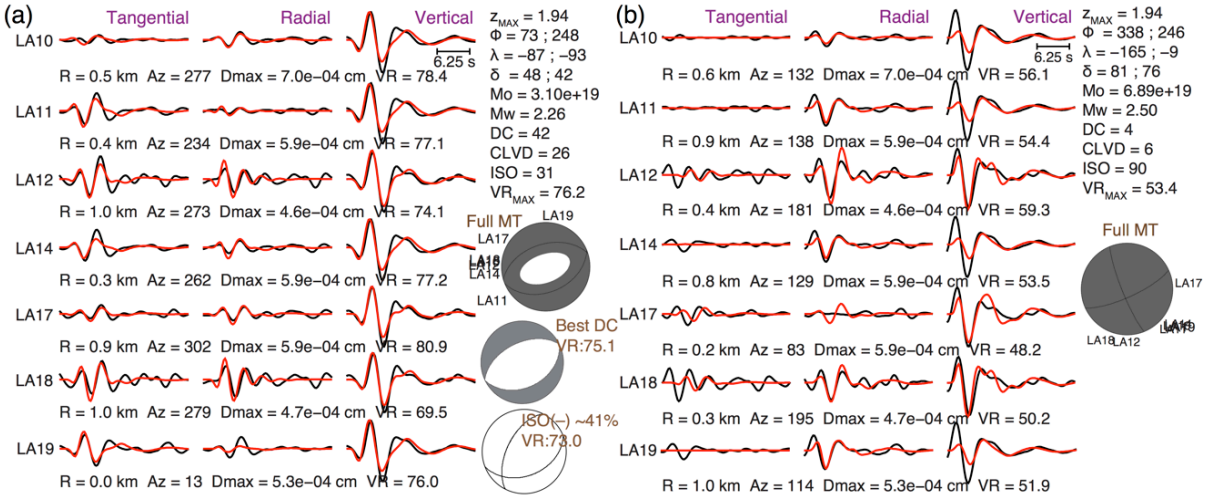

Figure 4.21: (a) Waveform fits and the best-fitting MT solution of the 01 January 2015 event recorded by TBLSN stations, obtained using GRiD MT with 3DGFs. The meaning of all symbols is same as in Fig. 4.6a except that the focal mechanism plots in Fig. 4.21 represent the upper hemisphere *P*-wave radiation pattern (instead of the lower hemisphere radiation pattern). Beach-balls "Full MT", "Best DC" and "ISO(–) ~41%" are the radiation patterns for the best-fitting MT solution (VR_{MAX} mentioned), the best DC solution and a MT with a large negative ISO component, respectively (VR for all three $\geq VR_{TH}$; VR for the latter 2 are mentioned: "VR:"), all placed at the best-fitting centroid location. (b) Same as (a) but for the best solution obtained using 1DGFs.

with 3DGFs and 1DGFs are shown in Figs 4.20 and 4.21. The 1DGFs provide significantly poorer fits to the waveforms (VR_{MAX} ~53%) compared to the 3DGFs (VR_{MAX} ~76%) with large amplitude mismatch for stations over the salt dome. The 1DGFs also result in a cycle-shifted origin time lagging the centroid time obtained with 3DGFs by 3 s. While the dominant energy is on the vertical components, the 3DGFs provide good fits to the small amplitude tangential and radial components as well. The NSS for just a single centroid location (Fig. 4.22) shows that we have little or no constraints on the source type of this event. This is possibly because the dominant vertical component ground motions recorded at the stations that are located almost directly above the centroid location, are weakly sensitive to the radiation pattern near the equatorial region of the focal sphere. Fig. 4.21 also shows expected upper hemisphere P-wave radiation patterns for the best-fitting DC solution and for a MT with a large negative ISO (volume decrease) component (~ 41%) that fit the waveforms quite well ($VR \geq VR_{TH}$).

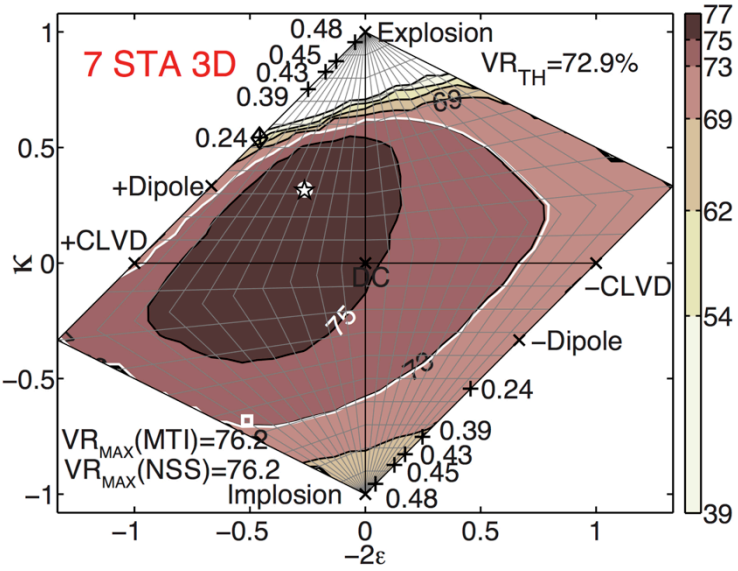

Figure 4.22: Network Sensitivity Solution (NSS) of the 01 January 2015 event at the best-fitting centroid location. The white square is the source type for the MT with ~41% negative ISO component represented by the beach-ball in Fig 15a. Meaning of other symbols is same as in Fig. 4.8a.

We conclude that for deeper events within the salt dome, the 3D velocity model is expected to be reasonable for GRiD MT analysis. Other events in the catalog of Mousavi et al. (2016) recorded at TBLSN stations during 2014-2015 are significantly smaller in magnitude and we were unable to analyze them in our passband ~0.1-0.3 Hz.

4.6 Overall Performance of the 3D Model

We separately applied GRiD MT to data prior to appearance of the sinkhole using 1DGFs to make sure that we are not missing any events that might have VR_{MAX} below the detection threshold due to possible deficiencies in the 3D velocity model. There are only ~21 events that were detected by 1DGFs and not by 3DGFs. These are events with generally low SNR, and VR_{MAX} values $\leq$ 43%, close to the detection threshold. The comparison between the waveform fits achieved by GRiD MT solutions of ~1130 common events obtained using both 1DGFs and 3DGFs for same combinations of stations is shown in Fig 4.23. On an average, 3DGFs provide better waveform fits compared 1DGFs for ~92%, ~93% and 100% of all detected events (detected by both at $VR_{MAX} \geq 40\%$) for 4-, 5- and 6-station GRiD MT solutions, respectively. 6-stations solutions show the most prominent difference in VR_{MAX} obtained using 3DGFs and 1DGFs as 3DGFs are likely necessary to fit the complex wavefield simultaneously at multiple azimuths from distances ~0.4 km (LA08) to ~1.6 km (LA06), over the salt dome and the adjacent sediment layers. As an example, the average difference between VR_{MAX} obtained with 3DGFs and 1DGFs is ~6.2%, ~4.0%, and ~7.2% at VR_{MAX} =63% (for 1DGFs) for 4-, 5-, and 6-station solutions, respectively. The difference generally increases with VR_{MAX} indicating that the similarity of VR_{MAX} values for generally smaller events with lower VR_{MAX} is caused by contamination from noise. As SNR decreases, the generally smaller amplitude tangential and vertical components of ground motions are overwhelmed by the background noise leading to poor waveform fits with both 3DGFs and 1DGFs.

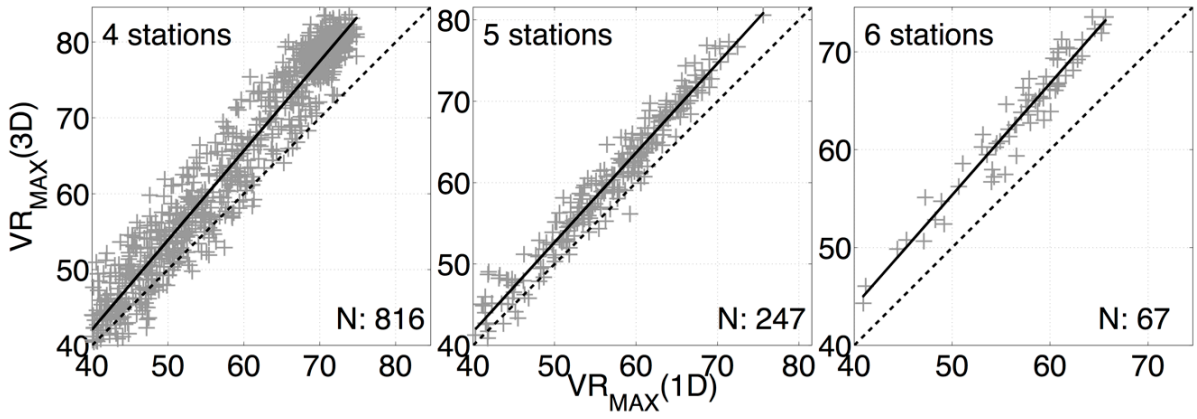

Figure 4.23: Comparison of VR_{MAX} values for GRiD MT solutions obtained using both 1DGFs ("1D") and 3DGFs ("3D") for various combinations stations (upper left corner). The number of events (N) in each subplot is indicated at bottom right corner. Gray '+' signs are data points, dashed black line is 1:1 relationship and solid black line is a straight line fit to the data.

Since most of the seismicity prior to the appearance of the sinkhole appears to be located at the edge of the salt dome, the approximation of the long period 3D wavefield by two separate 1D velocity models for the salt section and the sediment layers is still reasonable and we can

fit the waveforms quite well (difference in VR_{MAX} for 3DGFs and 1DGFs is less than 10%) and recover similar MT solutions. This is likely because the path to each station traverses primarily a single medium. However, for events that are located well within one of the media, such as the 01 January 2015 event that was located fairly deep inside the salt dome, 3DGFs fit the waveforms significantly better than the 1DGFs (difference in VR_{MAX} ~23%). The 1DGFs also fail to recover the correct location.

As computation of waveforms for 3D velocity models using numerical methods is computationally very expensive and time consuming, we refrain from examining differences in the MT solutions obtained for possible modifications to the 3D velocity model. However, ND14 and ND15 have analyzed MT solutions of some events in this sequence in great detail using 1DGFs for different passbands and 1D velocity models, and they have recovered isotropic volume-increase / opening crack-like MT solutions at shallow depths similar to this study. Given the long seismic wavelengths employed, we expect that the broad features of the seismicity and changes in its temporal behavior inferred from GRiD MT results should not be too sensitive to minor modifications to the 3D velocity model.

4.7 Discussions

During an energetic phase of the Bayou Corne sequence from 24-31 July 2012 when 4 stations were operational, the events with the best waveform fits are primarily located at the western edge of the salt dome at most probable depths of ~0.3-0.85 km, close to the horizontal positions of OG3 and the future sinkhole. The data are fit nearly equally well by opening crack MTs in the high velocity salt medium or by isotropic volume-increase MTs in the low velocity sediment layers. The addition of more stations further constrains the events to slightly shallower depths. Location errors can lead to large uncertainties in MT solutions in cases where the seismic events are located near interfaces with large seismic velocity contrasts. However, our best-fitting MT solutions are clearly non-deviatoric. We find that data recorded by 6 stations during 01-02 August 2012, right before the appearance of the sinkhole, indicate that some events are likely located in the lower velocity sediment layers just outside the salt dome at depths ~0.35-0.65 km, with preferred isotropic volume-increase MT solutions.

It has been suggested that the collapse of OG3 cavern was unusual in the sense that the collapse occurred at the thin sidewall of the cavern at great depth (Jones & Blom 2015; LADNR, OOC 2013). For more common cases of salt cavity roof collapses, a single-lobe surface compression pattern is expected (Jones & Blom 2014). UAVSAR analysis showed a precursory two-lobed pattern of primarily horizontal displacement towards the location of the ultimate sinkhole development, indicating that surface material likely flowed towards a chimney-like feature leading down the side of the salt dome to the breach location between June 2011 and 2 July 2012 (Jones & Blom 2014). While Jones & Blom (2015) did not detect any significant vertical deformation up to ~1 month before the appearance of the sinkhole,

there has been significant subsidence in the area after the appearance of the sinkhole (LADNR & CB&I 2013).

Many cases of seismicity associated with salt cavern collapses reported in the literature involve partial or complete collapse of the cavern roof. Trifu & Shumila (2010) analyzed locations and source mechanisms of microseismicity during the controlled collapse of a large solution-mined brine-filled cavity in salt deposits of Ocnele Mari, Romania over a ~10-month period. They reported strike-slip and normal-faulting mechanisms for most of the events around the cavern ceiling and up to 30% of the volume-increase failure components, which they attributed to caving of the roof by a gravity-driven collapse. Their analysis indicates that most of the seismicity (M_W ~ –2.6 to 0.2) was associated with the collapse of the roof. A gradual increase in b-value from ~0.5 to ~1.5 reflected the evolution of the collapse from a linear fracture pattern to planar shear fragmentations and finally to a 3D failure process. In another case, microseismicity was continuously monitored during the growth and subsequent collapse of a shallow (at depth ~0.2 km) underground brine cavity in a salt deposit at Cerville-Buissoncourt, Lorraine, France. At that location, the controlled collapse, achieved by incrementally pumping brine out of the cavern, led to reduced cavern fluid pressure and intense seismicity. During the period from 2005 to 2007, tremor-like seismic signals composed of superimposed seismic events of durations tens of seconds and frequencies ~20-80 Hz constituted ~90% of the recorded seismicity and the remaining 10% was composed of isolated microseismic events ($M_W \lesssim -1$; Mercerat *et al.* 2010). Periods of brine pressure increase during two transient pressure experiments were an exception to this. During these phases, only tremor-like signals were observed. Kinscher *et al.* (2015) analyzed the seismicity during a period of significant cavity growth (increase in height ~50 m) caused by caving of the overhead poorly consolidated anhydrite marl layer (volume removed ~$5x10^5$ m^3) in March-May 2008, during which 80% of the seismicity comprised of swarming sequences with complex clusters of superimposed microseismic events. Both the isolated events and tremor-like sequence of events had similar frequency content (~20-200 Hz) and there were episodes of cascade-like peaks in seismic activity followed by periods of quiescence. Kinscher *et al.* (2015) observed fascinating systematic cyclic spatio-temporal epicenter migration trends in the order of seconds to minutes and several tens of meters. Similar migrations were also observed in the distribution of epicentre clusters in the order of hours and days. They suggest that the microseismicity represents detachment and block breakage processes acting at the cavity's roof, indicating a zone of critical state of stress and where partial fractures cause chain reaction failures as a result of stress redistribution processes. While constraints on the source mechanisms are weak, S/P amplitude ratios indicate possible detachment cracking associated with mode 1 rupture with a vertical axis or dip-slip mechanisms. Kinscher *et al.* (2015) also argue that seismic energy released upon impacts of material falling through the pressurized cavern on the unconsolidated cavern floor should be small. Jousset & Rohmer (2012) have suggested that dynamic stresses associated with the surface waves from a M_W 7.2 teleseismic earthquake damaged the overburden and triggered the high frequency microseismcity at the cavern that was already at a near-critical state, leading to its final collapse in 2009. The efficiency of Rayleigh waves in triggering the microseismicity and the collapse was likely aided by the similar natural fundamental period of the cavern + overburden + brine system, ~10-20 s (Jousset & Rohmer 2012). The irreversible collapse of the Dolomite overburden was reflected in the sharp increase in the local high frequency (~1-

30 Hz) microseismicity rate (average ~50-70 earthquakes per hour) signifying brittle failure of stressed rocks, sharp increase in brine level inside the cavern and a strong increase in the subsidence rate (Jousset & Rohmer 2012; Contrucci *et al.* 2012). The high rate microseismicity lasted nearly ~34 hours till the final surface collapse that was recorded as a large amplitude VLP signal, which usually indicates inertial movement of material.

Unlike the salt cavity collapses at Ocnele Mari and Cerville-Buissoncourt, OG3's roof was found to be intact by the exploratory well OG3A (LADNR, OOC 2013). For at least a short time period during 01-02 August 2012, we find that there is a strong likelihood of some seismic events being located ~0.1-0.15 km off the roof of OG3 in XY plane. Furthermore, the seismic events at NSD are likely located $\gtrsim$ 0.15–0.3 km above the roof of OG3 in terms of depth and the repetitive, semi-regular and stable nature of the seismicity capped by a maximum magnitude along with the presence of $\gtrsim$ 57% isotropic volume-increase components in the MT solutions are difficult to reconcile with a gradual caving process. However, it remains to analyze possible variations in higher frequency waveforms of the seismic events to decipher any small-scale spatio-temporal migration of the seismicity as observed by Kinscher *et al.* (2015). It will also be interesting to examine the seismic radiation and deformation patterns for a mode 1 crack with a vertical axis, occurring immediately above a cavity roof represented by a free surface or an interface overlying a fluid medium, and if the source mechanism can be correctly recovered using a surface network and the given velocity model that doesn't include the cavity.

We have also examined the National Earthquake Information Center (NEIC) earthquake catalog to search for possible large earthquakes around the world that might have influenced the seismicity at NSD. There are no earthquakes with $M_W \geq 5.5$ on 24 July 2012, the day of a rapid increase in seismicity. There were no such earthquakes 1 hour before or during the 5 tremor-like episodes in the period 27 July-02 August 2012. During 02-03 August 2012, the largest recorded earthquake is only a M_W 6.1 earthquake in Peru (depth ~144 km).

A major difference between the salt cavern collapse at NSD and those at Ocnele Mari and Cerville-Buissoncourt is the intense natural gas influx from the DRZ below the sinkhole at NSD, which was suggested to be a possible driving force for the seismic events with large isotropic volume-increase moments (ND14). Bubbling of natural gas, primarily methane, in local water bodies was reported as early as 11 June 2012, much before the deployment of the seismic network (LADNR, OOC 2013). Natural gas was believed to be accumulating and spreading laterally in the MRAA over an area of ~5 km^2 around the sinkhole (CB&I 2013a). Until approximately March 2014, $\gtrsim$ 25 mmcf (~7.1×10^5 m^3 at standard conditions, pressure ~1 bar and temperature ~289 K) of natural gas was flared out of the subsurface using multiple venting wells (CB&I 2014), with an approximate volume of ~20 mmcf (~5.5×10^5 m^3 at standard conditions) left in the aquifer according to estimates made in April 2013 (CB&I 2013a). Approximating the daily flow rate of natural gas at known bubble sites by ~15 mcf per day (CB&I 2013a), we obtain a very crude volume of ~1.0×10^5 m^3 (at standard conditions) of natural gas that escaped the surface water bodies over ~8 months in the form of bubbles. The approximate total estimate of ~13.5×10^5 m^3 of natural gas at ~standard conditions likely present in the aquifer during the formation of the sinkhole, reduces to ~1.3×10^4 m^3 for conditions (pressure ~110 bars, temperature ~305 K) at ~0.55 km depth

(general depth of the seismic events) assuming ideal gas law, a lithostatic pressure gradient and a geothermal gradient of ~30°C/km. This is of the same order of magnitude or smaller than the net coseismic volume increase of all seismic events until ~2 August 2012, although there are significant uncertainties in both estimates. The coseismic volume increase value is likely to be a lower bound as our catalog is incomplete for smaller events. To compare, the subsidence volume was about ~2.37x10^6 m^3 in early 2014, which is slightly greater than the sinkhole volume (CB&I 2014). The volume of the original cavern was estimated to be ~3.67x10^6 m^3 (CB&I 2014), which is gradually filling up with consolidating debris (LADNR & CB&I 2013). 3D seismic surveys conducted during ~January–March 2013 identified probable natural gas sources at depths ~0.44 km (considered to be more likely) and ~0.61 km adjacent to or impinging on the DRZ and the salt dome (CB&I 2013b; LADNR & CB&I 2013), which are generally within the probable source depth range of most of the seismic events. In terms of horizontal XY position, the gas source at ~0.44 km depth and our probable source volume overlap to some extent (LADNR & CB&I 2013). Figs 4.24 and 4.25 shows location of possible natural gas sources.

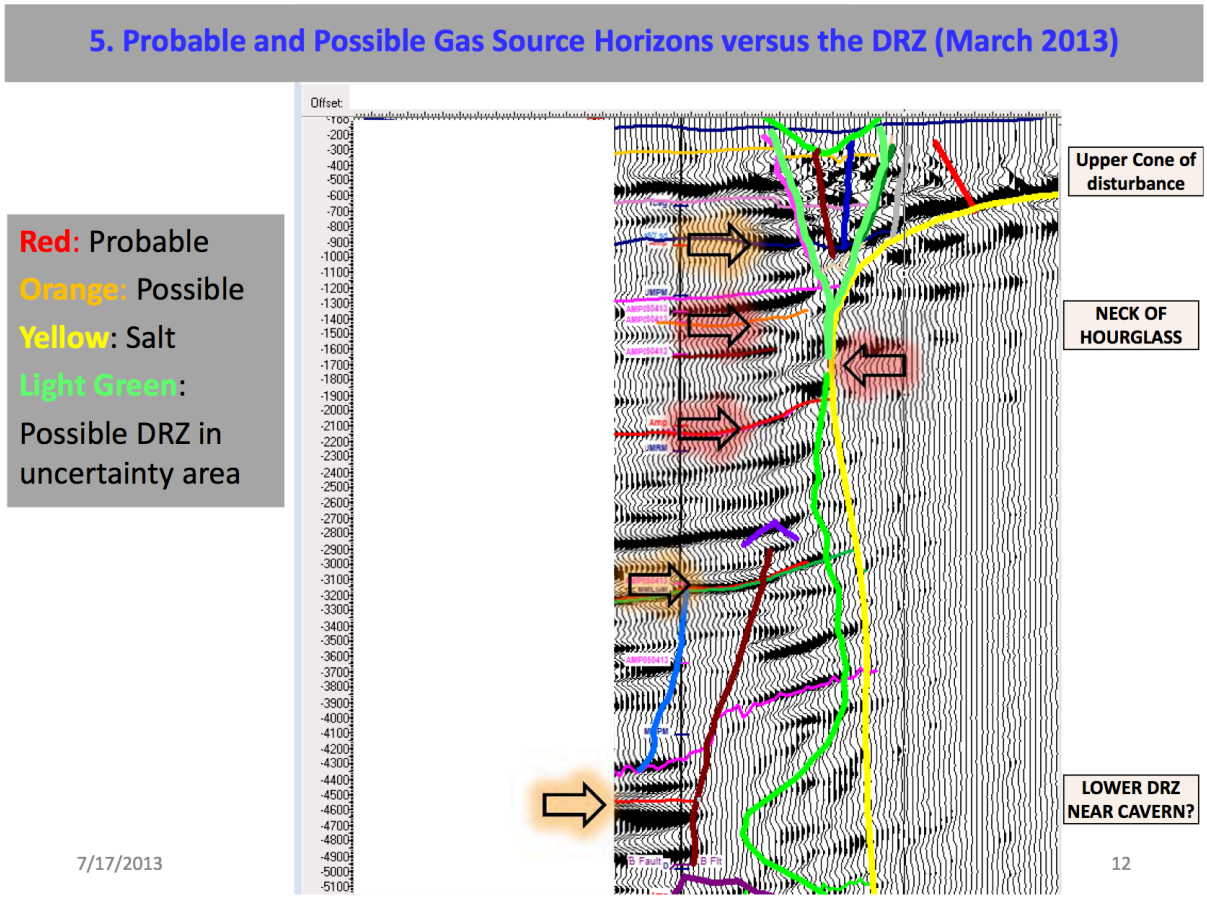

Figure 4.24: Figure marks the depths of probable natural gas sources at the western edge of NSD with arrows (reproduced from CB&I 2013b).

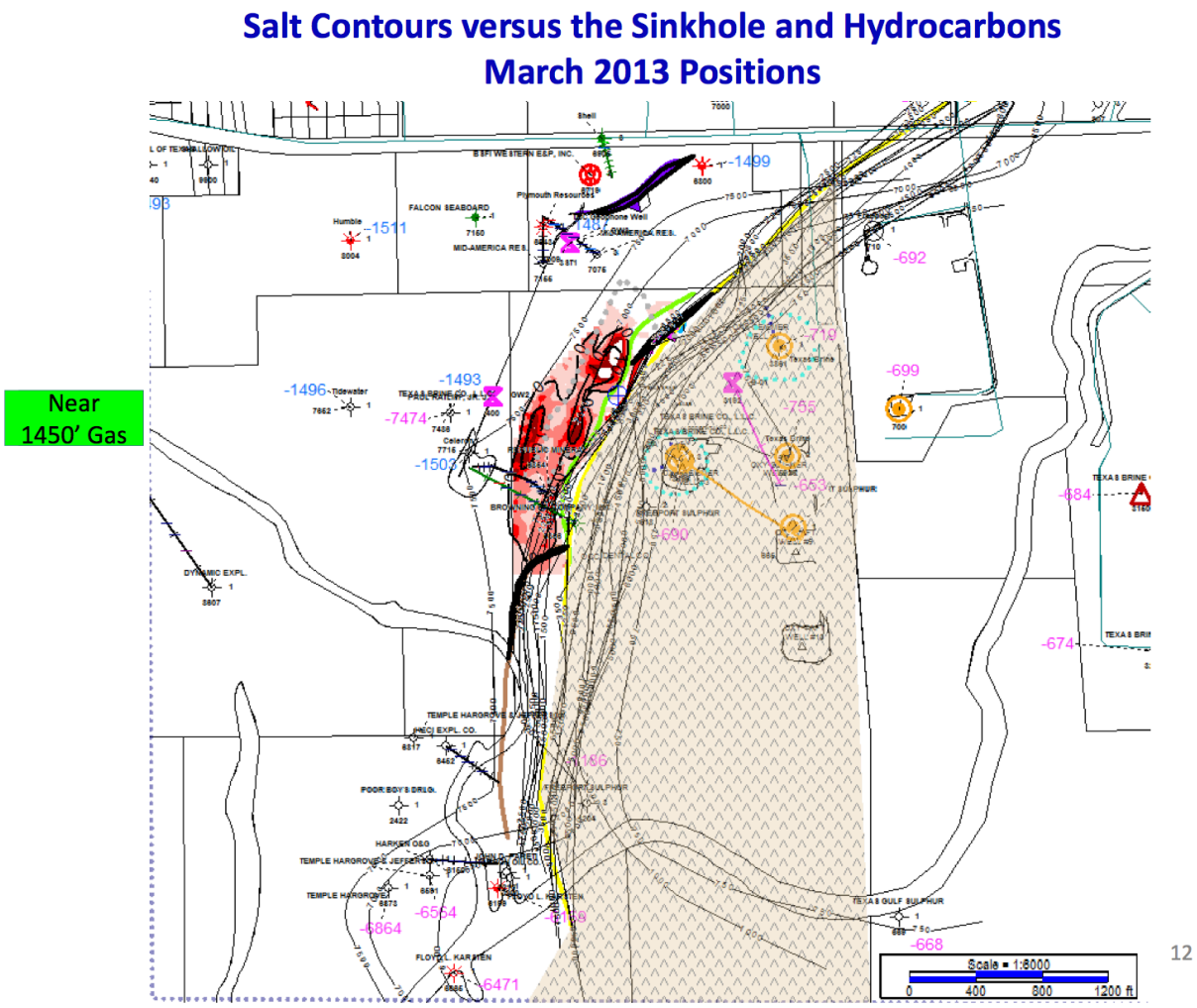

Figure 4.25: Figure indicates the horizontal extent of the natural gas source (marked by red colors) at the edge of the salt dome at ~440 m depth (reproduced from LADNR, OOC & CB&I 2013). The caverns are marked with yellow circles (OG3 is the westernmost cavern, immediately to the east of the gas-rich zone).

The emergent first-arrivals, complex waveforms and relatively long-period nature (dominant frequencies $\lesssim$ 2 Hz) of seismic events prior to appearance of the sinkhole at NSD (see figs. 3-4 in ND14, figs 2.3-2.4 in **chapter 2** for examples of waveforms) are similar to the Long-Period (LP) events (dominant frequencies ~0.5-5 Hz) observed in volcanic environments (Chouet & Matoza 2013). Seismic events at volcanoes are attributed to a diverse range of source mechanisms primarily involving fluids such as pressure-controlled inflow-and-outflow of steam or gases released by boiling of groundwater or exsolution of volatiles (Nakano *et al.* 2003; Maeda & Takeo 2011), transit of gas slugs through geometric discontinuities, various degassing and eruption phenomena, and ascent-expansion-burst cycles of gas slugs, etc. (see Chouet & Matoza 2013 and references therein). In some cases, LP events have been temporally correlated with visual observations of explosive gas emissions through cracks at the surface (e.g. Gil Cruz & Chouet 1997). The dominant volume-increase MT solutions, steady centroid locations, steady moment-release rates and a characteristic inter-event time

between dominant events, all point to a pressurization mechanism driving the seismicity. The rapid expansion of pressurized natural gas in a crack in the source region is a possible source mechanism. The triggering mechanism could be decompression caused by opening of a seal or a valve due to fluid pressure exceeding some threshold level. Previously, coseismic volumetric moment increase on the time scales of ~3-10 s has been attributed to pressure increase associated with steam/gas accumulation in cracks (Ohminato 2006; Maeda & Takeo 2011). It remains to be demonstrated if rapid expansion or injection of gases in a crack can lead to seismic moment release on time scales of $\lesssim$ 1s as observed in the seismic sequence at NSD. The variations in the temporal behavior of seismicity, i.e. isolated events and tremor-like episodes, can possibly be explained by the presence of a secondary intermediate reservoir feeding the crack. Slow and steady supply of natural gas to the crack might result in discrete seismic events whereas sudden release of all pressurized gas stored at the intermediate reservoir could cause rapid cascading tremor-like occurrence of seismic events at the same crack. Loss of enough pressurized fluids in the intermediate reservoir can possibly explain the seismic quiescence following tremor-like episodes with greater losses reflected in longer durations or larger amplitudes of ground motions resulting in longer quiet periods before pressure in the intermediate reservoir recovers to preexisting levels. Reduction in seismicity rates at Mount St. Helens (MSH) volcano following phreatic explosions has been similarly attributed to loss of pressurization (Moran *et al.* 2008). The seismic sequence at NSD has many remarkable similarities and also significant differences with sequences of highly repetitive LP events prior to the eruption of MSH and Redoubt volcanoes (Chouet *et al.* 1994; Moran *et al.* 2008). Seismicity at MSH was composed of 2 families of events separated by waveform cross-correlation: a dominant family of near-equal magnitude events occurring at regular intervals, T ~20-560 s (i.e., drumbeat seismicity; Moran *et al.* 2008) and a secondary family of generally smaller magnitude randomly occurring sub-events with a Poissonian inter-event time distribution (Matoza & Chouet, 2010). While the seismicity at NSD between 24-30 July 2012 shows similar behavior (Fig. 4.18c) with VR=70% threshold separating the populations of dominant opening crack-like events and relatively smaller events, we have not performed any broadband waveform similarity analysis to verify if the events belong to the same family or not, which will be a subject of future study. Another major difference is that first motions of events at MSH and Redoubt volcanoes were negative unlike the events at NSD that show clearly positive first motions for many events (e.g., see fig. 15 in ND14, fig 2.17 in **chapter 2**) and yield significant isotropic volume-increase MT solutions. At NSD, we also find that the transition from the steady sequence of discrete events to tremor-like episodes is quite abrupt with no discernable changes in the seismicity rates or moment-release rates prior to the onset of tremor (Figs 4.14a, 4.18a). In contrast, an increase in LP event amplitudes was observed prior to phreatic explosions at MSH and has been attributed to system pressurization (Matoza & Chouet 2010). If the seismic events at NSD are indeed related to fluids, possible volcanic LP event source mechanisms that involve phase changes at high temperatures (Ohminato 2006) or result in coseismic pressure drops (e.g., coupling-decoupling of shocks with the walls of a nozzle at unsteady choking of supersonic flow, Morrissey & Chouet 1997) are unlikely to be the cause of the events related to the sinkhole at NSD.

4.8 Conclusions

As a summary, a timeline of the important events associated with the formation of the sinkhole at NSD is shown in Fig. 4.26.

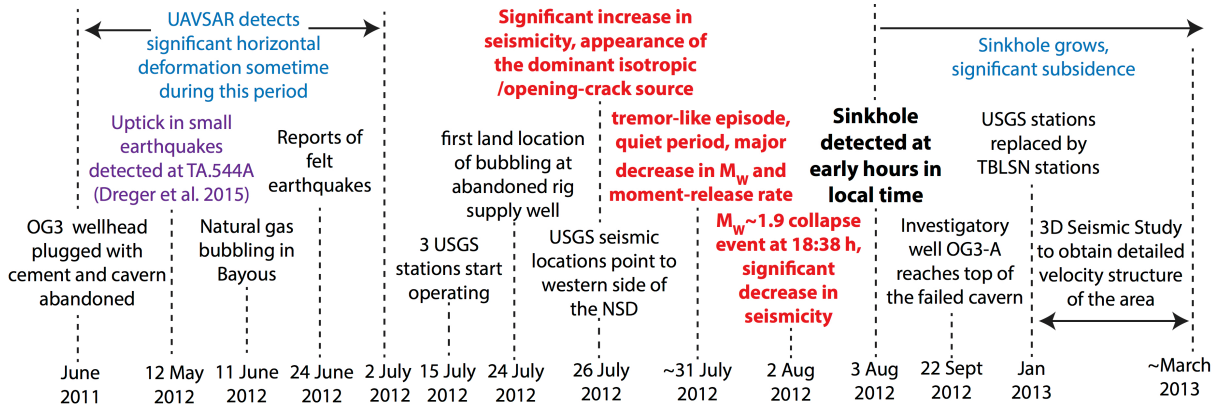

Figure 4.26: A timeline of important events associated with the formation of the sinkhole at NSD. Results from this study are shown in red. UAVSAR results are from Jones & Blum (2014). Sources of some of the other information are: CB&I (2013a), LADNR, OOC (2013), Texas Brine, Corp. (2013).

The application of a continuous scanning algorithm for the seismic moment tensor and the centroid location (Kawakatsu 1998), coupled with 3D velocity structure to compute Green's functions has enabled the clear imaging of seismicity associated with the collapse of OG3 and the formation of the sinkhole at NSD, Bayou Corne, Louisiana. We find that 3DGFs generally result in better fit to the data than 1DGFs, particularly for the smaller amplitude components, and result in better resolution of event locations and event source type. Location uncertainties and their effects on scalar moment estimates and mechanism source type were analyzed using an empirical approach, modified after Almendros & Chouet (2003).

As discussed previously, there are many nuances to the NSD seismicity. A clear increase in the number of events detected at the TA station 544A on 12 May 2012 indicates a significant growth in the process driving the seismicity at that time (Dreger *et al.* 2015). Our analysis of the local broadband seismic data shows that the seismicity and the driving process significantly accelerated from July 25 onwards. The dominant seismicity through 31 July 2012 is observed to localize, exhibit quasi-periodicity and contain large volume-increase components in the MT solutions, which suggest a pressurization driven crack-valve source mechanism operating on the flank of the salt dome. The volume-increase mechanisms could possibly be caused by rapid ex-solution and expansion of natural gas triggered by an initial decompression due to the opening of the valve when the fluid pressure in the crack reaches a threshold level. From July 31 to August 3 (when the sinkhole was discovered), the seismicity experiences a reduction in magnitude and takes on a possibly less localized character suggestive of a broadening area of damage on the flank of the salt dome.

The utilized method enabled the analysis of more than 1,500 small-magnitude ($M_W \lesssim 2$) seismic events. While our analysis was carried out offline, this approach with accurate 3D velocity models can be similarly applied to streaming data (e.g. Kawakatsu 1998; Tsuruoka *et al.* 2009; Guilhem & Dreger 2011) in real-time for the monitoring of microseismicity in volcanic and geothermal environments or microseismicity associated with energy production and mining operations. Such continuous monitoring could benefit operational objectives as well as provide a means for assessing ongoing hazard in such operations.

4.9 Data and Software

We are thankful to Julie Shemeta (MEQ Geo Inc.) and Mark Leidig (Weston Geophysical) for providing the 3D velocity model. The data used in this study were recorded by a U.S. Geological Survey temporary network (network code: GS), the Texas Brine Corporation Louisiana Seismic Network (YC) and the Earthscope Transportable Array (TA). The data were downloaded through the Incorporated Research Institutions in Seismology Data Management Center (http://www.iris.edu/dms/nodes/dmc/; last accessed June 2017). SW4 is hosted by the Computational Infrastructure for Geodynamics (CIG) which is supported by the NSF award NSF-0949446. Seismic Analysis Code (Goldstein *et al.* 2003) was used for basic analysis of seismograms. Some of the maps were prepared using Google Earth and Generic Mapping Tools (Wessel and Smith, 1998).

4.10 Acknowledgements

This study was funded by National Science Foundation (NSF) award 1447006. Julie Shemeta (MEQ Geo Inc.) is thanked for her help and discussions on this seismic sequence and on NSD throughout the course of this study. We thank Joel Warneke (formerly at Texas Brine) for help on the 01 January 2015 event. We are grateful for permission to use the *Baribu* cluster at BSL for preliminary testing of SW4 and for the synthetic tests. The final runs of SW4 were conducted on the cluster *Comet* at the San Diego Supercomputing Center (SDSC). Our allocation on *Comet* was through the Extreme Science and Engineering Discovery Environment (XSEDE; Towns *et al.*, 2014), which is supported by NSF grant ACI-1053575. We sincerely appreciate the efforts of personnel from U.S. Geological Survey, Center for Earthquake Research and Information (Univ. of Memphis) and others in rapidly deploying the temporary seismic network before the appearance of the sinkhole, which provided us the opportunity to study a fascinating dataset. A.N. greatly benefited from the CIG All Hands Meeting held at Univ. of California Davis in June 2016. We thank William Ellsworth (USGS) for preliminary velocity models, data, mapping resources, and helpful discussions leading to this study.

4.11 Appendix

Table 4.A.1: Average root-mean-square (RMS) displacement amplitudes of noise (cm) recorded by different components of stations of the temporary USGS network and the TBLSN. For USGS stations, the noise corresponds to period 15 July – 02 August 2012. For TBLSN stations, the noise corresponds to the period 26-31 December 2014.

	East-west	North-south	Vertical
USGS Stations			
LA01	1.97E-05	2.07E-05	1.29E-05
LA02	3.04E-05	3.23E-05	1.54E-05
LA03	1.40E-05	1.63E-05	8.69E-06
LA06	1.45E-05	1.49E-05	7.60E-06
LA08	1.97E-05	2.33E-05	7.99E-06
LA09	1.42E-05	1.45E-05	7.90E-06
TBLSN Stations			
LA10	2.85E-05	2.65E-05	1.81E-05
LA11	2.95E-05	3.20E-05	1.77E-05
LA12	6.49E-05	4.02E-05	2.64E-05
LA14	2.75E-05	3.36E-05	1.78E-05
LA17	3.24E-05	5.18E-05	2.78E-05
LA18	6.87E-05	4.61E-05	3.10E-05
LA19	2.70E-05	3.21E-05	1.64E-05

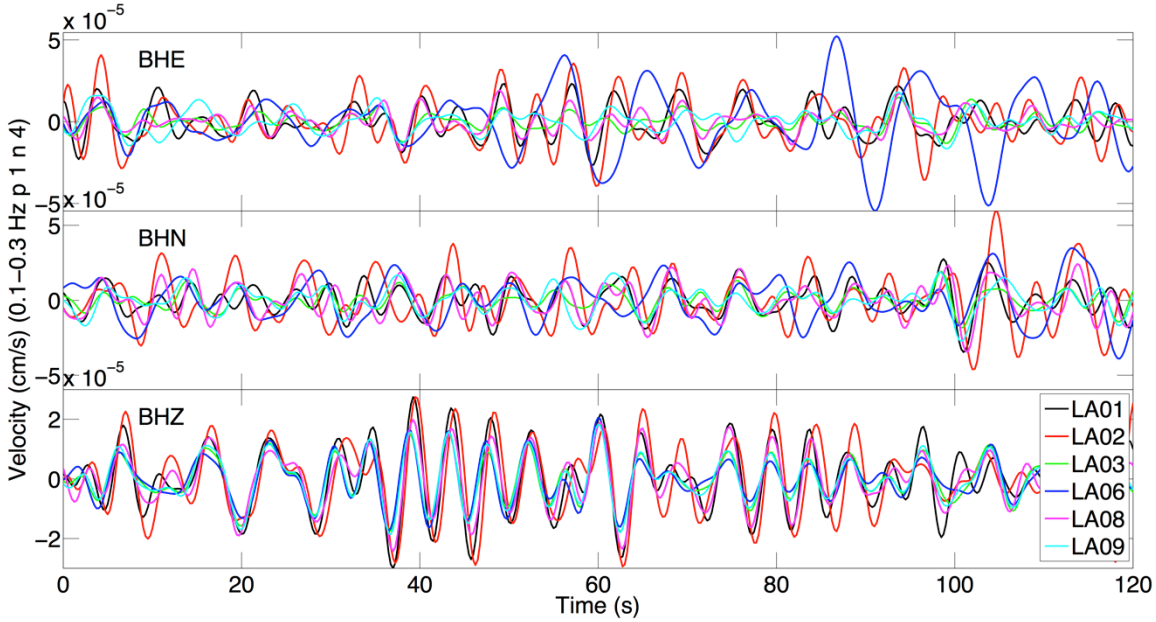

Figure 4.A.1: A randomly chosen segment of noise recorded by USGS stations (starting at 20:16:20 UTC, 01 August 2012). The ambient noise signals in the secondary microseism

passband (0.1-0.3 Hz) are highly correlated in the vertical component. The correlation is less in the horizontal components possibly because of ground-tilt noise.

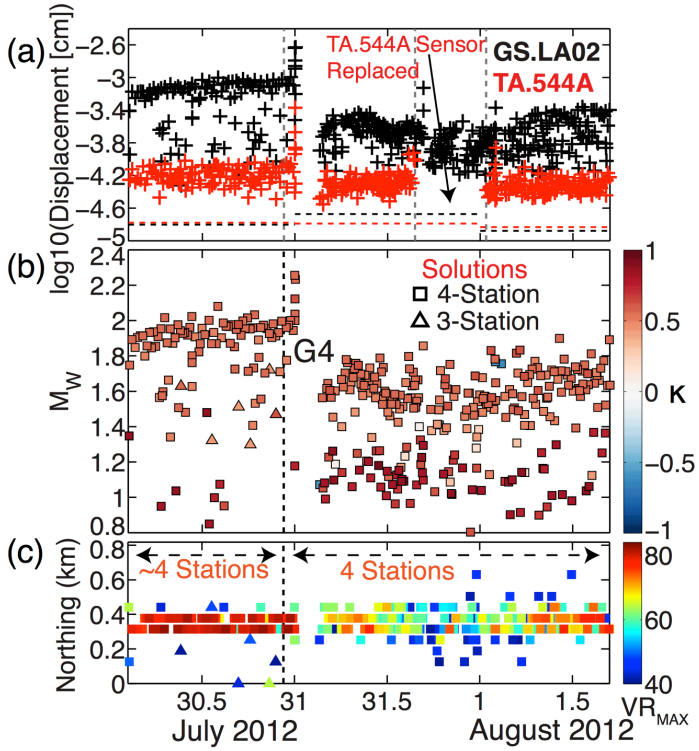

Figure 4.A.2: (a), (b) and (c) are same as Figs 4.11a,b,d except that the GRiD MT solutions ~22:33 hours, 30 July 2012 onwards were calculated with the 4 original stations from the earlier period.

Chapter 5

Empirical Green's Tensor retrieved from Ambient Noise Cross-Correlations at The Geysers Geothermal Field, Northern California

5.1 Chapter abstract

We retrieve empirical Green's Functions in the frequency range (~ 0.2-0.9 Hz) for interstation distances ranging from ~1 to ~30 km (~0.22 to ~6.5 times the wavelength) at The Geysers geothermal field, northern California, from cross-correlation of ambient seismic noise being recorded by a variety of sensors (broadband, short-period surface and borehole sensors, and one accelerometer). The applied methodology preserves the inter-component relative amplitudes of the 9-component Green's Tensor that allows us to directly compare noise-derived Green's Functions (NGFs) with normalized displacement waveforms of complete single-force synthetic Green's Functions (SGFs) computed with various 1D and 3D velocity models using the frequency-wavenumber integration method and a 3D finite-difference wave propagation method, respectively. These comparisons provide an effective means of evaluating the suitability of different velocity models to different regions of The Geysers, and assessing the quality of the sensors and the noise cross-correlations. In the T-Tangential, R-Radial, Z-Vertical reference frame, the TT, RR, RZ, ZR and ZZ components (first component: force direction, second component: response direction) of NGFs show clear surface-waves and even body-wave phases for many station pairs. They are also broadly consistent in phase and inter-component relative amplitudes with SGFs for the known local seismic velocity structure that was derived primarily from body wave travel-time tomography, even at interstation distances less than one wavelength. We also find anomalous large amplitudes in TR, TZ, RT and ZT components of NGFs at small interstation distances ($\lesssim$4 km) that can be attributed to ~10°-30° sensor misalignments at many stations inferred from analysis of longer period teleseismic waveforms. After correcting for sensor misalignments, significant residual amplitudes in these components for some longer interstation distance ($\gtrsim$ 8 km) paths are better reproduced by the 3D velocity model than by the 1D models incorporating known values and fast axis directions of crack-induced V_S anisotropy in the geothermal field. We also analyze the decay of Fourier spectral amplitudes of the TT component of NGFs at 0.72 Hz with distance in terms of geometrical spreading and attenuation. While there is considerable scatter in the NGF amplitudes, we find the average decay to be consistent with the decay expected from SGF amplitudes and with the decay of tangential component local-earthquake ground-motion amplitudes with distance at the same frequency.

5.2 Introduction

The Geysers in the Mayacamas Mountains of Northern California (NC), are the largest complex of geothermal power plants in the world today. Spread over an area of ~115 km^2, it currently produces ~835 MW of electricity (http://www.energy.ca.gov/tour/geysers/, last accessed August 2016). It is a vapor-dominated geothermal reservoir (Allis & Shook 1999), in which approximately 20 million gallons of reclaimed wastewater are injected on a daily basis (http://www.geysers.com/water.aspx, last accessed August 2016) from neighboring communities (Lake County, since 1998; City of Santa Rosa, since 2004). The water is injected to tap the heat in the volcanic reservoir rocks that are at ~240°C to ~300°C (Truesdell *et al.* 1991; Lowenstern & Janik 2003; Majer & Peterson 2007). While the injection of wastewater has successfully replenished the resource and the steam production that was in severe decline during the late 1980s, it has also been linked to elevated rates of microseismicity ($M_W \leq 3$) in the reservoir when compared to regional rates (Ludwin *et al.* 1982).

Many studies have demonstrated strong temporal correlation of microseismicity with both steam production and water injection at The Geysers, on both localized and field-wide scales (Oppenheimer 1986; Stark 1991; Majer & Peterson 2007; Trugman *et al.* 2016; Johnson *et al.* 2016). Detailed analysis of microseismicity has also revealed significant temporal variations in earthquake hypocenter distributions, in *b*-value and in the number of large magnitude ($M_W > 4$) earthquakes (Trugman *et al.* 2016). Investigations of focal mechanisms and moment tensors of these earthquakes using body-wave polarities, amplitude ratios, and low frequency displacement waveforms have shed some light on various aspects of their source mechanisms (Oppenheimer 1986; Ross *et al.* 1999; Guilhem *et al.* 2014; Boyd *et al.* 2015). However, imperfect knowledge of subsurface seismic velocity structure and assumption of 1D velocity models are believed to introduce considerable uncertainties in synthetic ray paths (Oppenheimer 1986) and in synthetic Green's functions required for source inversion. 3D P and S-wave travel-time tomography studies have revealed considerable heterogeneities in the subsurface (Julian *et al.* 1996; Ross *et al.* 1999; Gritto *et al.* 2013a) that must be taken into account in the inversion of polarities and seismic waveforms for recovery of accurate source mechanisms. In addition to the temporal changes in microseismicity, temporal changes in bulk medium properties of the reservoir such as fluid pressure and V_P/V_S ratio have also been observed from leveling and GPS studies, time-lapse body-wave travel time tomography, etc. (Foulger *et al.* 1997; Mossop & Segall 1999; Gritto *et al.* 2013b).

The response of a thermal reservoir to water injection or production, generally indicated by (1) the spatio-temporal behavior and mechanisms of seismicity, and/or (2) changes in seismic properties of the subsurface, is of great interest to further our understanding of induced seismicity and geothermal systems. This knowledge can help to better characterize and manage the seismic hazard by optimizing fluid injection into the subsurface for energy or storage purposes. In this study, we establish a framework for ambient seismic noise cross-correlation at The Geysers, which will aid in improving our understanding of the seismic velocity structure. The cross-correlations of ambient seismic noise obtained at pairs of seismic sensors have been shown to converge over a period of time to the empirical Green's Functions (GFs) or the seismic medium's response at one receiver to a unit force applied at the other

receiver (Shapiro & Campillo 2004; Shapiro *et al.* 2005; Bensen *et al.* 2007). In numerous studies, the body and surface waves in the noise-derived Green's Functions (NGFs) have been used for tomography at various scales (e.g. Shapiro *et al.* 2005; Lin *et al.* 2008, 2014; Nakata *et al.* 2015). Additionally, the coda of NGFs can be used for spatio-temporal monitoring of small subsurface seismic velocity changes (e.g. Sens-Schönfelder & Wegler 2006; Brenguier *et al.* 2014; Taira *et al.* 2015) that have previously been observed at The Geysers with body wave tomography. However, the non-uniformity in ambient noise source distribution results in systematic differences between recovered NGFs and the exact GFs in the real Earth (Tsai 2009). This can lead to errors in the estimates of subsurface seismic properties inferred from NGFs and limits their utility and reliability.

In this study, we retrieve NGFs, represented by interstation coherency (Prieto *et al.* 2011), in the frequency range of ~ 0.2-0.9 Hz for interstation distances from ~1 to ~30 km at the Geysers. We use seismic data that are continuously recorded by a wide variety of sensors in and around the geothermal reservoir. The minimum V_S is ~2 km/s and the interstation distances range from ~0.22 λ (near-field) to ~6.5 λ (far-field) assuming a phase velocity ~2.3 km/s at a frequency of ~0.5 Hz, where λ is the frequency-dependent surface-wave wavelength and distances $\gtrsim 1\lambda$–2λ are assumed to be far-field. For pairs of three-component sensors (T: Tangential, R: Radial, Z: Vertical), we retrieve nine components of NGFs (TT, TR, etc. where the first component is direction of the applied force and the 2nd component is the displacement direction). We directly compare NGF waveforms to normalized single force displacement Synthetic Green's Functions (SGF), computed using various 1D velocity models utilized for various monitoring applications at The Geysers.

We evaluate the similarity of NGF and SGF waveforms in terms of waveform fits, phase and relative inter-component amplitudes. NGFs with little or no coherent energy in the ballistic wave arrival time window or NGFs that bear little or no resemblance to SGFs expected for a wide variety of reasonable and expected velocity models are interpreted to be contaminated with errors possibly due to poor sensor coupling, or non-uniformity of ambient noise source distribution. After discarding these erroneous NGFs, we use the remaining NGFs to evaluate the applicability of various 1D velocity models to different sub-regions of The Geysers as NGFs contain information about real Earth 3D wave propagation (Ma *et al.* 2008). We examine if NGFs for station pairs in particular sub-region are systematically better fit by SGFs of a particular velocity model compared to SGFs of other velocity models. We interpret the phase differences between NGFs and SGFs in terms of the deficiencies in the velocity models. While some phase errors in the NGFs are expected due to the non-uniformity of ambient noise source distribution, our interstation paths are well distributed in azimuth, which allows us to draw inferences from spatially coherent phase differences pervasive over multiple azimuths.

We show that waveforms, phases and relative inter-component amplitudes of the primary non-zero components of retrieved NGFs (i.e., TT, RR, RZ, ZR, ZZ) are similar to those of SGFs, even at distances $< \lambda$. Our inferences on the features of subsurface seismic velocities at The Geysers from the NGF-SGF comparisons agree with the inferences drawn in many previous body-wave travel-time studies. We also examine if the NGFs compare better to

SGFs computed using a 3D velocity model of the geothermal field than with SGFs from the 1D velocity models.

Our study additionally includes: (1) an analysis of long period teleseismic waveforms to verify sensor orientations, (2) application of the Optimal Rotation Algorithm (Roux 2009) on the NGFs to detect any dominant noise source illumination direction, and (3) comparison with SGFs computed using the 1D models incorporating known values and fast axis directions of crack-induced V_S anisotropy in the geothermal field. We find significant non-zero amplitudes in TR, TZ, RT and ZT components of NGFs for many stations pairs that can be attributed to a combination of the effects of sensor misalignments and 3D velocity structure based on the above-mentioned evaluations.

We also compare the decay of Fourier spectral amplitudes of the TT component of NGFs at 0.72 Hz as a function of distance with the decay of synthetic spectral amplitudes for velocity models incorporating strong, weak and known values of anelastic attenuation. We find the average decay of NGF amplitudes to be consistent with the decay of SGF amplitudes and with the decay of tangential component local-earthquake ground-motion amplitudes with distance.

5.3 Background and motivation

Noise cross-correlation tomography studies typically involve phase velocity measurements on the fundamental-mode Rayleigh waves obtained from cross-correlation of ambient noise recorded on vertical components of broadband stations at far-field interstation distances (e.g. Yao *et al.* 2006; Lin *et al.* 2008, 2014). The theoretical proof for retrieval of ballistic surface waves from cross-correlation of diffused waves at two receivers was first provided by Snieder (2004) under a stationary phase approximation valid at far-field distances (Yokoi & Margaryan 2008; Zhan & Ni 2010). Subsequently, using source-receiver reciprocity, Wapenaar & Fokkema (2006) derived an expression for the velocity GF response at a receiver to a single force applied at another receiver in an inhomogeneous anisotropic loss-less medium from cross-correlation of responses of sources distributed over an enclosing surface. The variations of their basic formulation involve variations in the nature of the boundary and the outside medium, types of sources, types of responses cross-correlated or retrieved, distance of the enclosing source surface from the receivers and whether the cross-correlation operates on the responses of individual sources or the net ground motion field at the receivers. In practice, the application of most temporal and spectral normalization methods removes the absolute amplitude information in component-pair NGFs leading to their "empirical" nature (Bensen *et al.* 2007). However, significant relative amplitude information in addition to the phase information can still be retrieved from NGFs, although many aspects are still under considerable debate as discussed in section **5.9 Amplitude decay**.

Cross-correlation of spectrally whitened noise is equivalent to computing interstation coherency (Bensen *et al.* 2007; Prieto *et al.* 2011). For components i, j of velocity v recorded

at stations A, B at positions x_A, x_B respectively, coherency $\gamma_{ij}(x_A, x_B, \omega)$ as a function of frequency ω is defined as-

$$-G_{ij}(x_A, x_B, \omega) \approx \gamma_{ij}(x_A, x_B, \omega) = \langle \frac{v_i^*(x_A,\omega)\, v_j(x_B,\omega)}{\{|v_i(x_A,\omega)|\}\{|v_j(x_B,\omega)|\}} \rangle \quad (5.1)$$

$G_{ij}(x_A, x_B, \omega)$ is the displacement NGF with single force, displacement directions i, j at stations A, B that are acting as source and receiver, respectively; < > implies stacking results for data recorded over multiple time windows known as ensemble averaging, {} implies spectral amplitude smoothing (3-point ~ 0.02 Hz moving window average in our study). The directions i, j can be radial (R; positive outwards), transverse (T; positive clockwise 90° from radial) or vertical (Z; up positive). In equation 5.1, in the following and throughout this article, we define single force Green's Function $G_{ij}(x_A, x_B, \omega)$ as the displacement response to an input ***step*** force and directly relate it to interstation coherency obtained from ambient noise cross-correlation. This is different than the traditional definition of a Green's Function, in which it is defined as the displacement response to an input ***impulsive*** force (Aki & Richards 2002). For the traditional definition (i.e. impulsive force as an input), the Green's function can be related to the time derivative of coherency as in many other studies, i.e. Lin *et al.* 2008, Ma *et al.* 2008, etc.

For a particular component pair, γ has been shown to preserve geometrical spreading and anelastic attenuation information as a function of interstation distance and structure (Prieto *et al.* 2011; Lawrence *et al.* 2013). Additionally, if the same normalization factors are used for all components of a station, relative inter-component amplitudes for a particular station pair can be preserved enabling extraction of attributes such as the Rayleigh wave ellipticity from the amplitude ratio of R and Z components of NGFs (Lin *et al.* 2014). The amplitude spectrum of the noise at the source station can also be used to normalize the noise spectra at both stations, which yields the impulse response function (Prieto *et al.* 2011; Denolle *et al.* 2013), which is equivalent to deconvolution interferometry (Nakata *et al.* 2011). The impulse response function has been used to extract site response of basins and 3D structures at long periods, ~ 4-10 s (Prieto & Beroza 2008; Denolle *et al.* 2014). The retrieved phase information is the same for different spectral normalization methods (Prieto *et al.* 2011).

While interstation distances $\gtrsim \lambda$ are considered to be "far-field" for surface waves (Lin *et al.* 2013), phase velocity measurements from NGFs are usually restricted to interstation distances $\gtrsim 3\lambda$ in order to avoid bias at shorter distances caused by inhomogeneous noise source distributions (Lin *et al.* 2008, 2014). Various numerical studies have shown that phase velocity measurements derived from NGFs at interstation distances $\lesssim 3\lambda - 5\lambda$ can have significant error, even for seismic noise sources that are azimuthally widely distributed (Kimman & Trampert 2010; Zhan & Ni 2010). However, reliable phase velocities can be extracted from NGFs at distances down to ~1λ using sophisticated methods that are able to reduce biases caused by inhomogeneously distributed noise sources. These methods include measurement of phase velocities by phase-front tracking on dense arrays (Lin *et al.* 2013) and azimuthal averaging of multiple coherency measurements as in spatial autocorrelation (Tsai & Moschetti 2010).

The studies on relative amplitude extraction from NGFs, mentioned earlier, have also utilized NGFs at primarily far-field distances assuming Rayleigh waves on RZ, RR, ZR and ZZ components and Love waves on TT components, which are the non-zero components of the GF tensor for 1D isotropic media. The TR, TZ, RT and ZT components of the GF tensor can be non-zero in the presence significant 3D structure or anisotropy. In NGFs, these components can also be non-zero due to inhomogeneous noise source distribution (e.g., Parkfield, California [Durand *et al.* 2011]) and have not been analyzed in detail in crustal structure studies (e.g., some paths in Southern California [Denolle *et al.* 2013]). Sensor misalignments or incorrect knowledge of sensor gains and orientations may lead to incorrectly oriented NGFs and anomalous amplitudes in the TR, TZ, RT and ZT components as well. To the best of our knowledge, the retrieval of relative amplitude information in NGFs at distances $< \lambda$ has not yet been explored.

5.4 Methodology

5.4.1 Data

Fig. 5.1 shows a map of The Geysers, the seismic stations employed in this study and the approximate outline of the steam field of the reservoir area (Gritto *et al.* 2013a). Most of our data are recorded by the Lawrence Berkeley National Laboratory (LBNL) network at The Geysers consisting of ~30 short-period (4.5 Hz) three-component geophones (OYO-GS11D), one Nanometrics Titan accelerometer (station DRH) and three short-period (8.0 Hz) 3-component borehole sensors (OYO-GS11D8) at depths of ~35-150 m (stations DEB, JKB and SRB). We include data recorded by short-period (1.0 Hz) vertical component sensors (L4) and by one broadband STS2 sensor (station GDXB) at stations operated by the United States Geological Survey (USGS) in and around the geothermal field. Data recorded by the two closest broadband stations (an STS1 at HOPS and an STS2 at MNRC) of the Berkeley Digital Seismic Network (BDSN) are also included to provide a reference for quality control of data recorded at all other stations in our study.

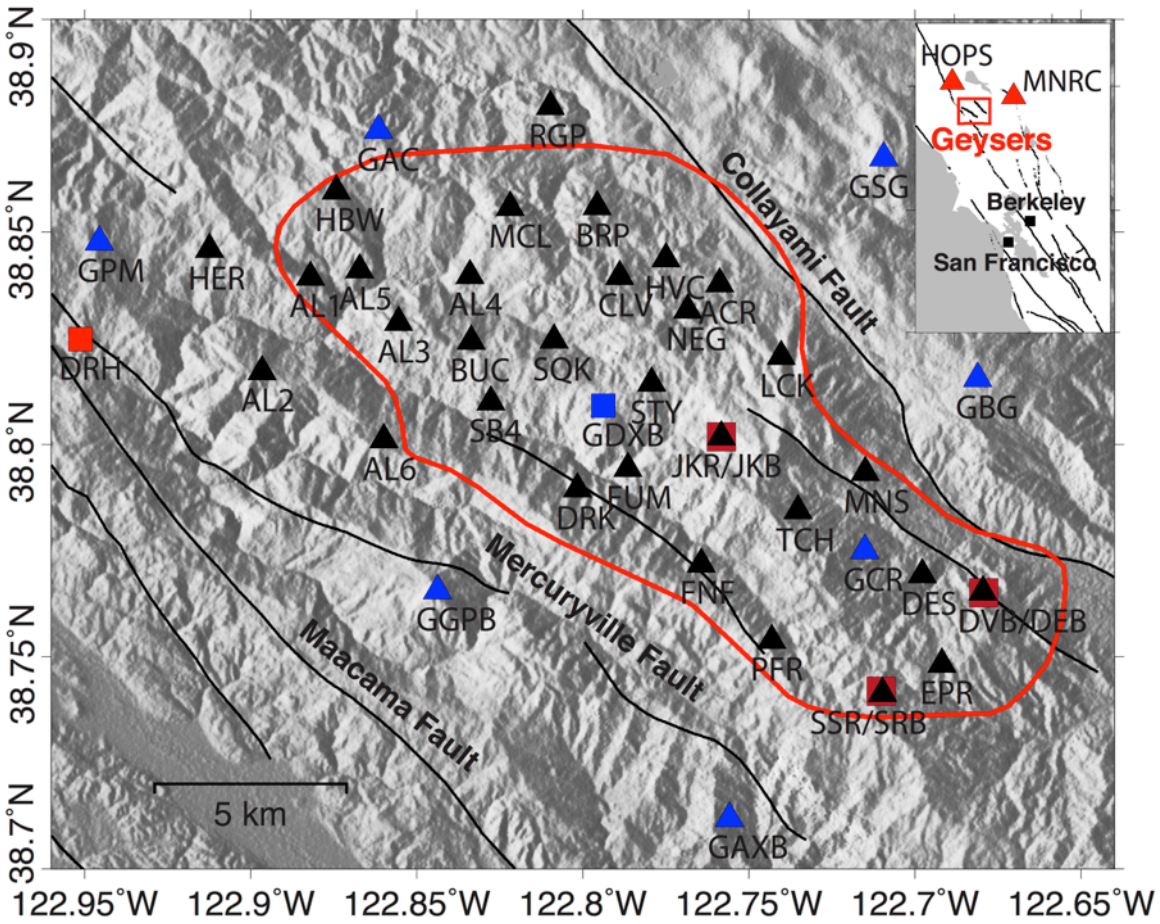

Figure 5.1: Map shows the outline of the reservoir area (red polygon), faults (solid black lines), and seismic stations plotted on the gradient of topography at The Geysers. Black triangles: LBNL 4.5 Hz geophones, brown squares: LBNL 8.0 Hz borehole geophones, red square: LBNL accelerometer, blue triangles: USGS 1.0 Hz vertical component sensors, and blue square: USGS broadband sensor. Inset shows the location of The Geysers (red square) and BDSN stations (red triangles) with respect to the San Francisco Bay area in northern California, USA.

5.4.2 Cross-correlation analysis

Our data pre-processing and cross-correlation workflows are derived from Bensen *et al.* (2007), Seats *et al.* (2012) and Lin *et al.* (2014). We download hourly time series from the Northern California Earthquake Data Center (NCEDC), discarding any data with gaps in time. The data are demeaned, detrended, tapered, decimated to 20 Hz using an antialiasing filter, and corrected for the corresponding instrument phase response to velocity. The waveforms are subsequently bandpass-filtered between 0.08 Hz and 4 Hz using a zero-phase 2-pole Butterworth filter. While large magnitude earthquakes at teleseismic distances are poorly recorded by the short-period sensors at The Geysers, high-rate microseismicity in the geothermal area, characterized by short duration (~ 3-5 s), high frequency ($\gtrsim$ 1.0 Hz) signals, is a major source of non-stationary signals contaminating the ambient noise wavefield. We

suppress the local earthquake signals present in the seismic records by applying a non-iterative water-level normalization (Bensen *et al.* 2007) with a threshold of five times the daily mean of absolute values. To each sample exceeding this threshold, we apply an inverse weight equal to 25 times the ratio of mean amplitude measured over a 5 s envelope around that sample. Following Seats *et al.* (2012), we select 75% overlapping, 150 s duration time windows for computing interstation coherency, applying amplitude response of an 8-pole Butterworth bandpass filter with corners at 0.2 Hz and 1.6 Hz as a band-limiting taper during spectral normalization (e.g., see fig. 7b in Bensen *et al.* 2007). Coherency has been shown to perform better at retrieving phase information than the impulse response function in the presence of highly variable and additive random noise (Nakata *et al.* 2011) and therefore, is expected to provide more accurate phase information at an industrial site such as The Geysers. We preserve the relative amplitudes between different components of the 3-component sensors by using the maximum of the temporal normalization weights of the three individual components and the mean of their spectral amplitudes for temporal and spectral normalization of all components, respectively (Lin *et al.* 2014). The cross-correlations for all windows in one day are stacked to form a daily average and the averages are stacked for all available days to form a final reference stack that we use as our estimate of NGF. Cross-correlations are done in an EW-NS-Z reference frame and are subsequently rotated to a T-R-Z reference frame relative to the source-receiver azimuths of the station pairs (Lin *et al.* 2014).

For quality control, we identify time periods when the cross-correlations of various stations with the broadband reference stations HOPS and MNRC return little or no coherent energy by cross-correlating daily stacks with reference stacks for the overall time period (correlation threshold $\lesssim 0.3$). These daily stacks are subsequently removed from the reference stacks after visual confirmation of all poor coherence time periods that lasted $\gtrsim 10$ days. Through this process, ~45% of all daily noise cross-correlations were removed. While the time period of our study is March 2012 - August 2015, the actual duration of usable data for different station pairs varies from ~25 days to the entire time period. The daily stacks are also corrected for large and obvious (> 0.05 s) clock or time stamp errors that were identified by cross-correlating daily stacks with the reference stack (e.g. Sens-Schönfelder 2008). Station pairs with little or no coherent energy in the ballistic wave arrival time window (6.0 km/s to 1.5 km/s) in the reference stacks are removed from further analysis. Most pairs involving the 4.5 Hz geophone stations BRP, EPR, JKR, RGP, SB4 and SQK were discarded during the quality control process indicating high sensor self-noise, poor coupling of the sensors to the ground, lack of coherent ambient noise at these sites, or other sensor/digitizer problems. We also observe strong narrow-band spikes in amplitude spectra of cross-correlations at specific frequencies, namely 1.00, 1.76, 1.80, 1.97, 2.28 and 2.57 Hz, similar to the ones observed at high frequencies in other studies (e.g. Wegler *et al.* 2009; Takagi *et al.* 2015). These peaks were also found in spectra of raw data and we speculate that they result from coherent data logger noise, with the peak at 1.00 Hz most likely resulting from GPS time calibration (Takagi *et al.* 2015). We manually reduce the amplitudes of noise spectra by a factor of $\sim 10^{-3}$ in narrow frequency bands of width ~0.02 to ~0.07 Hz around these frequencies during spectral whitening. Finally, we are left with NGFs of ~568 station pairs not including station HOPS or MNRC.

After quality control, we average the causal and anti-causal sides of the final stacked cross-correlations, extracting the symmetric component of NGFs in the T-R-Z reference frame. Fig. 5.2 shows ZZ and TT components of NGFs in the interstation distance range 0-25 km in which most of our station pairs are located. The waveforms are stacked in 0.5 km interstation distance bins. Rayleigh and Love waves can easily be identified in components ZZ and TT, respectively, with apparent velocities of ~2.5 km/s and ~2.8 km/s, respectively. ZZ components at distances of ~ 17 – 20 km also show faint but coherent body wave or higher-mode Rayleigh wave energy that is faster than the fundamental-mode Rayleigh waves but slower than direct P-waves, traveling at ~3.6 km/s (composition of waveforms further discussed in section **5.5.3 Contribution of body waves and surface waves**). We also estimate an empirical expression for distance-dependent approximate start time of coda waves following the passage of the surface waves by fitting a 4th degree polynomial to times at which envelopes of NGFs drop below a level of 0.2 times the peak absolute amplitude. This empirical coda-wave start time is used for selecting waveform segments that contain body-wave and surface-wave phases in order to evaluate waveform fits between NGFs and SGFs.

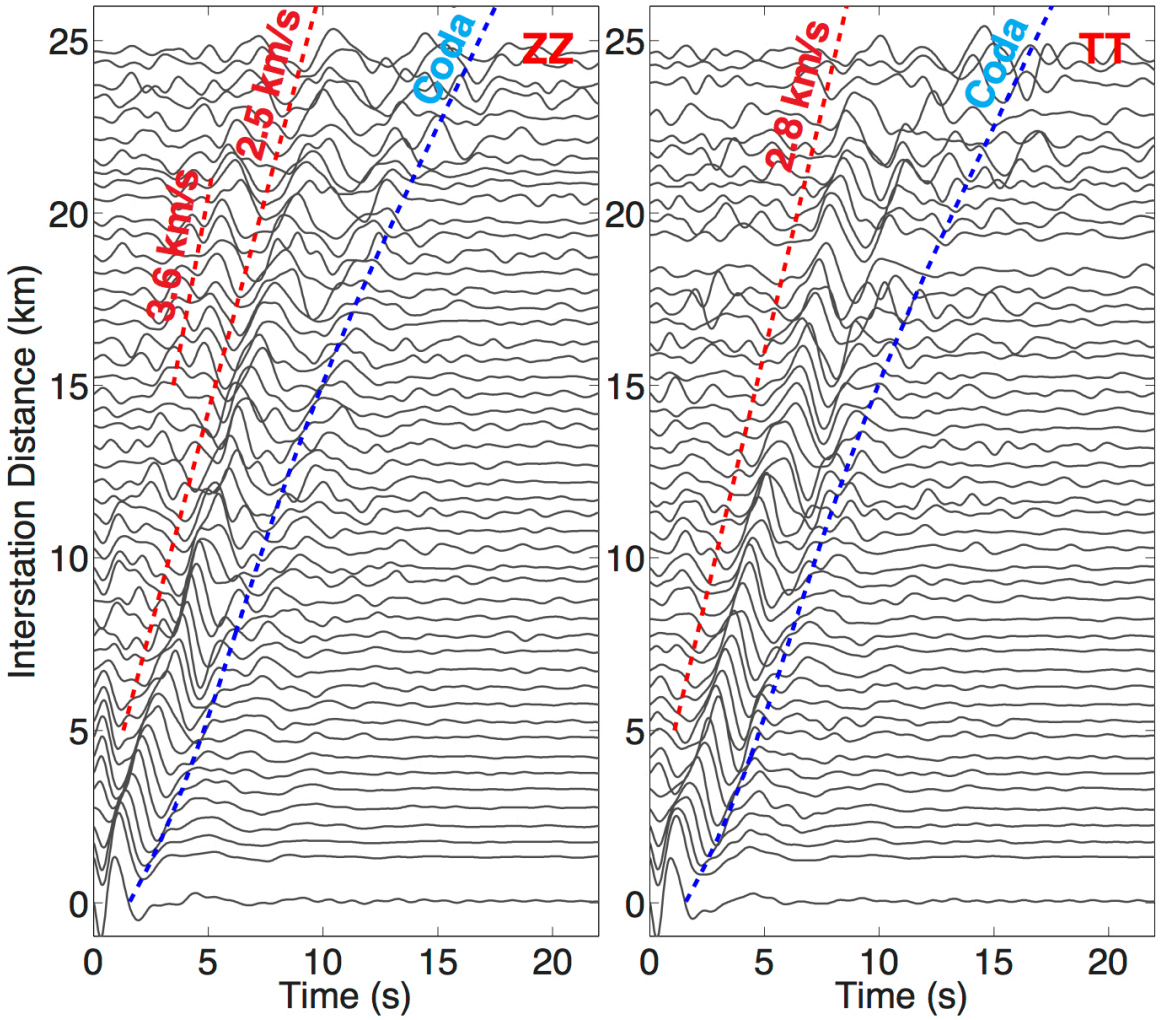

Figure 5.2: NGFs filtered between ~ 0.2-0.9 Hz and stacked in 0.5 km interstation distance bins. Dashed red curves are reference travel-time curves for various constant apparent

velocities (shifted to the left by 0.7 s for clarity). Dashed blue curve shows the empirically estimated approximate start time of coda waves after the passage of surface waves. The NGF waveforms are proportional to displacement response for an input step force.

5.4.3 Velocity models

Here we briefly describe the velocity structure of the reservoir area. Gritto *et al.* (2013a) conducted a tomographic campaign to jointly invert for the 3D P- and S-wave velocity structures and the hypocenter locations of microseismicity at The Geysers using body wave arrival times of ~32,000 earthquakes at the LBNL stations. The starting 3D velocity model based on 3D interfaces in the reservoir (interface of top steam entry and interface of felsite) coupled with P- and S-wave velocity estimates that were derived from a vertical seismic profiling (VSP) experiment in the center of the reservoir (O'Connell & Johnson 1991). The top of the steam interface is considered the top of the reservoir and separates mélange (a complex assemblage of Franciscan greywacke, greenstone and serpentinite) from the deeper metamorphosed reservoir rocks (Franciscan greywacke and metagraywacke) at depths of ~1-3 km. The top of the felsite interface demarks the transition from metamorphosed reservoir rock to the underlying granitic pluton at depths greater than ~3-5 km. On average, V_P, V_S values increase, respectively, from ~3.6 km/s and ~2 km/s at the surface, to ~5.9 km/s and ~3.3 km/s at depth of ~6 km, with typical values of ~4.8 km/s and ~2.8 km/s for reservoir rocks, and ~5.5 km/s and ~3.0 km/s for the underlying felsite (O'Connell & Johnson 1991). The reservoir area is bounded by NNW-SSE trending faults, namely the Mercuryville fault to the southwest and the Collayomi fault to the northeast. There is widespread lateral heterogeneity in and around the reservoir, with up to ~20% variations in V_P at shallow (less than ~2.5 km) depths (Julian *et al.* 1996; Ross *et al.* 1999). On average, the velocities in the northwestern section of The Geysers have been found to be lower by ~10% than in the central and southeastern section (Eberhart-Phillips 1986; Julian *et al.* 1996; Gritto *et al.* 2013a). The V_P/V_S ratio, believed to be relatively insensitive to lithology but quite sensitive to the saturation of rocks (Gritto & Jarpe 2014) and to the compressibility of pore fluids, shows a large negative anomaly (up to ~ –9%) at the center and southeast of the center of the reservoir (Julian *et al.* 1996; Foulger *et al.* 1997; Ross *et al.* 1999). This anomaly exists at depths up to ~2.5 km and is anti-correlated with a positive V_S anomaly (Gritto *et al.* 2013a).

We select four 1D velocity models (Fig. 5.3) at The Geysers to compute single force SGFs for comparison with the NGFs of all station pairs not including stations HOPS and MNRC. The models are, (1) REF, (2) BACK1, (3) VSP0, and (4) AVG1. Model REF is a slightly modified version of the 1D average of the 3D model of Julian *et al.* (1996) for the NW Geysers and was used by Guilhem *et al.* (2014) for modeling 0.5-2.5 Hz waveforms of M_W ~ 3.3-3.9 earthquakes at distances up to a few km. Model BACK1 is a 1D depth average of the 3D starting velocity model used in Gritto *et al.* (2013a), while model AVG1 is a 1D depth average of their final 3D velocity model within the reservoir area. VSP0 is the velocity profile shown in fig. 2 in Gritto *et al.* (2013a) and is derived from a VSP profile at the felsite peak in the SE Geysers (O'Connell & Johnson 1991). The depth-dependent density and anelastic attenuation quality factors (Q_P and Q_S) are borrowed from Guilhem *et al.* (2014). In our study, we ignore the surface topography at The Geysers and assume our reference datum to be ~

800 m above the mean sea level, which is the average elevation of stations that we are using. For all station pairs that include station HOPS or MNRC, we use the California Central Coast Ranges velocity model GIL7 (Stidham *et al.* 1999) and its modified version GIL7.1 (Fig. 5.3) to compute SGFs (modifications explained in section **5.8 NGFs with BDSN stations HOPS and MNRC**). Upper crustal Q_P and Q_S values in GIL7 and its modified versions are reduced to values comparable to those of REF.

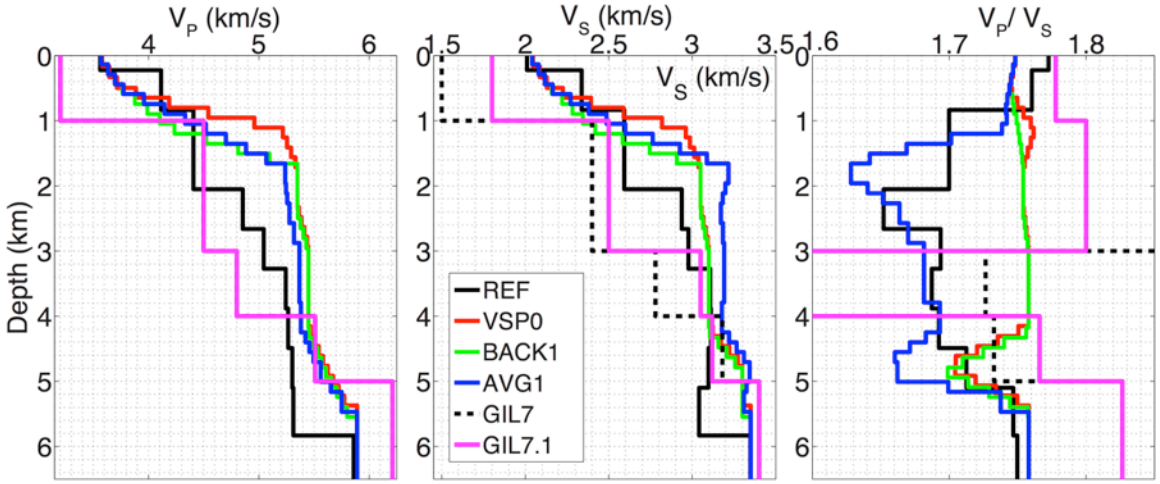

Figure 5.3: 1D velocity models used in our study.

Fig. 5.4 shows a few example depth slices of G3D1, a modified version of the 3D velocity model of Gritto *et al.* (2013a) used to compute SGFs accounting for the 3D structure in the reservoir in our study. G3D1 consists of a 3D velocity structure surrounded by a 1D background model (BACK1). The horizontal extent of the 3D structure is approximately restricted by the outline of the reservoir steam field at the surface (red polygon in Fig. 5.1) (except towards the northwest where the LBNL network extends beyond the outline; see stations HER, AL2 and DRH in Fig. 5.1), and decreases with increasing depth. The modifications to the model are explained as follows. For nodes with V_P/V_S ratio $< \sqrt{2}$, V_P and V_S values are increased and decreased respectively in small increments, until they satisfy the minimum V_P/V_S ratio criteria of $\sqrt{2}$ of our 3D wave propagation software. The velocities are tapered at the edges of the model so that they smoothly transition to model BACK1. The model is extended laterally assuming the values of BACK1, and extended in depth assuming a half-space with $V_P \sim 5.86$ km and $V_S \sim 3.35$ km at depths $\gtrsim 5.3$ km, which are comparable to the deepest velocities in BACK1 and velocities in model GIL7 at the same depths.

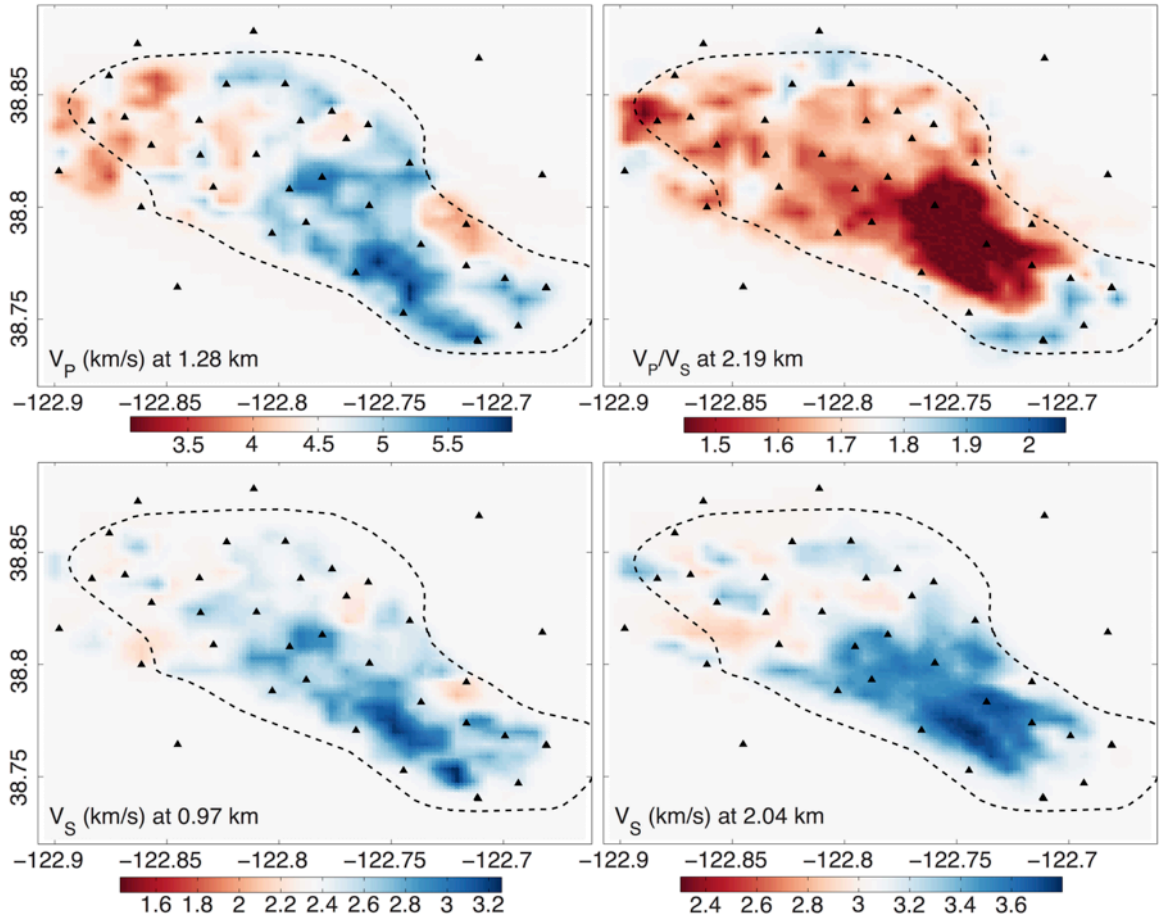

Figure 5.4: Depth slices of model G3D1 used to compute SGFs. Dashed line is the outline of the geothermal steam field and black triangles are locations of stations used in this study (same as in Fig. 5.5). Outside this domain, we extrapolate the velocity model to match the 1D model BACK1.

5.4.4 Synthetic Green's Functions

For all 1D models, single force SGFs were computed using the frequency-wavenumber integration (FKI) method based on Haskell (1964) and Wang & Herrmann (1980), as provided in Herrmann (2013a). The Herrmann (2013a) FKI code computes complete 3-component seismograms consisting of all the terms of the elastic wave equation solution (including the near- and intermediate-field terms) and all body-wave and surface-wave phases for isotropic 1D layered velocity models with anelastic attenuation. We use 10 m as source depth for all stations at the surface (the numerical integration method used requires a non-zero depth difference between the source and the receiver) and depths reported in NCEDC as source or receiver depths for borehole stations. For computation of all SGFs (both 1D and 3D) in this study, we use impulse or Dirac source-time functions for numerical stability. The ground motions thus obtained are displacement waveforms for an impulse input or effectively velocity waveforms for a step input. The velocity waveforms are subsequently integrated to displacement SGFs (for an input step force).

We use model G3D1 with the 3D seismic wave propagation code SW4 to compute SGF accounting for the 3D structure in the reservoir. SW4 is a 3D finite difference seismic wave propagation code that solves the elastic wave equation in displacement formulation with 4th order accuracy in space and time (Sjögreen & Petersson 2012; Petersson & Sjögreen 2014a,b). Absorbing supergrid boundary conditions are used at the far-field boundaries and anelastic attenuation is also allowed (Petersson & Sjögreen 2014b). Our grid spacing is 80 m, which allows ~27 grid points per shortest wavelength for the minimum V_S ~2.0 km/s in our model and the maximum frequency of our interest ~0.9 Hz. For the maximum V_P ~ 6.4 km/s in the model, the time step is set to ~1.18x10^{-2} s for numerical stability. Our model dimensions are ~36.6 km (NS) x ~41.2 km (EW) and ~14.0 km (Z), ~42 million grid points, with supergrid absorbing layer thickness of 75 grid points. Fig. 5.5 shows a snapshot of an example wavefield computed using SW4 in response to a single force applied at station DRH. The displacement time histories for this wavefield can be compared to NGFs with DRH as the "source" station. The effect of faster than background velocities in the central section of The Geysers is reflected in the bulge in the otherwise circular ~0.9 Hz wavefront along with reduced amplitudes. Note the absence of any significant reflections from the boundaries of the domain showing the effectiveness of the supergrid absorbing boundary conditions.

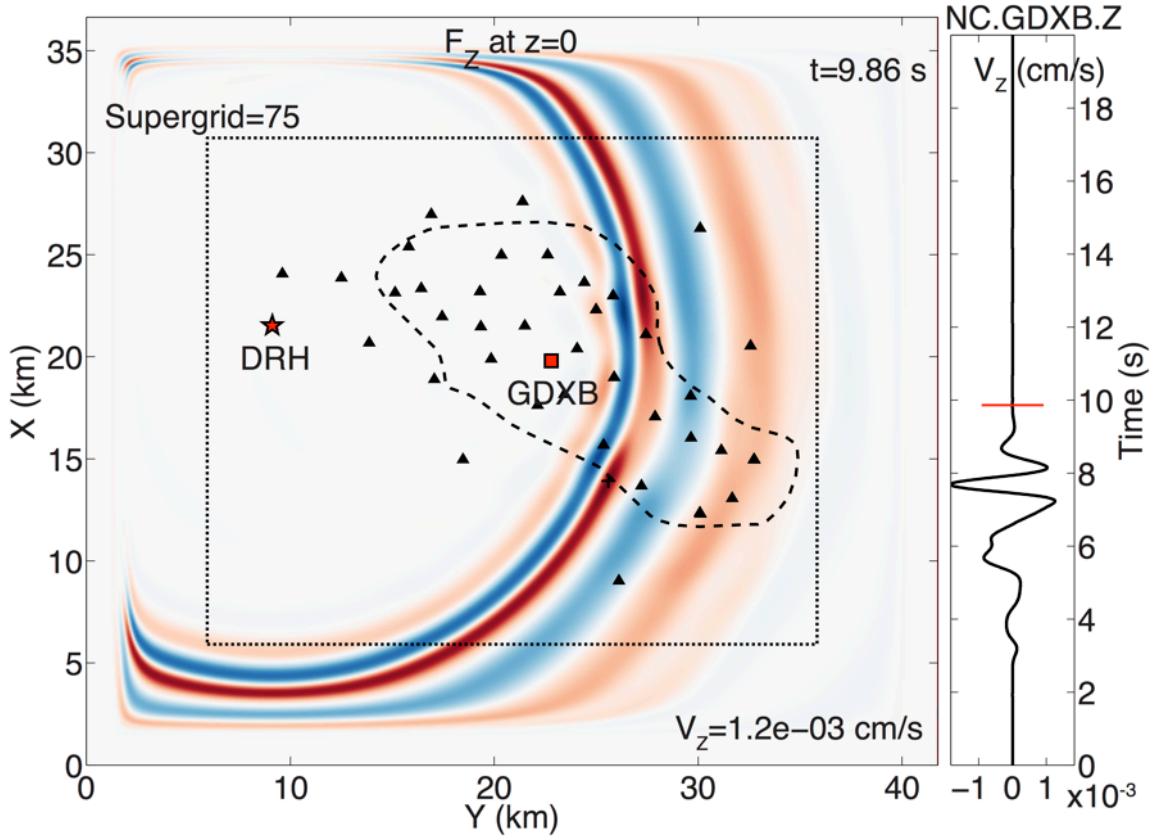

Figure 5.5: The left subplot shows snapshot of the vertical component velocity wavefield at the surface at elapsed time 9.86 s in response to a vertical force (1e+10 N) applied at location of station DRH (red star). The amplitudes of the wavefield are normalized by the instantaneous peak absolute amplitude (indicated at the bottom right corner) and plotted on a

red (-1) to blue (+1) color scale. The domain shown here corresponds to the computational domain used in SW4 and the dotted line marks the supergrid absorbing layer boundary. Explanation of other symbols on the map is the same as in Fig. 5.4. The right subplot shows the time history of the same wavefield at station GDXB (red square on the map). The red tick is the instant corresponding to the snapshot shown on the map. A Gaussian source time function with fundamental frequency ~ 0.9 Hz (*freq* parameter in SW4 ~ 5.65) was used for this particular wavefield.

5.4.5 Sensor orientations

Rotation of the NGF tensor to the T-R-Z reference frame with respect to the source-receiver azimuth requires precise knowledge of sensor orientations. Among the stations employed in our study, the exact orientation of the borehole sensors is unknown (http://www.ncedc.org/egs/, last accessed July 2016). Moreover, preliminary comparisons of NGFs and SGFs (described in the following section) indicated possible sensor misalignments, i.e., non-zero angles between the horizontal components of the 3-component sensors and the geographic NS-EW reference frame. We compare 3-component long period waveforms (~0.02-0.1 Hz) of regional and teleseismic earthquakes at all stations to the corresponding waveforms at the broadband USGS station GDXB to verify sensor orientations and determine the degree of misalignment, if any (e.g. Grigoli *et al.* 2012).

In the following, it is assumed that the sensor gains are correctly known at all the stations. We assume that the broadband USGS station GDXB, which is approximately at the center of the reservoir area, is correctly orientated to EW and NS directions. Using a grid search with a 1° interval, we estimate the anti-clockwise rotations in azimuth for which the long period velocity waveforms (0.02-0.05 Hz or 0.05-0.1 Hz) of selected large earthquakes (minimum distance ~200 km) recorded by the LBNL 3-component geophones are most similar to those recorded by GDXB (Table 5.1). All 3-component stations at The Geysers are within ~12 km from GDXB, which is a fraction of the shortest wavelength ~ 40 km (assuming a phase velocity of 4 km/s), so their waveforms should be very similar. Good quality waveform segments of different phases with duration of 80-460 s are compared in T-R-Z directions specific to the earthquakes. We allow for phase-specific time-shifts up to ± 5 s applied to all 3 components. The Z component waveforms are included to provide constraints on time-shifts and wavefield similarity.

Table 5.1: List of earthquakes used to determine the horizontal orientation of sensors in this study. All but three earthquakes are located at teleseismic distances (> 1000 km). FP is the frequency passband used: "1" and "2" are 0.02-0.05 Hz and 0.05-0.1 Hz, respectively; N is the number of phases or waveform segments in the waveforms of each earthquake that were used for measuring alignment angles.

Date (yyyy-mm-dd)	Origin Time (hh:mm:ss)	Latitude (°N)	Longitude (°E)	Depth (km)	Region	M_W	FP	N
2012-03-20	18:02:47	16.493	-98.231	20	Mexico	7.4	1	2
2012-04-11	08:38:37	2.327	93.063	20	Sumatra	8.6	1	2
2012-04-11	10:43:11	0.802	92.463	25.1	Sumatra	8.2	1	1
2012-04-12	07:15:48	28.696	-113.104	13	Mexico	7	1	1
2012-10-28	03:04:09	52.788	-132.101	14	Canada	7.8	1	1
2012-11-07	16:35:47	13.988	-91.895	24	Guatemala	7.4	1	1
2013-01-05	08:58:19	55.393	-134.652	10	Alaska	7.5	1	1
2013-02-06	01:12:26	-10.799	165.114	24	Solomon Isl.	8	1	2
2013-05-24	03:47:08	40.192	-121.059	9.7	California	5.7	2	1
2013-05-24	05:44:49	54.892	153.221	598.1	Okhotsk Sea	8.3	1	3
2014-03-10	05:18:13	40.829	-125.134	16.6	California	6.8	1	1
2014-04-12	20:14:39	-11.2701	162.1481	22.6	Solomon Isl.	7.6	1	1
2014-06-23	20:53:10	51.8486	178.7352	109	Alaska	7.9	1	2
2014-10-14	03:51:34	12.5262	-88.1225	40	El Salvador	7.3	2	3
2015-01-28	21:08:53	40.318	-124.607	17.2	California	5.7	2	1
2015-04-25	06:11:26	28.2305	84.7314	8.2	Nepal	7.8	2	4
2015-05-30	11:23:02	27.8386	140.4931	664	Japan	7.8	1	5
2015-11-24	22:45:39	-10.5372	-70.9437	606.2	Peru	7.6	2	1
2015-11-24	22:50:54	-10.0598	-71.0184	620.6	Brazil	7.6	2	1
2016-01-24	10:30:30	59.6363	-153.4051	129	Alaska	7.1	1	1

Fig. 5.6 shows the effects on waveforms of two earthquakes. The goodness-of-fit of the waveforms of all stations with respect to the GDXB waveforms is evaluated by VR and zero-lag normalized correlation coefficient CC with minimum values of 80% and 0.9, respectively (these criteria were slightly relaxed for station SRB). Alignment angles determined from multiple measurements (different earthquakes or different phases of the same earthquake) are averaged to obtain an average estimate of alignment angle and the standard deviation as a proxy for the uncertainty. Higher weights are assigned to measurements with higher VR, higher CC, longer period passband and higher peak displacement amplitudes (on a log scale). An example for two stations is shown in Fig. 5.7.

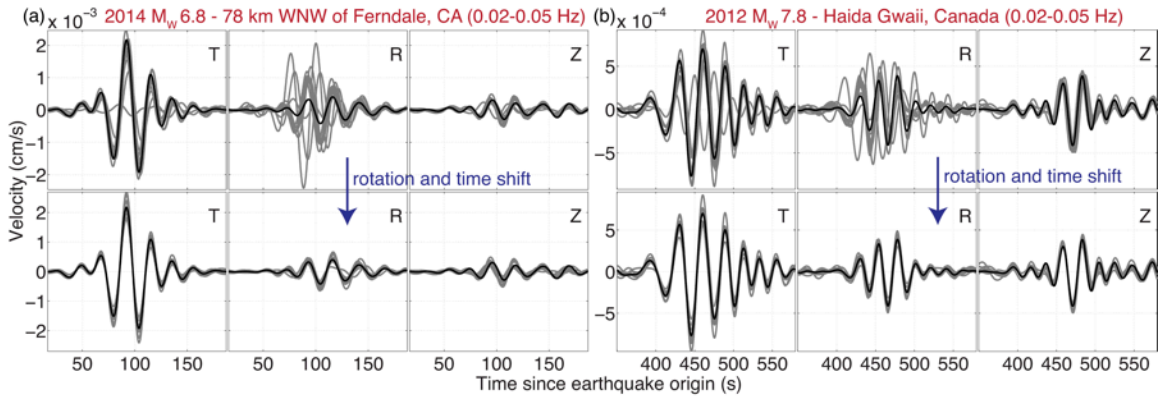

Figure 5.6: Filtered waveforms (black- reference station GDXB, gray- other stations) of two earthquakes used to determine the sensor misalignments at The Geysers. The earthquake, year, M_W and frequency passband are indicated at the top. The stations used for the two earthquakes (gray traces) are (a) ACR, AL6, CLV, DRK, DVB, FUM, HVC, MNS, TCH, JKB, DRH, and (b) ACR, CLV, DRK, DVB, FUM, HVC, MNS, NEG, TCH and DRH. Original waveforms are in the top panels, while the bottom panels show waveforms after they have been time-shifted and horizontal components have been the rotated to increase similarity with GDXB waveforms that remain fixed.

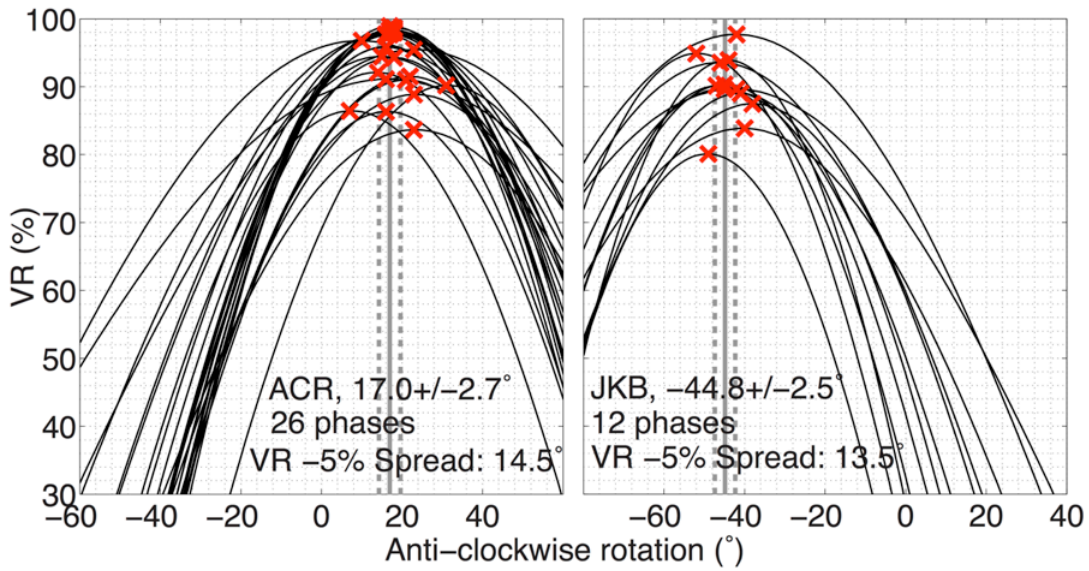

Figure 5.7: VR between waveforms of large earthquakes recorded at 3-component stations and corresponding waveforms at USGS broadband station GDXB as a function of anti-clockwise rotation in azimuth of that station. Black solid lines are curves for individual phases of the same or different earthquakes and the red crosses show coordinates of the maximum VR of each curve. The gray solid and dashed lines mark the mean rotation angle (of all the red crosses) and ±1 standard deviation. The station name, mean angle and standard deviation, number of phases used and the average spread (angle from the VR maxima at which VR drops by 5%) are indicated.

The overall results are shown in Table 5.2. These results provide the first orientation estimates for the borehole sensors and show surprisingly large alignment angles (> 10°) at many of the surface stations as well (stations ACR, AL6, CLV, DRK, DVB, FUM, HVC, LCK, MNS, NEG and TCH) with standard deviations < 5° over multiple measurements. The same procedure, when applied to BDSN stations HOPS and MNRC (~40 km away from GDXB), in the longer period passband with time-shifts up-to ± 7 s yields small angles, –1.4±4.4° and -3.9±2.9°, respectively indicating an overall consistency in our methodology and the correct orientation of GDXB. As of September 2016, the azimuth metadata of the LBNL network stations archived at NCEDC have not been revised with the results of this study, pending verification of sensor orientation at all sites.

Table 5.2: Mean azimuth of horizontal components of the sensors with respect to the geographic NS-EW reference frame (alignment angle), determined from the analysis of long period earthquake records and the associated uncertainty from multiple measurements. N is the number of measurements, i.e. total number of alignment angles measured on separate waveform segments or phases; stations with just one measurement are in italic. The values of uncertainties are likely underestimated in the case of stations with too few measurements. We consider the results of other stations, not listed in this table, to be unreliable owing to large scatter in the measurements on different teleseismic records or to poor quality of the noise cross-correlations. However, the alignment angle at station SQK was verified in the field to be ~14° (Ramsey Haught, personal communication, 2016).

	Station	Alignment angle (°)	Uncertainty (°)	N	Field Measurement (°)
Stations with small angles	*AL1*	*-2*	-	*1*	-
	AL2	4.5	3.2	5	-
	AL3	2.4	3.9	3	-
	AL4	-3.4	2.7	13	-
	AL5	6.3	2.7	10	-
	DES	-4.6	2.2	8	-
	FNF	-3.6	2.5	13	-
	HBW	3.6	3.8	12	-
	HER	*-6*	-	*1*	-
	PFR	*1*	-	*1*	-
	SSR	-4.9	3.1	7	-
	STY	8.4	3.8	11	-
	HOPS	-1.4	4.4	17	-
	MNRC	-3.9	2.9	9	-
Borehole Stations	DEB	-19.2	2.9	2	-
	JKB	-44.8	2.5	12	-
	SRB	29.6	3.4	2	-
Stations with large angles	DRH	-91.7	2.3	21	-
	ACR	17.0	2.7	26	-
	AL6	16.6	2.0	6	-
	CLV	18.1	2.1	9	-

	DRK	15.6	2.1	11	-
	DVB	35.5	3.5	7	-
	FUM	22.9	4.1	7	29
	HVC	21.2	6.8	25	-
	LCK	37.6	2.5	10	-
	MNS	-11.2	2.5	11	-
	NEG	14.0	3.0	16	14
	TCH	16.7	2.6	11	14

5.4.6 Procedure for comparison between NGFs and SGFs

We find that proper filtering of SGFs is a critical step for comparison with NGFs at small interstation distances. As a result of the band-limiting taper applied during spectral whitening and cross-correlation (see section **5.4.2 Cross-correlation analysis**), the NGFs are acausal. For positive correlation lag time, NGFs at short interstation distances will have non-zero acausal amplitudes leaking to $t < 0$ following zero-phase bandpass filtering that contaminate the symmetric time-reversed NGFs at negative correlation time and vice versa for $t > 0$ (e.g. Cho *et al.* 2007). Therefore, we zero pad the raw SGFs at $t < 0$, bandpass-filter them between 0.2 Hz and 1.6 Hz with a zero-phase 8-pole Butterworth filter (same as the taper applied during spectral normalization), time-reverse the SGFs and take the symmetric component. This is explained in detail in Fig. 5.8. All NGFs and SGFs are subsequently bandpass-filtered between 0.2 Hz and 0.9 Hz with a causal 2-pole Butterworth filter.

For comparison of the NGF and the SGF tensors, we choose waveform segments between 1 s prior to the theoretical P-wave arrival time or t=0 (whichever is later) and 5 s after the empirical coda-wave start time. The tensors are normalized by the overall L2 norm of all available components, which preserves relative inter-component amplitudes and makes the scaling factor invariant under the rotation of the station components. However, this also creates a slight bias against the SGFs of 1D velocity models, because TR, TZ, RT and ZT components of SGFs are identically zero, whereas corresponding components in NGFs are always non-zero. This is manifested by slightly greater amplitudes for the five primary, non-zero components- TT, RR, RZ, ZR and ZZ of the SGF tensors compared to the same for the NGF tensors for many station pairs, especially at greater distances at which the amplitudes in the other NGF components are dominated by noise in the NGF time-series (discussed further in section **5.6 Contribution of 3D structure and anisotropy**).

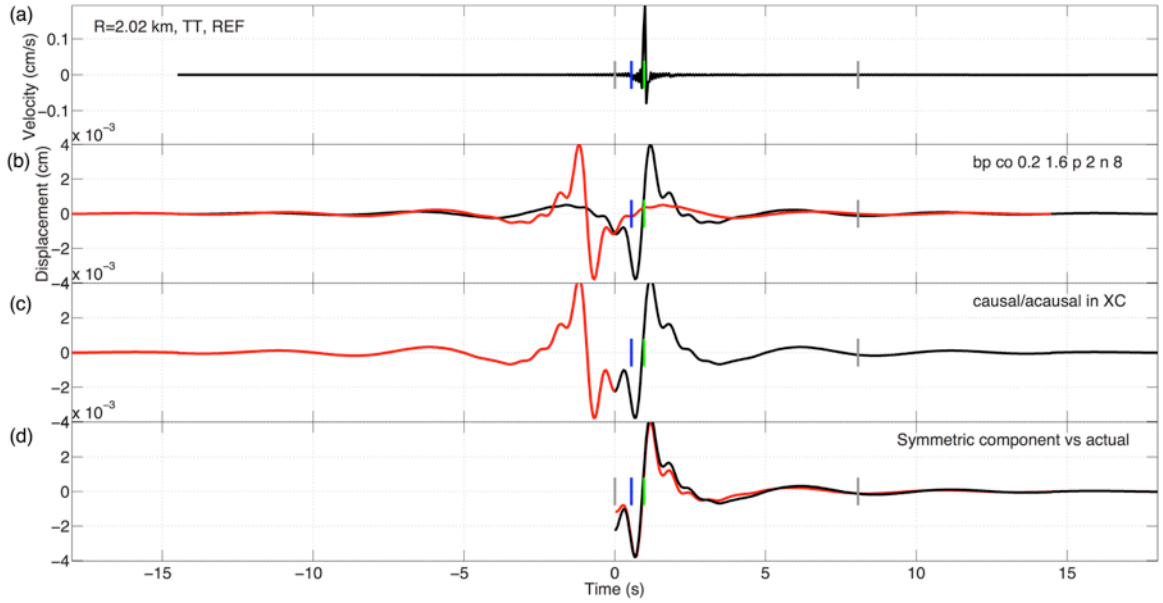

Figure 5.8: Figure explaining the processing of synthetics in this study. (a) Raw TT component synthetic velocity Green's function (GF) (velocity response to an input step function) at interstation distance ~ 2 km computed using the REF model. We use this raw velocity time-series as Raw Synthetic Green's Function (RSGF) for amplitude decay analysis in section **5.9 Amplitude decay**. (b) Time-series in (a) integrated to displacement and bandpass-filtered between 0.2 Hz and 1.6 Hz with a zero-phase 8-pole Butterworth filter (black trace) and its time-reversed version (red trace). The acausal filtering is the effect of the frequency domain taper applied to keep cross-correlation spectral amplitudes band-limited (see section **5.4.2 Cross-correlation analysis**). (c) Sum of causal and anti-causal (time-reversed) traces. Ideally, this is the perfect noise-derived Green's Function (NGF) we expect to recover from noise cross-correlation for our choice of parameters. (d) symmetric component (average of causal and anti-causal sides) of the trace in (c) as an estimate of Synthetic Green's Function (SGF; black trace). Comparing against the original filtered displacement time-series (red trace), the amplitudes of SGF at times $\lesssim$ 3 s are contaminated by the acausal amplitudes of the time-reversed trace (c). Blue and green ticks are theoretical P and S arrival times, respectively, and the gray tick at ~3.1 s corresponds to 5 s after the empirical coda start time. We choose the waveform segments between the two gray marks for calculating goodness-of-fit measures and spectral amplitude estimates in section **5.9 Amplitude decay**.

The overall similarity between the two tensors is evaluated by two estimates of goodness-of-fit, namely by the variance reduction (VR; e.g. Guilhem *et al.* 2014), and by the zero-lag normalized correlation coefficient (CC). P- and S-wave arrival times are computed using velocity model REF for all station pairs excluding stations MNRC and HOPS, and models GIL7 or GIL7.1 for all station pairs including stations MNRC or HOPS, respectively, and are shown on all the following figures that contain waveforms, for reference. We also examine the time delay of each component of SGFs with respect to the corresponding NGF component (e.g. Ma *et al.* 2008) if the normalized CC (not zero-lag) for that component exceeds 0.7.

Positive time delay implies that the NGF arrives earlier than the SGF and the actual velocities are faster than the model velocities (at these frequencies, waveforms are primarily sensitive to V_S).

5.4.7 Synthetic tests

Prior to comparing NGF and SGF tensors at The Geysers, we perform tests on "synthetic noise" to evaluate the extent to which phase and relative amplitude information can be retrieved from noise cross-correlation. Our synthetic tests are modified after synthetic tests done by Herrmann (2013b). We design a 100 km x 100 km domain with stations placed at various positions at the center allowing us to obtain Synthetic Noise Green's Functions (SNGFs), i.e. NGFs estimated from cross-correlation of synthetic noise, for interstation distances from 1 to 35 km (Fig. 5.9).

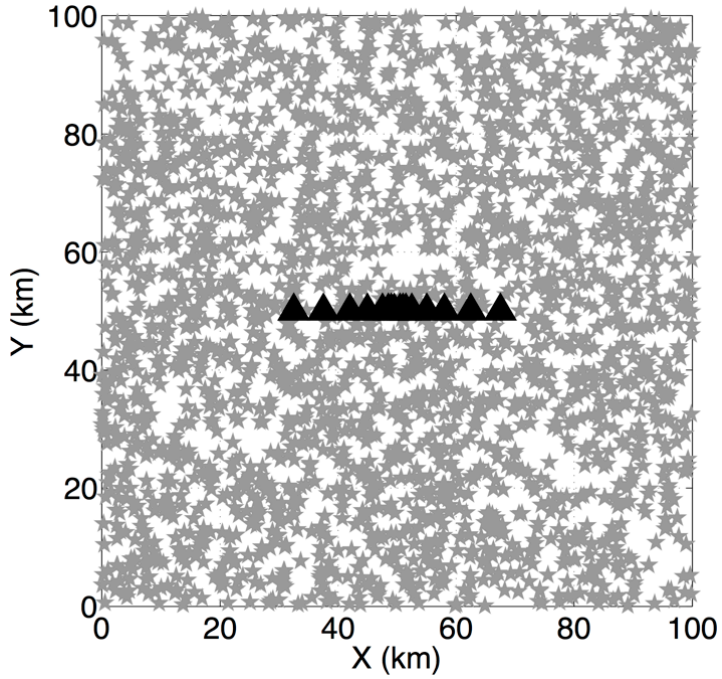

Figure 5.9: Computational domain for synthetic tests with the stations (black triangles) and ~2400 random noise source locations (gray stars) generated in 6 min over the earth's surface.

For constructing synthetic noise records at the stations, we sum filtered (0.2-0.9 Hz) 3-component velocity waveforms that are generated by randomly oriented force vectors (amplitude range -1 to +1) at random locations (but at least 50 m away from stations) on the surface with 20 sources acting together every three seconds. Different from the synthetic tests of Herrmann (2013b), we use sources overlapping in time as in Kimman & Trampert (2010) and the FKI method described earlier to compute complete single force responses on the REF model instead of surface wave responses computed by modal summation. The exact

methodology for noise cross-correlation described in section **5.4.2 Cross-correlation analysis** is applied to ~20 days of synthetic noise between 0.2 and 0.9 Hz.

Fig. 5.10 shows the comparison of the SGFs and the SNGFs (Synthetic Noise Green's Functions), i.e. NGFs estimated from cross-correlation of synthetic noise. At 1 km distance (~0.22 λ, where λ is surface-wave wavelength), filtered displacement SGFs are characterized by simple waveforms and the recovered SNGFs are almost equal to the SGFs with VR ~93%. With increasing interstation distances from 2-16 km (~0.44 λ to ~3.5 λ), as the SGF waveforms develop into clear body and surface wave phases, the fits to body waves arriving prior to the S-wave arrival time deteriorate considerably, especially in the RR component. As the source is at 10 m depth, the dominant arrivals on the waveforms are fundamental-mode surface waves and the relative peak-to-peak amplitudes of the SNGF waveforms are consistent with those of the SGF waveforms at all distances, even in cases where there is considerable difference in the waveform shape (e.g., RR component at 5 km). At distances ≥10 km (~2.2 λ), surface waves are exactly recovered in the SNGFs after the S-wave arrival time when compared to all non-zero components of the SGFs. While clear P-SV body wave energy can be easily identified between the P-wave and S-wave arrival times in the RR, RZ, ZR, and ZZ components of the SNGFs at distances ≥ 10 km, the waveforms are not exactly recovered. At short distances (<λ), even when the SNGFs are very similar to the SGFs, it is possible to obtain large spurious time delays (e.g., RR component at 3 km) that might be misinterpreted as deficiency of the velocity model. However, it is expected that measurements from multiple paths and multiple components weighted by the signal-to-noise ratios and effects of long-term averaging and scattering in the Earth's crust will minimize these delays and their influence in travel-time inversion. It is interesting that the fits for off-diagonal components, RZ and ZR, are equal to or better than those for RR and ZZ components at all distances. Compared to the ZZ and RR components, Rayleigh wave cross-term components (ZR and RZ) have been suggested to be less susceptible to artifacts of directional noise source incidence, such as spurious precursory arrivals prior to the expected P-wave arrival time, in both, observational (van Wijk *et al.* 2011) and numerical studies (Haney *et al.* 2012).

Based on the synthetic tests, we find that interstation coherency of velocity noise recorded at two stations compares well with normalized displacement SGFs (for an input step force) for the methodology and scenarios (distances and frequencies, layered attenuating medium) in our study (VR ≳ 80% for distances ~ λ and higher VR at shorter and longer distances) under the assumption of an idealized homogenous noise distribution on the Earth's surface. Our failure to retrieve the exact GFs (i.e., VR = 100%) can be attributed to the absence of depth sources, the absence of deformation rate or dipole sources, cross-terms of different phases, incomplete cancellation of overlapping sources and ubiquitous distribution of noise sources instead of their clustering near the stationary phase region (Kimman & Trampert 2010).

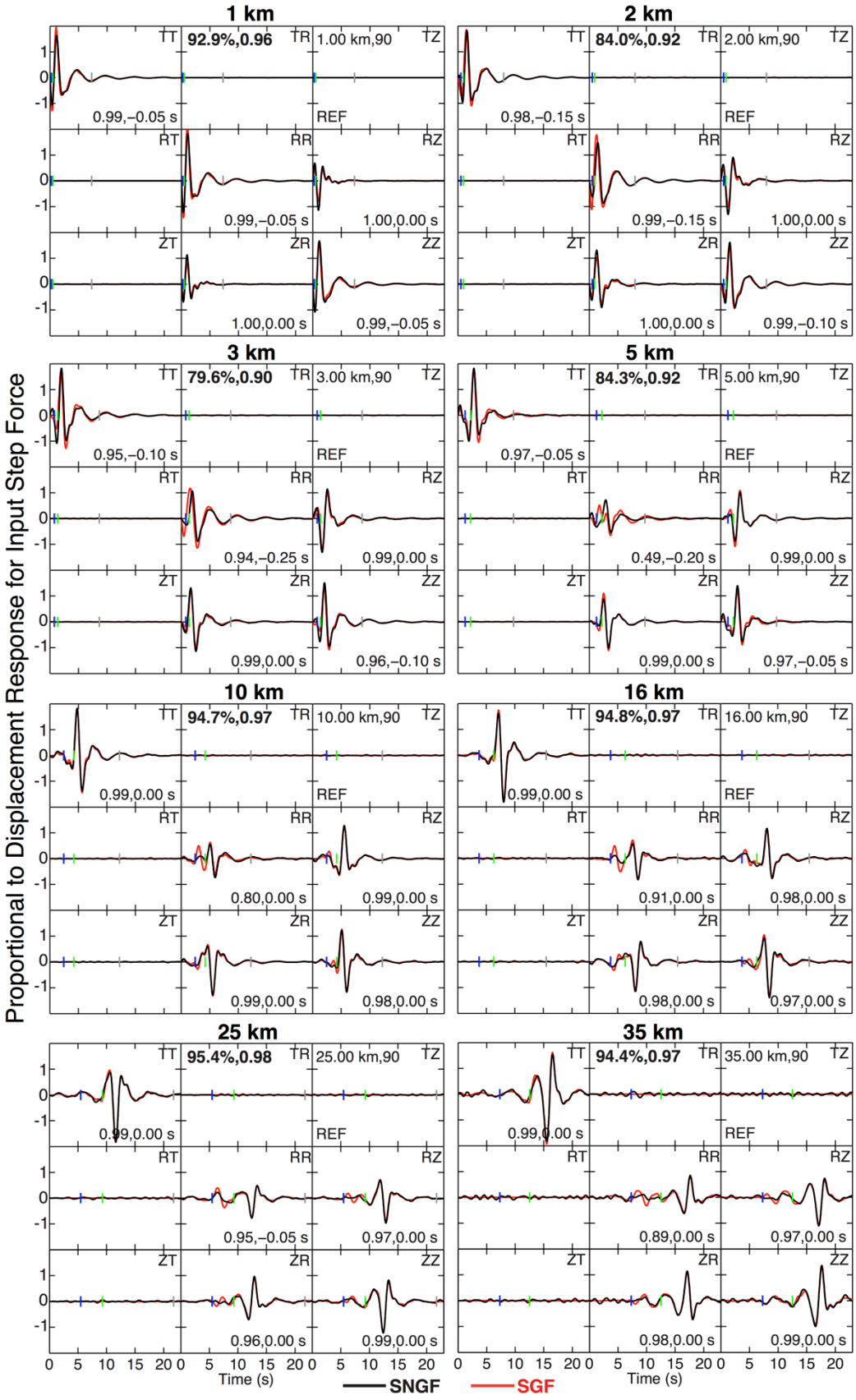
1 km
92.9%,0.96
1.00 km,90
0.99,–0.05 s
REF
0.99,–0.05 s
1.00,0.00 s
1.00,0.00 s
0.99,–0.05 s
2 km
84.0%,0.92
2.00 km,90
0.98,–0.15 s
REF
0.99,–0.15 s
1.00,0.00 s
1.00,0.00 s
0.99,–0.10 s
3 km
79.6%,0.90
3.00 km,90
0.95,–0.10 s
REF
0.94,–0.25 s
0.99,0.00 s
0.99,0.00 s
0.96,–0.10 s
5 km
84.3%,0.92
5.00 km,90
0.97,–0.05 s
REF
0.49,–0.20 s
0.99,0.00 s
0.99,0.00 s
0.97,–0.05 s
10 km
94.7%,0.97
10.00 km,90
0.99,0.00 s
REF
0.80,0.00 s
0.99,0.00 s
0.99,0.00 s
0.98,0.00 s
16 km
94.8%,0.97
16.00 km,90
0.99,0.00 s
REF
0.91,0.00 s
0.98,0.00 s
0.98,0.00 s
0.97,0.00 s
25 km
95.4%,0.98
25.00 km,90
0.99,0.00 s
REF
0.95,–0.05 s
0.97,0.00 s
0.96,0.00 s
0.99,0.00 s
35 km
94.4%,0.97
35.00 km,90
0.99,0.00 s
REF
0.89,0.00 s
0.97,0.00 s
0.98,0.00 s
0.99,0.00 s
TT
TR
TZ
RT
RR
RZ
ZT
ZR
ZZ
Proportional to Displacement Response for Input Step Force
Time (s)
SNGF
SGF

Figure 5.10: Comparison of 9-component SNGF (black) and SGF (red) tensors at various interstation distances. The SNGFs were obtained from cross-correlation of synthetic noise. Each panel (3x3 group of subplots) is specific to an interstation distance (shown at the top of the panels). Each subplot in a panel is specific to a component pair (component pair names are at top right corner of each subplot; distance and azimuth are at the top left corner of the TZ subplots). In component pairs (i.e., TR), the first component (T) corresponds to the force direction and second component (R) corresponds to the displacement direction at the receiver. The velocity model used to compute the SGF tensor and the synthetic noise waveforms is indicated at the bottom left corner of the TZ subplot. For the overall tensor comparisons of a station pair, two goodness-of-fit estimates, VR and normalized zero-lag CC, are mentioned at the top left corner of the TR subplots. For all non-zero component pairs, the normalized CC along with the time lag between the SNGF and SGF waveforms is indicated at the bottom right corners of the subplots, if the CC exceeds 0.7. For reference, blue and green marks are theoretical P and S arrival times, respectively, and the gray mark corresponds to 5 s after the empirical coda start time. For a particular station pair, following normalization of amplitudes of the SNGF and SGF tensors, only relative amplitudes are meaningful.

5.5 Results

In the context of noise cross-correlations, "distances" in the current and following sections implies interstation distances. In the comparisons of NGFs and SGFs, each SGF tensor corresponds to the velocity model that returns the highest VR with NGFs of that specific station pair, unless stated otherwise. First we discuss NGFs involving stations within the steam field or adjacent to it (i.e., all stations excluding HOPS and MNRC).

5.5.1 Effects of sensor misorientations on NGFs

In our preliminary analysis, we observed that the NGFs of some stations pairs at very small distances ($< \lambda$) had large amplitudes on the TR, TZ, RT, and ZT components (hereinafter referred to as T-[R,Z] components) that are unlikely the result of 3D velocity structure or anisotropy. These anomalous amplitudes were restricted to NGFs involving some specific stations that also returned fairly large alignment angles in the analysis of teleseismic waveforms. Fig. 5.11a shows some examples with surface stations FUM and DVB and borehole station JKB. We consider, sensor misalignments as a likely cause of these non-zero amplitudes. We use alignment angles obtained from earthquake waveforms to rotate the NGF tensors to correct orientations. For the NGFs in Fig. 5.11, rotation to the correct orientation reduces the large amplitudes on the T-[R,Z] components and significantly improves the VR between the SGFs and the NGFs (Fig. 5.11b). On an average, correcting the NGFs for all alignment angles >10° increases VR between the SGFs and the NGFs, and reduces the mean root mean square amplitude of the T-[R,Z] components for 76.4% and 79.8% of the 407 interstation pairs, respectively.

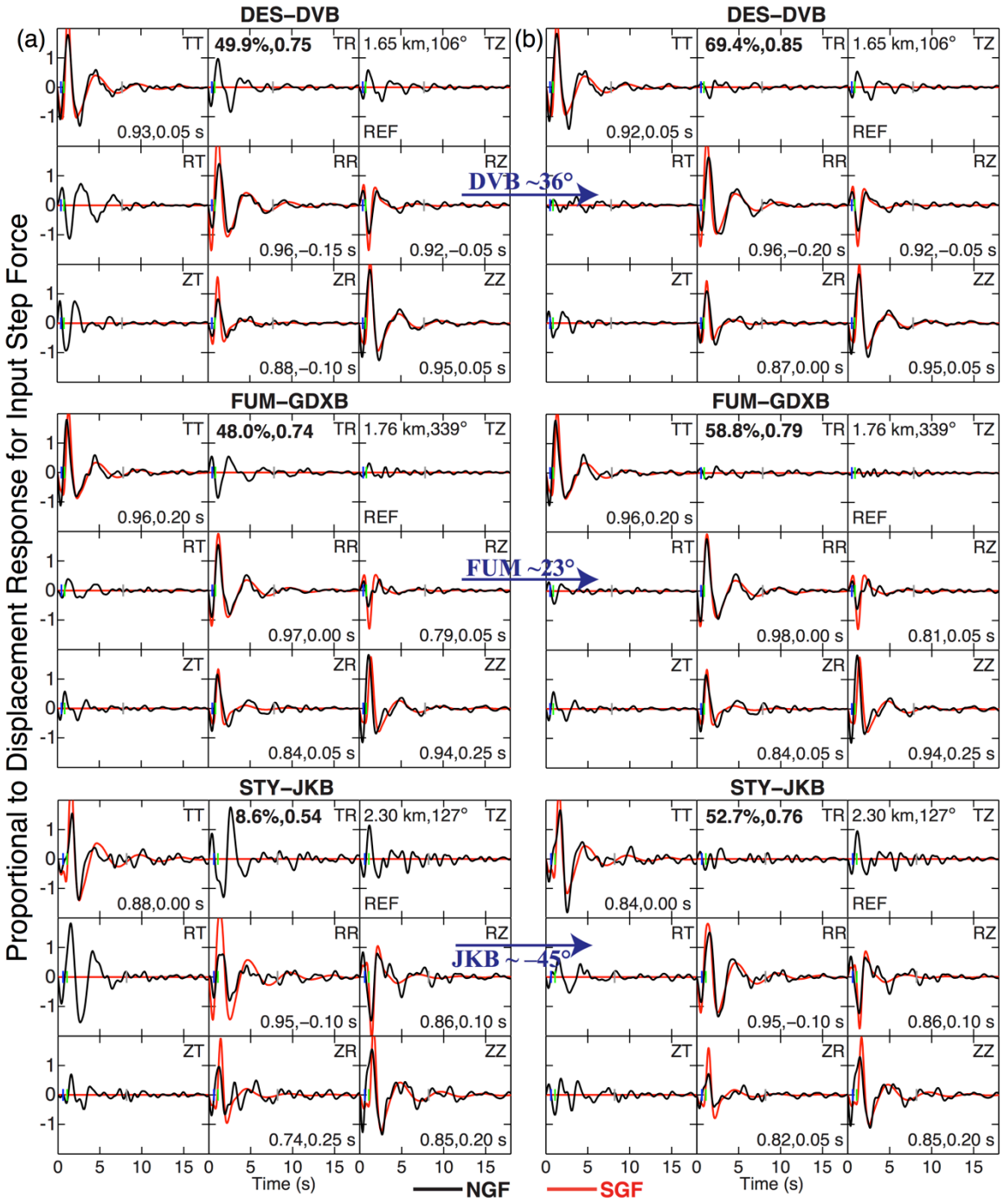

Figure 5.11: (a) 9-component NGF (black) and SGF (red) tensors for specific station pairs with large anomalous amplitudes on the T-[R,Z] components. Each panel (3x3 group of subplots) is specific to a station pair (names of stations shown at the top of the panels). Each subplot in a panel is specific to a component pair (component pair names are at top right corner of each subplot; distance and azimuth are at the top left corner of the TZ subplots). The first station/component corresponds to the force location/direction and the second station/component corresponds to the receiver location/direction. For each station pair, the velocity model used to compute the best fitting SGF tensor is indicated at the bottom left corner of TZ subplot. For the overall tensor comparisons of a station pair, two goodness-of-fit

estimates, VR and normalized zero-lag CC are mentioned at the top left corner of TR subplots. For all non-zero component pairs, the normalized CC along with the time lag between the NGF and SGF waveforms is indicated at the bottom right corners of the subplots, if the CC exceeds 0.7. For reference, the blue and green marks are the theoretical P- and S-wave arrival times, respectively, while the gray mark corresponds to 5 s after the empirical coda start time. For a particular station pair, following normalization of amplitudes of the NGF and SGF tensors, only relative amplitudes are meaningful. (b) Same as (a) but after the NGF tensors are corrected for sensor misalignments. The rotation angles for different stations are indicated on the arrows between (a) and (b). NGFs in all the following figures have been similarly corrected for sensor misorientations using alignment angles obtained from the analysis of earthquake waveforms.

We also consider DEB and SRB that were replacement borehole stations for surface stations DVB and SSR at depths ~150 m and ~140 m, and at horizontal distances of ~30 m and ~70 m, respectively from the surface sites. Both the surface and borehole stations were simultaneously operational for ~25 days. The NGFs and the SGFs for the two surface-borehole sensor pairs are shown in Fig. 5.12. At these small distances, GFs are primarily proportional to filtered source-time functions with the largest near-equal amplitudes on the TT, RR and ZZ components (e.g. Wielandt & Forbriger 1999). Orientation corrections to the NGFs significantly reduce the amplitudes in the off-diagonal components of these tensors (Fig. 5.12b). Although there can be other factors responsible for the off-diagonal terms, utilizing the NGF tensors may be a useful alternative approach for assessing orientations of borehole sensors. The successful validation of angles measured independently from long period teleseismic earthquake waves on higher frequency NGF tensors provides confidence in our results. Alignment angles at three stations (FUM, NEG and TCH) have also been independently obtained at the sites (Ramsey Haught, personal communication, 2016), which are reasonably close to our estimates within the uncertainties (Table 5.2). In the following sections, all NGFs have been corrected using alignment angles obtained from the analysis of earthquake waveforms.

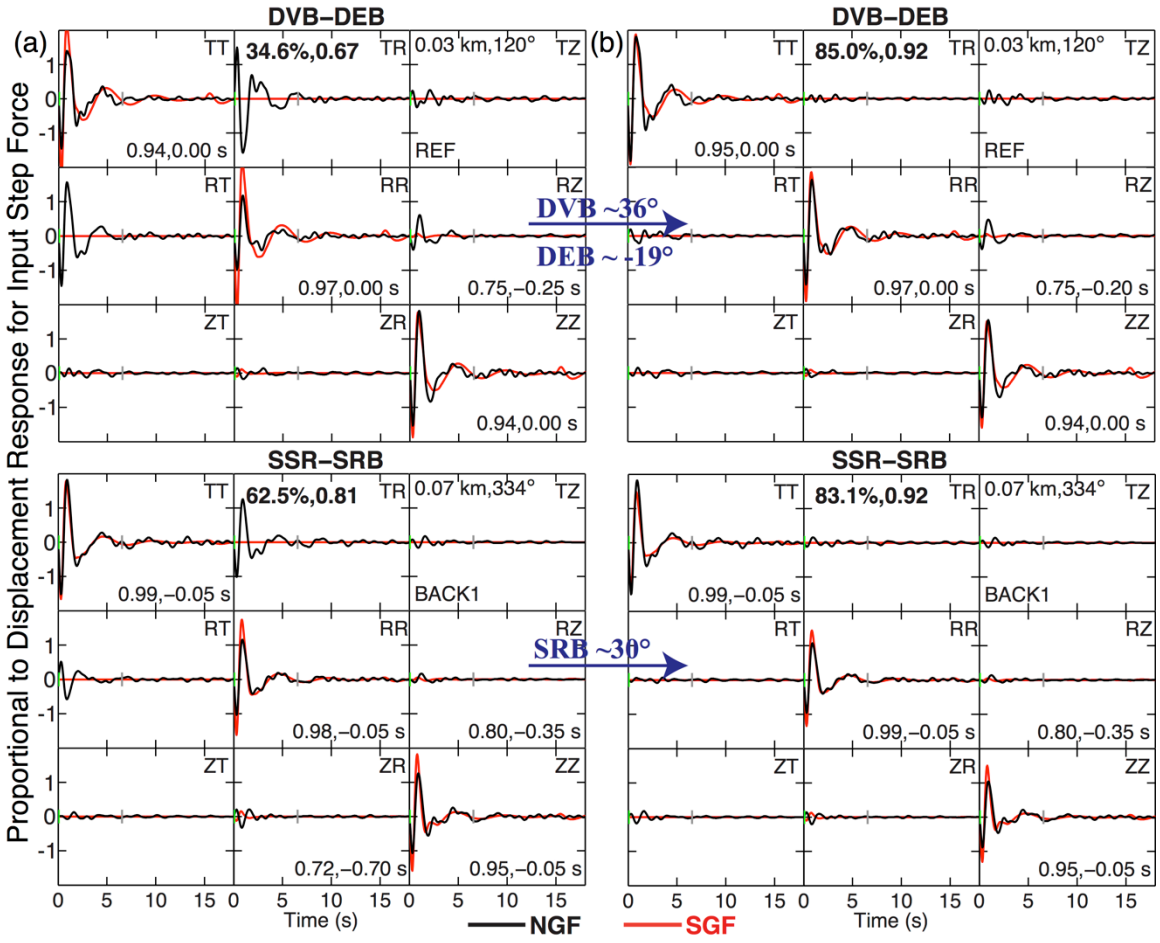

Figure 5.12: Same as Fig. 5.11, but for surface-borehole sensor pairs DVB-DEB and SSR-SRB.

5.5.2 NGF vs. SGF at various distances

Fig. 5.13 shows some examples of NGFs and SGFs at distances $\lesssim$ 2 km or ~0.46 λ. At these small distances, we observe simple waveforms, strong NGFs, low relative amplitudes of noise trailing the ballistic phases with respect to the peak amplitudes, good fits at VR $\gtrsim$ 40%, and consistency in relative amplitudes of different components of the tensors. Small time delays are sometimes observed between NGFs and SGFs (e.g. AL3-AL5 shown Fig. 5.13); however, these delays are not consistent across all components, and based on the synthetic tests it is unclear whether they are real or due to bias introduced by the noise distribution or by filtering or processing artifacts. For NGFs at distances > 2 km and $\lesssim$ 8 km (or > 0.44λ and $\lesssim$ 1.7λ) shown in Fig. 5.14, we observe a decrease in the quality of retrieved NGFs as evidenced by the increase in relative amplitude of trailing noise. The waveforms also grow slightly more complex and the amplitude misfit between NGFs and SGFs increases, with VR decreasing to ~20%. We start to see clear inadequacies in the velocity models; for example, in HBW-HER in Fig. 5.14, the TT component NGF is slower than the SGF indicating that the 3D model, which is not resolved in this region and therefore is essentially the same as the starting average 1D model (BACK1) in this area, is too fast for this path. While these distances are too

small for reliable phase measurements, large reliable time shifts measured on multiple components of the NGFs with good signal-to-noise ratio can be utilized as "broadband phase delays" in waveform tomography assuming that multiple scattering in the Earth's crust alleviates the ill-effects of inhomogeneous noise source distribution (Fichtner 2014; Lee *et al.* 2014).

Fig. 5.15 shows examples for distances > 8 km. These are characterized by lower signal-to-noise ratio, larger amplitudes of trailing noise and large amplitudes on the TR, TZ, RT and ZT components. The simple waveforms on the TT components consist of Love waves that depend on V_S structure only and show good fits, whereas the waveforms on the RR, RZ, ZR, and ZZ components consisting of P-SV and Rayleigh waves depend on both, V_P and V_S structure and exhibit rapidly increasing misfits with distance. However, the RR components of the NGFs in Fig. 5.15 compare well to the SGFs. P-SV body wave energy arriving before the theoretical S-wave arrival time can be clearly identified above the noise floor in the ZR components of AL6-NEG, AL2-STY, AL3-DES and AL2-DVB. Similar to results of Lin *et al.* (2008), but for a different distance and frequency range, we obtain higher amplitude noise cross-correlations in the TT component than in the RR and the ZZ components at distances > 2λ that compare well to the SGFs. Therefore, Love waves on the TT component NGFs should be used to constrain the shear wave velocity models in addition to Rayleigh waves whenever 3-component sensors are available, as the former are generally retrieved with better signal-to-noise ratio. Similar to our synthetic tests and observations in other studies (van Wijk *et al.* 2011), we generally find good fits between ZR and RZ component NGFs and SGFs at all distances.

Compiling overall results, the average peak-to-peak amplitude ratio of the primary components (TT, RR, RZ, ZR, ZZ) of NGFs to the corresponding components of SGFs for all station pairs is ~0.7. The standard deviation is ~0.18 in log10 units (i.e., difference of a factor of ~1.5, bigger or smaller) with respect to the mean amplitude ratio. To select only robust time delays between individual components of NGFs and corresponding components of the best-fitting SGFs for interpretation, we require that VR for a component pair is $\geq$ 35% following correction for the time delay estimated from normalized cross-correlation. This criterion ensures similarity in both waveform shape and amplitude. Out of 238 station pairs that have at least 2 such components, only ~19% of station pairs have large contrasting time delays on different components (maximum time delay $\geq$ 0.1 s and minimum time delay $\leq$ –0.1 s) indicating possible errors in the recovered NGFs. For many station pairs such as HBW-HER in Fig. 5.14, large robust time delays on different components of the tensors are of the same sign, indicating an overall consistency in observations.

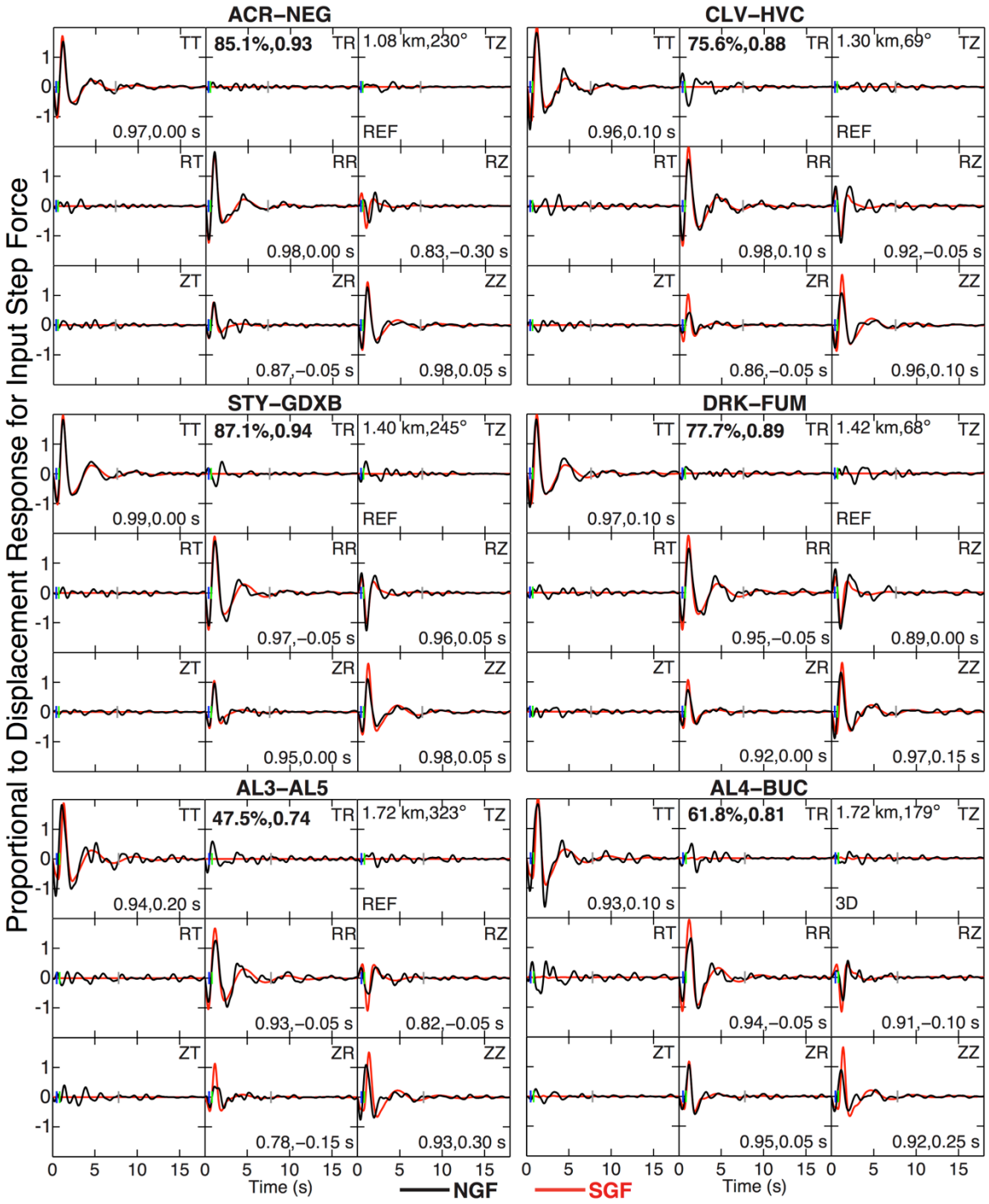

Figure 5.13: Same as Fig. 5.11b but for station pairs at interstation distances ≤ 2 km.

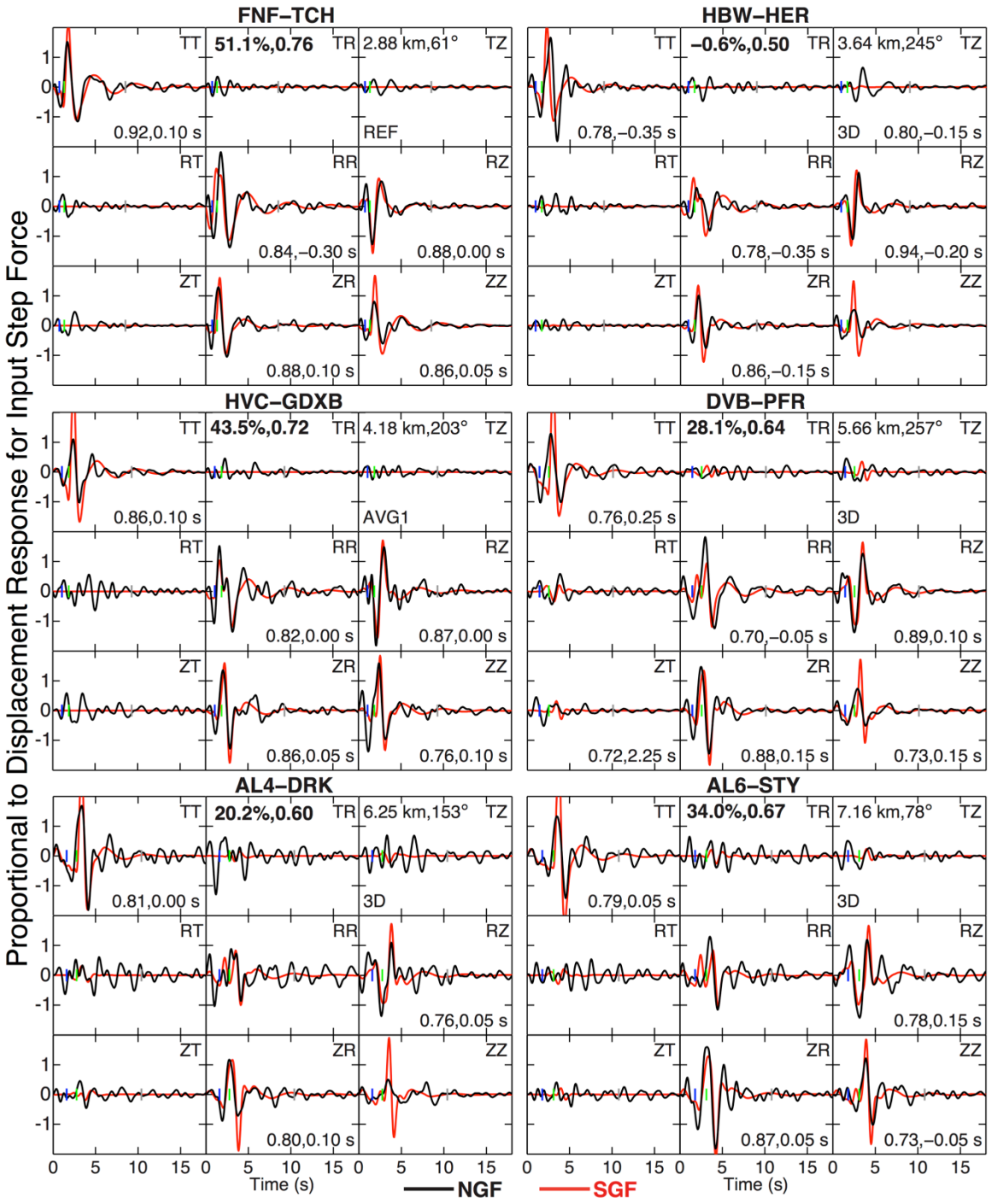

Figure 5.14: Same as Fig. 5.11b but for station pairs at interstation distances > 2 km and ≤ 8 km.

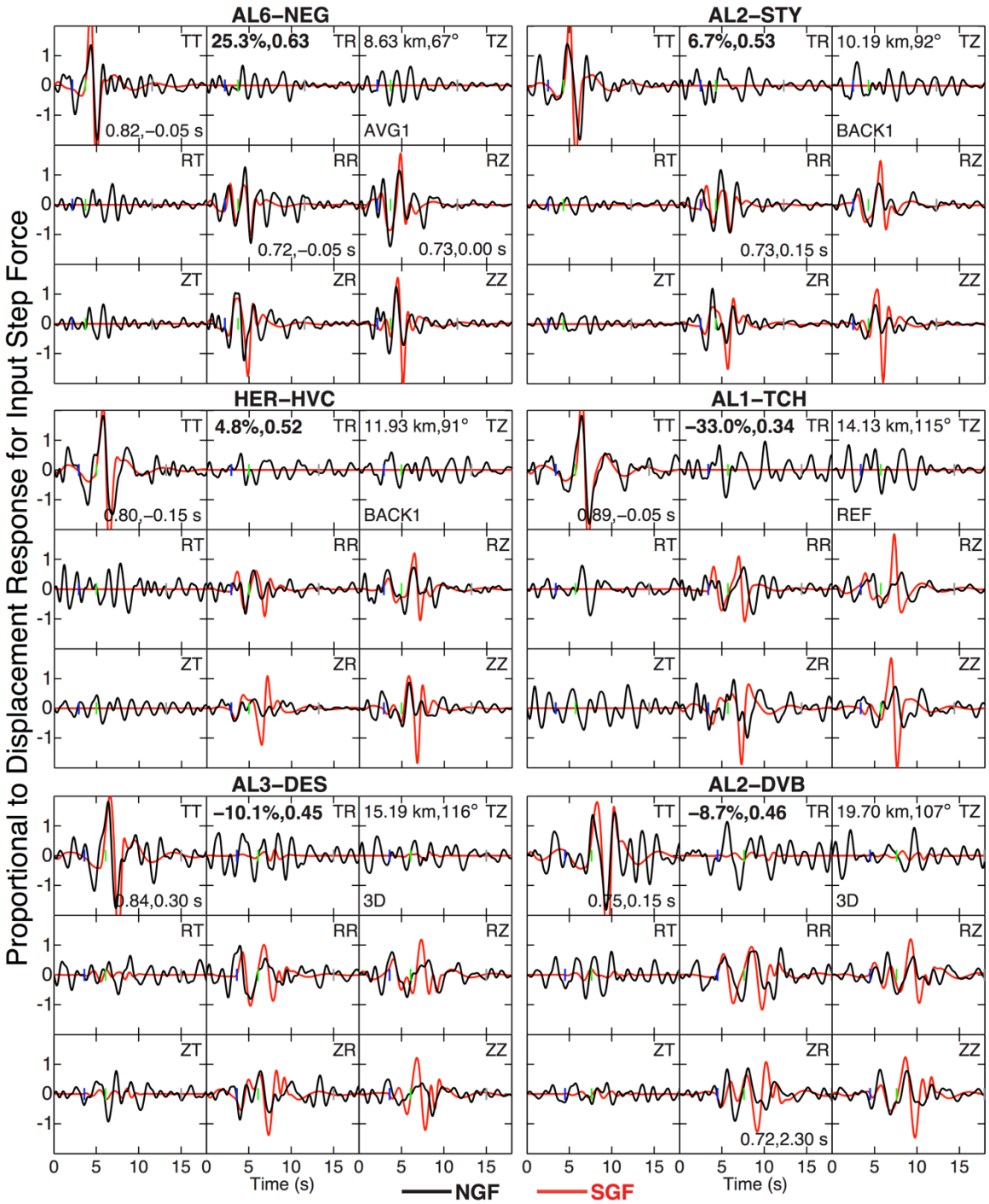

Figure 5.15: Same as Fig. 5.11b but for station pairs at interstation distances > 8 km.

5.5.3 Contribution of body waves and surface waves

To study the contributions of different body-wave and surface-wave phases to the observed NGF waveforms, we compare pure surface-wave SGFs computed using the modal summation method as provided in Herrmann (2013a) to complete FKI SGFs. We use the REF velocity model for this analysis; the synthetic phase velocities and depth-dependent eigenfunctions are computed using codes provided in Herrmann (2013a). Phases that are present in the complete FKI synthetics but absent in the surface-wave synthetics are interpreted to be body-wave phases. Synthetic phase velocity dispersion curves based on the REF model for fundamental- and first higher-mode Rayleigh waves are plotted in Fig. 5.16a. Fig. 5.16b shows an enlarged view of the fast arrivals at ~3.6 km/s in the ZZ component NGFs at distances 17-20 km in Fig. 5.2. Fig. 5.16c shows SGFs at similar distances containing the fundamental-mode ("Mode 0") and first higher-mode Rayleigh waves ("Mode 1") and their combination ("Mode 0+1"). For a source at ~10 m depth, the peak amplitudes of the higher-mode are ~14 times smaller than peak amplitudes of the fundamental-mode and therefore, the higher mode has a very small contribution to the total waveforms containing both modes. The amplitudes of the second higher-mode Rayleigh wave are even smaller and therefore, it is not discussed here. The recovery of higher-mode surface waves on land is more difficult than the recovery of fundamental-mode surface waves primarily due to the near-surface concentration of ambient noise sources (Kimman & Trampert 2010). However, some studies have reported success in this regard (e.g., Nishida *et al.* 2008; Lin *et al.* 2013). The body wave energy observed in the FKI synthetics is considerably weaker than energy observed in the ZZ component NGFs between the theoretical P-wave and S-wave arrival times. Compared to the SGFs, the NGFs appear to be depleted in high frequencies ($\gtrsim 0.5$ Hz) as well. More detailed analyses including the analysis of particle motions and SGFs computed with other velocity models are required to positively identify this phase in the ZZ component. However, since it has greater amplitudes and is faster (~3.6 km/s) than the first higher-mode Rayleigh wave expected for the REF model (phase velocity ~ 3.0–3.3 km/s), it is likely to be body-wave energy.

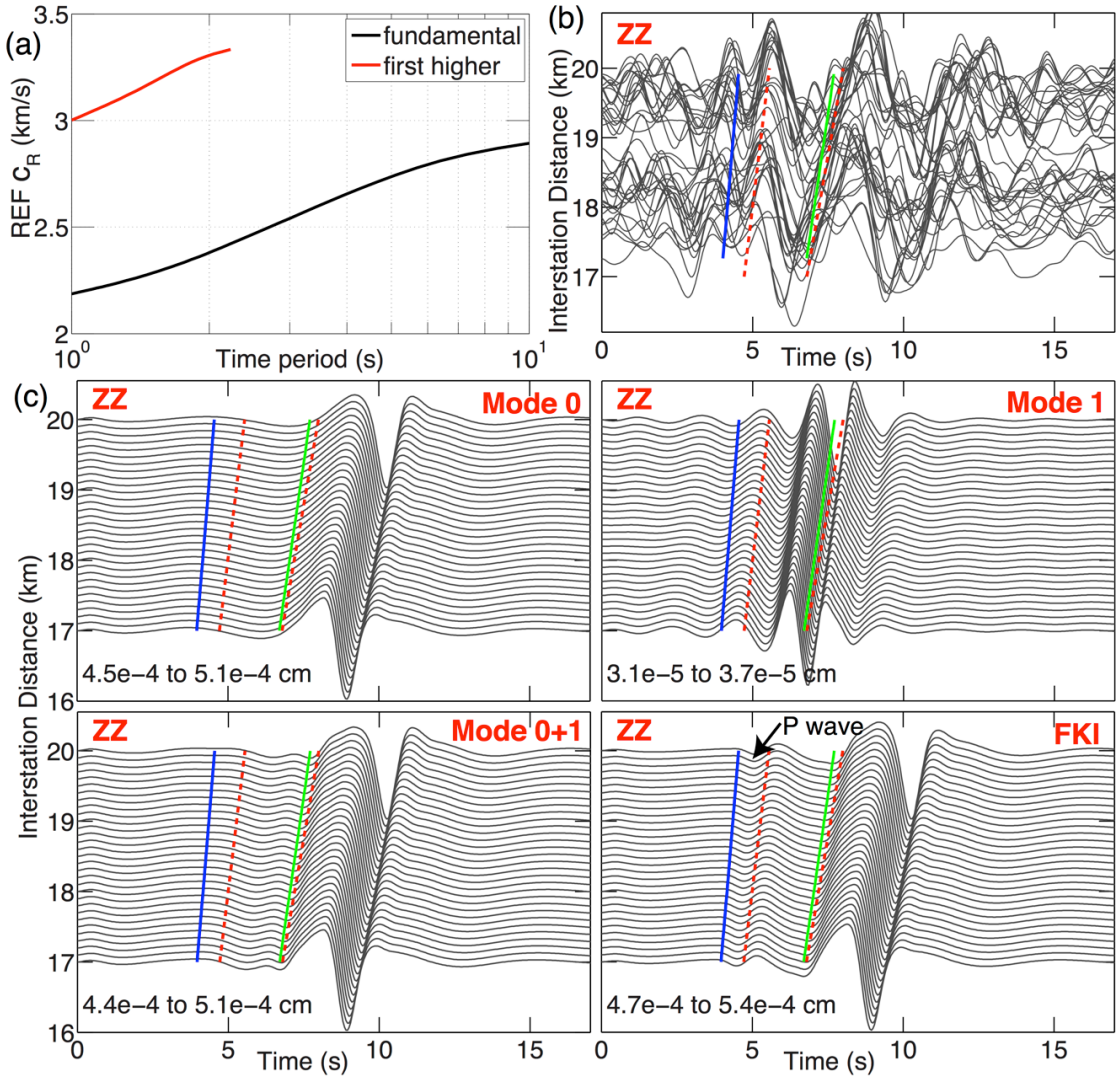

Figure 5.16: (a) Synthetic phase velocity dispersion curves for the fundamental-mode and first higher-order mode Rayleigh waves for the REF velocity model. (b) Record section of the ZZ component NGFs at interstation distances of 17–20 km. For reference, the blue and green solid lines denote the theoretical P- and S-wave arrival times, respectively. The two dashed red lines mark the arrival times for apparent medium velocities of 3.6 km/s and 2.5 km/s. (c) REF model ZZ component SGFs at interstation distances of 17–20 km for different Rayleigh waves modes ("Mode 0" and "Mode 1") computed using the modal summation technique, compared to complete synthetics computed using FKI. The type of modes/method is indicated at the top right corner of each subplot. "Mode 0" and "Mode 1" indicate fundamental and first higher-mode Rayleigh waves, respectively. "Mode 0+1" synthetics include both "Mode 0" and "Mode 1". The range of maximum absolute amplitudes of traces in each subplot is indicated in the bottom left corner. For example, the maximum absolute amplitude of ZZ component SGF computed using FKI varies from 4.7×10^{-4} cm to 5.1×10^{-4} cm over distances 14-17 km.

Comparing surface-wave ("Mode 0 / 1 / 0+1") SGFs and complete FKI SGFs at distances of 14-17 km for the ZR and RR components (Fig. 5.17), we positively identify strong P-wave energy in the RR and ZR component NGFs for many station pairs (e.g., AL3-DES in Fig. 5.15) in light of the negligible contribution of the first higher-mode Rayleigh wave compared to the fundamental mode.

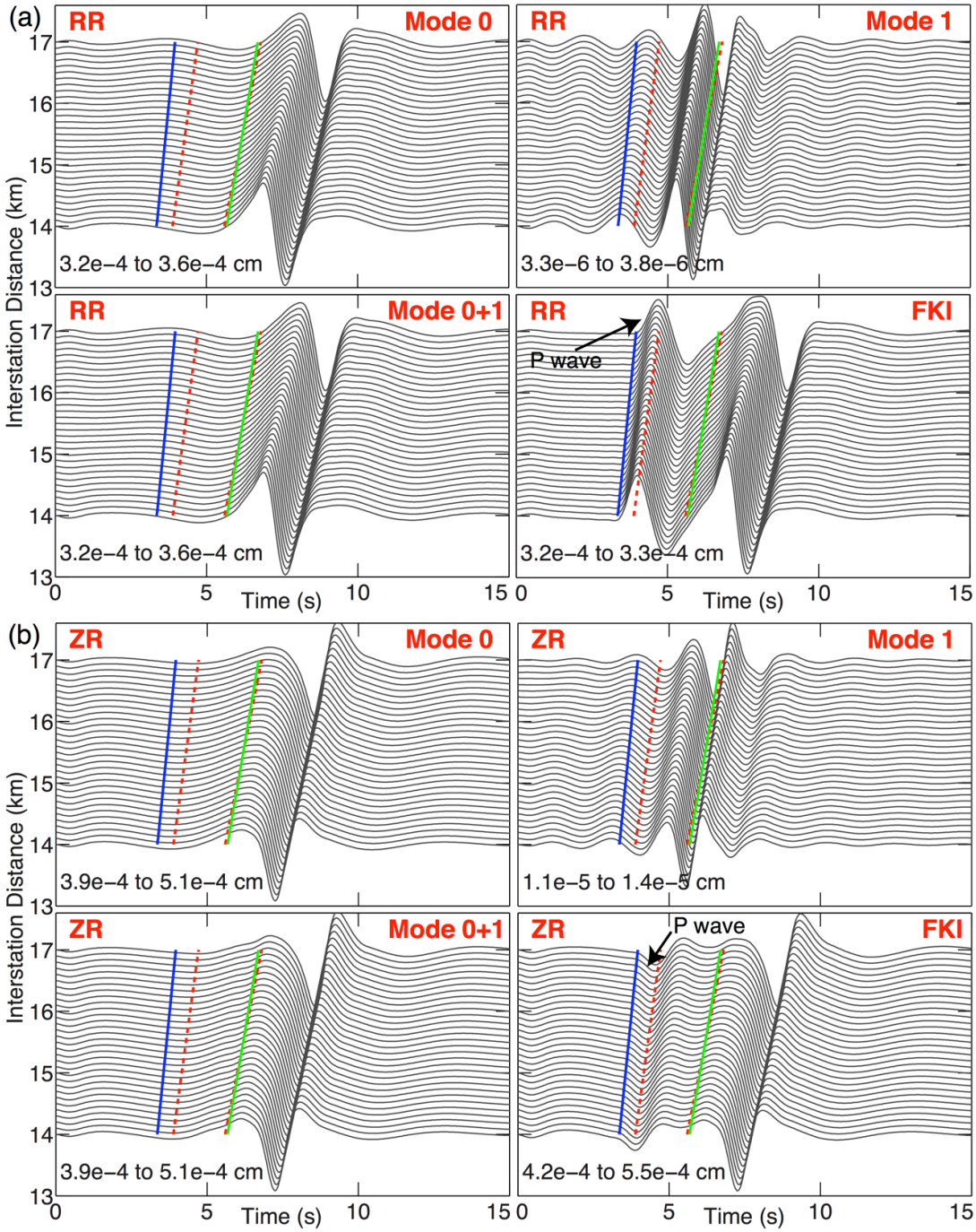

Figure 5.17: (a) Same as Fig. 5.16 but for RR component SGFs at interstation distances of 14-17 km. (b) Same as (a) but for ZR component SGFs.

5.5.4 NGFs with USGS 1.0 Hz sensors

Fig. 5.18 shows GF comparisons for station pairs with one station being a USGS vertical component short period (~ 1.0 Hz) station, for which only the TZ, RZ and ZZ components are available (with the vertical component station being the receiver). The NGF-SGF comparisons for these station pairs are important as four of these stations (GAXB, GBG, GGPB and GSG) lie well outside the reservoir area (> 3 km away from the reservoir outline and the LBNL network) and none of our 1D velocity models are calibrated to fit these paths. Moreover, a single background 1D model is assumed in model G3D1 for almost all regions outside the reservoir area and an artificial, unrealistic boundary exists between the 1D and the 3D models along the reservoir outline, except to the northwest. Model REF, which is a 1D average of a 3D model of NW Geysers, fits most paths to station GPM and GSG, that lie to the NW and NE of The Geysers, respectively. However, large time delays, -0.4 to -0.75 s, are clearly observed at station GSG (see waveforms for ACR-GSG, JKR-GSG, STY-GSG, FUM-GSG in Fig. 5.18) consistent with body wave tomography studies that have determined lower velocities to the northeast of The Geysers attributed to rocks of the Clear Lake volcanics and interbedded sedimentary deposits of the Great Valley sequence (Hearn *et al.* 1981; Eberhart-Phillips 1986; Julian *et al.* 1996). The delays are also consistent with a 0.25 s P-wave station correction at GSG with respect to GBG (Eberhart-Phillips & Oppenheimer 1984). The retrieval of robust NGFs from these sensors demonstrates their potential in supplementing temporary deployments of higher quality broadband sensors for ambient noise Rayleigh wave tomography studies (e.g. Porritt *et al.* 2011). This is especially true for regions like Northern California, where they are a significant part of pre-existing seismic infrastructure in the Northern California Seismic Network (http://www.ncedc.org/ncsn/, last accessed July 2016).
We were also able to retrieve robust NGFs with the accelerometer at station DRH (Fig. 5.19) that compare very well to SGFs at distances up to 20 km. The RR component NGFs for station pairs CLV-DRH, HVC-DRH and ACR-DRH also show strong P-waves (see Fig. 5.17a for comparison). Low gain accelerometers have been successfully used in some ambient noise tomography studies (e.g. Cho *et al.* 2007).

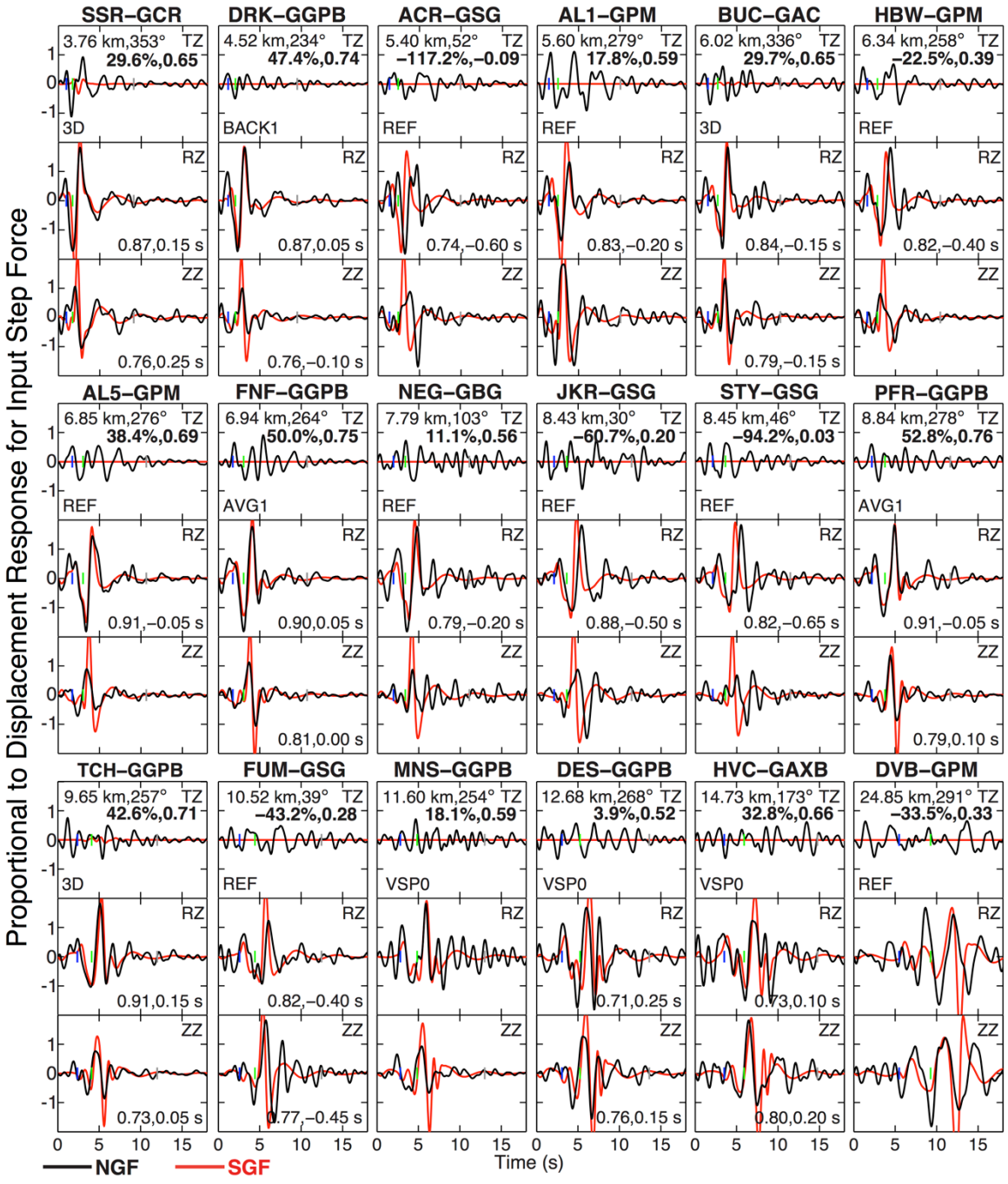

Figure 5.18: Same as Fig. 5.11b, but for all distances and stations pairs with one USGS vertical component 1.0 Hz sensor. Interstation distance and azimuth, and the overall goodness-of-fit estimates are at the top of TZ subplots.

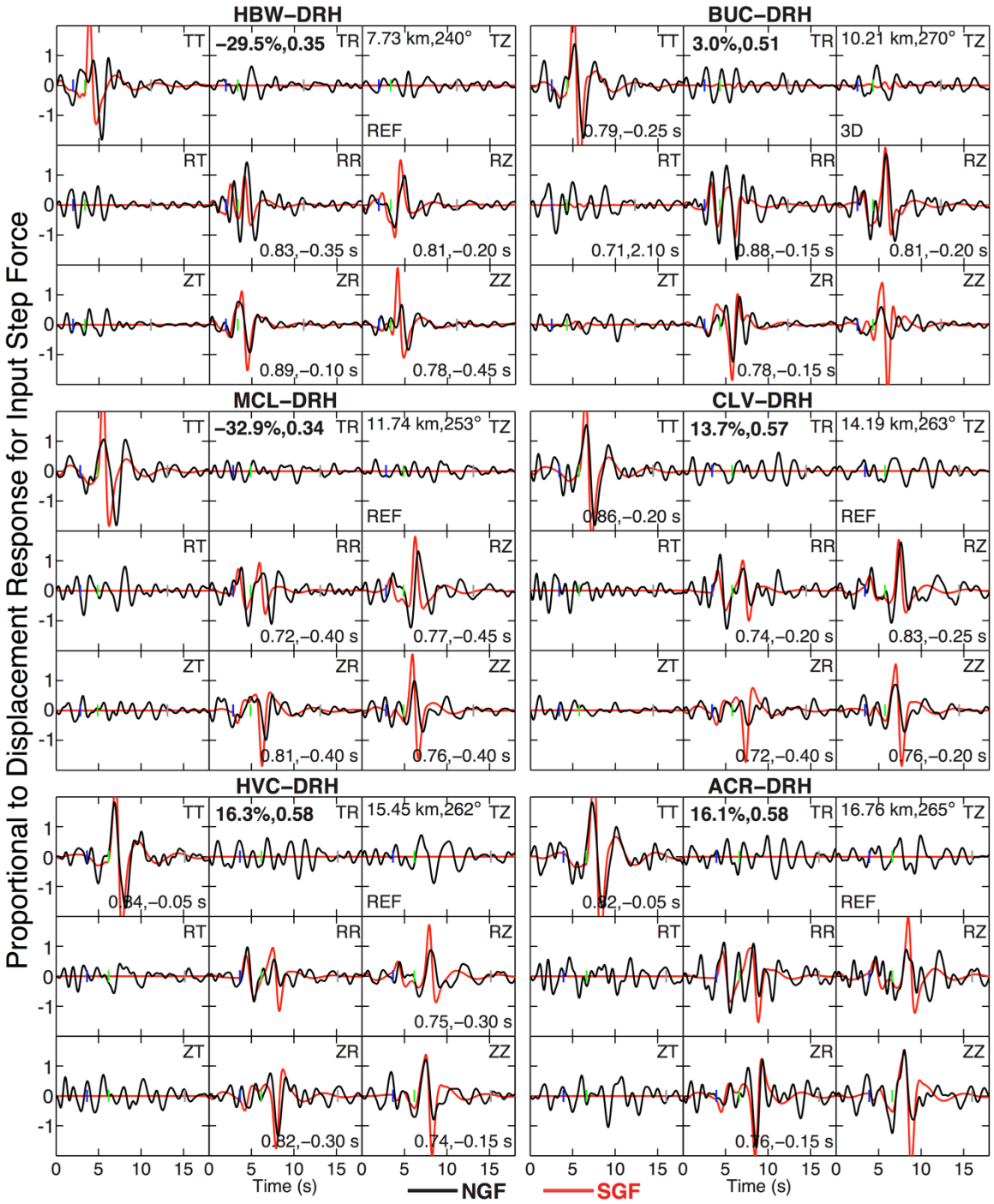

Figure 5.19: Same as Fig. 5.11b, but for all distances and stations pairs with station DRH.

5.6 Contribution of 3D structure and anisotropy

Even after the orientation corrections, the NGFs for some longer distance paths ($\gtrsim$ 8 km or ~1.7 λ) show significant non-zero amplitudes on the T-[R,Z] components that appear robust with respect to the trailing noise (Fig. 5.20). These waveforms are reproduced well by the SGFs computed using the 3D velocity model indicating the effects of significant 3D structure at distances $\gtrsim 2\,\lambda$. We visually identified these inter-station paths, which appear to be approximately parallel to the southwestern boundary of the reservoir area along the extent of the high-velocity region in the southeast section of the reservoir. While most of these paths involve stations SSR and SRB, the teleseismic wave analysis described in the section **5.4.5 Sensor orientations** indicates that the sensor installed at SSR was correctly oriented. It is possible that off-great-circle wave propagation or multi-pathing effects along the large velocity contrast cause these large amplitudes on the T-[R,Z] components. However, the 3D velocity model is poorly resolved outside the reservoir boundary (Gritto *et al.* 2013a). There are other interstation paths for which we see robust non-zero amplitudes on these components but they are not reproduced by the 3D velocity model.

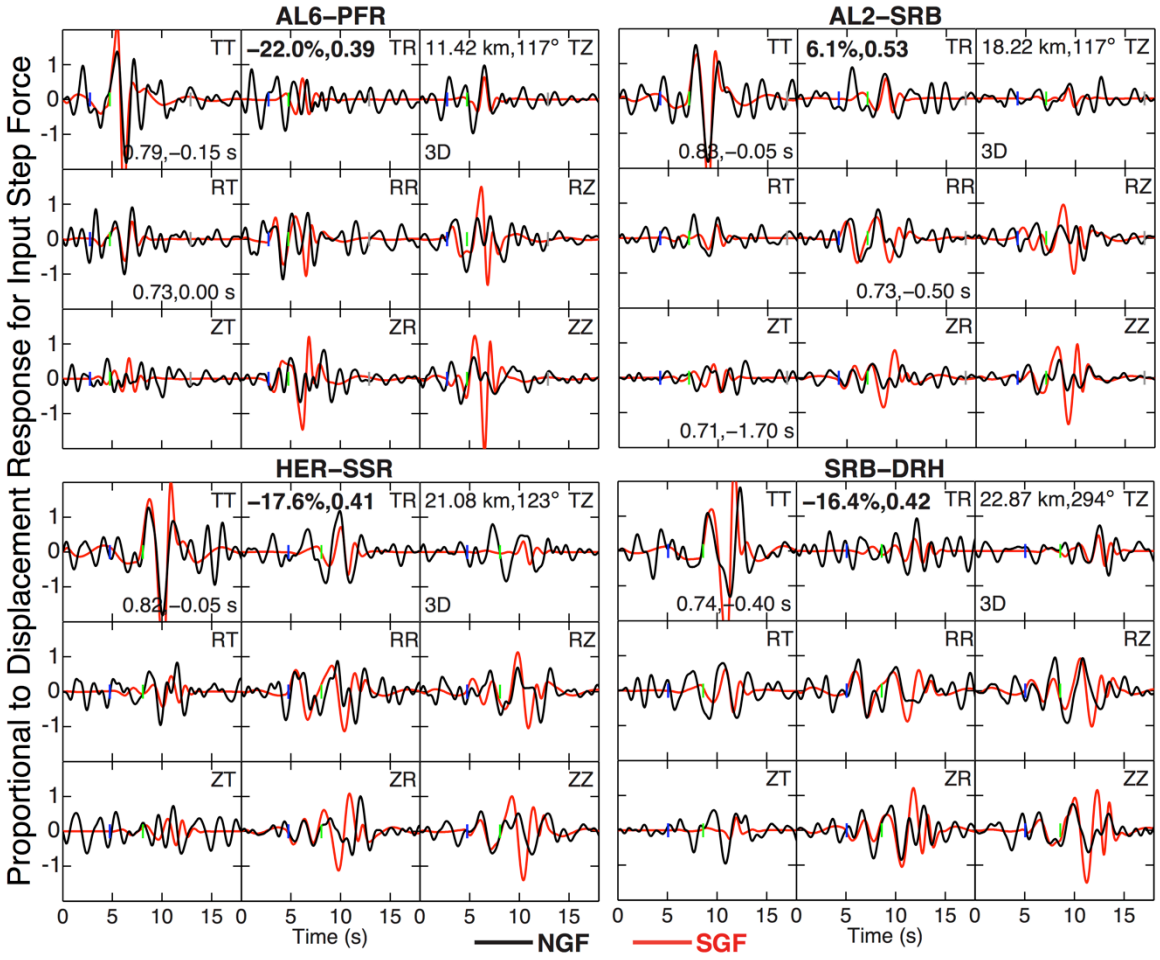

Figure 5.20: Same as Fig. 5.11b, but for some station pairs with significant non-zero amplitudes on the T-[R,Z] components of NGFs even after corrections for sensor misalignments. These amplitudes are reproduced well by the 3D velocity model.

Assuming far-field noise source incidence only, if the station pairs are not aligned with the dominant noise source incidence direction, non-zero amplitudes can be expected in T-[R,Z] components of NGFs (Roux 2009; Durand *et al*. 2011). It is possible to minimize the amplitudes in these components by rotating the reference frames at the two stations so that the new reference frames are approximately aligned with the azimuth of dominant noise source incidence direction (the method is referred to as Optimal Rotation Algorithm [ORA]; Roux 2009). We quantify the relative amplitudes of T-[R,Z] components of the NGFs at The Geysers, in terms of the misfit parameter φ, defined as the ratio of sum of squares of amplitudes of the four off-diagonal components to the sum of squares of all components of the NGF tensor (equation 17 in Saade *et al*. 2015). We used ~390 station pairs with the full 9-component NGF tensor and use the waveform segments described in section **5.4.6 Procedure for comparison between NGFs and SGFs**. Fig. 5.21a shows the logarithm of the misfit parameter φ as a function of the interstation distance and the actual azimuth/backazimuth in the range [0-180°]. We examine φ as a function of azimuth of the station pairs to investigate any systematic relationship.

While our passband (0.2-0.9 Hz) contains higher frequencies compared to secondary microseisms (~0.1-0.2 Hz), we assume that the dominant background noise in our passband is also generated along the coast and is incident on our study region at azimuths of ~30°–70° (Stehly *et al.* 2006; Roux 2009; Durand *et al.* 2011). If the amplitudes in T-[R,Z] components of NGFs were strictly a function of deviation of the station pair azimuth from the assumed dominant noise source incidence direction, we should see significant non-zero amplitudes for station pairs aligned at large angles to that direction. For NGFs at short interstation distances (< 4 km) that generally have good signal-to-noise ratios (i.e., Figs 5.11, 5.13, 5.14), misfits for many station pairs with azimuths outside the ~ [30°, 70°] range are as low ($\log10(\varphi)$ ~ –1.4 to –1.2) as misfits for station pairs with azimuths in the assumed dominant noise source direction, i.e. ~ [30°, 70°] (Fig. 5.21a). For example, station pairs ACR-HVC and FNF-PFR, oriented at azimuths 115° and 137°, respectively, have small amplitudes on the T-[R,Z] components with $\log10(\varphi)$ < –1.25 (Fig. 5.21c). For station pairs at distances ~ 4-8 km, it appears that the average misfits (~ –0.89) at azimuths ~ [30°, 70°] are marginally lower than those at other azimuths (~ –0.62). We apply ORA to minimize the amplitudes in the T-[R,Z] components by trying different values of ψ (grid search with 1° step) at all stations (e.g., Roux 2009). For station pairs ACR-HVC and FNF-PFR in Fig. 5.21c, we obtain small values of ψ or deviations from the actual azimuth (–6°, –10° and –1°, –2°, respectively). For ~48% of ~390 station pairs, the angles ψ that minimize amplitudes on the T-[R,Z] components also lead to a deterioration of the fits (lower overall VR) between the NGFs and the SGFs in the remaining TT, RR, RZ, ZR and ZZ components. Fig. 5.21b shows that the application of ORA fails to significantly reduce the large misfits for station pairs at distances ≥ 4 km. The reduced misfit values (~ –1.0 to –0.5 on log10 scale) for our NGFs in the frequency band of 0.2-0.9 Hz at distances ≳ 4 km at The Geysers are greater than misfits for NGFs at Parkfield estimated at shorter distances in terms of wavelengths, i.e., passbands ~0.1-0.2 Hz ($\log10(\varphi)$

$\lesssim -1.0$; Roux 2009) and ~0.075-0.2 Hz ($\log10(\varphi) \lesssim -1.3$; Durand *et al.* 2011) at distances $\lesssim$ 10 km. This indicates the non-zero signals in T-[R,Z] components of our NGFs at large distances are just leading or trailing noise in the NGF time-series rather than coherent signals resulting from systematic azimuthal deviation of interstation paths from a particular noise source direction (assuming pure noise on all nine components, misfit is $\sim -\log10(4/9) = -0.35$). For all stations, the final azimuthal polarizations corrected for ψ are considerably scattered instead of aligned sub-parallel to the direction of any dominant noise source direction (e.g., Roux 2009).

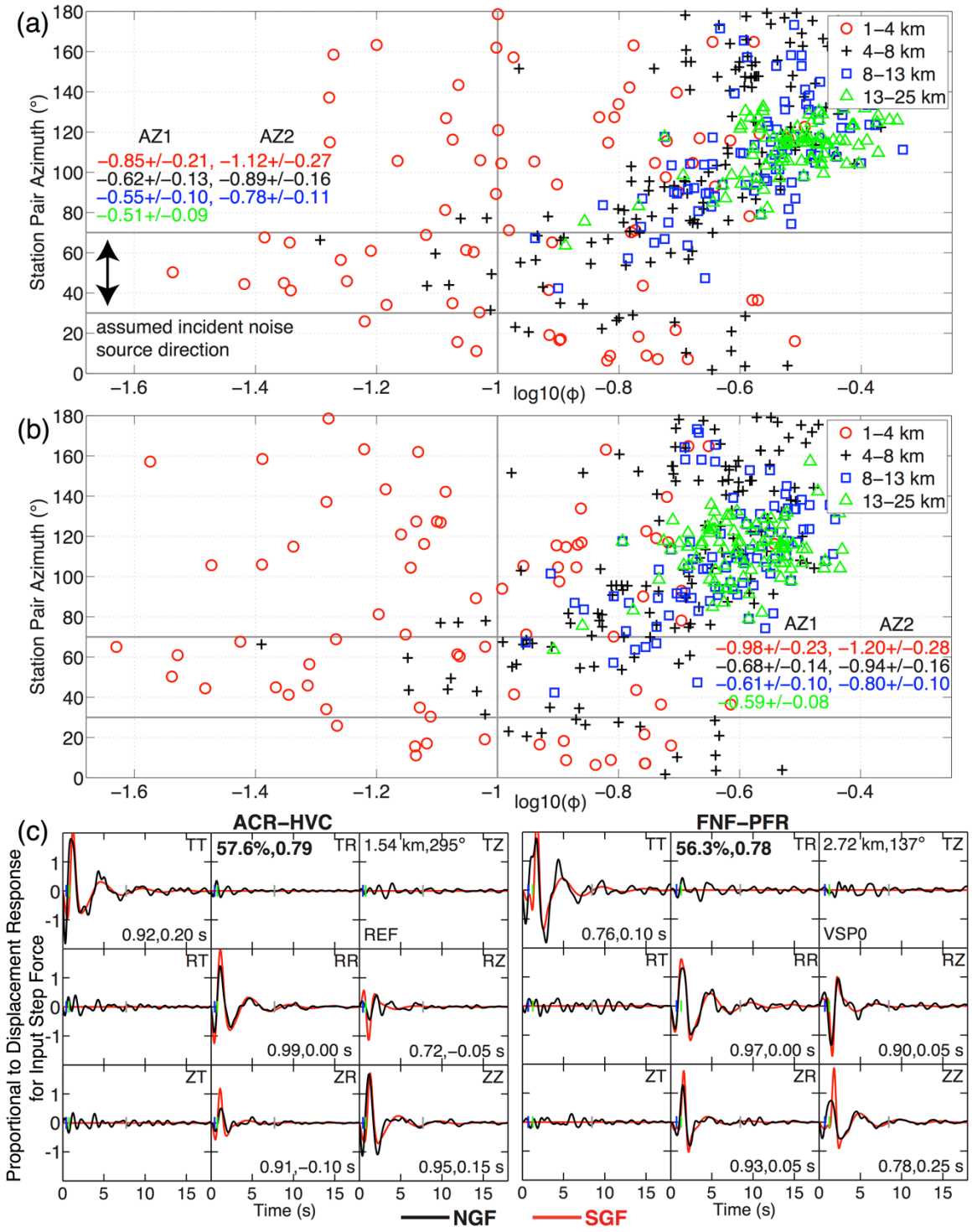

Figure 5.21: (a) Sum of squares of amplitudes on T-[R,Z] components of NGFs normalized by the sum of squares of amplitudes on all components, as a function of interstation distance and interstation azimuth/backazimuth in [0-180°] range. Colored symbols represent data points for different distance ranges. Horizontal gray lines represent the azimuth range of the assumed dominant noise source direction [30°, 70°]. Vertical gray line marks $\varphi = -1.0$, the quality threshold used by Roux (2009). Color coded numbers are the mean and standard

deviation of φ in different distance ranges. AZ2 and AZ1 refer to NGFs of station pairs in azimuth/backazimuth range [30°-70°] and all other azimuths, respectively. Note that unlike fig. 5 in Roux (2009), this figure shows the data points plotted at actual interstation azimuth/backazimuth. (b) Same as (a) but with reduced φ following application of Optimal Rotation Algorithm. The data points are plotted at original interstation azimuth/backazimuth. (c) Same as Fig. 5.11b, but for two station pairs with very small amplitudes in the T-[R,Z] components despite being oriented (115° and 137°, respectively) at large angles with respect to the assumed dominant noise-source direction.

It is possible that seismic anisotropy also contributes to the non-zero amplitudes in these components at larger distances by giving rise to quasi-Love or quasi-Rayleigh waves (Maupin & Park 2007). The shallow subsurface (top ~3-5 km) at The Geysers can be considered as a horizontal transversely isotropic (HTI) medium with an average ~4% V_S anisotropy (up to ~11% at some locations) estimated from shear-wave splitting measurements on local earthquakes records (Majer *et al.* 1988; Elkibbi & Rial 2005; Elkibbi *et al.* 2005). The V_S anisotropy is defined as $\frac{V_{S,fast}-V_{S,slow}}{V_{S,fast}}$x100 as in Elkibbi *et al.* (2005). The anisotropy at The Geysers is believed to be caused by stress-induced alignment of fractures and cracks. While the fast axes are generally parallel or sub-parallel to the N-to-NE direction of the regional maximum compressive stress, a smaller set of NW-SE oriented fast axes are also observed, primarily in the southeast Geysers and likely related to local fault shearing effects (Elkibbi & Rial 2005; Elkibbi *et al.* 2005). The 3D model of Gritto *et al.* (2013a, 2013b) was inverted utilizing a well distributed set of earthquakes and stations, and therefore can be considered as an isotropic average of the velocity structure at The Geysers, with a maximum of 19% ± 7% variation in V_S at depths between 0.5 km and 4.0 km. Therefore, seismic wave propagation at The Geysers at large distances is possibly controlled, to first order, by the average 3D isotropic structure in the reservoir. In order to test the amplitudes caused by anisotropy and expected in the T-[R,Z] components of the NGFs, we also compute SGFs for station pairs at The Geysers incorporating an HTI medium in the 1D velocity models. The 3D finite-difference seismic wave propagation code SW4 provides the capability to model seismic waveforms for layered anisotropic but purely elastic media. Therefore, we restrict this analysis to stations pairs at distances < 10 km, so that we can ignore the effects of anelastic attenuation (further discussed in section **5.9 Amplitude decay**). We also ignore the considerable scatter in the degree of anisotropy and in the fast axis directions across The Geysers that were observed by Elkibbi & Rial (2005) and Elkibbi *et al.* (2005).

We use the formulation of Hudson (1981, 1982) as provided in equations 1 to 4 in Crampin (1984) to estimate the five anisotropic elastic constants for an HTI medium – A, C, F, L, and N in Love notation (Saade *et al.* 2015). The differences between (A, C) and (L, N) determine the V_P and V_S anisotropy, respectively. A review on the $\eta = \frac{F}{A-2L}$ parameter can be found in Kawakatsu *et al.* (2015). The effective anisotropic elastic tensor in a cracked medium can be modeled as the sum of the elastic tensor for the uncracked solid and first and second order perturbation terms that depend on crack density (ϵ), crack aspect ratio (d), Lame's constants for the uncracked solid, and Lame's constants for the weak crack inclusions (λ', μ'). This formulation assumes a weak distribution of parallel disconnected penny-shaped cracks with

dimensions and spacing much smaller than the seismic wavelengths under consideration and is valid for small values of $\epsilon < 0.1$ (Crampin 1984; Peacock & Hudson 1990; Cheng 1993). The Geysers is characterized by a vapor-dominated geothermal field with a considerable volume of water injected into the reservoir. For this study, we assume that the cracks are filled with water ($V_P = 1.5\frac{km}{s}, \lambda' = 2.25e9\ Nm, \mu' = 0$). It is important to note that the presence of steam in water can drastically reduce V_P of the two-phase mixture, especially if the water and steam phases are in thermodynamic equilibrium. However, this effect is expected to decrease with increasing pressures and temperatures (Liu & Kieffer 2009). Majer *et al.* (1988) investigated one site at The Geysers and found little or no evidence for V_P anisotropy. Therefore, we assume thin cracks, $d \sim 0$, which gives A = C. An assumed value of $\epsilon \sim 0.036$ leads to an approximate V_S anisotropy ~ 4% in the layers of the top ~3.1 km of the 1D velocity models. We obtain values of $\eta \sim 0.82$-0.89, compared to $\eta = 1.1$ as adopted by Saade *et al.* (2015) based on scaling relationships (Montagner & Anderson 1989). We test two directions of crack normals, N60°W and N125°W, transverse to the average directions of the fast axes determined by Elkibbi and Rial (2005). For the computation in SW4, the crack normal is assumed to be in direction 1 and the station paths are rotated accordingly.

Fig. 5.22a shows NGF and SGF comparisons for 2 station pairs at distance < 10 km for which the significant non-zero amplitudes on the T-[R,Z] components of the NGFs are reproduced well by the SGFs computed using the 3D velocity model. Fig. 5.22b shows the same NGFs as Fig. 5.22a but with SGFs computed with an elastic (no anelastic attenuation) and anisotropic version of the 1D velocity model VSP0, incorporating ~4% V_S anisotropy in the top ~3.1 km layers with crack normal direction N125°W for station pairs FUM-SSR and DRK-SSR. The VR and the amplitudes on the T-[R,Z] components for the 1D anisotropic models are clearly smaller than those for the 3D model. The 1D anisotropic model SGFs yield higher VR compared to the isotropic 1D or 3D models for only 13 out of ~270 nine-component station pairs (~5%) at distances < 10 km; for 6 out of 13 station pairs, the improvement in VR was negligible (< 1%). In the case of the SGFs dominated by surface waves in an anisotropic medium, ORA can also be used to minimize the amplitudes in the T-[R,Z] components (Durand *et al.* 2011; Saade *et al.* 2015). We also perform a synthetic test, in which we compute SGFs assuming the anisotropic REF model with one reference station at the center of a circle and other stations placed at radial-distance intervals of 0.5 km up to a total distance of 10 km and 2.0° azimuthal spacing. For these GFs, the maximum value of φ ranges from ~4e-4 to ~1e-2 for distances between 0.5 to 10 km. These values are smaller than φ for our NGFs at The Geysers (Fig. 5.21a) at distances < 10 km. This observation, combined with the failure of ORA to significantly reduce φ in our NGFs (Fig. 5.21b), indicates that the large residual amplitudes in the T-[R,Z] components of the NGFs for most station pairs (< 10 km) at The Geysers correspond to just leading or trailing noise in the NGF time-series. These non-zero signals are unlikely to be real coherent signals resulting from systematic effects of non-uniform illumination from far-field noise sources or currently known subsurface anisotropy in the geothermal field. For at least some station pairs that have robust signals in the T-[R,Z] components, the 3D model provides better fits than the anisotropic 1D models. We leave analysis of the effects of anisotropy at distances > 10 km for future studies.

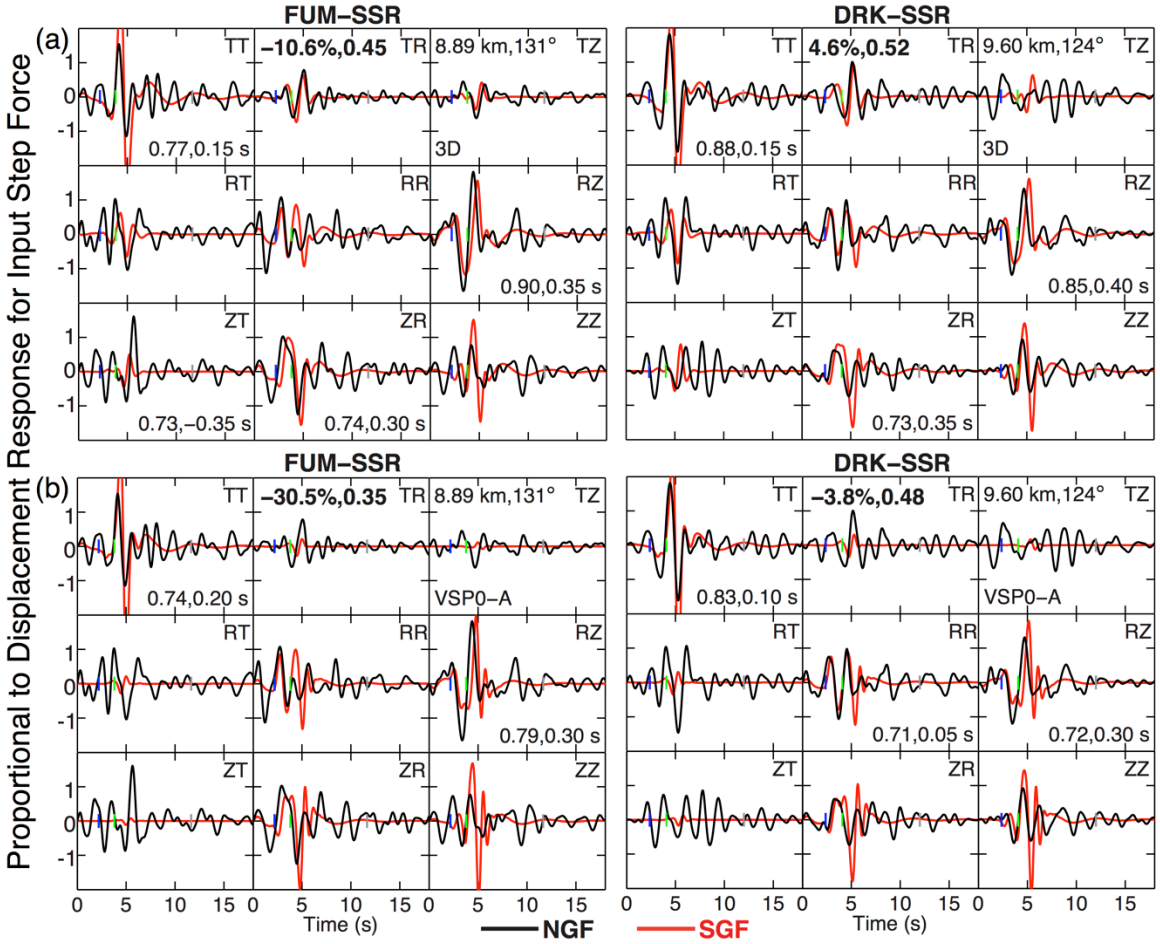

Figure 5.22: (a) Same as Fig. 5.20 but for 2 different station pairs at interstation distances < 10 km. (b) Same as (a) but for SGFs computed using an elastic and anisotropic version of the 1D velocity model VSP0 with ~4% V_S anisotropy to a depth of ~3.1 km and crack normal in the direction N125°W. '–A' has been added to the model names to indicate anisotropy. SGFs computed using the 3D velocity model fit the significant non-zero amplitudes on the T-[R,Z] components of NGFs better than SGFs computed using the 1D anisotropic velocity model.

5.7 Evaluation of velocity models

Fig. 5.23 shows a summary of ~385 interstation noise cross-correlation paths with the best-fitting VR between the NGFs and the SGFs ≥ –20%, grouped by the best-fitting velocity models, i.e., the models that provide the SGFs with the highest VR for the NGFs along these paths. The VR threshold of -20% is a quality check on both, the quality of the NGFs (poor quality NGFs will return poor VR upon comparison with SGFs), and the ability of velocity models to fit the NGFs (paths along which the velocity models are found to be deficient [e.g. paths to station GSG] are filtered out). Out of the four 1D models tested, REF provides the highest VR for the most number of paths, primarily across NW and central Geysers (Fig.

5.23a). This can be attributed to its origin from a 3D model of the NW Geysers region. Similarly, VSP0, which corresponds to a velocity profile in the SE Geysers, is the best-fitting velocity model for most NGFs across the SW- and the SE Geysers (Fig. 5.23c). The 3D model G3D1 provides the best-fitting SGFs for a slightly higher number of NGF paths compared to REF (Fig. 5.23e). To find regions where the 3D model fits the NGF waveforms significantly better than the 1D velocity models in a relative sense, we examine paths for which the VR of the 3D model SGFs exceeds those of the 1D models by an arbitrarily chosen threshold of 7% or more (Fig. 5.23f). Most of these paths are across the transition zone between the slower NW section and the faster SE section of The Geysers. The 3D model also incorporates a prominent low V_P/V_S ratio anomaly in this area with estimates (down to ~ 1.42) considerably lower than those in the 1D models (Figs 5.3, 5.4). Therefore, it is not surprising that the 3D model fits long distance paths across this complex region better than the 1D models. Models AVG1 and BACK1 provide minor improvements over other velocity models for a smaller number of paths in the NW Geysers (Figs 5.23b,d). As expected, the 1D models fit most of the paths to the stations outside the reservoir area (stations GAXB, GBG, GGPB, GSG) better than G3D1 (59 out of 62).

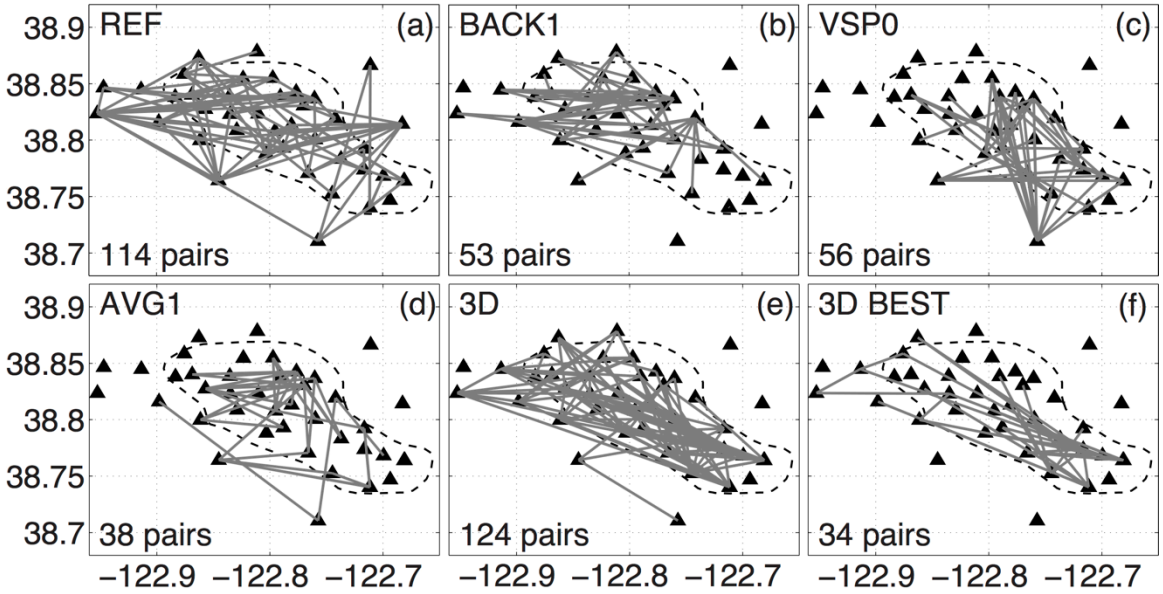

Figure 5.23: First five subplots (a-e) show interstation paths grouped by best-fitting velocity models. The velocity model and the number of paths are mentioned in the top and bottom left corner, respectively. Subplot (f) "3D BEST" shows paths for which VR of NGFs with the 3D model SGFs exceed the VR with the 1D model SGFs by 7% or more (34 out of 124). For all the paths shown in this figure, the best-fitting VR is ≥ –20%.

Next we examine phase differences represented by robust time delays (defined in ***NGF vs. SGF at various distances***) between NGFs and SGFs computed with different velocity models for some station pairs. We first consider NGFs and SGFs for intermediate distance (between 2 km and 12 km) interstation paths in ~NW and Central Geysers (Figs 5.23a,b), for which REF and BACK1 are the best-fitting velocity models. Barring some large outliers (< –1.0 s or > 1

s; ≲ 2% of measurements removed), the robust time delays for these pairs of NGFs and SGFs are ~ –0.02 ± 0.17 s (mean ± 1 standard deviation; for ~240 measurements). For NGFs along the same paths, SGFs computed using the faster velocity model VSP0 lead to time delays of ~ –0.12 ± 0.18 s, indicating slightly earlier arrival of SGFs with respect to NGFs. Similarly, time delays between NGFs between SGFs computed with the best-fitting model VSP0 for intermediate distance paths in ~SE Geysers (Fig. 5.23c) are ~ +0.12 ± 0.11 s (for ~75 measurements). The actual velocities could be slightly greater than VSP0 velocities. For NGFs along the same paths, SGFs computed using the slower velocity model REF lead to time delays of ~ +0.26 ± 0.16 s, indicating more delayed arrival of SGFs with respect to NGFs. Our interstation paths in Figs 5.23a-c are well distributed in azimuth which is expected to help reduce the effects of phase errors in NGFs due to non-uniform noise source distribution. The meaningful grouping of interstation paths in various sub-regions of The Geysers (Figs 5.23a-c) indicates an overall consistency of the results.

5.8 NGFs with BDSN stations HOPS and MNRC

We first analyze the simple waveforms of Love waves on the TT components of the NGFs from BDSN stations HOPS and MNRC to stations at the periphery of the reservoir area to gain insight into the shear wave velocity structure in the region to the northwest and to the east of The Geysers (Fig. 5.24a). The REF model SGFs are too fast compared to the NGFs (Figs 5.24b,c), which is consistent with body-wave travel-time studies that suggest that the reservoir area has faster than regional seismic velocities (Majer & McEvilly 1979; Eberhart-Phillips 1986). The SGFs of the regional velocity model, GIL7 (Fig. 5.3) can reasonably fit the Love waves on the paths from the eastern boundary of the reservoir to MNRC (Fig. 5.24b). GIL7 SGFs are also consistent with the NGFs of paths from some of these stations to station GSG (Fig. 5.24e), for which the REF model was determined to be too fast (Fig. 5.18). But we find that GIL7 is too slow for paths from the northwestern boundary of the reservoir area to HOPS (not shown here) with broadband phase delays from ~1.3 s to ~2.1 s. Therefore, we iteratively perturb the V_S values in the top ~5 km of GIL7 to improve the waveform fits of the TT components of the NGFs for these paths. Primarily deceasing the V_S values in the top ~4 km layers of GIL7 by ~0.1-0.3 km/s (model GIL7.1 shown in Fig. 3) produces satisfactory waveform fits (Fig. 5.24c). In addition to Love waves, clear SH waves can also be identified in the NGFs of some paths to station HOPS (from HBW, RGP, MCL, BRP) that compare well to the SGFs.

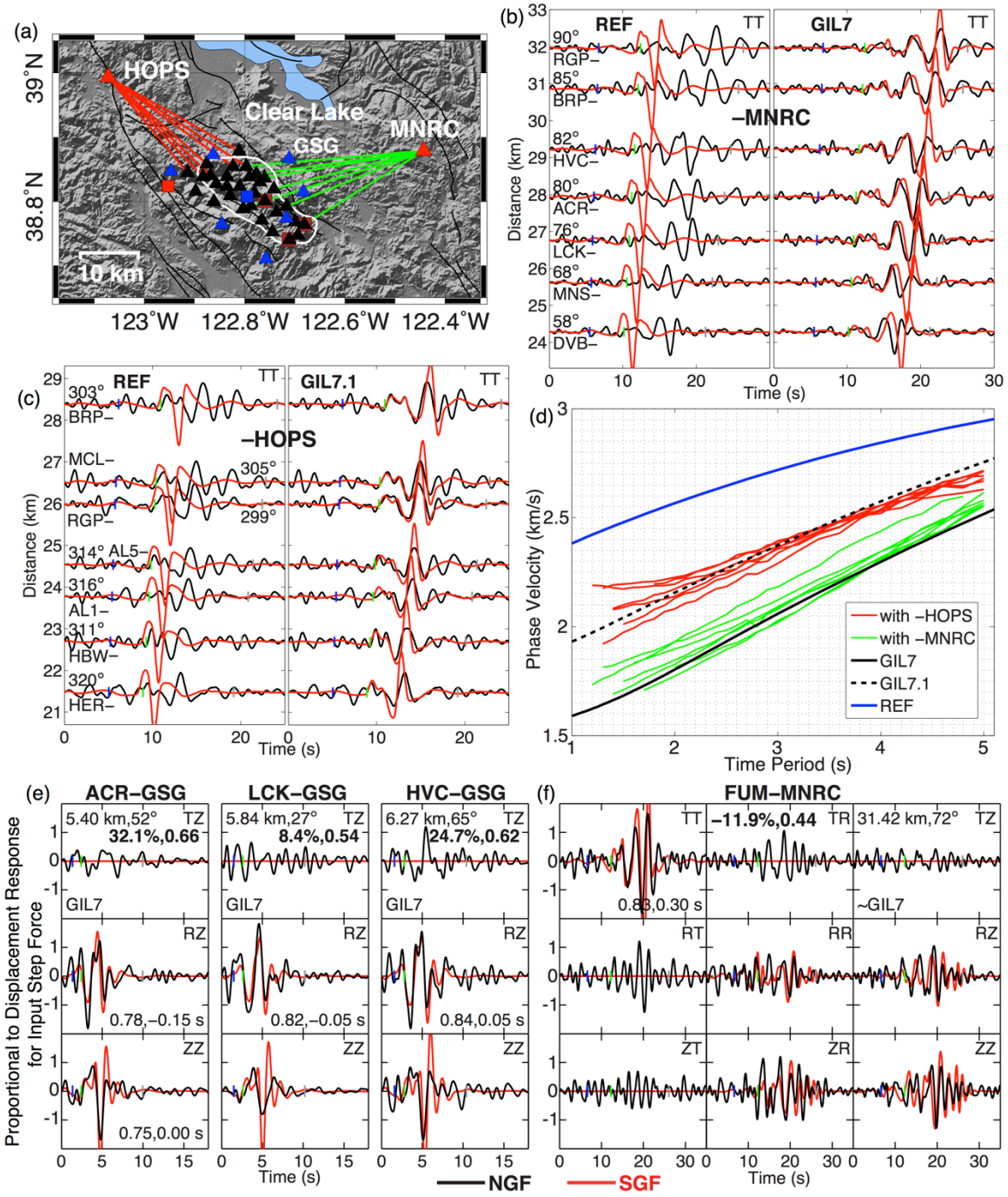

Figure 5.24: (a) Map showing interstation paths (red and green lines) from stations on the periphery of the reservoir area (white polygon) to BDSN stations HOPS and MNRC (red triangles), respectively. Meaning of other symbols is same as in Fig. 5.1; (b) TT component NGFs (black traces) and SGFs (red traces) computed using REF (left subplot) and GIL7 (right subplot) velocity models for paths from stations at the eastern boundary of The Geysers to station MNRC arranged in the order of increasing interstation distance. Station names and azimuths are shown near the traces; (c) same as (b) but for paths from stations at the northwestern boundary of The Geysers to HOPS. The velocity models are REF (left subplot) and GIL7.1 (right subplot); (d) Observed Love wave phase velocity dispersion curves

measured on TT component NGFs for paths in Figs 5.24a-c plotted against phase velocities predicted for models REF, GIL7.1 and GIL7; (e) same as Fig. 5.18 but for station pairs including GSG and stations at the northeastern boundary of the reservoir and using velocity model GIL7; (f) same as Fig. 5.15 but for a station pair including MNRC.

We also compare the Love wave phase velocities extracted from the TT component in the NGFs for these paths (in Figs 5.24b,c) with synthetic phase velocities for the 1D velocity models (Fig. 5.24d). We first apply multiple filter analysis (Dziewonski *et al.* 1969; Herrmann 1973, 2013b) on the NGFs to measure group velocities at periods ~1.1 s to ~5.0 s (or ~0.2 to ~0.9 Hz) and then determine phase velocities using the reference dispersion curves to resolve the $2\pi N$ ambiguity, in which N is an integer (Bensen *et al.* 2007; Lin *et al.* 2008). In this frequency passband, observed phase velocities for paths to station HOPS are clearly greater than those for station MNRC by ~0.1 to ~0.3 km/s, and they agree well with phase velocities predicted by GIL7.1 and GIL7 models, respectively. All of these phase velocities are slower than the REF model velocities by ~0.3 to ~0.7 km/s. While it is possible that other velocity models (different from GIL7 and GIL7.1) might provide equal or better fits to these NGFs, it appears that to the first order, shallow crustal shear wave velocities in the region to the northwest of The Geysers are higher than those to the east of The Geysers, and they are both lower than velocities within the reservoir area. Comparing the RR, ZZ, ZR and RZ components suggests that the NGFs at most stations at The Geysers with BDSN stations HOPS and MNRC at distances > 30 km are characterized by complicated waveforms, poor fits with synthetic waveforms of GIL7 and its modified versions, and higher relative amplitudes of trailing noise. However, for some stations pairs (e.g. FUM-MNRC), good quality NGFs are retrieved that show remarkable similarity to the SGFs computed with GIL7 with slightly modified values (V_S in top 3 layers increased by 100 m/s, 50 m/s and 20 m/s, respectively) in the shallow crust (Fig. 5.24f). Note the large amplitudes in the TR and RT component of the NGFs in Fig. 5.24f, in which FUM has already been corrected for sensor misalignment (Fig. 5.11).

5.9 Amplitude decay

We study the decay of ground motion amplitudes in the reservoir area by analyzing the NGF amplitudes as a function of frequency f and interstation distance R between 1 and 25 km.

5.9.1 Observations and interpretation of TT component amplitudes

First, we focus on the TT component as they consist of relatively simple SH and Love waves, and usually have the largest relative amplitudes among all components of NGFs (see Figs 5.11, 5.13–5.15, 5.19–5.20, 5.21c, 5.22). We use the NGF waveform segments in the data window prior to the causal filtering and the tensor amplitude normalization steps described in section **5.4.6 Procedure for comparison between NGFs and SGFs**. We extract spectral amplitudes from the smoothed Fourier amplitude spectra of the waveform segments at

multiple frequencies, $f = 0.25$ Hz, 0.42 Hz and 0.72 Hz. REF model Love wave group velocities $U_L(f)$ at these frequencies are ~2.44 km/s, 2.29 km/s and 2.22 km/s, respectively. The Fourier Spectral Amplitudes (FSAs) are extracted by interpolating the spectra at 7 points around the frequency of interest with half-width ~0.1 Hz and averaging the amplitudes with a 7-point Hanning window. We compare the NGF FSAs with the FSAs of the equivalent SGFs of the 3D and the 1D REF models that are computed the exact same way.

A second group of FSAs of Raw Synthetic Green's Functions (RSGFs) is extracted from the raw unfiltered velocity GFs of the same duration prior to the integration, zero-phase bandpass filtering, time-reversal and symmetric component steps in section **5.4.6 Procedure for comparison between NGFs and SGFs** (Fig. 5.8). This allows us to evaluate the degree of contamination of the SGF amplitudes from the "true" amplitudes and compare the decay characteristics better to earthquake ground-motion amplitudes. Without the contamination, the distance scaling of RSGF spectral amplitudes should be approximately similar to that of NGF amplitudes in a narrow frequency passband. To distinguish the effects of distance-dependent geometrical spreading, $G(R)$, and total anelastic attenuation, represented by the quality factor $Q(f)$, we also compare the FSAs of SGFs computed for velocity models with weak and strong anelastic attenuation. SW4 allows computation of synthetic seismograms for purely elastic 3D velocity models. Synthetic seismograms for the weak anelastic attenuation 1D models were computed by setting Q_P and Q_S to high values (1000 and 500, respectively) in all layers. For the strong anelastic attenuation 1D models, Q_P and Q_S are set to ~15 for depths < 5.8 km and ~25 for greater depths. In the article, we primarily focus on FSAs at 0.72 Hz, as the effects of anelastic attenuation are expected to be more prominent at higher frequencies.

Fig. 5.25a shows the TT component of the RSGF FSAs at 0.25 Hz as a function of R. The scatter in the amplitudes for the 3D velocity model is caused by smooth 3D variations in the seismic velocities. At 0.25 Hz and for $R < 25$ km, the ground motion decay is very similar for both, low Q and high Q models, implying that the effect of anelastic attenuation can be neglected at these low frequencies and small distances. Directly approximating $G(R)$ by the amplitude decay, we obtain $G(R) \sim R^{-0.82}$ to $G(R) \sim R^{-1.14}$, implying dominance of body waves. This decay is stronger than the surface wave geometrical spreading ($R^{-0.5}$) expected at distances $\gtrsim 1\lambda$ –2λ ($1\lambda \sim$ 11.4 km for Love wave phase velocity c_L~2.85 km/s at ~0.25 Hz) for surface sources. We also plot the RSGF FSAs of the 3D elastic model and 1D weak attenuation AVG1 model at 0.72 Hz. AVG1 is an average 1D model of the 3D velocity model within the reservoir area. Using various approximations, Menon *et al.* (2014) have shown that azimuthally averaging the coherence estimates of different station pairs for a 3D inhomogeneous but elastic velocity structure can introduce apparent anelastic attenuation in the decay of average coherence amplitudes if one were simply fitting an exponential decay model to the amplitudes. The similarity in decay characteristics of the FSAs obtained from the average 1D and 3D weak attenuation models at both 0.25 and 0.72 Hz suggests that it might be possible to detect amplitude decay caused by anelastic attenuation following proper averaging of a 3D velocity structure across all paths (including the ones outside the reservoir), at least for the wavelengths and heterogeneity scales analyzed in this study.

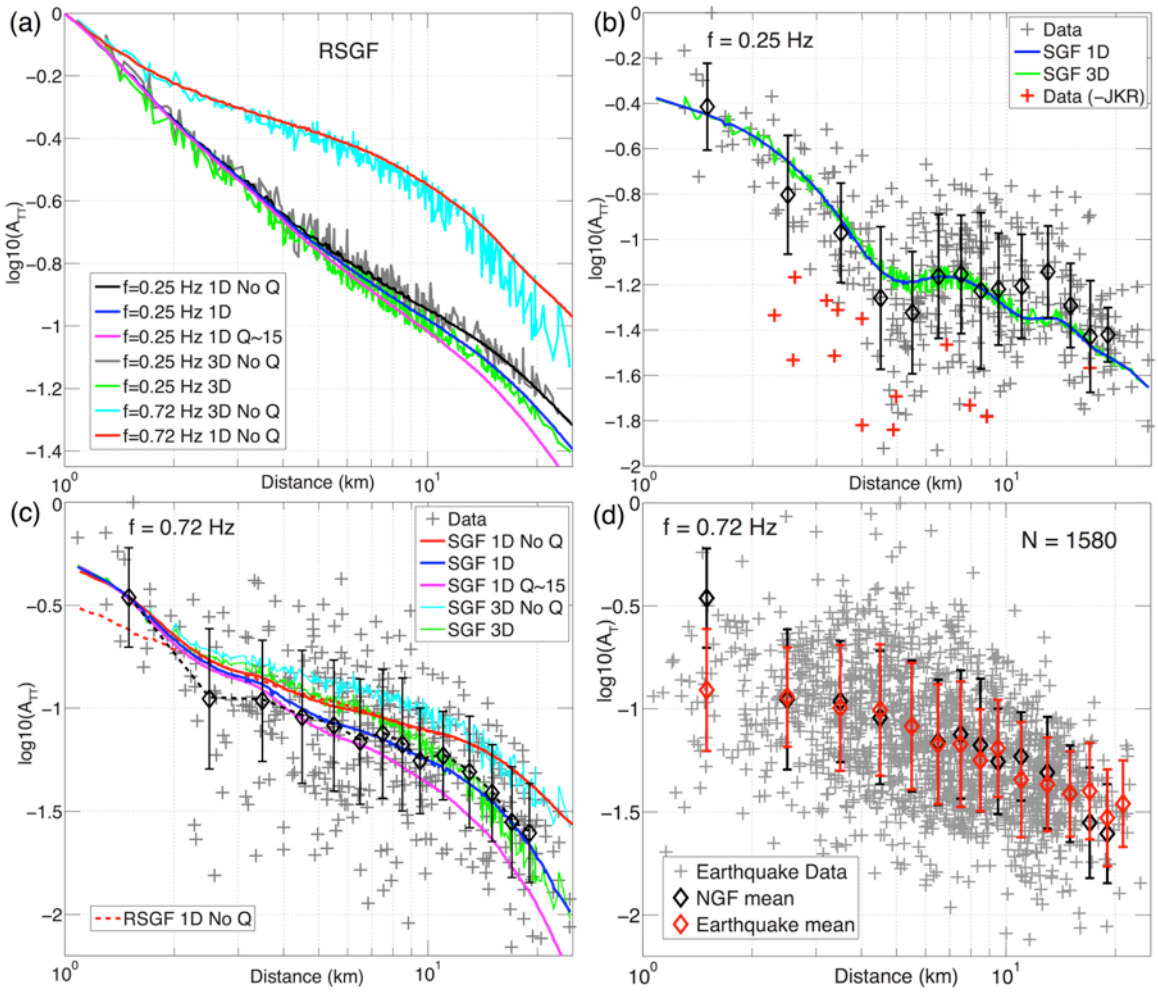

Figure 5.25: (a) TT component RSGF FSAs for different velocity models and frequencies on log10 scale as a function of distance. The decay curves are scaled so that they have similar amplitudes at ~1-2 km. 1D and 3D indicate FSAs of synthetics computed with 1D and 3D velocity models, respectively. "No Q" and "Q~15" indicate synthetics computed with weak and strong attenuation models, respectively. 1D RSGF decay curve at 0.72 Hz used the AVG1 model unlike other 1D model decay curves that use the REF model. (b) TT component NGF and SGF FSAs at 0.25 Hz as a function of interstation distance. The NGF FSAs (gray +) are uniformly scaled up by a constant such that the maximum value is 0. The frequency is indicated at the top left corner of the plots. Black diamonds and error bars represent the mean of NGF amplitudes and their standard deviation $\pm$ 1 σ in bins for all bins with more than five data points. The bin widths are 1 km and 2 km for distances $\leq$ 10 km and > 10 km, respectively. "SGF 3D" and "SGF 1D" are FSAs of equivalent SGFs of the 3D and 1D REF velocity models, respectively, plotted for the same station pairs. The FSAs of SGFs are uniformly scaled by a constant to minimize the L1 norm of their difference with the binned NGF FSAs. (c) Similar to (b) but for FSAs at 0.72 Hz. We also plot synthetic FSAs of weak and strong attenuation models. The SGF decay curves are scaled such that their amplitude at ~1.5 km is similar to the average amplitude of NGF FSAs in the 1-2 km range. Scaling the binned NGF decay curve instead, to directly fit the REF model SGF decay curve by

minimizing the L1 norm (black dashed line), doesn't change the absolute amplitudes significantly. The RSGF decay curve (red dashed line) is scaled to fit the REF model SGF decay curve at distances $\gtrsim$ 6 km. (d) The data (gray +) are tangential component FSAs of earthquake records at 0.72 Hz and the red diamonds and error bars represent the mean amplitudes and their standard deviation ± 1 σ in the bins. For comparison, we also plot binned TT component NGF FSAs at 0.72 Hz (black diamonds and error bars; same as [c]) that are scaled to minimize L1 norm of binned FSAs at distances $\gtrsim$ 3 km (~ 1 wavelength).

Fig 5.25b compares NGF and SGF FSAs at 0.25 Hz. Since the absolute amplitudes of the NGFs are unknown, we scale the FSA decay curves by increasing or decreasing all the data in the log scale by some constant for comparison. The shape of the decay of the SGF amplitudes is different from the decay seen for the RSGF amplitudes, because of the amplitude contamination as explained previously. The degree of contamination will be lower for higher frequencies and for gently decaying band-limiting tapers applied to cross-correlation spectral amplitudes such as a cosine taper. While there is considerable scatter in the NGF amplitudes, the mean amplitudes binned by distance show systematic decay with increasing distance. The variability in amplitudes (~0.3 in log10 units or a factor of ~2) is likely caused by significant differences in time periods over which daily NGFs of different station pairs were stacked (~25 days to ~3 years) or by effects of inhomogeneous noise source distribution or even by variability in the coupling of the sensors with the ground at different stations. For example, in Fig. 5.25b, amplitudes of NGFs for pairs with station JKR are systematically lower than mean amplitudes at the same distances. The amplitude decay characteristics of the NGFs provide useful information specifically for surface sources and they are expected to be free from earthquake radiation and source effects (but not from effects of inhomogeneous noise source distributions) that are likely present in earthquake ground motions at low frequencies and small epicentral distances. While the NGF amplitudes generally exhibit similar decay behavior as the SGF amplitudes, they appear to be systematically higher at $R \gtrsim 10$ km.

Fig. 5.25c compares SGF FSAs at 0.72 Hz for a variety of 1D and 3D models with NGF FSAs. In this figure, the decay curves are scaled such that the mean of the NGF FSAs at 1-2 km distance is similar to the SGF FSAs of different models at ~1.5 km. The decay of mean NGF amplitudes binned by distance is inside the domain spanned by the SGF amplitudes for 1D velocity models with weak and strong anelastic attenuation. The presence of NGF amplitudes well outside this domain would have led to the obvious conclusion that amplitude decay characteristics obtained from ambient noise cross-correlation at The Geysers are physically unrealistic and incorrect. If we assume that the relative interstation NGF amplitudes are correct and the REF model is a realistic 1D representation of the velocity structure at The Geysers, the difference between the average NGF FSAs binned by distance and the SGF FSAs for the weak attenuation REF model at $f = 0.72$ Hz can be attributed to anelastic attenuation. Fitting this difference in amplitudes by a factor of $e^{-\alpha R}$, where the attenuation coefficient α is defined as $\alpha = \frac{\pi f}{Q(f)U(f)}$, we obtain α ~0.03 km^{-1} and Q ~33 at 0.72 Hz (In Herrmann 2013, the attenuation coefficient's symbol is γ instead of α). The corresponding values of α and Q at 0.42 Hz are ~0.02 km^{-1} and ~27, respectively. By employing synthetic amplitudes from a realistic low-attenuation model as reference, we avoid any assumption regarding the functional form of geometrical spreading which can strongly

depend on crustal structure (Bowman & Kennett, 1991; Burger *et al.* 1987). Notwithstanding the scatter in the NGF FSAs, we find satisfactory agreement between the average NGF and the REF model SGF FSA decay curves at 0.72 Hz in Fig. 5.25c. Scaling the average NGF decay curve to directly fit the REF-model SGF decay curve by minimizing the L1 norm between the amplitudes doesn't lead to any significant change in amplitudes.

We reach similar conclusions for FSAs at 0.42 Hz (Fig. 5.26a). Measured values of α and Q are also comparable to Love wave α values predicted by the REF-model (~0.022 km^{-1} and ~0.04 km^{-1} at 0.42 Hz and 0.72 Hz, respectively) and constant S-wave Q values in the REF-model (~25 to ~40 in the top ~4.5 km), respectively. The similarity between the RSGF and the SGF FSAs at distances $R \gtrsim 3$ km shows that the contamination of the NGFs from the acausal amplitudes of the anti-causal component can be ignored at higher frequencies and large distances. For FSAs at 0.42 Hz, they are similar at distances $R \gtrsim 7$ km (Fig. 5.26a).

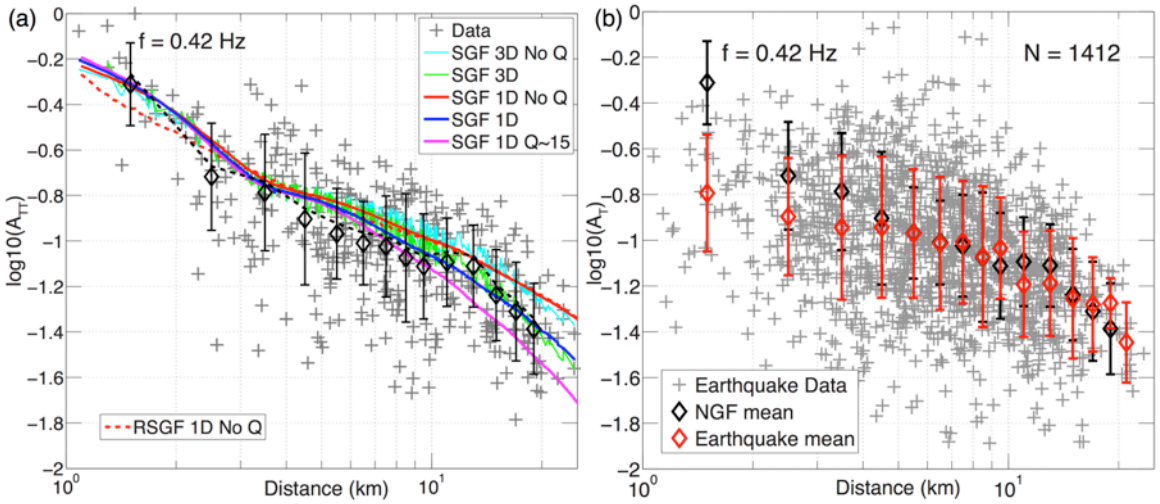

Figure 5.26: Figure similar to Fig. 5.25c,d but for TT component Fourier Spectral Amplitudes (FSAs) at 0.42 Hz instead of 0.72 Hz (a) TT component NGF and SGF FSAs at 0.42 Hz as a function of interstation distance. The NGF FSAs (gray +) are uniformly scaled up by a constant such that the maximum value is 0. The frequency is indicated at the top left corner of the plots. Black diamonds and error bars represent the mean of NGF amplitudes and their standard deviation $\pm$ 1 σ in bins for all bins with more than five data points. The bin widths are 1 km and 2 km for distances $\leq$ 10 km and > 10 km, respectively. "SGF 3D" and "SGF 1D" are FSAs of equivalent SGFs of the 3D and 1D REF velocity models, respectively, plotted for the same station pairs. "No Q" and "Q~15" indicate synthetics computed with weak and strong attenuation models, respectively. The SGF decay curves are scaled such that their amplitude at ~1.5 km is similar to the average amplitude of NGF FSAs in the 1-2 km range. Scaling the binned NGF decay curve instead, to directly fit the REF model SGF decay curve by minimizing the L1 norm (black dashed line), doesn't change the absolute amplitudes significantly. The RSGF decay curve (red dashed line) is scaled to fit the REF model SGF decay curve at distances $\gtrsim$ 8 km. (d) The data (gray +) are tangential component FSAs of earthquake records at 0.42 Hz and the red diamonds and error bars represent the mean amplitudes and their standard deviation $\pm$1 σ in the bins. For comparison, we also plot binned

TT component NGF FSAs at 0.42 Hz (black diamonds and error bars; same as [c]) that are scaled to minimize L1 norm of binned FSAs at distances $\gtrsim$ 4 km.

5.9.2 Comparison with earthquake ground motion amplitudes

We also examine the path attenuation of horizontal component ground motions of earthquakes at The Geysers. We selected ~121 earthquakes between M_D ~2.5-2.7 and depths < 4 km from the NCSN earthquake catalog available at NCEDC (Table 5.A.1). While earthquakes with greater magnitudes provide records with better signal-to-noise ratio, we find that the data recorded by the 4.5 Hz geophones are contaminated with long-period transients synchronous with the onset of strong shaking at many stations. For this analysis, we also use the co-located 3-component accelerometers at the USGS stations GAXB and GDXB and remove any record with maximum absolute value > 10^6 counts. The EW and NS component data were decimated to 20 Hz, corrected for instrument response to represent velocity, visually checked for quality and rotated to radial and tangential directions. Waveform segments of the same distance-dependent durations were selected and FSAs were extracted using the methodology similar to that adopted for the RSGFs. For the earthquakes, we also extract FSAs of similar duration noise-windows prior to the origin time and use only data, for which signal-to-noise ratio of FSAs is > 2. Fig. 5.27 shows examples of waveforms and Fourier amplitude spectra of an earthquake.

Fig. 5.25d shows tangential component earthquake FSAs at 0.72 Hz normalized by seismic moments of individual earthquakes calculated using M_D–M_0 relationships valid for central California (Bakun, 1984). At these low frequencies, M_W < 3 earthquakes can be treated as point sources and effects of source spectrum shape can be ignored. The earthquake ground motion amplitudes are not theoretically comparable to NGF amplitudes as they are a function of force-couple GFs (unlike single force GFs recovered by ambient noise cross-correlation), earthquake radiation patterns, earthquake depths and station azimuths. At distances $\gtrsim 1\lambda - 2\lambda$, the seismic phases that dominate waveforms of empirical surface-focus Green's functions and shallow earthquakes should be similar. Therefore, if the empirical GFs have been correctly retrieved from ambient noise cross-correlations in terms of the relative amplitudes, they should exhibit similar amplitude decay behavior as shallow-earthquake ground motions at far-field distances (e.g. Zhang & Yang 2013). Scattering at high frequencies and averaging across multiple paths and azimuths alleviates the effects of earthquake source radiation pattern. Most of the earthquakes used in our study are very shallow (94 out of 121 earthquakes are < 3 km deep; all earthquakes < 4 km deep; Table 5.A.1) with respect to the shortest wavelength examined in this section (λ ~ 3.2 km at ~0.72 Hz).

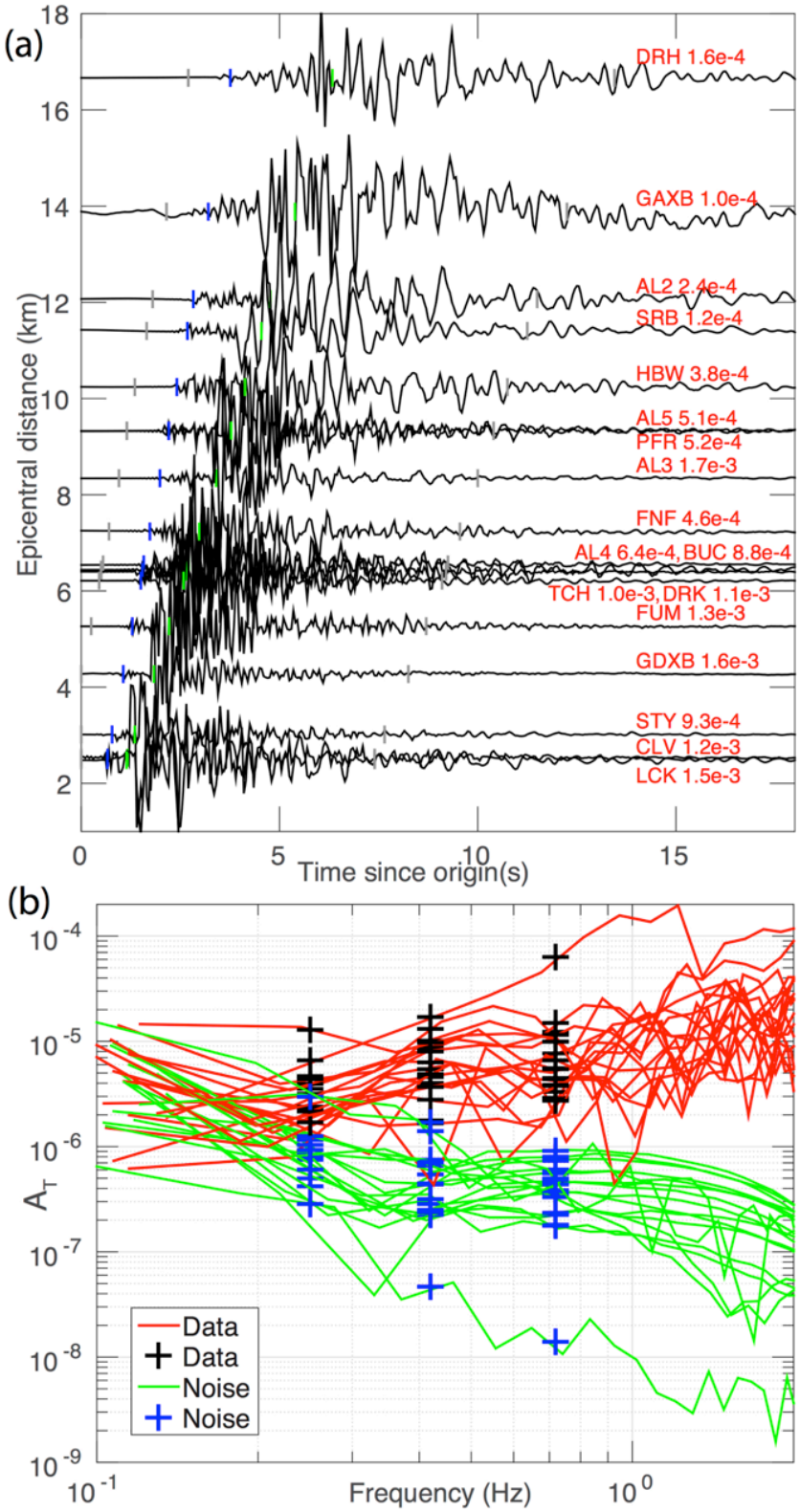

Figure 5.27: (a) Tangential component velocity waveforms of a M_D (duration magnitude) 2.68 earthquake at The Geysers on 2014-11-06, 09:54:57.50 (Northern California Seismic Network Event ID: 72336075). The waveforms are high-pass filtered at 0.1 Hz with a causal

2-pole Butterworth filter. The name of the recording station and the peak amplitude in m/s are indicated near each waveform. For reference, the blue and green marks are the theoretical P- and S-wave arrival times, respectively. The waveform segments between the two gray marks were used for extracting spectral amplitudes (shown in [b]). There are large differences between the observed S-wave arrival times and the ones predicted by the REF velocity model at large distances. (b) Fourier amplitude spectra of the earthquake ground-motion velocity waveforms (between the gray marks in [a]) along with spectra of pre-event noise windows of the same duration. Black '+' signs indicate the extracted earthquake FSAs at 0.25 Hz, 0.42 Hz and 0.72 Hz used in this study. They pass the quality criteria, i.e. they are greater than twice the noise FSAs (blue '+' marks) for 12, 18 and 18 out of 18 stations at 0.25 Hz, 0.42 Hz and 0.72 Hz, respectively.

In Fig. 5.25d, significant variability (standard deviation ~0.3 log10 units) can be observed in earthquake FSAs similar to other studies (e.g., Atkinson 2004). It is likely that many factors including effects of 3D structure, site amplification, and location and magnitude uncertainties (~0.2 units; Peggy Hellweg, personal communication, 2017) contribute to the scatter observed in the amplitudes. However, we find that the mean earthquake FSAs binned by distance show similar decay as the NGF FSAs at 0.72 for distances $\gtrsim$ 3 km. This provides strong evidence that our NGFs are recovering realistic path attenuation of ground motions. At closer distances, earthquake and NGF amplitudes are not comparable, because NGF amplitudes are contaminated and earthquake ground motion amplitudes are strongly dependent on depth and the source radiation pattern. Mean FSAs at slightly lower frequency 0.42 Hz seem to agree with each other at distances $\gtrsim$ 4 km (Fig. 5.26b). Following the large difference between the shape of the TT component SGF and RSGF attenuation curves at 0.25 Hz (Figs 5.25a,b), we don't attempt the comparison between the tangential component earthquake and TT component NGF attenuation curves at 0.25 Hz.

5.9.3 RR component amplitudes

In Fig. 5.28a, we compare RR component SGF and RSGF FSAs at 0.25 Hz with NGF FSAs. The SGF and RSGF decay curves are similar indicating lower contamination of amplitudes at small distances than for TT component SGFs and NGFs. However, unlike the TT component amplitudes that show systematic decay with increasing R, the RR component SGF amplitudes slightly increase with R between ~11–18 km. While the signal-to-noise ratio of the RR component NGFs is low, the NGF amplitude decay curve at 0.25 Hz shows flattening around the same distance range. At 0.42 Hz, the distance range featuring increased amplitudes shifts to lower distances (~9–14 km) for both, SGFs and NGFs (Fig. 5.28b). Wave propagation complexities caused by crustal velocity gradients, post-critical reflections from interfaces, etc. can lead to significant deviation of earthquake ground motion decay from simple body wave or surface wave $G(R)$ (Bowman & Kennett, 1991; Burger *et al.* 1987). However, the distance range of slightly increased spectral amplitudes in the RR component RSGFs is seen to some extent in synthetic amplitudes at 0.42 Hz for all 1D velocity models used in this study, for a half-space model (V_P ~ 4.79 km/s, V_S ~ 2.8 km/s, density ρ ~ 2.15 g/cm^3, Q_P ~ 40, and Q_S ~35) and also for a whole space model (same parameters as halfspace model). In the

following paragraph, we show that these oscillatory features are just an artifact of the Fourier Transform of the near-field term in the solution of elastic wave equation for a radial force and radial velocity response (Aki & Richards 2002). While there is considerable scatter in the NGF amplitudes, the average RR component NGF decay curves at 0.25 Hz and 0.42 Hz indicate at least partial recovery of the near-field term. We recommend that future noise cross-correlation studies, especially ones involving broadband sensors at short interstation distances, should explore any evidence for near-field terms. FSAs of radial component earthquake ground motions don't show this feature (Figs 5.28c,d) possibly because of the scatter introduced by effects of earthquake depths, radiation patterns and azimuths.

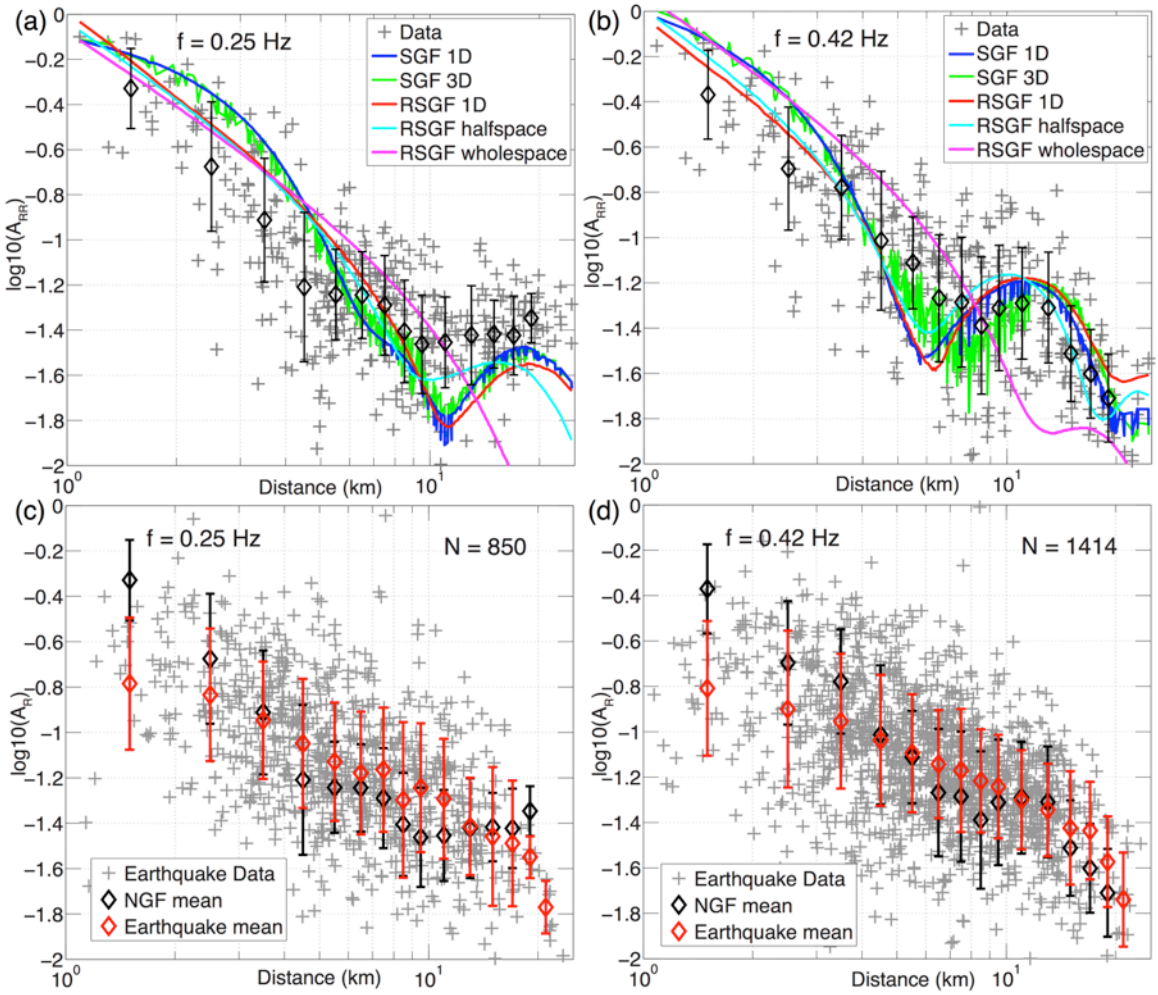

Figure 5.28: (a) RR component NGF and SGF/RSGF FSAs for a variety of models at 0.25 Hz (frequency indicated at the top) as a function of distance. Black diamonds and error bars represent the mean of NGF amplitudes and their standard deviation $\pm$ 1 σ in bins for all bins with more than 5 data points. The bin widths are 1 km and 2 km for distances $\leq$ 10 km and > 10 km, respectively. 3D and 1D indicate synthetic FSAs for 3D and 1D velocity models, respectively. The synthetic decay curves are uniformly scaled by a constant to minimize the L1 norm of their difference with the binned NGF FSAs. (b) same as (a) but for FSAs at 0.72 Hz. (c) The data (gray +) are radial component FSAs of earthquake records at 0.25 Hz and the

red diamonds and error bars represent the mean amplitudes and their standard deviation $\pm$ 1 σ in the bins. For comparison, we also plot binned RR component NGF FSAs at 0.25 Hz (black diamonds and error bars; same as [a]) that are scaled to minimize L1 norm of binned FSAs. "N" at the top right corner indicates the number of data points. (d) same as (c) but for FSAs at 0.72 Hz.

Equation 4.23 in Aki and Richards (2002) provides the response at a receiver to a unit force applied at a source position in an infinite isotropic homogenous medium without attenuation (P-wave velocity = $\alpha \sim 4.79$ km/s, S-wave velocity = $\beta \sim 2.8$ km/s, density = $\rho \sim 2.15$ g/cm^3). Assuming a source and a receiver separated by a distance r along axis 1 in the horizontal plane, the radial direction displacement (along axis 1) to an impulsive radial force $X_0(t) = \delta(t)$ (along axis 1) applied at the source can be evaluated by substituting direction cosines $\gamma_1 = 1, \gamma_2 = 0$ and $\gamma_3 = 0$, and $x_1 = r, x_2 = 0$, and $x_3 = 0$. The RR component Green's function G_{11} as a function of time t is given by –

$$G_{11}(t) = \frac{2}{4\pi\rho r^3}\int_{r/\alpha}^{r/\beta} \tau\delta(t-\tau)d\tau + \frac{1}{4\pi\rho\alpha^2 r}\delta\left(t-\frac{r}{\alpha}\right) \tag{5.2}$$

The first and second terms are the near-field term and the far-field P-wave term, while the contribution of the far-field S-wave is zero. The near-field term has contributions from both P wave and S wave. Taking the Fourier transform,

$$G_{11}(\omega) = \int_{-\infty}^{\infty} G_{11}(t)e^{-i\omega t}dt$$

$$G_{11}(\omega) = \frac{1}{2\pi\rho r^3}\int_{-\infty}^{\infty}\left[\int_{r/\alpha}^{r/\beta}\tau\delta(t-\tau)d\tau\right]e^{-i\omega t}dt + \frac{1}{4\pi\rho\alpha^2 r}\int_{-\infty}^{\infty}\delta\left(t-\frac{r}{\alpha}\right)e^{-i\omega t}dt \tag{5.3}$$

where ω is angular frequency. Exchanging the order of integration in the first term,

$$G_{11}(\omega) = \frac{1}{2\pi\rho r^3}\int_{r/\alpha}^{r/\beta}\tau\left[\int_{-\infty}^{\infty}\delta(t-\tau)e^{-i\omega t}dt\right]d\tau + \frac{e^{-i\omega r/\alpha}}{4\pi\rho\alpha^2 r} \tag{5.4}$$

$$G_{11}(\omega) = \frac{1}{2\pi\rho r^3}\int_{r/\alpha}^{r/\beta}\tau e^{-i\omega\tau}\,d\tau + \frac{e^{-i\omega r/\alpha}}{4\pi\rho\alpha^2 r} \tag{5.5}$$

$$G_{11}(\omega) = \frac{1}{2\pi\rho r^3}\left\{e^{-i\omega\tau}\left(\frac{1}{\omega^2}+\frac{i\tau}{\omega}\right)\right\}_{r/\alpha}^{r/\beta} + \frac{e^{-i\omega r/\alpha}}{4\pi\rho\alpha^2 r} \tag{5.6}$$

The absolute amplitude of $G_{11}(\omega)$ as a function of distance r and the near-field and far-field P-wave terms are plotted in Fig. 5.29 for frequencies 0.25 Hz and 0.42 Hz. The oscillatory features observed in the RR component noise-derived Green's Function (NGF) and in the synthetic Green's Function (SGF) Fourier spectral amplitude (FSA) decay curves at 0.42 Hz (Fig. 5.28b) are likely caused by the near-field term. The near-field and the far-field terms show the expected r^{-2} and r^{-1} decays, respectively.

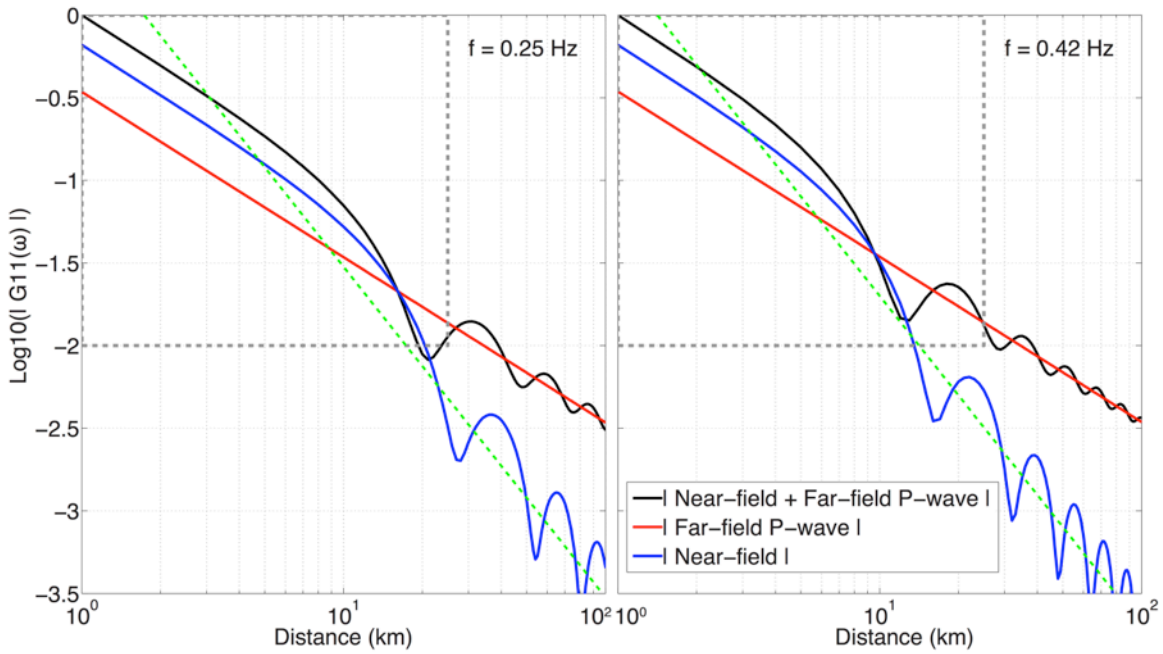

Figure 5.29: RR component Green's function Fourier spectral amplitude $|G_{11}(\omega)|$ (equation 5.6) as a function of distance r and various terms in the solution at two different frequencies (indicated at the top right corner). The average decay of the near-field term and the far-field term are proportional to r^{-2} and r^{-1}, respectively (indicated by the dashed green and red lines, respectively). The dashed gray box indicates the extent shown in Figs 5.28a,b.

5.9.4 Bias in NGF amplitudes

Accuracy of relative amplitude information retrieved from ambient noise cross-correlations has been widely discussed and debated in both theoretical and numerical studies (e.g., Cupillard & Capdeville 2010; Tsai 2011; Lawrence *et al.* 2013). Commonly, a wave equation solution of the form $e^{-\alpha R} J_0\left(\frac{\omega R}{c}\right)$ is assumed in which J_0 is the zero-order Bessel function of the first kind with c being the frequency-dependent phase velocity. This solution is valid for surface waves that are usually retrieved from noise cross-correlation, and consists of an implicit geometrical spreading factor in the Bessel function ($\propto R^{-0.5}$ in the far-field) and attenuation in the form of $e^{-\alpha R}$. For intrinsic attenuation in a homogenous medium, Tsai (2011) showed that retrieval of this solution from coherency measurements is possible only under the conditions of a uniform noise source distribution. The ambient noise source distribution at The Geysers is evidently not uniform as none of our NGFs are symmetric. In case that the noise source distribution is not uniform but is ubiquitous (present both inside and outside an array), then azimuthal averaging of coherency over same-distance station pairs may provide correct relative amplitudes (e.g., Zhang & Yang 2013; Lawrence *et al.* 2013; Weemstra *et al.* 2015). Whatever the source may be, the scatter in the observed NGF amplitudes requires some averaging for meaningful interpretation, which is also true for earthquake ground motions on the same spatial scale (Fig. 5.25d). Otherwise, to avoid loss of

local resolution from averaging, one can resort to more sophisticated techniques such as the C3 method for analyzing NGF amplitudes at receivers along a line (Zhang & Yang 2013).

In case of far-field noise source distribution, which is expected for continental regions in primary and secondary microseismic passbands (Stehly *et al.* 2006), correct intrinsic attenuation cannot be retrieved even if the illumination is uniform from all directions (Tsai 2011; Weemstra *et al.* 2015). In our study, the amplitude decay shown by the TT component RSGFs for the weak attenuation REF model at 0.72 Hz can be assumed to be equivalent to geometrical spreading, which gives us $R^{-0.53}$ for $1\lambda \lesssim R \lesssim 13$ km ($\lambda \sim 3.47$ km for $c_L \sim 2.5$ km/s at 0.72 Hz) and $R^{-1.17}$ for $R \gtrsim 16$ km, which are steeper than $R^{-0.5}$ (similar to SGF in Fig. 5.25c). Nevertheless, we compare our results for the TT component NGFs at 0.72 Hz with various conclusions drawn analytically by Tsai (2011) for different noise source distributions, assuming plane-wave incidence ($R \gg c/\omega$) and weak intrinsic attenuation (Fig. 5.30). We do not attempt to correct for deviations from the analytical formulations arising from orientations of components and polarizations of incident waves or effects of near-field distances (Aki 1957; Haney *et al.* 2012).

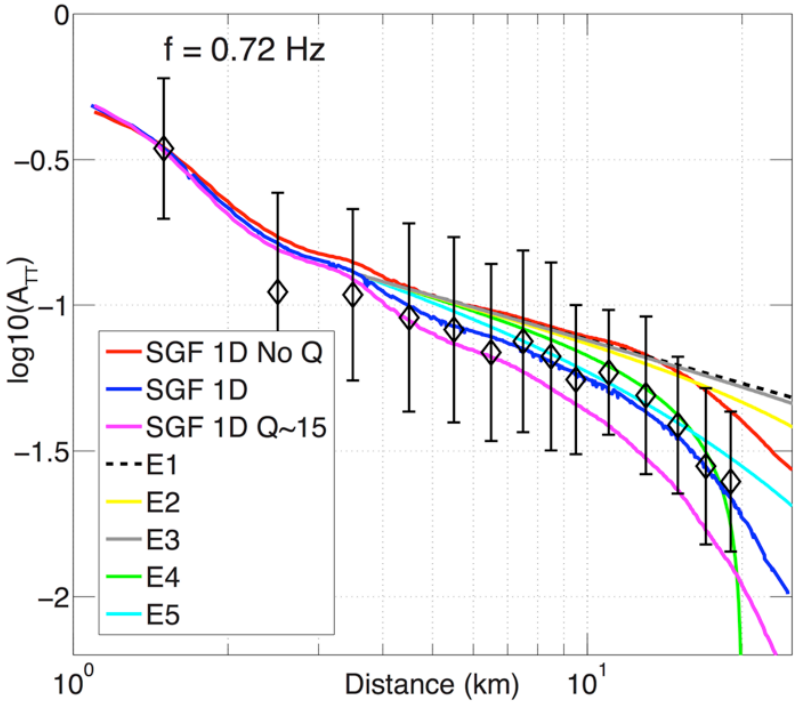

Figure 5.30: TT component binned NGF FSAs at 0.72 Hz (black diamonds) and REF model SGF FSAs with various degrees of anelastic attenuation are same as in Fig. 5.25c. Different analytical formulations from Tsai (2011) plotted for distances $R \gtrsim 3.6$ km ($\sim 1\lambda$) are $E2 = G(R)\times\left(I_0(\alpha R)\right)^{-1}$ and $E3 = G(R)\times\left(I_0^2(\alpha R) - L_0^2(\alpha R)\right)^{-0.5}$ for uniform and one-sided far-field noise source distributions, respectively, and $E4 = G(R)\times\left(1 - \frac{R^2}{4R'^2}\right)^{0.5}$ for truncated near-field noise source distribution. For comparison, we also plot simple $E1 = G(R)$ and $E5 = G(R)e^{-\alpha R}$. Geometrical spreading $G(R) = R^{-0.5}$, $\alpha \sim 0.04$ km^{-1} at 0.72 Hz and $R' \sim 12$ km. I_0 is the modified Bessel function of first kind and order 0 and L_0 is the modified Struve

function of order 0. The analytical decay curves are scaled to have the same amplitude as the REF model SGF decay curve at ~3.6 km.

Since we observe a decay that is stronger than the expected $G(R)$, we rule out the possibility of a single point noise source distribution that would have led to little or no decay in amplitudes with distance (Cupillard & Capdeville 2010; Table 1 in Tsai 2011). In case of uniform or one-sided far-field noise source distribution, a stronger than $G(R)$ decay is expected, which is observed in our NGF amplitudes (Cupillard & Capdeville 2010; equations 25 and 29 in Tsai 2011). The apparent attenuation factors for the two distributions are $\left(I_0(\alpha R)\right)^{-1}$ and $\left(I_0^2(\alpha R) - L_0^2(\alpha R)\right)^{-0.5}$, respectively, where I_0 is the modified Bessel function of first kind and order 0 and L_0 is the modified Struve function of order 0. The apparent attenuation decays are significantly weaker than the observed NGF amplitude decay. Given the scatter in the NGF amplitudes, it is difficult to constrain α, and it is possible that the decay observed in our NGF amplitudes might just be an artifact of a non-uniform far-field noise source distribution. However, 0.72 Hz is higher than the frequency band of secondary microseisms generated near the coast (Stehly *et al.* 2006) and our analysis of T-[R,Z] components of NGFs didn't reveal any preferred noise-source incidence direction. Another possible scenario includes that all background noise is generated from the anthropological activities in the geothermal field. While the long semi-axis of the geothermal field at R' ~12 km is not significantly smaller than the attenuation distance $1/\alpha$ ~ 1/0.04 ~ 25 km at 0.72 Hz, using equation 44 in Tsai (2011) for truncated near-field source distribution (apparent attenuation ~ $\left(1 - \frac{R^2}{4R'^2}\right)^{0.5}$), we obtain a decay that is still weaker than the observed decay for R < 20 km. This noise source distribution also predicts little or no recovery of coherence for stations outside the geothermal field whereas we obtain robust NGFs for many station pairs located at the edge of the reservoir area (e.g., SRB-DRH in Fig. 5.20). We are unable to discern any obvious stronger-than-actual amplitude decay at distances $\lesssim 2\lambda$ expected from equation 5.1 in which ensemble averaging is done after spectral normalization as opposed to ensemble averaging the cross-spectrum and the amplitude spectra separately prior to the normalization (Tsai 2011; Weemstra *et al.* 2014). It has been suggested that the approach followed in equation 5.1 might be helpful if the background noise in highly non-stationary (Weemstra *et al.* 2014).

Given the difficulty in analytically estimating coherency for realistic noise source distributions, Lawrence *et al.* (2013) employed numerical tests and showed that azimuthal averaging of same-distance coherency measurements, similar to averaging of FSAs in our study, can yield correct attenuation estimates under a wide range of noise source distributions. We note that while averaging should be performed within spatial dimensions with slowly and smoothly varying background medium properties (Weemstra *et al.* 2015), we average over the entire reservoir area, which doesn't seem to produce any obvious artifact in the average decay of amplitudes. Among other factors, incoherent noise locally observed at stations contributes to the autocorrelations in the denominator in coherency expression (equation 5.1) and may play an important role as the contribution of coherent wavefield weakens with distance (e.g., Tsai 2011; Lawrence *et al.* 2013). In recent studies, Weemstra *et al.* (2015) have shown that scattering attenuation in a non-dissipative medium, illuminated uniformly from far-field

sources, can be correctly recovered from cross-spectrums. At The Geysers geothermal field, given the high temperatures (Lowenstern & Janik 2003) and considerable heterogeneities and fractures present in the subsurface (Lockner *et al.* 1982; Thompson 1989; Gunderson 1991; O'Connell & Johnson 1991; Sammis *et al.* 1992; Elkibbi *et al.* 2005; Jeanne *et al.* 2014), both intrinsic (Romanowicz 1995) and scattering attenuation are expected to be high. The Q_S values adopted in the REF model, ~25 to ~40 in the top ~4.5 km and $\gtrsim$ 60 at greater depths, were estimated using the NetMoment method (Hutchings 2001; Viegas & Hutchings 2011). They are considerably lower than Q_S values expected from standard V_S-Q_S relationships (Brocher 2008), e.g., Q_S ~150-300 for V_S ~ 2.0-3.1 km/s in the top ~4.5 km in the REF model, implying stronger attenuation, and possible contribution of scattering attenuation that might be better recovered under more realistic noise-source distributions. Scattering outside the study region can also act to homogenize the noise source illumination, which would aid in the better recovery of amplitudes from NGFs.

In methodological aspects, some studies prefer using the same spectral normalization factors for all station pairs to obtain more appropriate relative amplitudes (e.g., Denolle *et al.* 2013; Bowden *et al.* 2015). However, studies applying spectral whitening at multiple stages have been successful in retrieving reliable estimates of anelastic attenuation as well (Handel *et al.* 2016).

The scatter in the NGF amplitudes observed at all frequencies necessitates a rigorous analysis of uncertainties and trade-offs in the ground motion attenuation parameters extracted from NGF FSAs, which is beyond the scope of this study. An investigation of ambient noise source distribution at The Geysers along with more NGF amplitude data are also required to properly resolve the individual contributions of possible biases, $G(R)$ and anelastic attenuation to the overall observed decay of NGF amplitudes with distance. Notwithstanding the incompleteness of our analysis, the similarity between the average attenuation curves of the NGF FSAs, earthquake ground motion FSAs and the SGF FSAs predicted from an appropriate velocity model is very compelling and indicates that NGF amplitudes at The Geysers are believable at the distances and frequencies examined here.

5.10 Conclusions and future work

When 3-component sensors are deployed for long durations, ambient noise cross-correlation techniques provide a robust empirical, 9-component, NGF tensor that can be used in a variety of different applications. The main conclusions of our study are summarized below:

(1) We were able to retrieve NGFs in the frequency range (~ 0.2-0.9 Hz) for a range of interstation distances from ~1-30 km (~0.22 λ – 6.5 λ) at The Geysers using a variety of sensors in and around the reservoir area. For many station pairs, the NGFs are found to be similar to the single force displacement SGFs computed using pre-existing and revised 1D velocity models in terms of waveforms, phase and the relative

amplitudes of all components of the tensors, even at distances < λ. We identify both body-wave and surface-wave phases in the NGF waveforms.

(2) The direct comparison of NGFs with SGFs helps to evaluate the quality of the retrieved NGFs and the suitability of different 1D velocity models to various sub-regions of The Geysers. SGFs computed with the faster model VSP0 and the slower model REF preferentially provide better waveform fits to the NGFs for interstation paths across SE and NW Geysers, respectively. We are also able to confirm the results of previous body-wave travel-time tomography studies such as the low velocities in the region around station GSG and higher velocities of the reservoir area relative to the surrounding region.

(3) Large anomalous amplitudes on the off-diagonal T-[R,Z] components of NGFs helped us detect sensor misalignments for many stations of The Geysers. We confirm the alignment angles estimated from the analysis of long period teleseismic waveforms by a significant reduction in these anomalous amplitudes upon rotation of the NGF tensors to correct orientations.

(4) The comparison between NGFs and SGFs computed using 1D anisotropic velocity models and a 3D isotropic velocity model of the reservoir suggests that robust amplitudes on the T-[R,Z] components of NGFs for some longer distance paths likely result from wave propagation effects caused by a strong heterogeneity in 3D structure. The 3D model that was derived from body-wave travel-times using an infinite frequency geometrical ray tomography approach (Gritto *et al.* 2013a) can fit low frequency NGF (0.2-0.9 Hz) waveforms remarkably well. We were unable to detect any dominant ambient noise source illumination direction applying ORA to our NGFs.

(5) While there is considerable scatter in the TT component NGF FSAs, we find their average decay with distance to be similar to the decay expected from SGF amplitudes and with the decay of tangential component local-earthquake ground-motion amplitudes at the same frequencies (~0.25-0.72 Hz). The flattening of RR component FSAs at distances ~9-16 km suggests possible recovery of the near-field term.

The similarity of the NGF and the SGF waveforms computed with appropriate velocity models in this study indicates that the full 9-component NGF tensor should be used in waveform tomography studies (e.g., Lee *et al.* 2014) whenever multi-component stations are available in dense networks. As demonstrated, higher amplitude TT components provide strong reliable constraints on V_S structure. ZR and RZ component NGFs are possibly less susceptible to effects of directional noise source incidence compared to the commonly used ZZ component. Broadband phase delays from NGF waveforms as in the case of the NGFs to station GSG can be potentially useful at short interstation distances. Calibration of starting velocity models using NGF waveforms rather than earthquake waveforms can be desirable in regions like The Geysers, where earthquakes might have non-double couple source mechanisms (Guilhem *et al.* 2014). At The Geysers, possibilities of future work include further refinement of the velocity models, monitoring of temporal changes in the coda of NGFs and characterization of background noise source distribution.

Given the excellent distribution of earthquakes and stations within the geothermal field at The Geysers, the 3D velocity model derived from body-wave tomography is well resolved in the reservoir area; therefore, it is generally successful fitting low frequency NGF waveforms.

However, the model is not well resolved at depths $\gtrsim$ 4.2 km owing to the shallow focal depths of the earthquakes ($\lesssim$ 4.5 km) or at very shallow depths ($\lesssim$ 1.0 km). Long period Rayleigh waves (~5–8 s; c_R ~ 2.6–2.9 km/s for the GIL7 model) derived from noise cross-correlation at interstation distances (~40-70 km; $R \gtrsim 3\lambda$) can be used to investigate the velocity structure of the deeper reservoir rocks and the underlying felsite (depth sensitivity ~ $\lambda/2$ ~ 6-12 km). We have demonstrated good results with some of the short period (~1.0 Hz) sensors of the NCSN that are located outside The Geysers. Retrieval of longer period measurements will also benefit from temporary broadband sensors deployed at The Geysers (Specht *et al.* 2014) that are expected to yield more stable and higher quality NGFs than the ~4.5 Hz geophones used in this study. We didn't find any significant energy above 1.0 Hz in our NGFs and the presence of multiple spectral peaks (see section **5.4.2 Cross-correlation analysis**) between 1.7-2.5 Hz precluded any meaningful interpretation at these frequencies. Therefore, retrieval of high frequency ($\gtrsim$ 1 Hz) empirical GFs from cross-correlation of coda waves of the numerous local earthquakes in the reservoir area can be attempted (e.g., Campillo & Paul 2003) to investigate shallow velocity structure (c_R ~ 2.2 km/s at ~1.0 Hz for REF model; depth sensitivity ~ $\lambda/2$ ~ 1.1 km). A refined version of the 3D velocity model can subsequently be applied to higher frequency (up to ~2.5 Hz) earthquake waveforms and should increase confidence in source inversion studies by facilitating the inclusion of more stations at longer distances (e.g. Guilhem *et al.* 2014). For any future study attempting improvement of velocity models at The Geysers, the results obtained in this study provide a framework for appropriate initial models for inversion.

Possible temporal changes in the coda of noise cross-correlations can be investigated to look for possible changes in subsurface V_S related to micro/macro seismicity or injection/production activities. Variations of the order of few percent in V_S similar to ~4-6% variations in V_P/V_S ratio inferred from earthquake body-wave travel times (Foulger *et al.* 1997; Gritto & Jarpe 2014) should be readily detectable in the coda of NGFs. However, it must be noted that many stations don't return stable or robust NGFs during the entire time period.

Characterization of ambient noise source distribution and incidence direction in the frequency range ~0.2-0.9 Hz at The Geysers and its temporal variation using beamforming analysis, etc. (e.g., Menon *et al.* 2014). As discussed previously, ambient noise source distribution has important implications for the decay of NGF amplitudes and amplitudes in the T-[R,Z] components of NGFs. It would be interesting to see if effects on NGFs expected from the inferred noise source distribution (Fichtner 2014) can be reconciled with our observations.

5.11 Data and Software

Data used in this study come from Berkeley Digital Seismic Network (BDSN; dx.doi.org/10.7932/BDSN), operated by the University of California Berkeley Seismological Laboratory, Northern California Seismic Network (NCSN), and Lawrence Berkeley National Laboratory (LBNL) Short Period Network at The Geysers, which are all archived at the

Northern California Earthquake Data Center (NCEDC; dx.doi.org/10.7932/NCEDC; http://www.ncedc.org, last accessed July 2016). Codes for computing SGFs for 1D velocity models by FKI and the modal summation method, codes for extracting Love wave group and phase velocities from NGFs and codes for forward modeling the same using 1D velocity models are all available in the software *Computer Programs in Seismology* available at http://www.eas.slu.edu/eqc/eqccps.html, last accessed June 2016. SW4 is hosted by the Computational Infrastructure for Geodynamics (CIG) which is supported by the National Science Foundation award NSF-0949446. SW4 can be downloaded from CIG website https://geodynamics.org/cig/software/sw4/, last accessed June 2016.

5.12 Acknowledgements

This study was supported by National Science Foundation award EAR-1053211 and partially supported by the France-Berkeley Fund 2014-0051. We are grateful for permission to use the *Baribu* cluster at BSL for running SW4. A.N. is indebted to R.B. Herrmann (St. Louis Univ.) and F.-C. Lin (Univ. of Utah) for their help and guidance on many noise cross-correlation and surface wave concepts, and for reviewing the first draft of this chapter submitted as a manuscript to *Geophysical Journal International*. We thank an anonymous reviewer, D.C. Bowden (Caltech), M.A. Denolle (Harvard Univ.) and GJI Editor L. Métivier for carefully reviewing this study, and for their comments and suggestions, which helped to significantly improve this study. We are thankful to V.H. Lai (Caltech), P. Hellweg (Berkeley Seismological Lab [BSL]), H. Rademacher (BSL), and V.C. Tsai (Caltech) for helpful comments and/or discussions. We also thank Ramsey Haught for visiting the stations and checking the sensor orientations. A.N. thanks V. Maupin (Univ. of Oslo) for pointing out the reference for the elastic tensor for crack-induced anisotropy.

5.13 Appendix

Table 5.A.1: Earthquakes at The Geysers used to study path attenuation of ground motions in section **5.9.2 Comparison with earthquake ground motion amplitudes**. This set of earthquakes is adopted from the Northern California Seismic Network (NCSN) earthquake catalog. The depths are relative to the Earth's geoid surface (approximately equal to mean sea level). Our reference datum is assumed to be ~800 m above the mean sea level. M_D = Duration Magnitude.

NCSN Event ID	Date (yy-mm-dddd)	Origin Time (hh:mm:ss.ss)	Latitude (°N)	Longitude (°E)	Depth (km)	M_D
71759110	2012-04-05	17:55:14.80	38.83267	-122.80217	1.17	2.69
71761585	2012-04-09	10:52:31.48	38.84100	-122.82433	1.41	2.69
71770245	2012-04-24	16:53:53.73	38.79483	-122.79483	3.14	2.70

71773650	2012-04-30	23:10:35.40	38.79016	-122.77750	1.85	2.69
71775630	2012-05-04	11:53:43.35	38.81433	-122.83500	-0.26	2.62
71784901	2012-05-13	15:24:08.56	38.82883	-122.80016	0.96	2.65
71793936	2012-05-31	02:50:35.89	38.83700	-122.77383	2.06	2.50
71799501	2012-06-11	02:00:42.28	38.81783	-122.82816	1.81	2.55
71804081	2012-06-20	20:56:46.01	38.83367	-122.81216	1.54	2.69
71806021	2012-06-24	18:53:11.85	38.84667	-122.82450	1.11	2.50
71813261	2012-07-09	00:00:44.74	38.81967	-122.80000	3.11	2.70
71817386	2012-07-16	11:41:38.02	38.83983	-122.82933	1.83	2.55
71828646	2012-08-08	23:27:15.83	38.83333	-122.87984	1.87	2.62
71862145	2012-10-19	07:33:28.68	38.80800	-122.82300	1.78	2.65
71862225	2012-10-19	09:47:27.59	38.81150	-122.82383	2.06	2.51
71870605	2012-10-29	05:48:41.55	38.81550	-122.78017	1.25	2.66
71888741	2012-11-18	10:43:43.38	38.83200	-122.79300	1.63	2.52
71888751	2012-11-18	10:55:54.04	38.82950	-122.78700	1.33	2.62
71895291	2012-11-28	05:11:30.03	38.81950	-122.79450	2.79	2.64
71904136	2012-12-13	07:34:00.48	38.82033	-122.79017	1.55	2.64
71910116	2012-12-25	10:48:22.65	38.83650	-122.77283	1.69	2.52
71914416	2013-01-03	10:51:46.24	38.83750	-122.79950	1.68	2.68
71922806	2013-01-16	16:39:12.61	38.81517	-122.79933	1.96	2.70
71929941	2013-01-28	02:26:43.80	38.82667	-122.84983	0.85	2.62
71934900	2013-02-10	19:05:40.60	38.76583	-122.73967	1.56	2.62
71945780	2013-02-28	15:06:31.10	38.82033	-122.80400	2.88	2.52
71955160	2013-03-15	06:07:03.51	38.77367	-122.71267	2.01	2.50
71956830	2013-03-18	18:38:49.71	38.78600	-122.76183	0.44	2.68
71960250	2013-03-25	10:20:28.53	38.83667	-122.80800	2.07	2.68
71961885	2013-03-28	05:04:36.76	38.75583	-122.71950	1.17	2.50
71967530	2013-04-07	05:34:07.11	38.82150	-122.76100	1.47	2.59
71986506	2013-05-06	15:16:22.19	38.83950	-122.83017	2.21	2.61
72049681	2013-08-15	10:43:27.17	38.79417	-122.78333	3.20	2.58
72058631	2013-08-29	00:09:54.56	38.82117	-122.81300	2.65	2.52
72060046	2013-08-30	19:28:21.95	38.81217	-122.78833	2.72	2.55
72079496	2013-10-01	17:51:26.15	38.83433	-122.79483	1.64	2.70
72083531	2013-10-08	14:06:41.14	38.83567	-122.78150	0.79	2.57
72084251	2013-10-09	18:34:52.01	38.83550	-122.76933	0.89	2.68
72084836	2013-10-10	19:28:02.96	38.81083	-122.82350	1.59	2.68
72086066	2013-10-11	23:23:24.19	38.82217	-122.79300	2.57	2.67
72095471	2013-10-25	21:01:31.94	38.80867	-122.81000	1.15	2.59
72098566	2013-10-31	02:10:50.85	38.83083	-122.80900	1.83	2.66
72101851	2013-11-06	02:06:47.06	38.81767	-122.81900	1.98	2.59
72105231	2013-11-11	05:13:53.24	38.80917	-122.82400	1.80	2.59
72105916	2013-11-12	05:32:32.11	38.80267	-122.77016	1.03	2.52
72107361	2013-11-14	08:49:56.51	38.79933	-122.77216	-0.60	2.64
72108125	2013-11-22	14:03:12.22	38.77617	-122.72900	1.16	2.53
72109855	2013-11-26	01:02:41.08	38.83484	-122.79950	1.73	2.54

72110115	2013-11-26	09:39:57.73	38.80883	-122.81817	2.54	2.56
72111515	2013-11-29	02:02:53.76	38.80900	-122.81184	1.40	2.51
72113505	2013-12-03	06:39:40.08	38.76250	-122.73867	2.24	2.70
72114715	2013-12-04	21:35:37.97	38.77934	-122.72417	1.34	2.50
72121715	2013-12-16	05:55:18.62	38.76017	-122.71767	1.30	2.64
72128776	2013-12-23	00:20:33.50	38.82200	-122.80800	2.68	2.62
72138151	2014-01-07	16:49:51.24	38.76950	-122.71484	1.41	2.56
72138561	2014-01-08	05:09:04.22	38.82267	-122.84317	1.86	2.53
72141956	2014-01-12	22:05:48.34	38.81767	-122.81316	1.59	2.52
72147905	2014-01-28	10:45:33.36	38.83650	-122.78183	1.73	2.57
72168971	2014-02-16	17:24:13.06	38.78083	-122.72150	1.62	2.66
72189040	2014-03-26	06:01:44.62	38.80750	-122.81233	2.19	2.57
72193565	2014-04-04	15:12:11.71	38.82033	-122.76117	2.10	2.66
72203250	2014-04-21	23:49:30.54	38.78717	-122.76266	1.12	2.63
72207455	2014-04-28	14:18:30.27	38.82217	-122.81250	2.67	2.51
72217591	2014-05-07	20:14:42.40	38.80467	-122.73583	1.95	2.57
72242601	2014-06-23	22:36:26.68	38.80800	-122.81167	1.79	2.54
72273625	2014-08-14	03:55:13.80	38.77583	-122.76067	0.74	2.57
72287451	2014-08-29	21:53:18.40	38.81833	-122.82600	2.52	2.66
72298871	2014-09-14	18:07:34.75	38.82833	-122.79433	1.81	2.69
72336075	2014-11-06	09:54:57.50	38.83583	-122.76133	0.14	2.68
72336105	2014-11-06	10:18:40.76	38.75633	-122.72517	2.20	2.61
72348121	2014-11-16	21:54:16.90	38.82883	-122.77666	0.34	2.51
72358056	2014-11-30	00:35:14.56	38.79900	-122.79984	2.63	2.70
72362701	2014-12-09	19:46:49.15	38.83200	-122.79833	1.45	2.70
72382136	2015-01-16	10:39:55.61	38.81233	-122.81966	1.96	2.56
72397995	2015-02-20	11:16:19.33	38.81283	-122.82050	2.73	2.64
72398140	2015-02-20	14:28:18.16	38.80650	-122.81150	2.62	2.67
72417480	2015-03-26	00:29:45.32	38.79583	-122.74900	-0.02	2.56
72429396	2015-04-10	08:54:03.28	38.80867	-122.81100	1.49	2.53
72430795	2015-04-19	05:44:19.74	38.78316	-122.74300	0.78	2.60
72430965	2015-04-19	14:13:37.29	38.84550	-122.81567	0.56	2.66
72432140	2015-04-21	16:34:41.53	38.82050	-122.81050	2.93	2.68
72432380	2015-04-21	21:14:25.34	38.74383	-122.70267	1.21	2.68
72435045	2015-04-25	15:56:32.53	38.78467	-122.72183	1.37	2.59
72435325	2015-04-25	21:25:49.80	38.82400	-122.82650	2.31	2.57
72439700	2015-05-04	01:11:27.55	38.80767	-122.82367	1.02	2.62
72446891	2015-05-11	02:03:26.54	38.80533	-122.79017	0.88	2.69
72460006	2015-06-02	21:06:12.90	38.81167	-122.81583	2.44	2.67
72463366	2015-06-09	20:23:58.34	38.84967	-122.78033	1.25	2.50
72464911	2015-06-12	10:19:46.31	38.78550	-122.76733	1.25	2.64
72466021	2015-06-14	10:21:09.91	38.84117	-122.82567	1.77	2.64
72487371	2015-07-17	07:37:33.00	38.83200	-122.78983	2.01	2.60
72497986	2015-07-31	06:24:51.46	38.78800	-122.73550	1.44	2.61
72499921	2015-08-03	11:17:44.04	38.75800	-122.72050	0.99	2.64

72504266	2015-08-11	03:50:51.71	38.83100	-122.81084	1.70	2.68
72514451	2015-08-27	06:37:36.51	38.79283	-122.75816	1.02	2.55
72558811	2015-11-22	01:24:56.16	38.80533	-122.73617	1.92	2.53
72560531	2015-11-25	18:31:18.22	38.81883	-122.77634	0.76	2.63
72572176	2015-12-25	23:57:30.92	38.83267	-122.80133	1.83	2.66
72583746	2016-01-23	17:28:11.46	38.79650	-122.81200	3.14	2.57
72588465	2016-02-09	17:03:59.83	38.81083	-122.82500	2.33	2.61
72597260	2016-02-24	23:54:40.38	38.81133	-122.81683	2.51	2.59
72599815	2016-02-29	10:14:07.17	38.82516	-122.79684	1.71	2.61
72600120	2016-02-29	21:34:13.04	38.76350	-122.74033	1.57	2.70
72603305	2016-03-07	17:38:07.40	38.84184	-122.83850	1.92	2.59
72603535	2016-03-08	06:36:21.51	38.83033	-122.80766	1.20	2.58
72603670	2016-03-08	11:27:10.63	38.80633	-122.81067	2.08	2.70
72604760	2016-03-10	10:52:01.05	38.81917	-122.80483	2.30	2.56
72607655	2016-03-17	06:58:25.87	38.81000	-122.82616	1.73	2.53
72613310	2016-03-27	03:28:59.15	38.80900	-122.82383	1.98	2.65
72621695	2016-04-13	16:18:47.56	38.84150	-122.82367	1.77	2.63
72655431	2016-06-26	02:58:17.60	38.84000	-122.82950	2.47	2.58
72666516	2016-07-26	09:06:33.04	38.77383	-122.74883	0.84	2.55
72672835	2016-08-10	07:47:15.95	38.82383	-122.84000	0.42	2.65
72678011	2016-08-16	01:58:56.05	38.75917	-122.71467	0.94	2.60
72689591	2016-09-03	20:08:36.73	38.83783	-122.74950	0.51	2.68
72701976	2016-09-24	18:56:14.52	38.81167	-122.81184	1.85	2.54
72714816	2016-10-20	10:33:26.16	38.82350	-122.80100	2.89	2.65
72720310	2016-11-04	09:28:18.70	38.83917	-122.82417	2.52	2.69
72735540	2016-12-10	22:18:15.15	38.82133	-122.76383	1.64	2.58
72738365	2016-12-14	19:24:08.64	38.81533	-122.84133	0.81	2.54
72740405	2016-12-17	19:09:31.09	38.83683	-122.78300	0.82	2.54

References

Aki, K., 1957. Space and time spectra of stationary stochastic waves, with special reference to microtremors, *Bull. Earthq. Res. Inst. Tokyo Univ.*, **25**, 415–457.

Aki, K. & Richards, P.G., 2002. Quantitative Seismology, *Second Ed., University Science Books, San Francisco, California*, 27-77.

Allis, R.G. & Shook G.M., 1999. An alternative mechanism for the formation of The Geysers vapor-dominated reservoir, *Proc. 24th Workshop on Geotherm. Reservoir Engg.*, 53–63.

Almendros, J. & Chouet, B., 2003. Performance of the Radial Semblance Method for the Location of Very Long Period Volcanic Signals, *Bull. Seismol. Soc. Am.*, 93(5), 1890–1903.

Atkinson, G., 2004. Empirical attenuation of ground motion spectral amplitudes in southeastern Canada and the northeastern United States, *Bull. Seism. Soc. Am.*, **94**(3), 1079-1095.

Bakun, W.H., 1984. Seismic moments, local magnitudes and coda-duration magnitudes for earthquakes in Central California, *Bull. Seism. Soc. Am.*, **74**(2), 439-458.

Beckman, J.D. & Williamson, A.K., 1990. Salt-dome locations in the Gulf coastal plains, south-central United States, *USGS Water-Resources Investigations Report 90-4060*.

Ben-Zion, Y., 2003. Key formulas in earthquake seismology, in International Handbook of Earthquake and Engineering Seismology, pp. 1857–1875, ed. Lee, W.H.K. & Part, B., Academic Press, Boston, MA, USA.

Bensen, G.D., Ritzwoller, M.H., Barmin, M.P., Levshin, A.L., Lin, F.-C., Moschetti, M.P., Shapiro, N.M. & Yang, Y., 2007. Processing seismic ambient noise data to obtain reliable broadband surface wave dispersion measurements, *Geophys. J. Int.*, **169**, 1239–1260, doi: 10.1111/j.1365-246X.2007.03374.x.

Bowden, D.C., Tsai, V.C. & Lin, F.-C., 2015. Site amplification, attenuation, and scattering from noise correlation amplitudes across a dense array in Long Beach, CA, *Geophys. Res. Lett.*, **42**, 1360–1367, doi:10.1002/2014GL062662.

Bowers, D. & Hudson, J.A., 1999. Defining the scalar moment of a seismic source with a general moment tensor, *Bull. Seismol. Soc. Am.*, **89**(5), 1390-1394.

Bowman, J.R. & Kennett, B.L.N., 1991. Propagation of Lg waves in the North Australian Craton: influence of crustal velocity gradients, *Bull. Seism. Soc. Am.*, **81**(2), 592-610.

Boyd, O.S., Dreger, D.S., Lai, V.H. & Gritto, R., 2015. A systematic analysis of seismic moment tensor at The Geysers geothermal field, California, *Bull. Seism. Soc. Am.*, **105**(6), 2969-2986, doi:10.1785/0120140285.

Brenguier, F., Campillo, M., Takeda, T., Aoki, Y., Shapiro, N.M., Briand, X., Emoto, K. & Miyake, H., 2014. Mapping pressurized volcanic fluids from induced crustal seismic velocity drops, *Science*, **345**, 80-81, doi: 10.1126/science.1254073.

Brocher, T.M., 2008. Key elements of regional seismic velocity models for long period ground motion simulations, *J. Seismol.*, **12**, 217–221, doi:10.1007/s10950-007-9061-3.

Burger, R.W., Somerville, P.G., Barker, J.S., Herrmann, R.B. & Helmberger, D.V., 1987. The effect of crustal structure on strong ground motion attenuation relations in Eastern

North America, *Bull. Seism. Soc. Am.*, **77**(2), 420-439.

Campillo, M. & Paul, A., 2003. Long range correlations in the diffuse seismic coda, *Science*, **299**, 547-549, doi: 10.1126/science.1078551

Cheng, C.H., 1993. Crack models for a transversely isotropic medium, *J. Geophys. Res*, 98(B1), 675-684.

Chiang, A., Dreger, D.S., Ford, S.R. & Walter, W.R., 2014. Source characterization of underground explosions from combined regional moment tensor and first motion analysis, *Bull. Seismol. Soc. Am.* **104**(4), 1587-1600, doi: 10.1785/0120130228.

Chiang, A., Dreger, D.S., Ford, S.R., Walter, W.R. & Yoo, S.-H., 2016. Moment tensor analysis of very shallow sources, *Bull. Seismol. Soc. Am.*, **106**(6), 2436-2449, 10.1785/0120150233.

Chicago Bridge & Iron Company (CB&I), 2013a. *Blue Ribbon Commission Initial Technical Briefing*, Louisiana State University, 5 April 2013, http://dnr.louisiana.gov/assets/OC/BC_All_Updates/Plans_Reports/BlueRibb.04.05.13.pdf (last accessed January 2017).

CB&I, 2013b. *Public Briefing and Status Update*, 16 July 2013, http://www.dnr.louisiana.gov/assets/OC/BC_All_Updates/Public.Briefing.2013.07.16.FullSlides.pdf (last accessed January 2017).

CB&I, 2014. Bayou Corne Public Briefing, 11 March 2014, http://www.dnr.louisiana.gov/assets/OC/BC_All_Updates/Public_Briefing_2014_03_11_CBI.pdf (last accessed August 2017).

Cho, K.H., Herrmann, R.B., Ammon, C.J. & Lee, K., 2007. Imaging the upper crust of the Korean peninsula by surface-wave tomography, *Bull. Seismol. Soc. Am.*, **97**(1B), 198–207, doi: 10.1785/0120060096.

Chouet, B.A., 1986. Dynamics of a Fluid-Driven Crack in Three Dimensions by the Finite Difference Method, *J. Geophys. Res.*, **91**, B14, 13967-13992.

Chouet, B.A. & Dawson, P.B., 2011. Shallow conduit system at Kilauea Volcano, Hawaii, revealed by seismic signals associated with degassing bursts, *J. Geophys. Res.*, **116**, B12317, doi:10.1029/2011JB008677.

Chouet, B.A., Dawson, P.B. James, M.R. & Lane, S.J., 2010. Seismic source mechanism of degassing bursts at Kilauea Volcano, Hawaii: Results from waveform inversion in the 10-50 s band, *J. Geophys. Res.*, **115**, B09311, doi:10.1029/2009JB006661.

Chouet, B.A., Dawson, P.B. & Martini, M., 2008. Shallow-conduit dynamics at Stromboli volcano, Italy, imaged from waveform inversions, *Geol. Soc. London Spec. Publ.*, **307**, 57-84, doi: 10.1144/SP307.5.

Chouet., B.A & Matoza, R.S., 2013. A multi-decadal view of seismic methods for detecting precursors of magma movement and eruption, *J. Volcanol. Geotherm. Res.* 252, 108–175, 10.1016/j.jvolgeores.2012.11.013.

Chouet, B.A., Page, R.A., Stephens, C.D., Lahr, J.C. & Power, J.A., 1994. Precursory swarms of long-period events at Redoubt Volcano (1989–1990), Alaska: their origin and use as a forecasting tool, *J. Volcanol. Geotherm. Res.* 62, 95–135.

Contrucci, I., Klein, E., Cao, N.-T., Daupley, X. & Bigarré, P., 2012. Multi-parameter monitoring of a solution mining cavern collapse: First insight of precursors, *C.R. Geosci.*, 343, 1–10, doi:10.1016/j.crte.2010.10.007.

Covellone, B.M. & Savage, B., 2012. A quantitative comparison between 1D and 3D source inversion methodologies: application to the Middle East, *Bull. Seismol. Soc. Am.*,

102(5), 2189–2199, doi: 10.1785/0120110278.

Crampin, S., 1984. Effective anisotropic elastic constants for wave propagation through cracked solids, *Geophys. J. R. astr. Soc.*, **76**, 135-145.

Cupillard, P. & Capdeville, Y., 2010. On the amplitude of surface waves obtained by noise correlation and the capability to recover the attenuation: a numerical approach, *Geophys. J. Int.*, **181**, 1687–1700, doi: 10.1111/j.1365-246X.2010.04586.x.

Denolle, M.A., Dunham, E.M., Prieto, G.A. & Beroza, G.C., 2013. Ground motion prediction of realistic earthquake sources using the ambient seismic field, *J. Geophys. Res.*, **118**, 2102–2118, doi:10.1029/2012JB009603.

Denolle, M.A., Miyake, H., Nakagawa, S., Hirata, N. & Beroza, G.C., 2014. Long-period seismic amplification in the Kanto Basin from the ambient seismic field, *Geophys. Res. Lett.*, **41**, 2319–2325, doi:10.1002/2014GL059425.

Dreger, D.S., Tkalcic, H. & Johnston, M., 2000. Dilational processes accompanying earthquakes in the Long Valley Caldera, *Science*, **288**, 122-125.

Dreger, D.S. & Helmberger, D.V., 1993. Determination of source parameters at regional distances with three-component sparse network data, *J. Geophys. Res.*, **98**(B5), 8107-8125.

Dreger, D.S., Ford, S.R. & Nayak, A., 2015. Long-period seismicity at the Napoleonville salt dome: implications for local seismic monitoring of underground hydrocarbon storage caverns, *AGU Fall Meeting 2015*, San Francisco, California, 12–16 December 2014, Abstract S13B-2815.

Dunkin, J.W., 1965. Computation of modal solutions in layered, elastic media at high frequencies, *Bull. Seismol. Soc. Am.*, **55**(2), 335-358.

Duputel, Z., Rivera, L., Fukahata, Y. & Kanamori, H., 2012. Uncertainty estimations for seismic source inversions, *Geophys. J. Int.*, **190**, 1243–1256 doi: 10.1111/j.1365-246X.2012.05554.x

Durand, S., Montagner, J.P., Roux, P., Brenguier, F., Nadeau, R.M. & Ricard, Y., 2011. Passive monitoring of anisotropy change associated with the Parkfield 2004 earthquake, *Geophys. Res. Lett*., **38**, L13303, doi:10.1029/2011GL047875.

Dziewonski, A.M., Bloch, S. & Landisman, M., 1969. A technique for the analysis of transient seismic signals, *Bull. Seismol. Soc. Am.*, **59**, 427–444.

Eberhart-Phillips, D. & Oppenheimer, D.H., 1984. Induced seismicity in The Geysers geothermal area, California, *J. Geophys. Res.*, **82**(B2), 1191-1207.

Eberhart-Phillips, D., 1986. Three-dimensional velocity structure in northern California Coast Ranges from inversion of local earthquake arrival times, *Bull. Seismol. Soc. Am.*, **76**(4), 1025-1052.

Eisner, L. & Clayton, R.W., 2001. A reciprocity method for multiple-source simulations, *Bull. Seismol. Soc. Am.*, **91**(3), 553–560.

Elkibbi, M. & Rial, J.A., 2005. The Geysers geothermal field: results from shear-wave splitting analysis in a fractured reservoir, *Geophys. J. Int.*, **162**, 1024–1035, doi: 10.1111/j.1365-246X.2005.02698.x.

Elkibbi, M., Yang, M. & Rial, J.A., 2005. Crack-induced anisotropy models in The Geysers geothermal field, *Geophys. J. Int.*, **162**, 1036–1048, doi:10.1111/j.1365-246X.2005.02697.x.

Ellsworth, W.L., Horton, S., Benz, H., Chouet, B., Dawson, P., Hickman, S., Leeds, A., Leith, W.S., Meremonte, M., Rubinstein, J.L., Shelly, D., Withers, M.M. & Herrmann, R.B.,

2012. Tremors in the Bayou: The events on the Napoleonville Salt Dome, Louisiana, *AGU Fall Meeting 2012*, San Francisco, California, 3–7 December 2012.

Ezersky, M., 2006. The seismic velocities of Dead Sea salt applied to the sinkhole problem, *J. Appl. Geophys.*, **58**, 45-58.

Fichtner, A., 2014. Source and processing effects on noise correlations, *Geophys. J. Int.*, **197**, 1527–1531, doi: 10.1093/gji/ggu093.

Ford, S., Dreger, D.S. & Walter, W.R., 2008. Source characterization of the August 6, 2007 Crandall Canyon Mine seismic event in Central Utah, *Seismol. Res. Lett.*, **79**, 637-644, doi: 10.1785/gssrl.79.5.637.

Ford, S.R., Dreger, D.S. & Walter, W.R., 2009a. Identifying isotropic events using a regional moment tensor inversion, *J. Geophys. Res.*, **114**, B01306, doi:10.1029/2008JB005743.

Ford, S.R., Dreger, D.S. & Walter, W.R., 2009b. Source analysis of the Memorial Day Explosion, Kimchaek, North Korea, *Geophys. Res. Lett.*, **36**(21), L21304, doi:10.1029/2009GL040003.

Ford, S.R., Dreger, D.S. & Walter, W.R., 2010. Network sensitivity solutions for regional moment-tensor inversions, *Bull. Seismol. Soc. Am.*, **100**(5A), 1962-1970, doi: 10.1785/0120090140.

Ford, S.R., Walter, W.R. & Dreger, D.S., 2012. Event discrimination using regional moment tensors with teleseismic-P constraints, *Bull. Seismol. Soc. Am.*, **102**(2), 867-872, doi: 10.1785/0120110227.

Foulger, G.R., Grant, C.C., Ross, A. & Julian, B.R., 1997. Industrially induced changes in earth structure at The Geysers geothermal area, California, *Geophys. Res. Lett*., **24**(2), 135-137.

Friedrich, A., Kruger, F. & Klinge, K., 1998. Ocean-generated microseismic noise located with the Gräfenberg array, *J. Seismol.*, 2, 47–64.

Gardner, G.H.F., Gardner, L.W. & Gregory, A.R., 1974. Formation velocity and density—the diagnostic basics for stratigraphic traps, *Geophysics*, **39**, 770-780.

Gil Cruz, F., & Chouet, B.A., 1997. Long-period events, the most characteristic seismicity accompanying the emplacement and extrusion of a lava dome in Galeras Volcano, Columbia, in 1991, *J. Volcanol. Geotherm. Res.*, 77, 121-158.

Goldstein, P., Dodge, D., Firpo, M. & Minner, L., 2003. SAC2000: Signal processing and analysis tools for seismologists and engineers. Invited contribution to *The IASPEI International Handbook of Earth- quake and Engineering Seismology*, W. H. K. Lee, H. Kanamori, P. C. Jennings, and C. Kisslinger (Editors), Academic Press, London.

Graves, R.W. & Wald, D., 2001. Resolution analysis of finite fault source inversion using one- and three-dimensional Green's functions 1. Strong motions, *J. Geophys. Res.*, **106**(B5), 8745-8766.

Grigoli, F., Cesca, S., Dahm, T. & Krieger, L., 2012. A complex linear least-squares method to derive relative and absolute orientations of seismic sensors, *Geophys. J. Int.*, **188**, 1243–1254, doi: 10.1111/j.1365-246X.2011.05316.x

Gritto, R., Yoo, S.-H. & Jarpe, S.P., 2013a. 3D seismic tomography at The Geysers geothermal field, CA, USA, in proceedings of *Thirty-Eighth Workshop on Geothermal Reservoir Engineering*, Stanford University, California, 11-13 February 2013.

Gritto, R., Yoo, S.-H. & Jarpe, S., 2013b. Seismic Imaging of reservoir structure at The Geysers geothermal reservoir, *AGU Fall Meeting 2013* S33D-2460, San Francisco, USA, 9–13 December 2013.

Gritto, R. & Jarpe, S.P., 2014. Temporal variations of V_P/V_S-ratio at The Geysers geothermal field, USA, *Geothermics*, **52**, 112-119, doi: 10.1016/j.geothermics.2014.01.012.

Guilhem, A. & Dreger, D.S., 2011. Rapid detection and characterization of large earthquakes using quasi-finite source Green's functions in continuous moment tensor inversion, *Geophys. Res. Lett.*, **38**, L13318, doi:10.1029/2011GL047550.

Guilhem A., Dreger, D.S., Tsuruoka, H. & Kawakatsu, H., 2013. Moment tensors for rapid characterization of megathrust earthquakes: the example of the 2011 M9 Tohoku-oki, Japan earthquake, *Geophys. J. Int.*, **192**(2), 759-772 doi:10.1093/gji/ggs045.

Guilhem, A., Hutchings, L., Dreger, D.S. & Johnson, L.R., 2014. Moment tensor inversions of M ~ 3 earthquakes in The Geysers geothermal fields, California, *J. Geophys. Res.*, **119**, 2121-2137, 10.1002/2013JB010271.

Gunderson, R.P., 1991. Porosity of reservoir greywacke at The Geysers, in *Monograph on The Geysers Geothermal Field*, Geothermal Resources Council Spl. Rept. No. 17, pp. 89-93.

Handel, A., Ohrnberger, M. & Krüger, F., 2016. Extracting near-surface Q_L between 1–4 Hz from higher-order noise correlations in the Euroseistest area, Greece, *Geophys. J. Int.*, **207**, 655–666, doi: 10.1093/gji/ggw295.

Haney, M., Mikesell, T.D., van Wijk, K. & Nakahara, H., 2012. Extension of the spatial autocorrelation (SPAC) method to mixed-component correlations of surface waves, *Geophys. J. Int.*, **191**, 189-206, doi: 10.1111/j.1365-246X.2012.05597.x.

Hardebeck, J.L., & Shearer, P.M., 2002. A new method for determining first-motion focal mechanisms, *Bull. Seismol. Soc. Am.*, **92**, 2264–2276.

Haskell, N.A., 1964. Radiation pattern of surface waves from point sources in a multi-layered medium, *Bull. Seismol. Soc. Am.*, **54**(1), 377-393.

Hearn, Jr., B.C., Donnelly-Nolan, J.M. & Goff, F.E., 1981. The Clear Lake volcanics: Tectonic setting and magma sources, *U.S. Geol. Surv. Prof. Pap.* 1141, 25-45.

Herrmann, R.B., 1973. Some aspects of band-pass filtering of surface waves, *Bull. Seismol. Soc. Am.*, **63**(2), 663-671.

Herrmann, R.B., Benz, H. & Ammon, C.J., 2011. Monitoring the earthquake source process in North America, *Bull. Seismol. Soc. Am.*, **101**(6), 2609-2625.

Herrmann, R.B., 2013a. Computer programs in seismology: An evolving tool for instruction and research, *Seism. Res. Lett.*, **84**, 1081-1088, doi:10.1785/0220110096.

Herrmann, R.B., 2013b. Update to *do_mft* for the determination of phase velocities from empirical Green's functions from noise cross-correlation, http://www.eas.slu.edu/eqc/eqc_cps/TUTORIAL/EMPIRICAL_GREEN/index.html, last accessed June 2016.

Horton, S.P., Ellsworth, W.L., Rubinstein, J.L. & Withers, M., 2013. Seismological observations associated with the development of a sinkhole near the Napoleonville Salt Dome, Louisiana, *SSA Annual Meeting 2013*, Salt Lake City, Utah, 17–19 April 2013.

Hudson, J.A., 1981. Wave speeds and attenuation of elastic waves in material containing cracks, *Geophys. J. R. astr. Soc.*, **64**, 133-150.

Hudson, J.A., 1982. Overall properties of a cracked solid, *Math. Proc. Camb. Phil. Soc.*, **88**, 371-384.

Hudson, J.A., Pearce, R.G. & Rogers, R.M., 1989. Source type plot for inversion of the moment tensor, *J. Geophys. Res.*, **94**(B1), 765–774.

Hutchings, L., 2001. Program NetMoment; simultaneous calculation of moment, source corner frequency, and site specific t* from network recordings, *Lawrence Livermore National Laboratory Report* UCRL-ID-135693-REV-1.

Jeanne, P., Rutqvist, J., Hartline, C., Garcia, J., Dobson, P.F. & Walter, M., 2014. Reservoir structure and properties from geomechanical modeling and microseismicity analyses associated with an enhanced geothermal system at The Geysers, California, *Geothermics*, **51**, 460-469, doi: 10.1016/j.geothermics.2014.02.003.

Johnson, C.W., Totten, E.J. & Bürgmann, R., 2016. Depth migration of seasonally induced seismicity at The Geysers geothermal field, *Geophys. Res. Lett*., **43**, 6196-6204, doi:10.1002/ 2016GL069546.

Jones, C.E. & Blom, R.G., 2014. Bayou Corne, Louisiana, sinkhole: Precursory deformation measured by radar interferometry, *Geol.*, **42**, 111-114, doi: 10.1130/G34972.1.

Jones, C.E. & Blom, R.G., 2015. Pre-event and post-formation ground movement associated with the Bayou Corne sinkhole, *NCKRI Symposium 5*, *Proceedings of the 14th Multidisciplinary Conference on Sinkholes and Engineering and Environmental Impacts of Karst*, 415-422, doi:10.5038/9780991000951.1083.

Jost, M.L. & Herrmann, R.B., 1989. A student's guide to and review of moment tensors, *Seism. Res. Lett.*, **60**(2), 37-57.

Jousset, P. & Rohmer, J., 2012. Evidence for remotely triggered microearthquakes during salt cavern collapse, *Geophys. J. Int.*, 191, 207–223, doi: 10.1111/j.1365-246X.2012.05598.x

Julian, B.R., Miller, A.D. & Foulger, G.R., 1998. Non-Double-Couple earthquakes – 1. Theory, *Rev. Geophys.*, **36**(4), 525-549.

Julian, B.R., Ross, A., Foulger, G.R. & Evans, J.R., 1996. Three-dimensional seismic image of a geothermal reservoir: The Geysers, California, *Geophys. Res. Lett*., **23**(6), 685-688.

Julian, B.R. & Sipkin, S.A., 1985. Earthquake processes in the Long Valley Caldera Area, California, *J. Geophys. Res.*, **90**(B13), 11155-11169.

Kawakatsu, H., 1998. On the realtime monitoring of the long-period seismic wavefield, *Bull. Earthq. Res. I. Tokyo*, 73, 267–274.

Kawakatsu, H., Montagner, J.-P. & Song, T.-R.A., 2015. On DLA's η, in Foulger, G.R., Lustrino, M. & King, S.D., eds., The Interdisciplinary Earth: A Volume in Honor of Don L. Anderson, *Geol. Soc. Am. Spl. Pap. 514 and Amer. Geophys. Union Spl. Publ. 71*, 33–38, doi:10.1130/2015.2514(03).

Kimman, W.P. & Trampert, J., 2010. Approximations in seismic interferometry and their effects on surface waves, *Geophys. J. Int.*, **182**, 461-476, doi: 10.1111/j.1365-246X.2010.04632.x.

Kinscher, J., Bernard, P., Contrucci, I., Mangeney, A., Piguet, J.P. & Bigarre, P., 2015. Location of microseismic swarms induced by salt solution mining, *Geophys. J. Int.*, 200, 337–362, doi: 10.1093/gji/ggu396.

Kumagai, H., Chouet, B.A., & Nakano, M., 2002. Waveform inversion of oscillatory signatures in long-period events beneath volcanoes, *J. Geophys. Res.*, **107**, B11, 2301, doi:10.1029/2001JB001704.

Kumagai, H., Chouet, B.A., & Dawson, P.B., 2005. Source process of a long-period event at Kilauea volcano, Hawaii, *J. Geophys. Res.*, **161**, 243-254, doi: 10.1111/j.1365-246X.2005.02502.x.

Lahr, J.C., 1999. HYPOELLIPSE: A computer program for determining local earthquake hypocentral parameters, magnitude, and first motion pattern, *U.S. Geological Survey Open-File Report 99-23*.

Lawrence, J.F., & Prieto, G.A., 2011. Attenuation tomography of the western United States from ambient seismic noise, *J. Geophys. Res.*, **116**, B06302, doi:10.1029/2010JB007836.

Lawrence, J.F., Denolle, M.A., Seats, K.J. & Prieto, G.A., 2013. A numeric evaluation of attenuation from ambient noise cross-correlation functions, *J. Geophys. Res.*, **118**, 6134–6145, doi:10.1002/2012JB009513.

Lee, E.-J., Chen, P., Jordan, T.H., Maechling, P.B., Denolle, M.A. & Beroza, G.C., 2014. Full-3-D tomography for crustal structure in Southern California based on the scattering-integral and the adjoint-wavefield methods, *J. Geophys. Res. Solid Earth*, **119**, 6421–6451, doi:10.1002/2014JB011346.

Lin, F.-C., Moschetti, M.P. & Ritzwoller, M.H., 2008. Surface wave tomography of the western United States from ambient seismic noise: Rayleigh and Love wave phase velocity maps, *Geophys. J. Int.*, **173**, 281-298, doi: 10.1111/j.1365-246X.2008.03720.x.

Lin, F.-C., Li, D., Clayton, R.W. & Hollis, D., 2013. High-resolution 3D shallow crustal structure in Long Beach, California: Application of ambient noise tomography on a dense seismic array, *Geophys*., **78**(4), Q45–Q56, doi: 10.1190/GEO2012-0453.1

Lin, F.-C., Tsai, V.C. & Schmandt, B., 2014. 3-D crustal structure of the western United States: application of Rayleigh-wave ellipticity extracted from noise cross-correlations, *Geophys. J. Int.* **198**, 656-670, doi: 10.1093/gji/ggu160.

Liu, X. & Kieffer, S.W., 2009. Thermodynamics and mass transport in multicomponent, multiphase H_2O systems of planetary interest, *Annu. Rev. Earth Planet. Sci.*, **37**, 449–77, doi: 10.1146/annurev.earth.031208.100109.

Lockner, D.A., Summers, R., Moore, D. & Byerlee, J.D., 1982. Laboratory Measurements of Reservoir Rock from the Geysers Geothermal Field, California, *Int. J. Rock Mech. Min. Sci. & Geomech. Abstr.*, **19**, 65-80.

Longuet-Higgins, M.S., 1950. A theory of the origin of microseisms, *Philos. Trans. R. Soc. London*, 243, 857, 1-35, doi:10.1098/rsta.1950.0012.

Louisiana Department of Natural Resources, Office of Conservation [LADNR, OOC], 2013. Louisiana DNR, Office of Conservation – Bayou Corne, ongoing investigation and response, presentation to the Joint Legislative Committees, Baton Rouge, Louisiana, 19 February 2013, http://dnr.louisiana.gov/assets/OC/BC_All_Updates/DNR.House.Senate.19Feb13.pdf (last accessed January 2017).

LADNR & CB&I (2013). Bayou Corne Public Briefing, 17 September 2013, http://www.dnr.louisiana.gov/assets/OC/BC_All_Updates/BCPublic.Briefing.9172013.pdf (last accessed January 2017).

Lowenstern, J.B. & Janik, C.J., 2003. The origins of reservoir liquids and vapors from The Geysers geothermal field, California (USA), in *Volcanic, geothermal and ore-forming fluids: Rulers and witnesses of processes within the Earth*, Society of Economic Geologists Special Publication 10, pp. 181-195.

Ludwin, R.S., Cagnetti, V. & Bufe, C.G., 1982. Comparison of seismicity in The Geysers geothermal area with the surrounding region, *Bull. Seismol. Soc. Am.*, **72**(3), 863–871.

Ma, S., Prieto, G.A. & Beroza, G.C., 2008. Testing community velocity models for southern California using the ambient seismic field, *Bull. Seismol. Soc. Am.*, **98**(6), 2694–2714, doi: 10.1785/0120080947.

Maeda, Y. & Takeo, M., 2011. Very-long-period pulses at Asama volcano, central Japan, inferred from dense seismic observations, *Geophys. J. Int.*, 185, 265-282, doi: 10.1111/j.1365-246X.2011.04938.x

Majer, E.L. & McEvilly, T.V., 1979. Seismological investigations at The Geysers geothermal field, *Geophys.*, **44**, 2, 246-269.

Majer, E.L. & Peterson, J.E., 2007. The impact of injection on seismicity at The Geysers, California geothermal field, *Int. J. Rock Mech. Min. Sci.*, **44**, 1079-1090.

Majer, E.L., McEvilly, T.V., Eastwood, F.S. & Myer, L.R., 1988. Fracture detection using P-wave and S -wave vertical seismic profiling at The Geysers, *Geophys*., **53(1)**, 76-84.

Matoza, R.S. & Chouet, B.A., 2010. Subevents of long-period seismicity: Implications for hydrothermal dynamics during the 2004–2008 eruption of Mount St. Helens, *J. Geophys. Res.*, 115, B12206, doi:10.1029/2010JB007839.

Maupin, V. & Park, J., 2007. Theory and observations—wave propagation in anisotropic media, in *Treatise on Geophysics*, Vol. 1: *Seismology and the Structure of the Earth*, pp. 289–321, eds Romanowicz, B. & Dziewonski, A., Elsevier, Boston.

Menon, R., Gerstoft, P. & Hodgkiss, W.S., 2014. On the apparent attenuation in the spatial coherence estimated from seismic arrays, *J. Geophys. Res. Solid Earth*, **119**, 3115–3132, doi:10.1002/2013JB010835.

Mercerat, E.D., Driad-Lebeau, L. & Bernard, P., 2010. Induced seismicity monitoring of an underground salt cavern prone to collapse, *Pure Appl. Geophys.*, 167, 5–25, doi: 10.1007/s00024-009-0008-1.

Miller, A.D., Foulger, G.R. & Julian, B.R., 1998. Non-Double-Couple earthquakes – 2. Observations, *Rev. Geophys.*, **36**(4), 551-568.

Minson, S.E., Dreger, D.S., Burgmann, R., Kanamori, H. & Larson, K.M., 2007. Seismically and geodetically determined non-double couple source mechanisms from the Miyakejima volcanic earthquake swarm, *J. Geophys. Res.*, **112**, B10308, doi:10.1029/2006JB004847.

Minson, S.E. & Dreger, D.S., 2008. Stable inversions for complete moment tensor, *Geophys. J. Int.*, **174**, 585-592, doi: 10.1111/j.1365-246X.2008.03797.x.

Montagner, J.P. & Anderson, D.L., 1989. Petrological constraints on seismic anisotropy, *Phys. Earth Planet. In.*, **54**, 82-105.

Moran, S.C., Malone, S.D., Qamar, A.I., Thelen, W., Wright, A.K. & Caplan-Auerbach, J., 2008. 2004–2005 seismicity associated with the renewed dome-building eruption of Mount St. Helens. In: Sherrod, D.R., Scott, W.E., Stauffer, P.F. (Eds.), A Volcano Rekindled: The Renewed Eruption of Mount St. Helens, 2004–2006: *U.S. Geological Survey Professional Paper*, 1750, 27–60 (Chap. 2).

Morrissey, M.M. & Chouet, B.A., 1997. A numerical investigation of choked flow dynamics and its application to the triggering mechanism of long-period events at Redoubt Volcano, Alaska, *J. Geophys. Res.*, 102, 7965–7983.

Mossop, A. & Segall, P., 1999. Volume strain within The Geysers geothermal field, *J. Geophys. Res.*, **104**(B12), 29113-29131.

Mousavi, S.M., Horton, S.P., Langston, C.A. & Samei, B., 2016. Seismic features and automatic discrimination of deep and shallow induced-microearthquakes using neural

network and logistic regression, *Geophys. J. Int.*, 207, 29–46, doi: 10.1093/gji/ggw258.

Mustać, M. & Tkalčić, H., 2016. Point source moment tensor inversion through a Bayesian hierarchical model, *Geophys. J. Int.*, 204, 311–323, doi: 10.1093/gji/ggv458.

Nakano, M., Kumagai, H. & Chouet, B.A., 2003. Source mechanism of long-period events at Kusatsu-Shirane Volcano, Japan, inferred from waveform inversion of the effective excitation functions, *J. Volcanol. Geoth. Res.*, **122**, 149-164.

Nakano, M. & Kumagai, H., 2005. Waveform inversion of volcano-seismic signals assuming possible source geometries, *Geophys. Res. Lett.*, **32**, L12302, doi:10.1029/2005GL022666.

Nakata, N., Snieder, R., Tsuji, T., Larner, K. & Matsuoka, T., 2011. Shear wave imaging from traffic noise using seismic interferometry by cross-coherence, *Geophys*., **76**(6), SA97-SA106, doi: 10.1190/GEO2010-0188.1.

Nakata, N., Chang, J., Lawrence, J.F. & Boué, P., 2015. Body wave extraction and tomography at Long Beach, California, using ambient noise interferometery, *J. Geophys. Res.*, **120**, 1159-1173, doi: 10.1002/2015JB011870.

Nayak, A & Dreger, D.S., 2014 [ND14]. Moment tensor inversion of seismic events associated with the sinkhole at Napoleonville Salt Dome, Louisiana, *Bull. Seismol. Soc. Am.*, **104**(4), 1763-1776, doi: 10.1785/0120130260.

Nayak, A & Dreger, D.S., 2015 [ND15]. Source-type-specific inversion of moment tensors, *Bull. Seismol. Soc. Am.*, **105**(6), 2987–3000, doi: 10.1785/0120140334.

Neal, J.T. & Magorian, T.R, 1997. Geologic site characterization principles derived from storage and mining projects in salt, with application to environmental surety, *Environ. Geol.*, **29**, 165-175.

Neal, J.T., Bauer, S.J. & Ehgartner, B.L., 1998. Mine-induced sinkholes over U.S. Strategic Petroleum Reserve Storage Facility at Week's Island: Geologic causes and effects, in Borchers, J., ed., Land subsidence: Current research and case histories, Proceedings of Dr. Joseph F. Poland Symposium on Land subsidence: Sacramento, California, October 4-5, 1995, Association Engineering Geologists Special Publication 8.

Nishida, K., Kawakatsu, H. & Obara, K., 2008. Three-dimensional crustal S wave velocity structure in Japan using microseismic data recorded by Hi-net tiltmeters, *J. Geophys. Res.*, **113**, B10302, doi:10.1029/2007JB005395.

O'Connell, D.R.H. & Johnson, L.R., 1991. Progression inversions for hypocenters and P wave and S wave velocity structure: application to The Geysers, California, geothermal field, *J. Geophys. Res.*, **96**(B4), 6223-6236.

Ohminato, T., 2006. Characteristics and source modeling of broadband seismic signals associated with the hydrothermal system at Satsuma–Iwojima volcano, Japan, *J. Volcanol. Geotherm. Res.*, 158, 467-490.

Oppenheimer, D.H., 1986. Extensional tectonics at The Geysers geothermal area, California, *J. Geophys. Res.*, **91**(B11), 11463-11476.

Panning, M., Dreger, D.S. & Tkalcic, H., 2001. Near-source velocity structure and isotropic moment tensors: a case study of the Long Valley Caldera, *Geophys. Res. Lett.*, **28**, 1815-1818.

Pasyanos, M.E., Dreger, D.S. & Romanowicz, B., 1996. Towards real-time estimation of regional moment tensors, *Bull. Seismol. Soc. Am.*, **86**, 1255-1269.

Peacock, S. & Hudson, J.A., 1990. Seismic properties of rocks with small distributions of

cracks, *Geophys. J. Int.*, **102**, 471-484.

Petersson, N.A. & Sjögreen, B., 2012. Stable and efficient modeling of anelastic attenuation in seismic wave propagation, *Comm. Comput. Phys.*, **12**(1), 193–225.

Petersson, N.A. & Sjögreen, B., 2014a. SW4-v1.1 Users Guide, https://geodynamics.org/cig/software/sw4/, last accessed, December 2015.

Petersson, N.A. & Sjögreen, B., 2014b. Super-grid modeling of the elastic wave equation in semi- bounded domains, *Comm. Comput. Phys.*, **16**, 913-955.

Petersson, N.A. & Sjögreen, B., 2015. SW4-v1.18 Users Guide, https://github.com/geodynamics/sw4

Porritt, R.W., Allen, R.M., Boyarko, D.C. & Brudzinski, M.R., 2011. Investigation of Cascadia segmentation with ambient noise tomography, *Earth Planet. Sci. Lett.*, **309**, 67–76, doi:10.1016/j.epsl.2011.06.026.

Prieto, G.A. & Beroza, G.C., 2008. Earthquake ground motion prediction using the ambient seismic field, *Geophys. Res. Lett.*, **35**, L14304, doi:10.1029/2008GL034428.

Prieto, G.A., Lawrence, J.F. & Beroza, G.C., 2009. Anelastic Earth structure from the coherency of the ambient seismic field, *J. Geophys. Res.*, **114**, B07303, doi:10.1029/2008JB006067.

Prieto, G.A., Denolle, M.A., Lawrence, J.F. & Beroza, G.C., 2011. On amplitude information carried by the ambient seismic field, *C. R. Geosci.*, **343**, 600-614, doi:10.1016/j.crte.2011.03.006

Ratigan, J.L. & Hill, K.B., 2013. Proximity of Class II and Class III well caverns to the edge of the Napoleonville Salt Dome, Topical Report PB-0374 developed by Ratigan Engineering & Consulting LLC and Hill Geophysical under subcontract to PB Energy Storage Services, Inc., http://www.dnr.louisiana.gov/assets/OC/im_div/ProximityofClassIIandIIIWellCaverns totheEdgeoftheNapoleonvilleSaltDome_Ratigan_2013.pdf, last accessed January 2017.

Reasenberg, P.A. & Oppenheimer, D., 1985. FPFIT, FPPLOT, and FPPAGE: Fortran computer programs for calculating and displaying earthquake fault-plane solutions, *U.S. Geol. Surv. Open-File Rep. 85-739*.

Romanowicz, B., 1995. A global tomographic model of shear attenuation in the upper mantle, *J. Geophys. Res.*, **100(B7)**, 12375-12394.

Roux, P., 2009. Passive seismic imaging with directive ambient noise: application to surface waves and the San Andreas Fault in Parkfield, CA, *Geophys. J. Int.*, **179**, 367-373, doi: 10.1111/j.1365-246X.2009.04282.x.

Saade, M., Montagner, J.P., Roux, P., Cupillard, P., Durand, S. & Brenguier, F., 2015. Influence of seismic anisotropy on the cross correlation tensor: numerical investigations, *Geophys. J. Int.*, **201**, 595-604, doi: 10.1093/gji/ggu470.

Saikia, C.K., Kafka, A.L., Gnewuch, S.C. & McTigue, J.W., 1990. Shear wave and intrinsic *Q* structure of the shallow crust in southeastern New England from *Rg* wave dispersion, *J. Geophys. Res.*, **95**(B6), 8527-8541.

Saikia, C.K., 1994. Modified frequency-wavenumber algorithm for regional seismograms using Filon's quadrature: modeling Lg waves in eastern North America, *Geophys. J. Int.*, **118**, 142–158.

Sammis, C.G., An, L. & Ershaghi, I., 1992. Determining the 3-D fracture structure in the Geysers geothermal reservoir, in proceedings of *seventeenth Workshop on Geothermal*

Reservoir Engineering, Stanford University, California, 29-31 January 1992.

Seats, K.J., Lawrence, J.F. & Prieto, G.A., 2012. Improved ambient noise correlation functions using Welch's method, *Geophys. J. Int.*, **188**, 513–523, doi: 10.1111/j.1365-246X.2011.05263.x.

Sens-Schönfelder, C. & Wegler, U., 2006. Passive image interferometry and seasonal variations of seismic velocities at Merapi Volcano, Indonesia, *Geophys. Res. Lett.*, **33**, L21302, doi:10.1029/2006GL027797.

Sens-Schönfelder, C., 2008. Synchronizing seismic networks with ambient noise, *Geophys. J. Int.*, **174**, 966–970, doi: 10.1111/j.1365-246X.2008.03842.x.

Shani-Kadmiel, S., Tsesarsky, M., Louie, J.N. & Gvirtzman, J., 2014. Geometrical focusing as a mechanism for significant amplification of ground motion in sedimentary basins: analytical and numerical study, *Bull. Earthq. Eng.*, **12**, 607–625, doi:10.1007/s10518-013-9526-4.

Shapiro, N.M. & Campillo, M., 2004. Emergence of broadband Rayleigh waves from correlations of the ambient seismic noise, *Geophys. Res. Lett.*, **31**, L07614, doi:10.1029/2004GL019491.

Shapiro, N.M., Campillo, M., Stehly, L. & Ritzwoller, M.H., 2005. High resolution surface wave tomography from ambient seismic noise, *Science*, **307**, 1615-1618, doi: 10.1126/science.1108339.

Šílený, J., Hill, D.P., Eisner, L. & Cornet, F.H., 2009. Non-double-couple mechanisms of microearthquakes induced by hydraulic fracturing, *J. Geophys. Res.*, **114**, B08307, doi: 10.1029/2008JB005987.

Silwal, V. & Tape, C., 2016. Seismic moment tensors and estimated uncertainties in southern Alaska, *J. Geophys. Res. Solid Earth*, 121, 2772–2797, doi:10.1002/2015JB012588.

Sjögreen, B. & Petersson, N.A., 2012. A fourth order accurate finite difference scheme for the elastic wave equation in second order formulation, *J. Sci. Comput.*, **52**, 17-48, doi:10.1007/s10915-011-9531-1.

Snieder, R., 2004. Extracting the Green's function from the correlation of coda waves: A derivation based on stationary phase, *Phys. Rev. E*, **69**, 046610.

Specht, S., Jousset, P., Zang, A., Gritto, R. & Bruhn, D., 2014. Velocity structure of The Geysers geothermal area (California) from ambient noise cross-correlation, *AGU Fall Meeting 2014* S51A-4425, San Francisco, USA, 15-19 December 2014.

Stark, M.A., 1991. Microearthquakes – A tool to track injected water in The Geysers reservoir, in *Monograph on The Geysers Geothermal Field*, Geothermal Resources Council Spl. Rept. No. 17, pp. 111-117.

Stehly, L., Campillo, M. & Shapiro, N.M., 2006. A study of the seismic noise from its long-range correlation properties, *J. Geophys. Res.*, **111**, B10306, doi:10.1029/2005JB004237.

Stidham, C., Antolik, M., Dreger, D.S., Larsen, S. & Romanowicz, B., 1999. Three-dimensional structure influences on the strong motion wavefield of the 1989 Loma Prieta earthquake, *Bull. Seism. Soc. Am.*, **89**, 1184-1202.

Stover, C.W. & Coffman, J.L., 1993. Seismicity of the United States 1568-1989 (Revised), *U.S. Geological Survey Professional Paper 1527*, *United States Government Printing Office, Washington*, 243-244.

Takagi, R., Nishida, K., Aoki, Y., Maeda, T., Masuda, K., Takeo, M., Obara, K., Shiomi, K., Sato, M. & Saito, K., 2015. A single bit matters – coherent noise of seismic data

loggers, *Seism. Res. Lett.*, **86**(3), 901-907, doi: 10.1785/0220150030.

Taira, T., Brenguier, F. & Kong, Q., 2015. Ambient noise-based monitoring of seismic velocity changes associated with the 2014 Mw 6.0 South Napa earthquake, *Geophys. Res. Lett.*, **42**, 6997–7004, doi:10.1002/2015GL065308.

Tape, W. & Tape, C., 2012a. A geometric setting for moment tensors, *Geophys. J. Int.*, **190**, 476–498, doi: 10.1111/j.1365-246X.2012.05491.x

Tape, W. & Tape, C., 2012b. A geometric comparison of source-type plots for moment tensors, *Geophys. J. Int.*, **190**, 499–510, doi: 10.1111/j.1365-246X.2012.05490.x

Tape, W. & Tape, C., 2013. The classical model for moment tensors, *Geophys. J. Int.*, **195**(3), 1701-1720, doi: 10.1093/gji/ggt302.

Tape, W. & Tape, C., 2015. A uniform parametrization of moment tensors, *Geophys. J. Int.*, 202, 2074–2081, doi: 10.1093/gji/ggv262.

Templeton, D.C. & Dreger, D.S., 2006. Non-Double-Couple earthquakes in the Long Valley volcanic region, *Bull. Seismol. Soc. Am.*, **96**(1), 69-79, doi: 10.1785/0120040206.

Texas Brine, Corp., 2013. Bayou Corne 3D—3D Reflection Seismic Results in response to LADNR, Directive 2A, 5th Amendment to Declaration of Emergency and Directive, 20 April 2013, http://dnr.louisiana.gov/assets/OC/BC_All_Updates/Plans_Reports/BayouCorne.T5.Seismic.Results.0420.2013.pdf (last accessed August 2013).

Thompson, R.C., 1989. Structural stratigraphy and intrusive rocks at The Geysers geothermal field, *Trans.* Geothermal Resources Council, **13**, 481-485.

Thoms R.L. & Gehle, R.M., 2000. A brief history of salt cavern use (keynote paper), in: Geertman, R.M., ed., *Proceedings of 8th World Salt Symposium*, 7-11 May 2000, part 1, Elsevier B.V. 207-214.

Towns, J., Cockerill, T., Dahan, M., Foster, I., Gaither, K., Grimshaw, A., Hazlewood, V., Lathrop, S., Lifka, D., Peterson, G.D., Roskies, R., Scott, J.R. & Wilkins-Diehr, N., 2014. XSEDE: Accelerating Scientific Discovery, *Comput. Sci. Eng.*, **16**(5), 62-74, doi:10.1109/MCSE.2014.80.

Trifu, C-I., Angus, D. & Shumila, V., 2000. A fast evaluation of the seismic moment tensor for induced seismicity, *Bull. Seismol. Soc. Am.*, **90**(6), 1521-1527.

Trifu, C-I. & Shumila, V., 2002. The use of uniaxial recordings in moment tensor inversions for induced seismic sources, *Tectonophysics*, **356**, 171-180.

Trifu, C.-I. & Shumila,V, 2010. Microseismic monitoring of a controlled collapse in Field II at Ocnele Mari, Romania, *Pure Appl. Geophys.* 167, 27–42, doi: 10.1007/s00024-009-0013-4.

Truesdell, A.H., Haizlip, J.R., Box, Jr., W.T. & Amore, F.D', 1991. A geochemical overview of The Geysers geothermal reservoir, in *Monograph on The Geysers Geothermal Field*, Geothermal Resources Council Spl. Rept. No. **17**, 121-132.

Trugman, D.T., Shearer, P.M., Borsa, A.A. & Fialko, Y., 2016. A comparison of long-term changes in seismicity at The Geysers, Salton Sea, and Coso geothermal fields, *J. Geophys. Res.*, **121**, 225–247, doi: 10.1002/2015JB012510.

Tsai, V.C., 2009. On establishing the accuracy of noise tomography travel-time measurements in a realistic medium, *Geophys. J. Int.*, **178**, 1555–1564, doi: 10.1111/j.1365-246X.2009.04239.x.

Tsai, V.C., 2011. Understanding the amplitudes of noise correlation measurements, *J. Geophys. Res.*, **116**, B09311, doi:10.1029/2011JB008483.

Tsai, V.C. & Moschetti, M.P., 2010. An explicit relationship between time-domain noise correlation and spatial autocorrelation (SPAC) results, *Geophys. J. Int*, **182**, 454–460, doi: 10.1111/j.1365-246X.2010.04633.x.

Tsuruoka, H., Kawakatsu, H. & Urabe, T., 2009. GRiD MT (grid-based real-time determination of moment tensors) monitoring the long period seismic wavefield, *Phys. Earth Planet. In.*, **175**, 8–16, doi:10.1016/j.pepi.2008.02.014.

Um, J., & Thurber, C., 1987. A fast algorithm for two-point seismic ray tracing, *Bull. Seismol. Soc. Am.*, **77**(3), 972-986.

van Wijk, K., Mikesell, T.D., Schulte-Pelkum, V. & Stachnik, J., 2011. Estimating the Rayleigh-wave impulse response between seismic stations with the cross terms of the Green tensor, *Geophys. Res. Lett*., **38**, L16301, doi:10.1029/2011GL047442.

Vavryčuk, V., 2011. Tensile earthquakes: Theory, modeling, and inversion, *J. Geophys. Res.*, **116**, B12320, doi:10.1029/2011JB008770.

Vavryčuk, V., 2013. Is the seismic moment tensor ambiguous at a material interface? *Geophys. J. Int.* 194, 395–400, doi: 10.1093/gji/ggt084.

Vavryčuk, V., 2015. Moment tensor decompositions revisited, *J. Seism.*, **19**(1), 231-252, doi: 10.1007/s10950-014-9463-y.

Viegas, G. & Hutchings, L., 2011. Characterization of Induced Seismicity near an Injection Well at the Northwest Geysers Geothermal Field, California, *Trans.* Geothermal Resources Council, **35**, 1773-1780.

Waite, G.P., Chouet, B.A. & Dawson, P.B., 2008. Eruption dynamics at Mount St. Helens imaged from broadband seismic waveforms: interaction of the shallow magmatic and hydrothermal systems, *J. Geophys. Res.*, 113, B02305, doi:10.1029/2007JB005259.

Wang, C.Y. & Herrmann, R.B., 1980. A numerical study of P-, SV- and SH-wave generation in a plane layered medium, *Bull. Seismol. Soc. Am.*, **70**(4), 1015-1036.

Watson, T.H., 1970. A note on fast computation of Rayleigh wave dispersion in the multi-layered elastic half-space, *Bull. Seismol. Soc. Am.*, **60**(1), 161-166.

Weemstra, C., Westra, W., Snieder, R. & Boschi, L., 2014. On estimating attenuation from the amplitude of the spectrally whitened ambient seismic field, *Geophys. J. Int.*, 197, 1770–1788, doi: 10.1093/gji/ggu088.

Weemstra, C., Snieder, R. & Boschi, L., 2015. On the estimation of attenuation from the ambient seismic field: inferences from distributions of isotropic point scatterers, *Geophys. J. Int.*, **203**, 1054–1071, doi: 10.1093/gji/ggv311.

Wegler, U., Nakahara, H., Sens-Schonfelder, C., Korn, M. & Shiomi, K., 2009. Sudden drop of seismic velocity after the 2004 Mw 6.6 mid-Niigata earthquake, Japan, observed with Passive Image Interferometry, *J. Geophys. Res.*, **114**, B06305, doi:10.1029/2008JB005869.

Wessel, P. & Smith, W.H.F., 1998. New, improved version of Generic Mapping Tools released, *Eos Trans. AGU*, 79, 579.

Wielandt, E. & Forbriger, T., 1999. Near-field seismic displacement and tilt associated with the explosive activity of Stromboli, *Ann. Geofis.*, **42**(3), 407-416.

Yokoi, T. & Margaryan, S., 2008. Consistency of the spatial autocorrelation method with seismic interferometry and its consequence, *Geophys. Prospect.*, **56**, 435-451.

Zhang, J. & X. Yang, 2013. Extracting surface wave attenuation from seismic noise using correlation of the coda of correlation, *J. Geophys. Res.*, **118**, 2191–2205, doi:10.1002/jgrb.50186, 2013.

Zhan, Z. & Ni, S., 2010. Stationary phase approximation in the ambient noise method revisited, *Earthq Sci*, **23**, 425-431, doi: 10.1007/s11589-010-0741-7.

Zhu, L. & Ben-Zion, Y., 2013. Parametrization of general seismic potency and moment tensors for source inversion of seismic waveform data, *Geophys. J. Int.*, 194, 839–843, doi: 10.1093/gji/ggt137.

Zhu, L. & Zhou, X., 2016. Seismic moment tensor inversion using 3D velocity model and its application to the 2013 Lushan earthquake sequence, *Phys. Earth Planet. Inter.*, **95**, 10-18, doi: 10.1016/j.pce.2016.01.002.

Zong, J., 2014. Elastic properties of salt: Laboratory measurements, well-log analysis, and a seismic survey over the Hockley salt mine, Texas, *M.Sc. Thesis, Dept. of Earth and Atmospheric Sciences, Univ. of Houston, USA*.